Variations to a bio-electrochemical nitro-reduction catalyst for the production of amines

Maya Ann Landis

Jesus College
University of Oxford

A thesis submitted for the degree of Doctor of Philosophy
Michaelmas 2024

Acknowledgements

First and foremost, I would like to extend my gratitude to my supervisors, Kylie Vincent and Nicole Grobert, for allowing me the opportunity to work on this project. My four years at Oxford would not have been the same without Kylie's patient and kind support, and of course her inspiring ideas. Thank you to Nicole for her project guidance and insightful career advice, which I am sure will prove invaluable in the future.

Working alongside the members of the Vincent and Grobert groups has been a privilege and I am grateful to all of you for your companionship and advice. Thank you to Tim Sudmeier and Basia Maciejewska for the fantastic training. I am especially grateful to Lucy, Yu Sun, Alison, Tara, Daria, Liz, Shoba, and Luna, for the memories we made together. I can't wait to meet again and hear about your fantastic futures! In the Grobert group, thank you to George for always being my TEM partner in crime, and to Dillon for his CVD magic.

I am grateful to the OxICFM CDT for funding me, and for affording me the opportunity to undertake two placements during my DPhil studies. Thank you to Maitane for all her help.

The staff at Begbroke, at the DCCEM, and of course in the ICL are invaluable to all of our research, and I am grateful for their support.

Thank you to Bertrand Reuillard and Vincent Artero for welcoming me during my three months in the Solhycat team in Grenoble, where I was able to learn a great deal from their expertise.

Thank you, the amazing friends I have met in Oxford, – to Tiffany for supporting all of my plans, to Mila for always taking care of me, to the volleyball group, to the Jesus College choir and MCR, to Matt and Charlie for taking me to concerts; to Kam, Helen, James, Joe, Nina, and Emma for being housemates that made my rooms feel like home.

To the friends who supported me from afar I am truly grateful – Allison, Ester, and Deborah, thank you! Last but not least, I am indebted to my family, without whom I could not have written this thesis.

Abstract

Variations to a Bio-electrochemical Nitro-reduction Catalyst for the Production of Amines

A thesis submitted for the degree of Doctor of Philosophy

Maya Landis, Jesus College, Michaelmas 2024

This thesis aims to unite materials and catalysis research to establish new directions for a biocatalytic nitro-reduction system developed by the Vincent group, consisting of hydrogenase enzyme immobilised on conductive carbon particles. In this system, the nitro-group can be reduced on the carbon surface using the electrons provided by the hydrogenase through H_2 oxidation. In the first part of the thesis, the carbon support is varied while the second part of the thesis focuses on replacing the enzyme with a synthetic H_2 oxidation catalyst.

In the first part, a set of nitrogen-doped carbon nanotubes (NCNTs), along with comparable pristine CNTs, are synthesized through chemical vapour deposition and their nitro-reduction activity is electrochemically assessed. The NCNTs lead to the nitro-reduction occurring at a significantly milder potential as opposed to the CNTs or any other trialled carbon-based electrode material. This electrocatalytic effect is then used to both electrosynthesize amines using milder conditions and to tune the hydrogenase-on-carbon (Hyd/C) catalyst system to hydrogenate more difficult to reduce nitro-groups.

In the second part of the thesis, an established Ni-based biomimetic H_2-oxidation catalyst is employed. The complex on carbon constitutes a highly selective, active, and recyclable catalyst system for the production of amines from nitro-groups in aqueous media, room temperature, and at atmospheric H_2 pressure. Interestingly, the complex in solution is found to catalyse the clean synthesis of the partially reduced product, hydroxylamine.

List of Abbreviations

ACN	Acetonitrile
APIs	Active pharmaceutical ingredients
CE	Counter electrode
CF	Carbon felt
CP	Carbon paper
CV	Cyclic voltammogram
CVD	Chemical vapour deposition
FE	Faradaic efficiency
Hyd-1	Hydrogenase 1 from *Escherichia Coli*
NAD(P)H	Nicotinamide adenine dinucleotide (phosphate)
NCNTs	Nitrogen doped carbon nanotubes
NMR	Nuclear magnetic resonance
ORR	Oxygen reduction reaction
PB	Phosphate buffer (here, always sodium phosphate buffer)
PGMs	Platinum group metals
PHA	Phenylhydroxylamine

RE	Reference electrode
RPM	Rotations per minute
RT	Room temperature
scc/min	Standard cubic centimetre per minute
SCE	Saturated calomel electrode
SLM	Standard litre per minute
SW-, DW-, MW- CNTs	Single walled, double walled, multi walled- carbon nanotubes
SEM	Scanning electron microscopy
TEM	Transmission electron microscopy
TGA	Thermogravimetric analysis
WE	Working electrode
XPS	X-ray photoelectron spectroscopy

Prizes and Publications

Prizes

Jamie Ferguson Innovation Award, Oxford University Innovation, June 2024
Project: Hydro-green-ation: Towards cleaner hydrogen use in chemical synthesis
Best Poster Prize, 14th ECHEMS Meeting 2024, October 2024
Variations of a bio-electrochemical nitro-reduction catalyst for the production of amines

Publications

Maya A. Landis, Tim Sudmeier, Dillon McGurty, Barbara Maciejewska, Nicole Grobert, Kylie a. Vincent. Tuning the reduction potential of nitro-compounds via the nitrogen-doping of multi- ealled carbon nanotubes facilitates hydrogenation of aliphatic nitro-compounds. *In preparation.*

Maya A. Landis, Daria Sokolova, Bertrand Reuillard, Nicole Grobert, Vincent Artero, Kylie A. Vincent. Hydrogenation of nitro-compounds to amines at room temperature and atmospheric hydrogen pressure using a DuBois-type biomimetic nickel complex. *In preparation.*

Browne, L. B. F.; Sudmeier, T.; Landis, M. A.; Allen, C. S.; Vincent, K. A. Controlled Biocatalytic Synthesis of a Metal Nanoparticle-Enzyme Hybrid: Demonstration for Catalytic H2-driven NADH Recycling. *Angewandte Chemie International Edition* **2024**, *63* (27).

List of Figures

List of Tables

Table of Contents

1 Introduction

The reduction of nitro-groups to amines is a reaction of immense industrial importance, both historically and today. Indeed, the largest chemical producer in the world, BASF, still clings to the name *'Badische Anilin und Soda Fabrik'* – Baden Aniline and Soda Factory - that harkens back to the dye industry of the 19th century that grew dramatically through the development of nitro-reduction methods for the production of anilines.[1,2] This thesis explores the nitro-reduction reaction through an interdisciplinary lens by first evaluating carbon nanomaterials as electrocatalysts, subsequently employing them in a bio-hybrid hydrogenation system, and finally exploring alternative inorganic biomimetic hydrogenation catalysts, with the goal of elucidating the role of the carbon support and further tuning a green and selective biocatalytic nitro-reduction method developed in the Vincent group.

1.1 Production of amines

1.1.1 Importance of the nitro-to-amine transformation

A 2011 survey of reaction types used to pursue novel drug candidates found that the R-NO_2 to amine transformation was the most common of all reductions at 19.2%.[4] Indeed, many of the essential medicines listed by the World Health Organisation (WHO) are synthesized from nitrated building blocks that are transformed into the corresponding amine, including notably

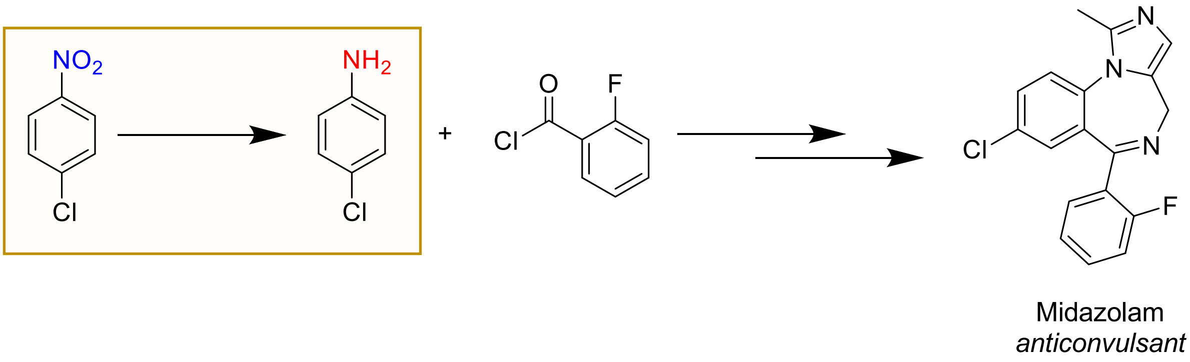

Scheme 1 Anticonvulsant midazolam is synthesized from 4-chloroaniline, which in turn is produced in large volume from p−nitrochlorobenzene. Adapted from reference 5.

the pain reliever paracetamol, the anaesthetic midazolam (Scheme 1),[5] and the anticonvulsant carbamazepine, among many others.[6] Besides their crucial importance for the synthesis of active pharmaceutical ingredients (APIs), amines produced from nitrated precursors also feature commonly in the polyurethane industry, the production of fertilizers and explosives, as well as the production of dyes.[7,8] Today, aryl amines are produced at large scale through heterogeneous hydrogenation over precious metal catalysts, a process that is well-established but can suffer from low functional group selectivity and cements the chemical industry’s continuing reliance on rare and expensive elements as catalysts.[9]

1.1.2 Pathways and intermediates in the nitro-to-amine transformation

The full reduction of the nitro-group to the amine consists of the transfer of six electrons and six protons, and is understood to follow the pathways shown in Scheme 2 – a mechanism first described by Haber in 1900.[10] Sequential 2 electron reduction steps produce the nitroso (**1D**, N=O), then the hydroxylamine (**1B**, PHA, NHOH), and finally the amine (**1C**). Condensation of the nitroso-compound and PHA leads to the formation of the azoxybenzene (**1E**), which can be reduced to the amine via the azobenzene (**1F**).[11] Over-hydrogenation, which can occur under some conditions when using palladium on carbon catalysts, for example, can produce a wide

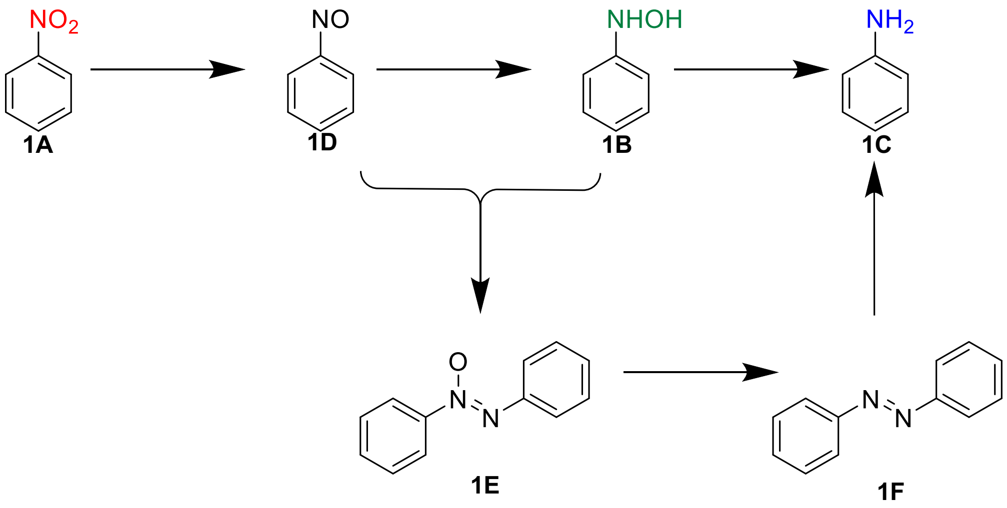

Scheme 2 Nitro-reduction pathways for the aromatic nitrobenzene. Adapted from reference 11.

range of by-products (Scheme 3) including cyclohexanone (**1G**), cyclohexanol **(1H),** cyclohexylamine (**1I**), N-cyclohexylaniline (**1J**), and dicyclohexylamine (**1K**).[12] Catalytic systems for the production of amines from nitro-groups must not only show good functional group selectivity, but must be highly selective towards the fully reduced amine as there are multiple possible intermediates for this reaction.

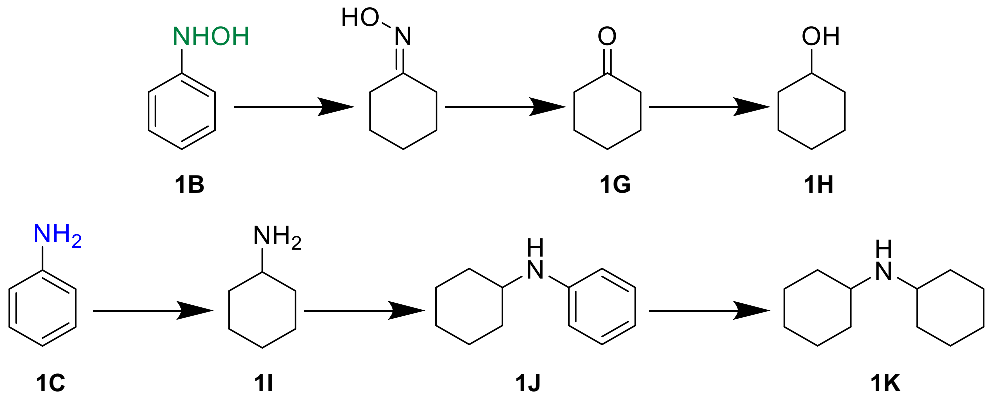

Scheme 3 Over-reduction pathways for PHA and aniline. Adapted from reference 12.

1.1.3 Nitro-to-amine: Current heterogeneous and stoichiometric methods

Heterogeneous hydrogenation using platinum group metals (PGMs) can activate many nitro-groups and is well established in industry; however, achieving selectivity for nitro-group hydrogenation in the presence of sensitive functional groups requires modification of the catalyst or addition of modifying reagents, which complicates catalyst preparation and increases waste. For example, Mao *et al* reported in 2017 that introducing lattice strain to a ruthenium catalyst particle improved selectivity for nitro-styrene to vinylamine hydrogenation from 66% to 99%.[13] Other approaches in literature include the use of an intermetallic Pd-Pb system to establish polar catalytic active sites to tune activity[14] or the addition of reagents capable of partially poisoning the catalyst, such as diphenylsulfide as a poison to Pd/C[15].

Apart from heterogeneous catalytic hydrogenation, a historically relevant approach to the nitro-reduction reaction has been the use of stoichiometric reductants – note, for example, the Bechamp Reduction using hydrochloric acid and iron, first reported in 1854 (*Scheme 4*).[16] Other possible stoichiometric reducing agents include tin chloride[17], siloxanes[18], sodium borohydride[19], and sodium hydrosulfide[20]. While these reagents negate the need for pressurized H_2 gas, they introduce significant waste and complexity to the process and can themselves add chemical hazards.

$$4\ C_6H_5NO_2 + 9\ Fe + 4\ H_2O \longrightarrow 4\ C_6H_5NH_2 + 3\ Fe_3O_4$$

Scheme 4: *Bechamp reduction of nitrobenzene. Adapted from reference 16.*

1.1.4 Nitro-to-amine: Molecular catalysts

As opposed to the heterogeneous catalytic and stoichiometric systems described above, molecular, homogeneous catalysts are more defined and more readily tuneable through their ligand scaffold. Nevertheless, molecular catalysts for the nitro-to-amine hydrogenation are only rarely reported, and typically still suffer from their need for harsh conditions. In 2013, Wienhoefer *et al* reported the use of a defined iron-phosphine complex able to activate hydrogen, at 20 bar pressure and elevated temperature, and hydrogenate a range of substituted nitroarenes.[21] Sun *et al* have reported a nickel-catalysed hydrogenation using polymethylhydrosiloxane as the reductant.[18] The reported use of a molecular manganese complex as a hydrogenation catalyst of a wide range of nitroarenes is also interesting – however, this system requires high pressures of hydrogen gas (80 bar), as well as a temperature of 130 °C, introducing significant safety and energy-efficiency concerns.[22]

1.1.5 Nitro-to-amine: Biocatalytic methods

Nature, 'herself a brilliant chemist and by far the best engineer of all time',[23] has developed enzymes as efficient catalysts for countless chemical reactions. These natural catalysts rely on affordable metals, most commonly magnesium, zinc, or iron, are biodegradable, and often highly selective as well as tuneable.[24, 25] Applying enzymes to industrial processes can;

- Decrease the toxicity associated with the chemical reaction
- Decrease energy and solvent usage
- Improve chemo- and regio-selectivity
- Decouple the process from expensive and environmentally degrading rare element mining.[26]

However, even with the above benefits of biocatalysis, its possible positive impact can be diminished by the conditions required for an individual reaction. While the use of water as the solvent is often described as a benefit of biocatalysis because of its safety and availability, the low solubility of many chemically interesting species forces the use of low starting material concentrations near the tens of millimolar range; consequently, a typical biocatalytic reaction produces large amounts of waste water as compared with the amount of product.[27] In addition, nearly half of all enzymatically catalysed reactions require cofactors – chemical species that are required for the enzyme's activity, by, for example, supplying a reducing equivalent.[28] These species (e.g., nicotinamide adenine dinucleotide (phosphate), NAD(P)H), are prohibitively expensive, necessitating a cofactor recycling system as part of the overall reaction, which introduces process complexity and diminishes atom economy.[29, 30]

Biocatalytic nitro-reduction systems reported in literature have required both cofactor-recycling systems and the addition of metal cocatalysts to reach the fully reduced amine product. Bornadel and coworkers, for example, reported a system based on the use of vanadium oxide as a disproportionation catalyst, and glucose as the terminal reductant (Figure 1).[31]

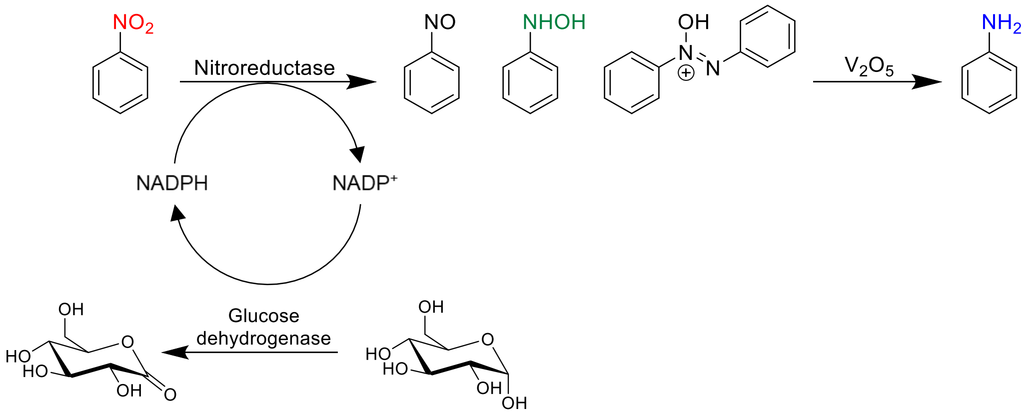

Figure 1 A nitro-to-amine process relying on a nitroreductase enzyme for partial reduction of the nitrogroup with a following disproportionation catalysed by V_2O_5 and using a glucose-based cofactor recycling system. Adapted from reference 31.

The Vincent group studies the use of hydrogenase enzyme to fuel biocatalytic transformation using hydrogen gas. By linking hydrogenase, capable of oxidising dihydrogen, and an NAD-reductase on a conductive carbon support, the electrons gained through hydrogen oxidation can be used to regenerate the NADH cofactor, greatly improving the atom economy associated with the reaction.[32] Interestingly, the hydrogenase enzyme was also found to directly regenerate flavin cofactors FMN and FAD under hydrogen gas – a non-native activity that was then employed to establish a nitro-reduction method based on a flavin-containing nitroreductase and the vanadium oxide co-catalyst, but avoiding the use of the waste-intensive glucose recycling system.[33, 34]

1.1.6 Electrochemical nitro-to-amine transformation

Many nitro-aromatic compounds are acutely toxic, carcinogenic, and relatively stable, meaning that nitroarene contaminated wastewater can have significant negative effects on people and the environment.[35] Indeed, many of these compounds are listed on the US Environmental

Protection Agency Priority Pollutant List.[36] The need for cheap and effective detection and remediation of these contaminants has inspired much of the previous research into the electrochemical reduction of the nitro-group. Electrochemical reduction of contaminants is energy-efficient, requires only a simple set up and no other chemical reagents; however, the reduced products, hydroxylamines and amines, remain highly toxic.[37] To completely remove the contaminants, the resulting amines can be subsequently polymerized leading to a precipitate, or can be adsorbed by cation exchangers.[38,39] Aside from its possible use for wastewater treatment, the study of the electrochemical nitro-reduction could lead to novel electro-synthetic methods for the production of amines and could provide valuable insights into the reduction mechanism of relevance to more traditional chemical hydrogenation systems.

1.1.7 Bio-electro-catalytic nitro-to-amine transformation

Recently, the Vincent group has reported a cofactor-free biocatalytic nitro-reduction method employing hydrogenase enzyme on a carbon black support, in which the hydrogenase enzyme oxidises dihydrogen, supplying electrons that are then available to reduce the nitro-group electrochemically at the conductive carbon surface.[2] The enzyme employed in this system, hydrogenase 1 (Hyd-1, see 1.3.1) from *Escherichia Coli* (E. *coli*), is robust, oxygen-tolerant, and can activate low concentrations of hydrogen gas.[40] The thermodynamic potential of the

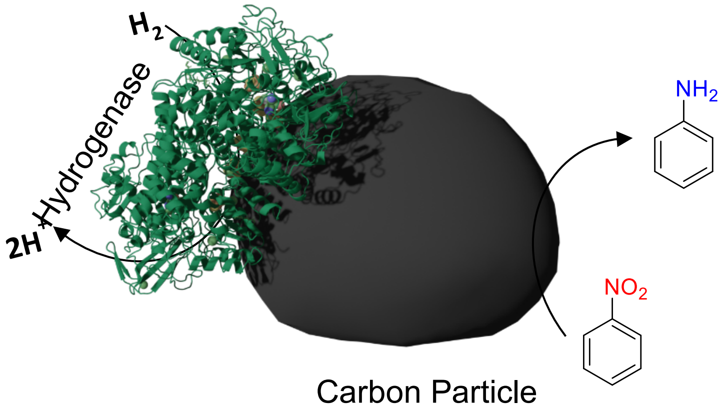

Figure 2: Hyd-1 on carbon (Hyd/C) catalyst for cofactor free, biocatalytic nitro-reduction towards amine. As described in reference 2.

$2H^+/H_2$ couple lies at -0.355 V at pH 6 and 1 bar hydrogen, while Hyd-1 operates with a mild overpotential and provides electrons at -0.296 V at the same conditions.[2] Any nitro-reduction that occurs on a carbon electrode at a more positive potential than -0.296 V should be accessible to the **Hyd1/C** catalyst, and indeed, the group has demonstrated the applicability of this system to a wide range of substituted nitro-arenes while at room temperature and atmospheric pressures of H_2.[2] Because the nitro-reduction is thought to occur electrochemically on the carbon support, methods such as cyclic voltammetry and bulk electrolysis can be used to reach a deeper understanding of this catalytic system. This catalyst system will be referred to as **Hyd/C**, or if specifically Hyd-1 is relevant, as **Hyd1/C** throughout this thesis.

1.2 Electrosynthesis and -catalysis

1.2.1 Fundamentals behind electrochemical reactions: Current and Potential

In electrochemistry, a given redox couple of oxidized species A and reduced species B (Eq. 1) is described based on a measured current and/or potential at a solution-electrode interface.

$$A + ne^- \leftrightarrows B \qquad \textit{Eq. 1}$$

For a given reduction reaction, the flow of electrons (*i.e.*, the current I) from the cathode to species A is influenced by the concentration of A at the electrode surface (and, it follows, by the mass transport of A to the electrode), and by the rate of the heterogeneous electron transfer reaction (k_{red}). In turn, k_{red} is governed by the relevant free energy of activation $\Delta G^\ddagger$ and by the interfacial potential difference between electrode and solution.[41]

Under equilibrium conditions, the potential of the electrode (as measured relative to a suitable reference electrode RE) reaches a steady value E_e, which can be described according to the Nernst equation (Eq. 2) as depending on the concentration of the relevant species as well as the standard reduction potential E^o of A.[41]

$$E_e = E^o - \frac{RT}{nF}\ln\frac{[B]}{[A]} \qquad Eq.\ 2$$

Where R is the gas constant, T the temperature in K, n the number of electrons passed, and F the Faraday constant.

In order to shift the reaction away from the equilibrium, a potential E unequal to E_e must be applied to the electrode (Figure 3). Many electrochemical transformations are only observed at a harsher potential E than the relevant E^o. The potential difference between the experimentally observed redox potential and the thermodynamic potential is known as the overpotential η:[42]

$$\eta = E - E_e \qquad Eq.\ 3$$

1.2.2 Electrosynthesis

Despite its long history – Faraday reported his electrolysis of sodium acetate in 1834 - electrosynthesis has been greatly underutilized by synthetic chemists.[43] There are, nonetheless, some examples of electro-synthetic processes that are important to the chemical industry. One of the earliest examples of industrial electrosynthesis is the Kolbe reaction, in which a C(sp^3)-C(sp^3) bond is formed through the electro-oxidative radical coupling of two carboxylic acids.[44] Today, adiponitrile (ADN), a precursor to Nylon-6,6, is produced through electro-reductive coupling on large scale – around 100,000 tonnes annually[45] – by BASF, Soluta, and Asahi Chemical. The reaction is carried out using a reduction potential of -0.56 V in aqueous

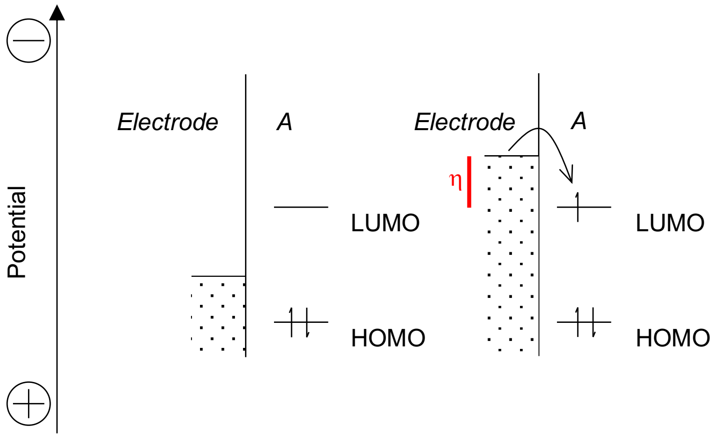

Figure 3: Graphic representation of electron transfer from the electrode to species A as an overpotential η is applied.

electrolyte, at mild temperatures, and atmospheric pressures (Figure 4). These mild conditions stand in stark contrast to the other well-known chemical method towards AND, which rely on elevated temperatures and pressures as well as the highly toxic hydrogen cyanide for the hydrocyanation of 1,3 butadiene. [46, 47] Recently, electrosynthesis has gained attention by virtue of being a relatively safe and cost-effective method that can be designed to be environmentally benign, depending on the choice of solvent and electrolyte, as well as the source of electricity in its role as the most fundamental reductant. [48, 49]

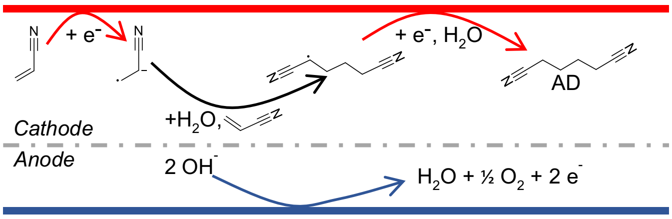

Figure 4 Pathway for the electrochemical synthesis of adiponitrile (ADN). Adapted from reference 46.

Electrochemical proton/electron transfer mechanisms can also be relevant to traditional hydrogenation catalysis. A recent publication by An *et al* has investigated the mechanism of aqueous 4-nitrophenol hydrogenation using unbiased two-compartment electrochemical cells (H-cells). The H_2 oxidation on a Pd/C catalyst is separated in one half of the H-cell, while the nitro-reduction can occur both on metal sites and on the carbon support in the other half of the cell using the electrons from the H_2 oxidation and solvent protons.[50] This result underlines that electrochemical research of the nitro-reduction reaction could also lead to the thoughtful design of novel hydrogenation catalysts.

1.3 Bio- and chemo- catalysts for the hydrogen oxidation reaction (HOR)

Catalysts capable of facilitating the $2H^+/H_2$ transformation are of great interest because of their possible application in hydrogen fuel cells and electrolysers – technologies thought by many to be central to the transition towards a carbon-free energy system.[51] In addition, the Vincent group has already successfully coupled H_2 oxidation to the nitro-reduction reaction, as described in 1.1.7, warranting a closer look at current H_2 oxidation catalysts reported in literature. Today, the interconversion of water and hydrogen generally relies on the use of platinum-based catalysts, a rare element that renders the resulting technologies prohibitively expensive.[52] Catalysts that rely on more common metals can be found in nature: hydrogenases, enzymes that catalyse the reversible cleavage of H_2, contain either a di-iron, nickel-iron, or mono-iron metal-carbonyl active site.[51] Many microorganisms contain some form of hydrogenase, whether they be endemic to volcanic extreme environments or the mammalian intestines, in which H_2 is produced through the fermentation of carbohydrates.[53] Indeed, the enzyme most relevant to this thesis, hydrogenase-1 (Hyd-1), is synthesized by the enterobacterium *Escherichia coli* (*E. coli*).

1.3.1 Escherichia coli hydrogenase 1

Hyd-1 is a membrane-bound hydrogen-uptake enzyme that is one of at least three [NiFe]-hydrogenases expressed by *E. coli*. Like all [NiFe]-hydrogenases, Hyd-1 consists of a large subunit housing the bimetallic active site and a small subunit capable of shuttling electrons to the protein surface through a series of iron sulphur clusters.[53] The active site contains a cysteine-bound Ni with another two bridging cysteine residues linking it to the Fe, which itself is ligated to two cyanides and one carbonyl – unusual ligands in biology, that have been exploited as spectroscopic handles in infrared absorption studies probing the catalytic cycle of the enzyme, shown in Figure 5.[54] Hyd-1 is known to have a strong catalytic bias towards H_2

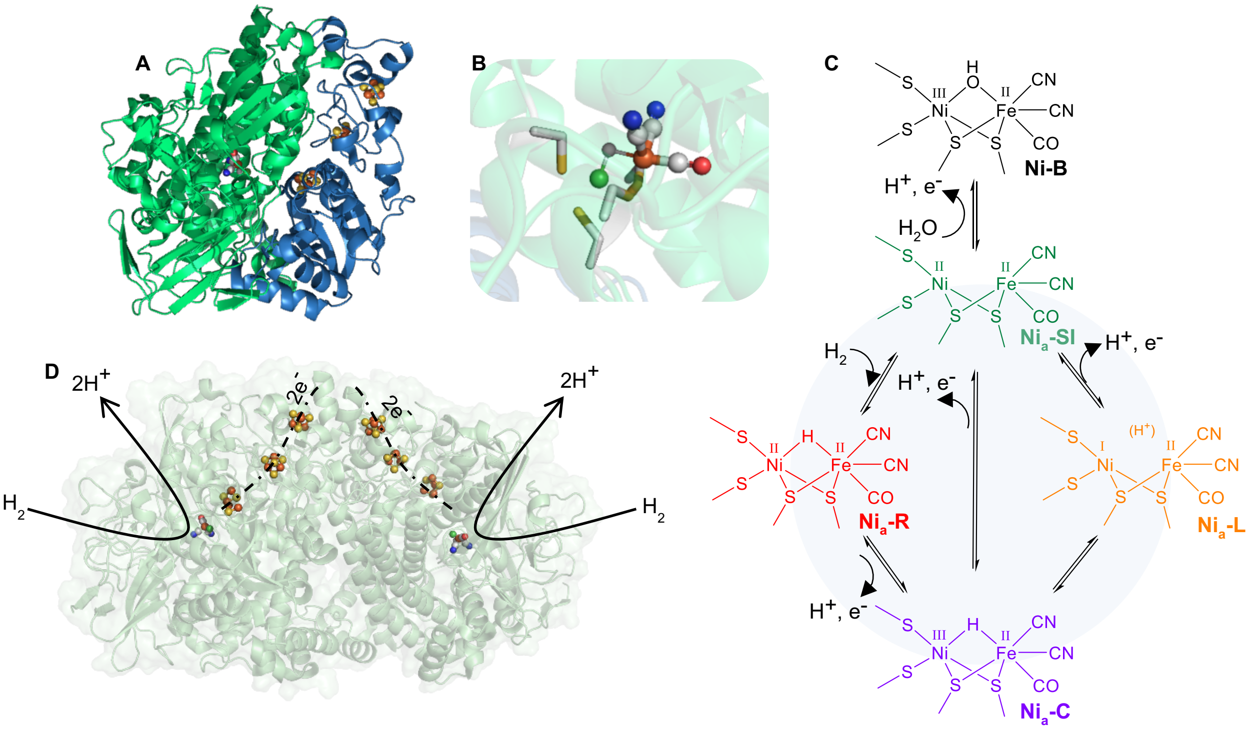

Figure 5 ***A*** *Structure of Hyd-1 showing large subunit containing active site (green) and small subunit containing iron sulphur clusters (blue).* ***B*** *Detailed view of Hyd-1 active site, showing cysteine sulphur ligands in yellow surrounding Ni (green), iron atom (orange) ligated to two CN and one CO.* ***C*** *Skeletal mechanism for catalytic cycle at Hyd-1 active site.* ***D*** *Natively, Hyd-1 exists as a homodimer comprising two subunits of the heterodimer shown in* ***A****. Structure solved by Carr et al.*[3] *(PDB 6FPW). Catalytic cycle adapted from reference 54.*

oxidation and can activate H_2 even under aerobic conditions, a quality that sets it apart from other hydrogenases that typically require strictly anaerobic conditions. [40]

1.3.2 Biomimetic catalysts for H_2 oxidation and proton reduction

The oxygen sensitivity of many hydrogenases is only one disadvantage that might make them less attractive for possible industrial application. Another important barrier to their widespread use is that their production in the active form remains challenging and a scale-up to meet industrial demand for fuel cell purposes is currently not achievable. [52, 55] Inorganic complexes that are designed to mimic the active site chemistry found in hydrogenases could offer a promising alternative, because the technology needed to produce such synthetic complexes at large scale is well established. A variety of inorganic complexes that are structurally inspired by hydrogenase active sites has been reported. Notably, Ogo *et al* have reported both [NiRu] and [NiFe] complexes with similar structural features as the [NiFe] hydrogenase active site that can activate H_2 in water and at room temperature. [56, 57] Structural models have also been useful in the elucidation of the active site chemistry because specific oxidation and protonation states can be targeted synthetically. Eilers *et al*, for example, were able to study the protonation of metal or ligand sites on a diirion complex which mirrors the [FeFe] hydrogenase active site. [58]

Another approach is to target the design of functional models, rather than structurally identical models, of the hydrogenase active sites.[51] Several characteristics of the natural active sites have been identified to produce such functional models. First, the unique cyanide and CO ligands found in hydrogenase active sites are strong field ligands that cause low-spin states, resulting in open sites for the coordination of hydride ligands during the heterogeneous cleavage of H_2.[59] Accordingly, the work of DuBois, Shaw, and others, has tuned low-spin $[Ni(diphosphine)_2]^{2+}$ complexes for heterogeneous H_2 cleavage. By increasing the bulk of the phosphine substituents, the square planar geometry is distorted towards a tetrahedron, introducing conformational strain, and the complex becomes a better hydride acceptor.[59, 60] Indeed, initial work had found that a $[Ni(Et_2PCH_2CH_2CH_2PEt_2)_2]^{2+}$ complex was capable of cleaving H_2 in the presence of an external base. [61] To mimic the pendent amine in [FeFe]-hydrogenase that can act as a proton acceptor while the metal centre accepts the hydride, an amine was introduced to the six-membered ring of the diphosphine ligand. Finally, to force at least one amine to remain in immediate proximity to the metal centre, which requires the ring to assume the boat conformation, complexes containing four such rings were synthesized ($[Ni(P^R{}_2N^R{}_2)_2]^{2+}$), as illustrated in Figure 6.[59] This family of complexes can be further designed by carefully choosing R'' which can tune the amine pK_a. H_2 oxidation activity can be further enhanced by choosing amino acid substituents as R'' which improve proton movement in the outer coordination sphere. [62] Indeed, a $[Ni(P^{Cy}{}_2N^{Gly}{}_2)_2]^{2+}$ complex (where Cy = cyclohexyl and Gly = glycine) was shown to outperform a [NiFe]-hydrogenase from *Desulfovibrio vulgaris* at low pH or in the presence of CO. [63] This family of complexes has been immobilised on graphene oxide or carbon nanotubes to form electrodes for possible fuel cell applications. [64, 65]

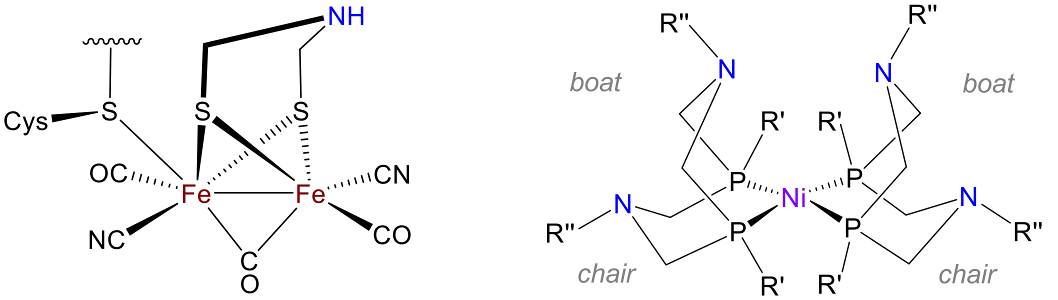

Figure 6 Structure of the [FeFe] hydrogenase active site (left) and the general structure of the 'DuBois-type' Ni complexes following the general formula $[Ni(P^R{}_2N^R{}_2)_2]^{2+}$, with chair and boat conformations labelled.

1.4 Production methods and applications of carbon nanotubes

1.4.1 Carbon nanotube discovery and impact

The first synthesis of carbon nanotubes (CNTs) was reported by IIjima in 1991,[66] sparking decades of research into the production, properties, and applications of these materials. CNTs can be thought of as sheets of graphene rolled up into cylindrical shape, and are categorized by their number of walls into single-walled, double-walled, or multi-walled CNTs (SW-, DW-, or MW- respectively). Depending on their diameter, wall number, and structural characteristics, the properties of these materials will vary widely, and the term 'carbon nanotube' should be thought of as an umbrella for many different, if related, materials. [67] Today, CNTs are applied as electrode materials, [68, 69] catalyst supports, [70] for sensing applications, [71] for the development of flexible electronics, [72] and have already been used as supports for hydrogenase enzyme immobilisation in the Vincent group and beyond. [73, 74]

1.4.2 Synthesis of carbon nanotubes

Several methods for the production of carbon nanotubes have been developed, including chemical vapour deposition (CVD), arc discharge, and laser ablation. Many types of CNTs are now commercially available.

The arc discharge method relies on a constant high current between two electrodes in a pressurized chamber, filled with a mixture of inert and carbon precursor gas, with the plasma between the electrodes reaching temperatures of 4000-6000K. The catalyst needed to initiate CNT growth can be supplied by simply placing a small piece of iron onto the anode, which vaporizes to interact with the decomposing precursor when a high current and voltage is applied between the electrodes.[75] Arc discharge has been used since the 1980s for the production of fullerenes,[76] with Iijima employing this method in 1991 for the first reported synthesis of SW-CNTs.[66] Specifically, Ijima's method relied a reactor was filled with argon and methane before applying a current of 200 A at 20 V between the electrodes, where a piece of elemental iron was placed onto the cathode to provide the nucleation catalysis for the CNT growth. The SW-CNTs were found not on the cathode but deposited in the reactor chamber, indicating that the material was formed in the gas phase. Current research using arc discharge to produce CNTs includes, for example, the production of mixed SnO_2/CNT composites for battery applications. [77]

A second among the most well-known methods for the synthesis of CNTs is the laser ablation of bulk graphite. The possible use of laser ablation for the production of CNTs was first discovered in the group of Richard Smalley in the 1990s: A control experiment, in which a pure carbon rod was exposed to a pulsed 532 nm laser in a high-temperature furnace, surprisingly yielded MW-CNTs. [78] Notable is that laser ablation allows for a catalyst-free synthesis of CNTs, while metal contamination of CNTs produced through other methods remains an important concern in the analysis of their proposed chemical or electronic behaviours.[79, 80]

In the first reported production of CNTs through chemical vapour deposition (CVD), published in 1993, iron nanoparticles were prepared on a graphite support prior to the CNT growth process and placed into a quartz reactor. Acetylene was then pyrolyzed at 700 °C over the pre-prepared catalyst, leading to the formation of CNTs whose diameter corresponded to the catalyst particle diameter, and whose length depended on reaction time.[81] Current CVD methods still follow this general procedure: A precursor carbon source and a metal catalyst are fed into a furnace, the catalyst decomposes and forms nanoparticles on which the CNTs can nucleate. CVD offers a myriad of possible parameters for fine tuning of the produced material, including temperature, flow rate of the precursor mixture, catalyst and precursor concentration and identity, synthesis time, and substrate or possible template identity. [82] In addition, CVD as a one-step scalable technique is employed in industry for the large-scale production of CNTs.[83]

1.4.3 Substitutional heteroatom doping of carbon materials

The introduction of heteroatoms into the sp2 lattice of carbon materials causes structural defects, changes in charge density distribution, and altered chemical behaviour, offering a route of modifying the structure and properties of the material. [84, 85] Elements near carbon in the periodic table are the most likely choices for heteroatom doping, with boron and nitrogen being most common, but with many others (such as phosphorous[86] and silicon[87]) also being reported. Different dopants will lead to different structural and electronic effects. Boron dopants are known to enhance conductivity by increasing the number of hole-type charge carriers because of their three valence electron electronic configuration. [88] Boron dopants can easily substitute for a carbon atom in the material's lattice, while phosphorous, for example, has a significant distortive effect and can increase the d-spacing of the material – a quality that can lead to easier interlayer ion storage, making the material more interesting in battery applications. [89] The general effect of different heteroatom dopants is summarised in Figure 7 in terms of the possible battery or supercapacitor application of the resultant material.[89]

While many possible dopants have been demonstrated in literature, nitrogen is thrown into relief due to the methodological ease of nitrogen doping, the relative chemical stability of the

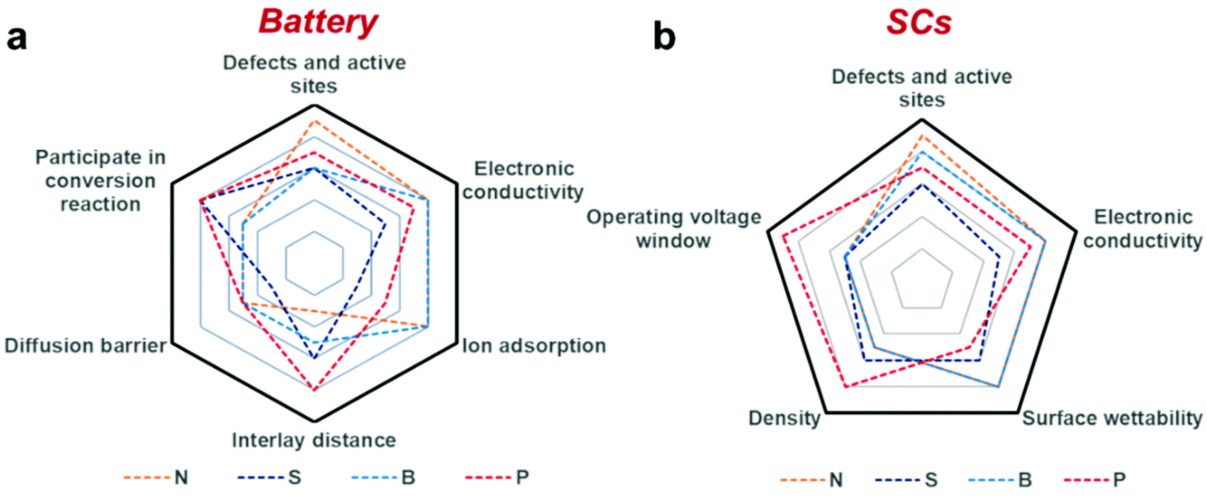

*Figure 7 Generalised effects of different heteroatom dopants in carbon nanomaterials for use in batteries (**a**) or supercapacitors (**b**). Reproduced from reference 87 with permission.*

C-N species formed, and the similar size of carbon and nitrogen. [84] Nitrogen heteroatoms introduce significant defects into the sp2 lattice, with the possible NC bonding environments being defined as graphitic, pyridinic, or pyrrolic. [90] These defects could act as active sites, can lead to easier adsorption of other species in gas sensing or protein immobilisation applications, [91, 92] and increase the surface wettability of the material through the introduction of permanent dipoles. [93] Interestingly, the activity of metal catalysts such as metal nanoparticles on carbon may be tuned by the introduction of heteroatom dopants into the carbon support, with nitrogen being one of the most widely studied cases. For example, nitrogen-doped carbon black was shown by Yang *et al* to improve dispersion of Pt-M nanoparticles on carbon, while inducing a positive shift of the onset potential of the oxygen reduction reaction (ORR) as compared to the control Pt-M on undoped carbon black. [94]

The heteroatom dopant is either introduced directly during the material synthesis (i.e., by enriching the precursor species with the desired element) or post-synthesis by chemical and thermal treatment of the existing sp2 material. For the synthesis of nitrogen-doped CNTs by CVD, the precursor molecule can simply be chosen to contain a nitrogen-based functional group, for example by exchanging benzylamine for toluene. [95] A typical post-synthesis doping method involves treatment of the carbon nanomaterial with a precursor – such as sodium dodecyl sulphate as a sulphur source[96] – and subsequent calcination at high temperature.

1.4.4 (Doped) CNTs in electrocatalysis

CNTs have since their discovery garnered the interest of electrochemists due to their large electrochemically active surface area, their excellent conductivity, and reported electrocatalytic effects on depletion of overpotential or increases in current densities. [97] Xiong *et al* use vertically aligned nitrogen-doped CNTs as the anode in the oxygen reduction reaction (ORR), showing high current densities and a small anodic shift of the onset potential, a result with possible implications for fuel cell research. [98] Similarly, NCNTs have been used in a composite material alongside nitrogen-doped graphene in order to boost the electrochemically active surface area by preventing re-stacking of the individual graphene layers; a paper that also includes interesting examples of post-synthesis doping: Graphene oxide and MW-CNTs are combined and only then treated with either urea (material NC-1) or dicyandiamide (material NC-2) at 800 °C. Electron microscopy was used to demonstrate that while some restacking of graphene nanosheets was observable, larger scale agglomeration was prevented. This composite material was found to be highly active as an ORR electrocatalyst in alkaline media, while doping with urea versus dicyandiamide led to materials with differing electrocatalytic behaviour, an observation that is not fully explained but indicates a possible tuning of the catalysis through slight differences in the bonding environment of the nitrogen heteroatoms.[99]

While literature may sometimes describe CNT-based electrocatalysts as ‘metal-free’, metal contamination could play an important role in at least some of the reported electrocatalytic behaviour ascribed to the materials. Metal contamination is to be expected in CNTs stemming from production processes (vide supra) that rely on iron, cobalt, or nickel-based catalyst for the growth mechanism.[80]

1.5 Towards green chemistry? Electrosynthesis and bio-electrocatalysis

1.5.1 Motivation for the pursuit of green chemistry

The chemical industry has an important and global impact on the environment, human health, and climate change, and concrete examples of such impacts are easy to find. Infamously, five survey regions around a chloroprene production plant in Louisiana, built by DuPont and now run by the Japanese chemical company Denka, have the highest cancer risk in the United States, hundreds of times the national average, with pollutant numbers still trending upwards in 2018.[100] Zavarsky and Duester have shown that the temperature of the river Rhine in southern Germany fluctuates with the turnover of BASF, whose largest production facility utilizes river water for cooling purposes.[101] Chemical companies feature prominently on the U.S.-based Top 100 Polluter Indexes published by the University of Massachusetts Amherst, with a selection shown in Table 1 (based on 2021 Data from the U.S. Environmental Protection Agency).[102]

Corporation	**Rank in…**		
	Toxic 100 Air	**Greenhouse 100 Polluters**	**Toxic 100 Water**
LyonellBasell Industries	1	74	33
BASF	3	137	
Indorama Ventures	4		
Dow Inc.	8	35	123
Westlake Chemical	12	95	
Evonik Industries	33		
Solvay	38		

Table 1 Chemical companies feature prominently on the U.S.-based Top 100 Polluter Indexes published by the University of Massachusetts Amherst.

With the concurrent and connected crises of biodiversity loss and global heating threatening every aspect of (human) life, a transition towards green practices is long overdue and only increasing in urgency.[103] While the United Nations Environment Programme advises that the current scale of manufacture of some of the products of the chemical industry should be lowered to reach environmental sustainability,[104] many are essential to human quality of life, necessitating the development and application of green production methods.[105] Biocatalysis as well as electrosynthesis are two methodologies explored in this thesis that can help lower the environmental impact of chemical production, through milder conditions and greater material efficiency (with caveats introduced above).

1.6 Aims and overview of this thesis

The **Hyd/C** catalyst system for the hydrogenation of nitro-groups towards the production of amines can be separated into the two half-reactions: First, H_2 oxidation catalysed by hydrogenase enzyme and second, nitro-reduction occurring on a carbon particle. The feasibility of the overall reaction is governed by the potentials associated with the two half reactions. At pH 6, the thermodynamic potential of the $2H^+/H_2$ couple lies at -0.355 V vs SHE – depending on the catalyst used, there may be an additional overpotential (as with Hyd-1, where the onset for dihydrogen oxidation lies at -0.296 V vs SHE at pH 6). In the combined system, where the half reactions are linked through a conductive carbon, any nitro-compound with a reduction potential (under the relevant conditions) that is more positive than the $2H^+/H_2$ couple should be within the substrate scope of the system. It follows that this hydrogenation system can be modified if the potentials of the respective half reactions are shifted. This thesis will attempt to tune the nitro-reduction reaction by varying the carbon particle used as the enzyme support. For this purpose, a set of NCNTs is synthesized and an electrochemical study of the nitro-reduction on these NCNTs as well as other commercial carbon nanomaterials is undertaken. After an electrocatalytic effect is observed on the NCNTs in Chapter 3, they are employed for the electrosynthesis and biocatalytic synthesis of amines in Chapter 4. Finally, Chapter 5 will focus on the H_2 oxidation reaction and will establish a chemo-catalytic nitro-hydrogenation catalyst system inspired by **Hyd/C** using a Ni(bisdiphosphine) complex known for its excellent H_2 oxidation catalysis, introduced above.

1.7 References

(1) Formenti, D.; Ferretti, F.; Scharnagl, F. K.; Beller, M. Reduction of Nitro Compounds Using 3d-Non-Noble Metal Catalysts. *Chemical Reviews* **2019**, *119* (4), 2611-2680. DOI: 10.1021/acs.chemrev.8b00547.

(2) Sokolova, D.; Lurshay, T. C.; Rowbotham, J. S.; Stonadge, G.; Reeve, H. A.; Cleary, S. E.; Sudmeier, T.; Vincent, K. A. Selective hydrogenation of nitro compounds to amines by coupled redox reactions over a heterogeneous biocatalyst. *Nature Communications* **2024**, *15* (1), 7297. DOI: 10.1038/s41467-024-51531-2.

(3) Evans, R. M.; Ash, P. A.; Beaton, S. E.; Brooke, E. J.; Vincent, K. A.; Carr, S. B.; Armstrong, F. A. Mechanistic Exploitation of a Self-Repairing, Blocked Proton Transfer Pathway in an O_2-Tolerant [NiFe]-Hydrogenase. *Journal of the American Chemical Society* **2018**, *140* (32), 10208-10220. DOI: 10.1021/jacs.8b04798.

(4) Roughley, S. D.; Jordan, A. M. The medicinal chemist's toolbox: an analysis of reactions used in the pursuit of drug candidates. *J Med Chem* **2011**, *54* (10), 3451-3479. DOI: 10.1021/jm200187y.

(5) 王志训. Industrial preparation method of midazolam. WO2016146049A1, 2016.

(6) John Ralph, S. K., Justin Mobley. Synthesis of paracetamol (acetaminophen) from biomass-derived p-hydroxybenzamide. US 10,286,504 B2, 2018.

(7) Niesiobędzka, J.; Datta, J. Challenges and recent advances in bio-based isocyanate production. *Green Chemistry* **2023**, *25* (7), 2482-2504, 10.1039/D2GC04644J. DOI: 10.1039/D2GC04644J.

(8) Chandrashekhar, V. G.; Baumann, W.; Beller, M.; Jagadeesh, R. V. Nickel-catalyzed hydrogenative coupling of nitriles and amines for general amine synthesis. *Science (American Association for the Advancement of Science)* **2022**, *376* (6600), 1433-1441. DOI: 10.1126/science.abn7565.

(9) Orlandi, M.; Brenna, D.; Harms, R.; Jost, S.; Benaglia, M. Recent Developments in the Reduction of Aromatic and Aliphatic Nitro Compounds to Amines. *Org. Process Res. Dev.* **2016**, *22* (4), 430-445. DOI: 10.1021/acs.oprd.6b00205.

(10) Haber, F. Uber die elektrolytische Reduction der Nitrokorper. *Angew. Chem.* **1900**, *18*. DOI: doi.org/10.1002/ange.19000131802.

(11) Campbell, C. D.; Stewart, M. I. Reflections on the Teaching Practices for the Reduction of Nitroarenes: Updating Methodologies and Considerations of the Mechanism. *Journal of Chemical Education* **2023**, *100* (9), 3171-3178. DOI: 10.1021/acs.jchemed.3c00283.

(12) McCullagh, A. M.; Davidson, A. L.; Ballas, C. E.; How, C.; MacLaren, D. A.; Boulho, C.; Brennan, C.; Lennon, D. The application of an alumina-supported Ni catalyst for the hydrogenation of nitrobenzene to aniline. *Catalysis Today* **2024**, *442*, 114933. DOI: https://doi.org/10.1016/j.cattod.2024.114933.

(13) Mao, J.; Chen, W.; Sun, W.; Chen, Z.; Pei, J.; He, D.; Lv, C.; Wang, D.; Li, Y. Rational Control of the Selectivity of a Ruthenium Catalyst for Hydrogenation of 4-Nitrostyrene by Strain Regulation. *Angewandte Chemie International Edition* **2017**, *56* (39), 11971-11975. DOI: https://doi.org/10.1002/anie.201706645.

(14) Furukawa, S.; Yoshida, Y.; Komatsu, T. Chemoselective Hydrogenation of Nitrostyrene to Aminostyrene over Pd- and Rh-Based Intermetallic Compounds. *ACS Catalysis* **2014**, *4* (5), 1441-1450. DOI: 10.1021/cs500082g.

(15) Mori, A.; Mizusaki, T.; Miyakawa, Y.; Ohashi, E.; Haga, T.; Maegawa, T.; Monguchi, Y.; Sajiki, H. Chemoselective hydrogenation method catalyzed by Pd/C using diphenylsulfide as a reasonable catalyst poison. *Tetrahedron* **2006**, *62* (51), 11925-11932. DOI: https://doi.org/10.1016/j.tet.2006.09.094.

(16) Bechamp, A. J. De l'action des protosels de fer sur la nitronaphtaline et la nitrobenzine. Nouvelle méthode de formation des bases organiques artificielles de Zinin. *Anal. Chim. Phys.* **1854**, *42*, 186.

(17) Bellamy, F. D.; Ou, K. Selective reduction of aromatic nitro compounds with stannous chloride in non acidic and non aqueous medium. *Tetrahedron Letters* **1984**, *25* (8), 839-842. DOI: https://doi.org/10.1016/S0040-4039(01)80041-1.

(18) Sun, S.; Quan, Z.; Wang, X. Selective reduction of nitro-compounds to primary amines by nickel-catalyzed hydrosilylative reduction. *RSC Advances* **2015**, *5* (103), 84574-84577. DOI: 10.1039/c5ra17731f.

(19) Piña, S.; Cedillo, D. M.; Tamez, C.; Izquierdo, N.; Parsons, J. G.; Gutierrez, J. J. Reduction of nitrobenzene derivatives using sodium borohydride and transition metal sulfides. *Tetrahedron Lett.* **2014**, *55* (40), 5468-5470. DOI: 10.1016/j.tetlet.2014.08.068.

(20) Vu, C. B.; Bemis, J. E.; Disch, J. S.; Ng, P. Y.; Nunes, J. J.; Milne, J. C.; Carney, D. P.; Lynch, A. V.; Smith, J. J.; Lavu, S.; et al. Discovery of Imidazo[1,2-b]thiazole Derivatives as Novel SIRT1 Activators. *Journal of Medicinal Chemistry* **2009**, *52* (5), 1275-1283. DOI: 10.1021/jm8012954.

(21) Wienhöfer, G.; Baseda-Krüger, M.; Ziebart, C.; Westerhaus, F. A.; Baumann, W.; Jackstell, R.; Junge, K.; Beller, M. Hydrogenation of nitroarenes using defined iron–phosphine catalysts. *Chemical Communications* **2013**, *49* (80), 9089-9091, 10.1039/C3CC42983K. DOI: 10.1039/C3CC42983K.

(22) Zubar, V.; Dewanji, A.; Rueping, M. Chemoselective Hydrogenation of Nitroarenes Using an Air-Stable Base-Metal Catalyst. *Organic Letters* **2021**, *23* (7), 2742-2747. DOI: 10.1021/acs.orglett.1c00659.

(23) Arnold, F. H. Innovation by Evolution: Bringing New Chemistry to Life (Nobel Lecture). *Angewandte Chemie International Edition* **2019**, *58* (41), 14420-14426. DOI: https://doi.org/10.1002/anie.201907729.

(24) Andreini, C.; Bertini, I.; Cavallaro, G.; Holliday, G. L.; Thornton, J. M. Metal ions in biological catalysis: from enzyme databases to general principles. *JBIC Journal of Biological Inorganic Chemistry* **2008**, *13* (8), 1205-1218. DOI: 10.1007/s00775-008-0404-5.

(25) Arnold, F. H. The nature of chemical innovation: new enzymes by evolution. *Quarterly Reviews of Biophysics* **2015**, *48* (4), 404-410. DOI: 10.1017/S003358351500013X From Cambridge University Press Cambridge Core.

(26) Garske, A. L.; Kapp, G.; McAuliffe, J. C. Industrial Enzymes and Biocatalysis. In *Handbook of Industrial Chemistry and Biotechnology*, Kent, J. A., Bommaraju, T. V., Barnicki, S. D. Eds.; Springer International Publishing, 2017; pp 1571-1638.

(27) Domínguez de María, P.; Hollmann, F. On the (Un)greenness of Biocatalysis: Some Challenging Figures and Some Promising Options. *Frontiers in Microbiology* **2015**, *6*, Mini Review. DOI: 10.3389/fmicb.2015.01257.

(28) Fischer, J. D.; Holliday, G. L.; Rahman, S. A.; Thornton, J. M. The Structures and Physicochemical Properties of Organic Cofactors in Biocatalysis. *Journal of Molecular Biology* **2010**, *403* (5), 803-824. DOI: https://doi.org/10.1016/j.jmb.2010.09.018.

(29) Wilkinson, I. V. L.; Pfanzelt, M.; Sieber, S. A. Functionalised Cofactor Mimics for Interactome Discovery and Beyond. *Angewandte Chemie International Edition* **2022**, *61* (29), e202201136. DOI: https://doi.org/10.1002/anie.202201136.

(30) Lee, Y. S.; Gerulskis, R.; Minteer, S. D. Advances in electrochemical cofactor regeneration: enzymatic and non-enzymatic approaches. *Current Opinion in Biotechnology* **2022**, *73*, 14-21. DOI: https://doi.org/10.1016/j.copbio.2021.06.013.

(31) Bornadel, A.; Bisagni, S.; Pushpanath, A.; Slabu, I.; LePaih, J.; Cherney, A. H.; Mennen, S. M.; Hedley, S. J.; Tedrow, J.; Dominguez, B. Process Development and Protein Engineering Enhanced Nitroreductase-Catalyzed Reduction of 2-Methyl-5-nitro-pyridine. *Org. Process Res. Dev.* **2020**, *25* (3), 648-653. DOI: 10.1021/acs.oprd.0c00464.

(32) Reeve, H. A.; Lauterbach, L.; Lenz, O.; Vincent, K. A. Enzyme-Modified Particles for Selective Biocatalytic Hydrogenation by Hydrogen-Driven NADH Recycling. *ChemCatChem* **2015**, *7* (21), 3480-3487. DOI: 10.1002/cctc.201500766.

(33) Ramirez, M. A.; Joseph Srinivasan, S.; Cleary, S. E.; Todd, P. M. T.; Reeve, H. A.; Vincent, K. A. H2-Driven Reduction of Flavin by Hydrogenase Enables Cleaner Operation of Nitroreductases for Nitro-Group to Amine Reductions. *Frontiers in Catalysis* **2022**, *2*, Original Research.

(34) Joseph Srinivasan, S.; Cleary, S. E.; Ramirez, M. A.; Reeve, H. A.; Paul, C. E.; Vincent, K. A. E. coli Nickel-Iron Hydrogenase 1 Catalyses Non-native Reduction of Flavins: Demonstration for Alkene Hydrogenation by Old Yellow Enzyme Ene-reductases**. *Angewandte Chemie International Edition* **2021**, *60* (25), 13824-13828. DOI: https://doi.org/10.1002/anie.202101186.

(35) Tiwari, J.; Tarale, P.; Sivanesan, S.; Bafana, A. Environmental persistence, hazard, and mitigation challenges of nitroaromatic compounds. *Environmental Science and Pollution Research* **2019**, *26* (28), 28650-28667. DOI: 10.1007/s11356-019-06043-8.

(36) *Priority Pollutant List*. U.S. Environmental Protection Agency (EPA), 2014. https://www.regulations.gov/document/EPA-HQ-OPPT-2019-0080-0173 (accessed 21/08/2024).

(37) Rodgers, J. D.; Bunce, N. J. Treatment methods for the remediation of nitroaromatic explosives. *Water Research* **2001**, *35* (9), 2101-2111. DOI: https://doi.org/10.1016/S0043-1354(00)00505-4.

(38) Huang, L.-Z.; Hansen, H. C. B.; Bjerrum, M. J. Electrochemical reduction of nitroaromatic compounds by single sheet iron oxide coated electrodes. *Journal of Hazardous Materials* **2016**, *306*, 175-183. DOI: https://doi.org/10.1016/j.jhazmat.2015.12.009.

(39) Tang, H.; Li, J.; Bie, Y.; Zhu, L.; Zou, J. Photochemical removal of aniline in aqueous solutions: Switching from photocatalytic degradation to photo-enhanced polymerization recovery. *Journal of Hazardous Materials* **2010**, *175* (1), 977-984. DOI: https://doi.org/10.1016/j.jhazmat.2009.10.106.

(40) Lukey, M. J.; Parkin, A.; Roessler, M. M.; Murphy, B. J.; Harmer, J.; Palmer, T.; Sargent, F.; Armstrong, F. How *Escherichia coli* is equipped to oxidize hydrogen under different redox conditions. **2010**.

(41) Jean-Michel Saveant, C. C. Single-Electron Transfer at an Electrode. In *Elements of Molecular and Biomolecular Electrochemistry*, 2019; pp 1-80.

(42) Bard, A. J. *Electrochemical Methods: Fundamentals and Applications*; Wiley, 2001.

(43) Faraday, M. VI. Experimental researches in electricity.-Seventh Series. *Philosophical Transactions of the Royal Society of London* **1997**, *124*, 77-122. DOI: 10.1098/rstl.1834.0008 (acccessed 2023/07/24).

(44) Zhang, S.; Findlater, M. Kolbe reaction goes reductive. *Nature Synthesis* **2022**, *1* (6), 417-419. DOI: 10.1038/s44160-022-00088-3.

(45) Brazil, R. Sparking industry's interest in electrosynthesis. In *Chemistry World*, Royal Society of Chemistry: 2024.

(46) Blanco, D. E.; Dookhith, A. Z.; Modestino, M. A. Enhancing selectivity and efficiency in the electrochemical synthesis of adiponitrile. *Reaction Chemistry & Engineering* **2019**, *4* (1), 8-16. DOI: 10.1039/c8re00262b.

(47) Karimi, F.; Mohammadi, F.; Ashrafizadeh, S. N. An Experimental Study of the Competing Cathodic Reactions in Electrohydrodimerization of Acrylonitrile. *Journal of The Electrochemical Society* **2011**, *158* (12). DOI: 10.1149/2.016112jes.

(48) Cardoso, D. S. P.; Šljukić, B.; Santos, D. M. F.; Sequeira, C. A. C. Organic Electrosynthesis: From Laboratorial Practice to Industrial Applications. *Organic Process Research & Development* **2017**, *21* (9), 1213-1226. DOI: 10.1021/acs.oprd.7b00004.

(49) Leech, M. C.; Lam, K. A practical guide to electrosynthesis. *Nat Rev Chem* **2022**, *6* (4), 275-286. DOI: 10.1038/s41570-022-00372-y.

(50) An, H.; Sun, G.; Hülsey, M. J.; Sautet, P.; Yan, N. Demonstrating the Electron–Proton-Transfer Mechanism of Aqueous Phase 4-Nitrophenol Hydrogenation Using Unbiased Electrochemical Cells. *ACS Catalysis* **2022**, *12* (24), 15021-15027. DOI: 10.1021/acscatal.2c03133.

(51) Artero, V.; Fontecave, M. Some general principles for designing electrocatalysts with hydrogenase activity. *Coordination Chemistry Reviews* **2005**, *249* (15), 1518-1535. DOI: https://doi.org/10.1016/j.ccr.2005.01.014.

(52) Artero, V.; Fontecave, M.; Palacin, S.; Le Goff, A.; Jousselme, B. Novel materials and their use for the electrocatalytic evolution or uptake of H_2. WO2010046774A1, 2009.

(53) Vincent, K. A.; Parkin, A.; Armstrong, F. A. Investigating and Exploiting the Electrocatalytic Properties of Hydrogenases. *Chemical Reviews* **2007**, *107* (10), 4366-4413. DOI: 10.1021/cr050191u.

(54) Ash, P. A.; Hidalgo, R.; Vincent, K. A. Proton Transfer in the Catalytic Cycle of [NiFe] Hydrogenases: Insight from Vibrational Spectroscopy. *ACS Catalysis* **2017**, *7* (4), 2471-2485. DOI: 10.1021/acscatal.6b03182.

(55) Fan, Q.; Neubauer, P.; Lenz, O.; Gimpel, M. Heterologous Hydrogenase Overproduction Systems for Biotechnology—An Overview. *International Journal of Molecular Sciences* **2020**, *21* (16), 5890. DOI: 10.3390/ijms21165890.

(56) Ogo, S.; Ichikawa, K.; Kishima, T.; Matsumoto, T.; Nakai, H.; Kusaka, K.; Ohhara, T. A Functional [NiFe]Hydrogenase Mimic That Catalyzes Electron and Hydride Transfer from H_2. *Science* **2013**, *339* (6120), 682-684. DOI: 10.1126/science.1231345.

(57) Ogo, S.; Kabe, R.; Uehara, K.; Kure, B.; Nishimura, T.; Menon, S. C.; Harada, R.; Fukuzumi, S.; Higuchi, Y.; Ohhara, T.; et al. A Dinuclear Ni(μ-H)Ru Complex Derived from H_2. *Science* **2007**, *316* (5824), 585-587. DOI: 10.1126/science.1138751.

(58) Eilers, G.; Schwartz, L.; Stein, M.; Zampella, G.; de Gioia, L.; Ott, S.; Lomoth, R. Ligand versus Metal Protonation of an Iron Hydrogenase Active Site Mimic. *Chemistry – A European Journal* **2007**, *13* (25), 7075-7084. DOI: https://doi.org/10.1002/chem.200700019.

(59) Shaw, W. J.; Helm, M. L.; DuBois, D. L. A modular, energy-based approach to the development of nickel containing molecular electrocatalysts for hydrogen production and oxidation. *Biochimica et Biophysica Acta (BBA) - Bioenergetics* **2013**, *1827* (8), 1123-1139. DOI: https://doi.org/10.1016/j.bbabio.2013.01.003.

(60) Berning, D. E.; Miedaner, A.; Curtis, C. J.; Noll, B. C.; Rakowski DuBois, M. C.; DuBois, D. L. Free-Energy Relationships between the Proton and Hydride Donor Abilities of $[HNi(diphosphine)_2]^+$ Complexes and the Half-Wave Potentials of Their Conjugate Bases. *Organometallics* **2001**, *20* (9), 1832-1839. DOI: 10.1021/om0100582.

(61) Curtis, C. J.; Miedaner, A.; Ciancanelli, R.; Ellis, W. W.; Noll, B. C.; Rakowski DuBois, M.; DuBois, D. L. $[Ni(Et_2PCH_2NMeCH_2PEt_2)_2]^{2+}$ as a Functional Model for Hydrogenases. *Inorganic Chemistry* **2003**, *42* (1), 216-227. DOI: 10.1021/ic020610v.

(62) Dutta, A.; Roberts, J. A. S.; Shaw, W. J. Arginine-Containing Ligands Enhance H_2 Oxidation Catalyst Performance. *Angewandte Chemie International Edition* **2014**, *53* (25), 6487-6491. DOI: https://doi.org/10.1002/anie.201402304.

(63) Rodriguez-Maciá, P.; Dutta, A.; Lubitz, W.; Shaw, W. J.; Rüdiger, O. Direct Comparison of the Performance of a Bio-inspired Synthetic Nickel Catalyst and a [NiFe]-Hydrogenase, Both Covalently Attached to Electrodes. *Angewandte Chemie International Edition* **2015**, *54* (42), 12303-12307. DOI: https://doi.org/10.1002/anie.201502364.

(64) Ghedjatti, A.; Coutard, N.; Calvillo, L.; Granozzi, G.; Reuillard, B.; Artero, V.; Guetaz, L.; Lyonnard, S.; Okuno, H.; Chenevier, P. How do H_2 oxidation molecular catalysts assemble onto carbon nanotube electrodes? A crosstalk between electrochemical and multi-physical characterization techniques. *Chemical Science* **2021**, *12* (48), 15916-15927, 10.1039/D1SC05168G. DOI: 10.1039/D1SC05168G.

(65) Reuillard, B.; Blanco, M.; Calvillo, L.; Coutard, N.; Ghedjatti, A.; Chenevier, P.; Agnoli, S.; Otyepka, M.; Granozzi, G.; Artero, V. Noncovalent Integration of a Bioinspired Ni Catalyst to Graphene Acid for Reversible Electrocatalytic Hydrogen Oxidation. *ACS Appl Mater Interfaces* **2020**, *12* (5), 5805-5811. DOI: 10.1021/acsami.9b18922.

(66) Iijima, S. Helical microtubules of graphitic carbon. *Nature* **1991**, *354* (6348), 56-58. DOI: 10.1038/354056a0.

(67) Fadeel, B.; Kostarelos, K. Grouping all carbon nanotubes into a single substance category is scientifically unjustified. *Nat. Nanotechnol.* **2020**, *15* (3), 164. DOI: 10.1038/s41565-020-0654-0.

(68) Díez, N.; Botas, C.; Mysyk, R.; Goikolea, E.; Rojo, T.; Carriazo, D. Highly packed graphene–CNT films as electrodes for aqueous supercapacitors with high volumetric performance. *Journal of Materials Chemistry A* **2018**, *6* (8), 3667-3673, 10.1039/C7TA10210K. DOI: 10.1039/C7TA10210K.

(69) Foremny, K.; Konerding, W. A.-O.; Behrens, A.; Baumhoff, P. A.-O.; Froriep, U. P.; Kral, A. A.-O.; Doll, T. Carbon-Nanotube-Coated Surface Electrodes for Cortical Recordings In Vivo. LID - 10.3390/nano11041029 [doi] LID - 1029. (2079-4991 (Print)). From 2021 Apr 17.

(70) Kweon, D. H.; Okyay, M. S.; Kim, S.-J.; Jeon, J.-P.; Noh, H.-J.; Park, N.; Mahmood, J.; Baek, J.-B. Ruthenium anchored on carbon nanotube electrocatalyst for hydrogen production with enhanced Faradaic efficiency. *Nature Communications* **2020**, *11* (1), 1278. DOI: 10.1038/s41467-020-15069-3.

(71) Norizan, M. N.; Moklis, M. H.; Ngah Demon, S. Z.; Halim, N. A.; Samsuri, A.; Mohamad, I. S.; Knight, V. F.; Abdullah, N. Carbon nanotubes: functionalisation and their application in chemical sensors. *RSC Adv.* **2020**, *10* (71), 43704-43732. DOI: 10.1039/d0ra09438b.

(72) Park, S.; Vosguerichian M Fau - Bao, Z.; Bao, Z. A review of fabrication and applications of carbon nanotube film-based flexible electronics. (2040-3372 (Electronic)). From 2013 Mar 7.

(73) Zor, C.; Reeve, H. A.; Quinson, J.; Thompson, L. A.; Lonsdale, T. H.; Dillon, F.; Grobert, N.; Vincent, K. A. H2-Driven biocatalytic hydrogenation in continuous flow using enzyme-modified carbon nanotube columns. *Chem. Commun.* **2017**, *53* (71), 9839-9841. DOI: 10.1039/c7cc04465h.

(74) Lojou, E. Hydrogenases as catalysts for fuel cells: Strategies for efficient immobilization at electrode interfaces. *Electrochimica Acta* **2011**, *56* (28), 10385-10397. DOI: https://doi.org/10.1016/j.electacta.2011.03.002.

(75) Iijima, S.; Ichihashi, T. Single-shell carbon nanotubes of 1-nm diameter. *Nature* **1993**, *363* (6430), 603-605. DOI: 10.1038/363603a0.

(76) Haufler, R.; Conceicao, J.; Chibante, L.; Chai, Y.; Byrne, N.; Flanagan, S.; Haley, M.; O'Brien, S. C.; Pan, C. Efficient production of C60 (buckminsterfullerene), C60H36, and the solvated buckide ion. *Journal of Physical Chemistry* **1990**, *94* (24), 8634-8636.

(77) Zhang, D.; Tang, Y.; Zhang, C.; Dong, Q.; Song, W.; He, Y. One-Step Synthesis of SnO2/Carbon Nanotube Nanonests Composites by Direct Current Arc-Discharge Plasma and Its Application in Lithium-Ion Batteries. In *Nanomaterials*, 2021; Vol. 11.

(78) Guo, T.; Nikolaev, P.; Rinzler, A. G.; Tomanek, D.; Colbert, D. T.; Smalley, R. E. Self-Assembly of Tubular Fullerenes. *The Journal of Physical Chemistry* **1995**, *99* (27), 10694-10697. DOI: 10.1021/j100027a002.

(79) Ismail, R. A.; Mohsin, M. H.; Ali, A. K.; Hassoon, K. I.; Erten-Ela, S. Preparation and characterization of carbon nanotubes by pulsed laser ablation in water for optoelectronic application. *Physica E: Low-dimensional Systems and Nanostructures* **2020**, *119*, 113997. DOI: https://doi.org/10.1016/j.physe.2020.113997.

(80) Pumera, M. Materials Electrochemists' Never-Ending Quest for Efficient Electrocatalysts: The Devil Is in the Impurities. *ACS Catal.* **2020**, *10* (13), 7087-7092. DOI: 10.1021/acscatal.0c02020.

(81) José-Yacamán, M.; Miki-Yoshida, M.; Rendón, L.; Santiesteban, J. G. Catalytic growth of carbon microtubules with fullerene structure. *Applied Physics Letters* **1993**, *62* (6), 657-659. DOI: 10.1063/1.108857.

(82) Andrews, R.; Jacques, D.; Rao, A. M.; Derbyshire, F.; Qian, D.; Fan, X.; Dickey, E. C.; Chen, J. Continuous production of aligned carbon nanotubes: a step closer to commercial

realization. *Chemical Physics Letters* **1999**, *303* (5), 467-474. DOI: https://doi.org/10.1016/S0009-2614(99)00282-1.

(83) Ma, Y.; Dichiara, A. B.; He, D.; Zimmer, L.; Bai, J. Control of product nature and morphology by adjusting the hydrogen content in a continuous chemical vapor deposition process for carbon nanotube synthesis. *Carbon* **2016**, *107*, 171-179. DOI: https://doi.org/10.1016/j.carbon.2016.05.060.

(84) Ayala, P.; Arenal, R.; Rümmeli, M.; Rubio, A.; Pichler, T. The doping of carbon nanotubes with nitrogen and their potential applications. *Carbon* **2010**, *48* (3), 575-586. DOI: 10.1016/j.carbon.2009.10.009.

(85) Zhang, Y.; Zhang, J.; Su, D. S. Substitutional Doping of Carbon Nanotubes with Heteroatoms and Their Chemical Applications. *ChemSusChem* **2014**, *7* (5), 1240-1250. DOI: https://doi.org/10.1002/cssc.201301166.

(86) Chen, X.; Shen, Q.; Li, Z.; Wan, W.; Chen, J.; Zhang, J. Metal-Free H(2) Activation for Highly Selective Hydrogenation of Nitroaromatics Using Phosphorus-Doped Carbon Nanotubes. *ACS Appl Mater Interfaces* **2020**, *12* (1), 654-666. DOI: 10.1021/acsami.9b17582.

(87) Zeferino González, I.; Chiu, H.-C.; Gauvin, R.; Demopoulos, G. P.; Verde-Gómez, Y. Silicon doped carbon nanotubes as high energy anode for lithium-ion batteries. *Materials Today Communications* **2022**, *30*, 103158. DOI: https://doi.org/10.1016/j.mtcomm.2022.103158.

(88) Hsu, W. K.; Firth, S.; Redlich, P.; Terrones, M.; Terrones, H.; Zhu, Y. Q.; Grobert, N.; Schilder, A.; Clark, R. J. H.; Kroto, H. W.; Walton, D. R. M. Boron-doping effects in carbon nanotubes. *Journal of Materials Chemistry* **2000**, *10* (6), 1425-1429, 10.1039/B000720J. DOI: 10.1039/B000720J.

(89) Feng, X.; Bai, Y.; Liu, M.; Li, Y.; Yang, H.; Wang, X.; Wu, C. Untangling the respective effects of heteroatom-doped carbon materials in batteries, supercapacitors and the ORR to design high performance materials. *Energy & Environmental Science* **2021**, *14* (4), 2036-2089, 10.1039/D1EE00166C. DOI: 10.1039/D1EE00166C.

(90) Bulusheva, L. G.; Okotrub, A. V.; Fedoseeva, Y. V.; Kurenya, A. G.; Asanov, I. P.; Vilkov, O. Y.; Koos, A. A.; Grobert, N. Controlling pyridinic, pyrrolic, graphitic, and molecular nitrogen in multi-wall carbon nanotubes using precursors with different N/C ratios in aerosol assisted chemical vapor deposition. *Phys. Chem. Chem. Phys.* **2015**, *17* (37), 23741-23747. DOI: 10.1039/c5cp01981h.

(91) Burch, H. J.; Contera, S. A.; de Planque, M. R.; Grobert, N.; Ryan, J. F. Doping of carbon nanotubes with nitrogen improves protein coverage whilst retaining correct conformation. *Nanotechnology* **2008**, *19* (38), 384001. DOI: 10.1088/0957-4484/19/38/384001.

(92) Adjizian, J.-J.; Leghrib, R.; Koos, A. A.; Suarez-Martinez, I.; Crossley, A.; Wagner, P.; Grobert, N.; Llobet, E.; Ewels, C. P. Boron- and nitrogen-doped multi-wall carbon nanotubes for gas detection. *Carbon* **2014**, *66*, 662-673. DOI: 10.1016/j.carbon.2013.09.064.

(93) Lee, W. J.; Maiti, U. N.; Lee, J. M.; Lim, J.; Han, T. H.; Kim, S. O. Nitrogen-doped carbon nanotubes and graphene composite structures for energy and catalytic applications. *Chemical Communications* **2014**, *50* (52), 6818-6830, 10.1039/C4CC00146J. DOI: 10.1039/C4CC00146J.

(94) Yang, H.; Ko, Y.; Lee, W.; Züttel, A.; Kim, W. Nitrogen-doped carbon black supported Pt–M (M = Pd, Fe, Ni) alloy catalysts for oxygen reduction reaction in proton exchange

membrane fuel cell. *Materials Today Energy* **2019**, *13*, 374-381. DOI: https://doi.org/10.1016/j.mtener.2019.06.007.

(95) Reyes-Reyes, M.; Grobert, N.; Kamalakaran, R.; Seeger, T.; Golberg, D.; Rühle, M.; Bando, Y.; Terrones, H.; Terrones, M. Efficient encapsulation of gaseous nitrogen inside carbon nanotubes with bamboo-like structure using aerosol thermolysis. *Chem. Phys. Lett.* **2004**, *396* (1-3), 167-173. DOI: 10.1016/j.cplett.2004.07.125.

(96) Waqas, M.; Wu, L.; Tang, H.; Liu, C.; Fan, Y.; Jiang, Z.; Wang, X.; Zhong, J.; Chen, W. Cu2O Microspheres Supported on Sulfur-Doped Carbon Nanotubes for Glucose Sensing. *ACS Applied Nano Materials* **2020**, *3* (5), 4788-4798. DOI: 10.1021/acsanm.0c00847.

(97) Banks, C. E.; Crossley, A.; Salter, C.; Wilkins, S. J.; Compton, R. G. Carbon nanotubes contain metal impurities which are responsible for the "electrocatalysis" seen at some nanotube-modified electrodes. *Angew. Chem. Int. Ed. Engl.* **2006**, *45* (16), 2533-2537. DOI: 10.1002/anie.200600033.

(98) Xiong, W.; Du, F.; Liu, Y.; Perez Jr., A.; Supp, M.; Ramakrishnan, T. S.; Dai, L.; Jiang, L. 3-D Carbon Nanotube Structures Used as High Performance Catalyst for Oxygen Reduction Reaction. *J. Am. Chem. Soc.* **2010**, *132*, 15839-15841.

(99) Ratso, S.; Kruusenberg, I.; Vikkisk, M.; Joost, U.; Shulga, E.; Kink, I.; Kallio, T.; Tammeveski, K. Highly active nitrogen-doped few-layer graphene/carbon nanotube composite electrocatalyst for oxygen reduction reaction in alkaline media. *Carbon* **2014**, *73*, 361-370. DOI: https://doi.org/10.1016/j.carbon.2014.02.076.

(100) Hersher, R. After Decades Of Air Pollution, A Louisiana Town Rebels Against A Chemical Giant. In *NPR*, NPR.org, 2018.

(101) Zavarsky, A.; Duester, L. Anthropogenic influence on the Rhine water temperatures. *Hydrol. Earth Syst. Sci.* **2020**, *24* (10), 5027-5041. DOI: 10.5194/hess-24-5027-2020.

(102) *Combined Toxic 100 / Greenhouse 100 Indexes*. Political Economy Research Institute, 2023. https://peri.umass.edu/combined-toxic-100-geenhouse-100-indexes (accessed 2024 November 20th).

(103) Ipbes. Summary for policymakers of the global assessment report on biodiversity and ecosystem services. Díaz, S., Settele, J., Brondizio, E. S., Ngo, H. T., Gueze, M., Agard, J., Arneth, A., Balvanera, P., Brauman, K. A., Butchart, S. H. M., et al. Eds.; IPBES Secretariat, 2019; pp XIV-LXI.

(104) UNEP. Turning off the Tap. How the world can end plastic pollution and create a circular economy. *Nairobi* **2023**.

(105) UNEP. *UN Environment Global Chemicals Outlook II - From Legacies to Innovative Solutions: Implementing the 2030 Agenda for Sustainable Development.*; 2019.

2 Analytical Techniques and Characterisation Methods

A wide range of characterisation methods was needed throughout the research for this thesis. Electrochemical techniques play a key role throughout the results chapters. The carbon nanomaterials that were used throughout the project were characterised by microscopic (transmission and scanning electron microscopy) and spectroscopic means (Raman spectroscopy and X-ray photoelectron spectroscopy (XPS)). The execution of the hydrogenation of small molecules necessitated the use of nuclear magnetic resonance spectroscopy to identify organic products and inductively coupled plasma – optical emission spectroscopy to investigate possible catalyst leaching.

Table of Contents

2.1 Electrochemical methods

All electrochemical experiments were performed in inert atmosphere (N_2 atmosphere of an anaerobic glovebox by *Glove Box Technology*) to prevent the appearance of oxygen-mediated electrochemical features.

2.1.1 Cyclic voltammetry

To record a cyclic voltammogram, the potential applied to the working electrode (WE) as compared to the potential measured at some stable reference electrode (RE) is swept between a start potential E_1 and end potential E_2 while the current output at the WE is recorded. [1] To complete the electrical circuit and enable the current flow, a counter electrode (CE) and a sufficiently concentrated electrolyte, serving as a charge carrier, are required. The observed current can be separated into two distinct portions, the capacitive current I_C and the Faradaic current I_F. [1]

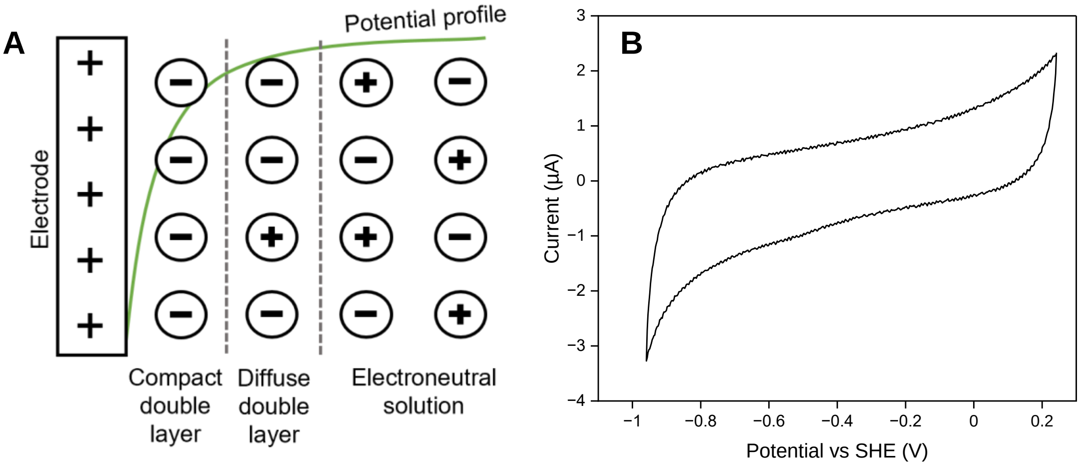

Figure 8 **A** Illustration of the double layer forming through electrostatic interactions between the charged electrode and the ions in solution, adapted from reference 2 and **B** Cyclic voltammogram recorded on a clean carbon electrode in pure sodium phosphate buffer (100 mM) illustrating capacitive current.

As the WE surface is polarized with regard to the bulk solution, electrolyte ions are attracted or repulsed from the charge of the WE and form a so-called double layer. If the surface is polarized positively, negatively charged ions in solution will be selectively attracted to the surface (and vice-versa for a negatively polarized electrode), resulting in a concentration (and electrical potential) gradient towards the bulk solution. As the WE potential is varied, a double layer charging current or capacitive current I_C is observed. This phenomenon leads to the typical appearance of the voltammogram in the shape of a parallelogram in the absence of electron transfer or Faradaic current I_F (Figure 8).[2]

The Faradaic current I_F results from electron-transfer events occurring at the electrode surface and depends on the concentration of redox active species near the electrode. For a given reduction reaction, the flux of oxidized species to the electrode plays an important role in determining the magnitude of I_F. Possible migration, or the movement of species in response to the electric field, is minimized by the presence of excess concentration of electrolyte. Convection can be applied through stirring, rotation of the electrode, or heating of the solution in specific experiments if desired, though cyclic voltammetry is often performed under conditions in which diffusion is the only form of mass transport. [2] Assuming fast electron transfer, the consumption of species *A* to form species *B* near the electrode surface and the diffusion of species to and from the bulk solution results in the well-known 'duck' shape of the CV wave of a reversible redox process. The diffusion layer is defined as the area near the electrode in which the concentrations of *A* and *B* differ from the bulk concentrations[3], and diffusion to and from an electrode with a diameter significantly larger than the diffusion layer is treated as linear.

2.1.2 Electrodes used for cyclic voltammetry measurements

Cyclic voltammetry was performed using a glass electrochemical cell (made in house by academic glass blower Terri Adams) equipped with a water jacket, which was used to stabilise the temperature at 25 °C, and with side arms designed to hold the three required electrodes – working, reference, and counter - in the electrolyte solution.

The main prerequisites for suitable working electrodes are that they be chemically inert in the potential range to be studied and that they be clean. Most of the electrochemistry presented in this thesis is recorded using a pyrolytic graphite electrode manufactured in house using a pyrolytic graphite rod (2 mm diameter) that was attached to a *Delrin* rotating disk electrode case using a small amount of silver-loaded epoxy resin (from *RS Components*), and then sealed to a cylindrical shape using insulating epoxy resin (from *Robnor Resin Lab*). The disk of pyrolytic graphite is exposed on the edge-plane; hence, this type of electrode will be referred to as a pyrolytic graphite edge, or PGE electrode. The PGE WE surface can be prepared before each experiment by manual polishing on increasingly fine abrasive paper to achieve a clean surface. A counter electrode is required to close the electrical circuit and accept any equal and opposite current to or from the working electrode. To ensure that the current flow between WE and CE is never limited by the CE, the surface area of the CE should always exceed that of the WE. For the purposes of this project, the WE is most often experiencing reducing potentials, and it follows that some oxidation event must occur at the CE to complete the electrical circuit. As gas was sometimes observed at the CE, it can be assumed that some amount of the aqueous media is oxidised to produce O_2. For any cyclic voltammetry experiments involving low Faradaic currents, a counter electrode (CE) consisting of a small piece of platinum wire was simply dipped into the solution. For any experiments involving longer time periods or higher currents, the Pt electrode was separated from the bulk solution using a fritted compartment to avoid re-oxidation of the reduced product.

A saturated calomel electrode (SCE, *ItalSens*) was used as the reference electrode in all electrochemical experiments in this thesis. The SCE consists of a platinum pin connected to volume of Hg, which is surrounded by a layer of mercuric chloride (Hg_2Cl_2 (s)) and dipped into a saturated KCl solution. [4] The potential of the SCE is set by the redox reactions between elemental Hg, Hg^{2+}, and Hg_2Cl_2 and can, at 25 ^oC, be corrected to the standard hydrogen electrode (SHE) using Eq. 1.[4] Because the solubility of Cl^- is a variable in determining the potential of the SCE, and is in turn influenced by temperature, use of the water jacket of the electrochemical cell is key to ensure reproducibility. In addition, the validity of the SCE was regularly scrutinized by using it to determine the half point potential in the redox chemistry of ferrocenemethanol, which can be compared to a literature value.

$$E_{SHE} = E_{SCE} + 0.242V \qquad \textit{Eq. 1}$$

2.1.3 Chronoamperometry

In cyclic voltammetry, only the species close to the working electrode are converted while the concentration of starting material in the bulk solution remains essentially unchanged.[1] To convert a sufficient amount of starting material to then be able to use other analytical methods to identify possible products, for example through nuclear magnetic resonance (NMR) spectroscopy, a different electrochemical technique known as chronoamperometry or bulk electrolysis is needed. Two different versions of electrolysis are commonly featured in the chemical literature: Either, a controlled measure of current is passed through the working electrode into the solution (galvanostatic electrolysis), or a controlled potential is applied at the working electrode (potentiostatic electrolysis).[5] As described in detail in the results chapters, for the purposes of this thesis, bulk electrolysis was used to determine which product would form at a specific potential, so galvanostatic electrolysis would have been unsuitable.

Similar to the cyclic voltammetry electrode set up described above, three electrodes are needed for potentiostatic electrolysis. The counter electrode is separated using a glass frit to prevent possible undesired further transformations of the organic starting materials or products at the counter electrode. The conversion of larger amounts of starting material is made easier by the use of a large surface area WE, the preparation of which will be described in the results chapters. The same SCE RE can be used for the electrolysis. To ensure that the species to be converted comes into contact with the WE, the electrolyte is stirred and the experiment is conducted within a cylindrical glass vial without any side-arms in which pockets of still electrolyte could remain.

During potentiostatic electrolysis, a current-versus-time dataset is recorded. The integral under the curve reflects the charge Q passed into the solution. If the amount and identity of product formed can be determined by a complementary analytical technique, the faradaic efficiency (FE) of a process can be calculated.

$$FE(\%) = \frac{N \times n \times F}{Q} \times 100\% \qquad \textit{Eq. 2}$$

Where N is the number of moles of product, n is the number of electrons required to produce the product, and F is the Faraday constant

The FE describes the efficiency of a process in terms of what fraction of the passed electrons are used to make the desired product. [6]

2.2 Aerosol assisted chemical vapour deposition (AA-CVD)

CNTs were synthesized using a CVD system consisting of a single-zone horizontal tubular furnace (*Elite Thermal Systems*; 60 cm x 4 cm inner dimensions; *Eurotherm* 2416 temperature controller), into which a quartz tube (*Robson Scientific*; 80 cm length and 2.1 cm inner diameter) was fed (Figure 9). The inlet of the quartz tube was connected to a piezo-driven

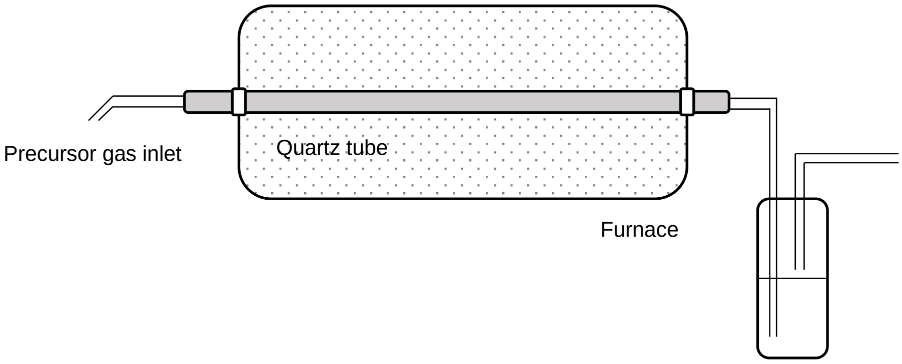

Figure 9 Schematic representation of the furnace set-up used to perform CVD synthesis of CNTs.

aerosol generator (*RBI Pyrosol* 7901). A temperature gradient in the furnace was measured to confirm the area most closely reaching the set temperature (Figure 10). The temperature drops significantly near the inlet and outlet of the furnace; subsequently, only material deposited between approximately 20.5 cm to 34.5 cm into the furnace was collected during future synthetic experiments. For a typical CNT synthesis, the precursor solution (350 mL, 1-5 wt% ferrocene in liquid hydrocarbons) was fed into the piezo-driven aerosol generator, which was then connected to the quartz tube. The set up was flushed with Ar before the furnace was isolated until the synthesis temperature (750-900 ^{o}C) was reached. The precursor solution was vaporised and allowed to flow through the furnace under flow of Ar (1.5 standard litre per minute (slpm)) for the synthesis duration (25 - 120 min). The furnace was allowed to cool to 350 ^{o}C before the Argon flow was stopped to prevent oxidation of the synthesised material upon contact with air.

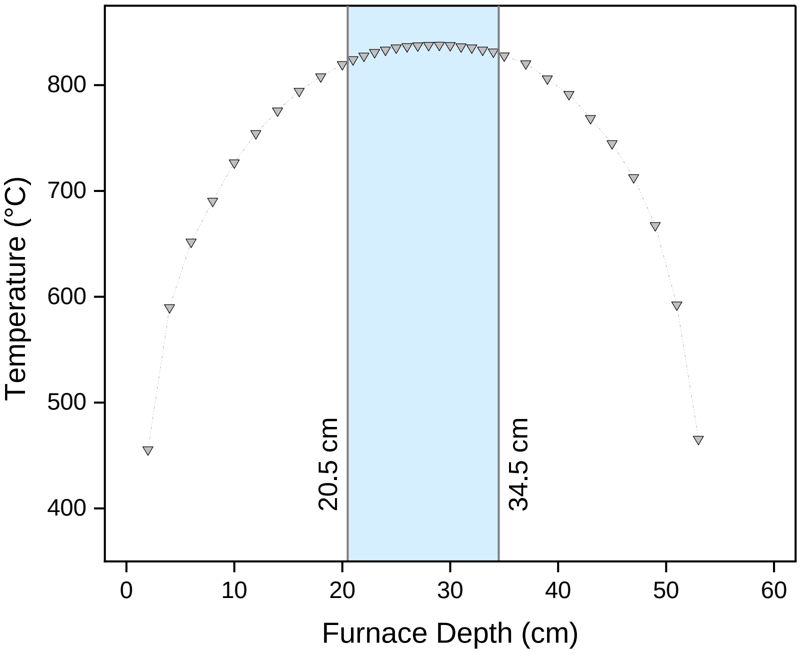

Figure 10 Measured temperature gradient in the tube furnace used for CVD synthesis of CNTs. Note the furnace was open to air on both sides during this measurement to allow insertion of the temperature probe.

2.3 Electron microscopy

As opposed to optical light microscopes, electron microscopes use a beam of electrons rather than a beam of light to illuminate a sample. According to the Abbe equation (Eq. 3), proposed by German physicist Ernst Abbe to describe the formation of images in optical light microscopes, the resolution of an instrument will improve at smaller λ while being inversely related to n – the refractive index of the medium between the objective and the sample, and α – the opening angle of the objective. [7] While visible light has wavelengths of multiple hundreds of nanometres, a much smaller De Broglie wavelength of the electron beam in a typical electron microscope can be achieved by tuning the momentum of the beam, following the De Broglie equation (Eq. 4), leading to a much better resolution. [7] The resolution of an instrument can be understood as the minimum distance between two objects for them to appear as separate in the produced image. [7]

$$d = \frac{0.612\lambda}{nsin\alpha} \qquad \textit{Eq. 3}$$

$$\lambda = \frac{h}{p} \qquad \textit{Eq. 4}$$

Electrons from an electron gun (today, often a tungsten or LaB6 cathode filament) emitted into a vacuum can be attracted towards a positively charged plate – the anode – with a hole in it, through which the beam can pass to travel to the sample. The voltage applied to the anode will determine the acceleration of the electrons, which will then determine the associated wavelength and thus influence the resolution of the instrument. Instead of the glass lenses used in optical microscopes, electric or magnetic fields are applied to the electron beam to achieve focusing action before the electrons hit the sample.[7] In transmission electron microscopy (TEM), the electron beam travels through the sample to produce an image on a fluorescent screen. In scanning electron microscopy (SEM), a focused beam moves (or scans) across the sample and reflected electrons are used to form an image.[7] It follows that samples for TEM must be of very low thickness, while thicker bulk materials can be analysed directly by SEM.

2.3.1 Transmission electron microscopy (TEM)

The typical elements of a transmission electron microscope are listed in Figure 11. The electron gun has usually been a heated tungsten filament, but brighter beams are achieved using lanthanum hexaboride or a field emission gun (FEG), in which an electrostatic field is used to induce electron emission from a tungsten wire. The condenser lenses are used to vary the intensity of the illumination of the sample by focusing the electron beam at, below, or above the plane of the specimen stage. [8] The objective lens helps refocus the beam and the objective aperture can be chosen to select between transmitted or diffracted (i.e., inelastically scattered) electrons. Here, a choice can be made between dark field imaging, where the diffracted electrons are used to form the image and areas of the sample with high mass will appear bright[9] (as these areas will scatter more electrons), or bright field imaging, in which transmitted electrons are used to form the image and areas of the sample with high mass will appear dark (as few electrons pass through these areas). [10] The projector lenses are the final lenses in the

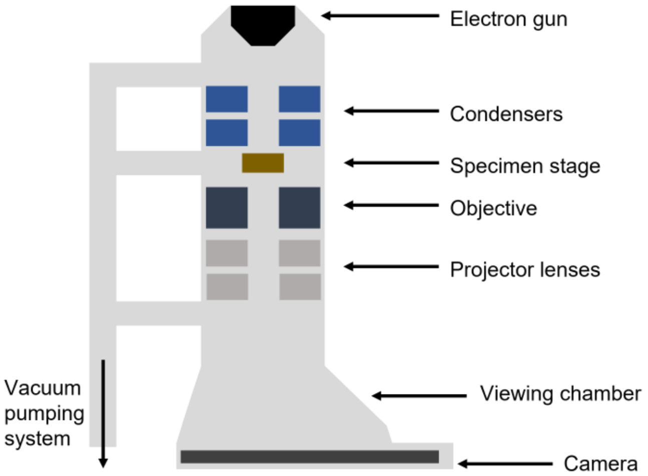

Figure 11 Representation of the features of a transmission electron microscope, adapted from 8.

TEM column and are responsible for further magnification of the image before the beam hits the fluorescent screen in the viewing chamber or the camera where the image can be recorded.[8]

Resolution in TEM has not been limited by the accelerating voltage of the instrument but rather by spherical aberrations caused by an imperfect objective lens, an effect described by the term C_s: Rays passing through the centre of a lens focus at a point further from the lens than those rays passing through the outer edges of the lens. The development of excellent aberration correctors around the turn of the millennium has made resolutions of 0.1 nm achievable and single atom imaging more widely available.[8]

2.3.2 TEM Procedure

Sample inks were prepared by dispersing some milligrams of material in isopropanol by sonication. Some drops of this suspension were then applied onto a 400 mesh copper TEM grid with a lacey carbon film (*Agar Scientific*) and left to dry.

Two transition electron microscopes were available for the purposes of this thesis through the David Cockayne Centre for Electron Microscopy (DCCEM), a multi-user facility in the Department of Materials. The first is a JEOL JEM-3000F 300 kV FEG TEM which was disassembled in 2023. The second is a JEOL ARM-200F, which was used in high resolution TEM mode with images collected through a Gatan Imaging Filter (GIF).

2.3.3 Scanning electron microscopy (SEM)

Early scanning electron microscopes were already constructed in the 1930s. [11] In simple terms, a probe of electrons is focused on the surface of a sample and scanned across it in a series of parallel lines, giving rise to signals of electrons and radiations that are collected and used to construct a three-dimensional representation of the sample. The magnification of the SEM arises from the difference in size between the area scanned by the electron probe and the size of the screen on which the output is displayed. It follows that the resolution of the SEM depends principally on the diameter of the electron probe, since this will determine the size of the smallest area the instrument can reasonably analyse.[8] In practice, the resolving power will also be influenced by the geometry and identity of the sample, because electrons can enter into the sample surface and diffuse within the sample, effectively enlarging the illuminated area and thus lowering the resolution.[8]

2.3.4 SEM Procedure

Some milligrams of dry material (as synthesised, unless otherwise stated) was applied to a carbon adhesive disk (*Agar Scientific*), which could then be applied to the relevant SEM pin to be inserted into the instrument.

Multiple SEMs were used during this project. The main instrument used to analyse synthesized nanomaterials was a JEOL 840F operated at 10 kV acceleration voltage. Images collected in 2024 were provided by Dr. Ryan Schofield using a Carl Zeiss Merlin high resolution FEG SEM operated at 20 kV acceleration voltage. For low magnification images of high-surface area electrodes, a table-top Merlin-60 SEM was used at 3 kV acceleration voltage.

2.4 X-ray photo-electron spectroscopy

N.B. X-ray photo-electron spectroscopy data was kindly collected by Philip Holdway and Wai Man Chan of the Oxford Materials Characterisation Service (OMCS). Data analysis was performed by the author.

X-ray photo-electron spectroscopy (XPS) is a surface-sensitive technique that can offer information on elemental composition and bonding in exquisite detail. Typically, an aluminium anode is bombarded with high-energy electrons, leading to the emission of Al Kα photons, which are micro-focussed and mono-chromated before hitting the solid sample within an ultra-high vacuum chamber (Figure 12). Exposure of the material to incoming photons of energy hν leads to the emission of an electron from a core shell. The kinetic energy KE of the ejected electron is measured and used to quantify the initial binding energy BE associated with the bonding environment of the electron, using Eq. 5, where all quantities other than BE are known.[12] While the KE will vary based on the specific spectrometer used, the BE can be compared across different instruments. [13] In addition, the peak intensity is proportional to the relative atomic percentage of each species, allowing the determination of the surface composition of a sample. [14]

$$BE = hv - KE - \varphi \qquad \textit{Eq. 5}$$

**where φ is the work function of the spectrometer*

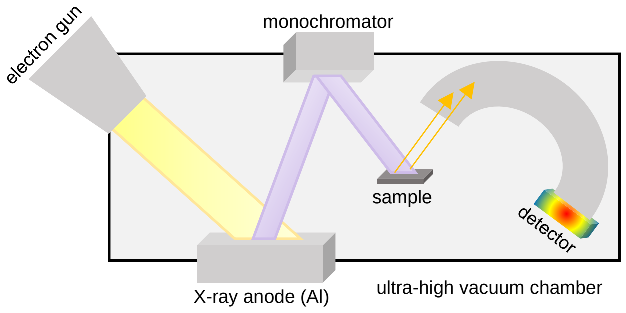

Figure 12 Simplified cartoon of a spectrometer for X-ray photo-electron spectroscopy. Adapted from 12.

The BE – or level of attraction between electron and nucleus – is influenced not only by the identity of the relevant atom, but also by its specific oxidation state or bonding environment, and the resulting change in peak position is described as the chemical shift. In general terms, nuclei with greater electronegativity will eject electrons with relatively higher BE and lower KE. More oxidized nuclei will have a stronger interaction with the leaving electron and again eject electrons with higher BE. Binding of the nucleus to electron withdrawing groups will lead to de-shielding and thus a higher affinity (BE) of the nucleus to the ejected electron. [15]

Aside from shifts due to varied bonding environments, satellites are another important feature of XPS peaks (Figure 13). As a valence electron travels away from the nucleus, it may excite another electron to a higher energy level (shake-up), leading to a decrease in the KE of the ejected electron and a resulting increase in the observed BE. This phenomenon is especially relevant to this thesis, as the shake-up peak (in some cases labelled π-π*) is typically pronounced in conductive materials with many possible energetic transitions, such as conjugated sp^2 carbon materials. If the second electron is removed completely through its interaction with the initially ejected electron, it can contribute to the spectral background as a shake-off satellite. [16]

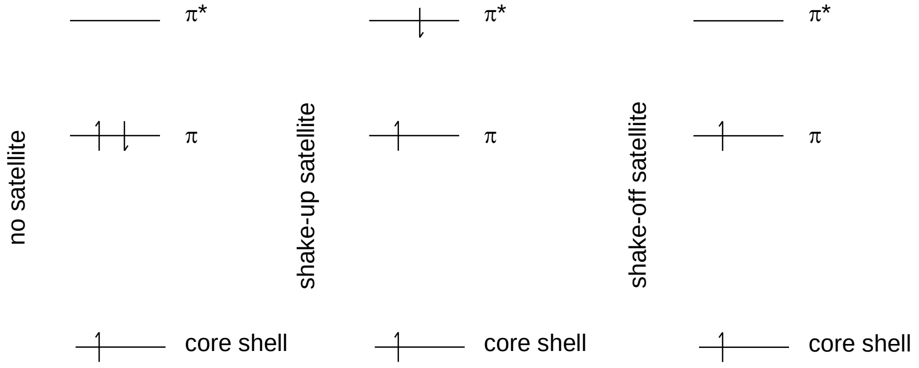

Figure 13 Graphic representation of electron configuration after shake-up (excitation of a second electron) and shake-off (ejection of a second electron) phenomena.

2.5 Raman spectroscopy

Raman spectroscopy measures vibrational transitions which typically correspond to the energy of infrared radiation. However, instead of directly exciting vibrational transition using infrared light as in IR spectroscopy, Raman spectroscopy employs an ultra-violet (UV) laser to induce an excitation to a 'virtual state' below the electronic states in the sample, after which perpendicularly scattered light is detected. The scattered light consists primarily of light of the same frequency ν^o as the incident excitation beam (a result of the elastic Rayleigh scattering), but some amount of the light is scattered inelastically and has frequency $\nu^o \pm \nu_m$, where ν_m is the frequency of a vibrational transition in the sample.[17] Because the population in the vibrational ground state can be expected to greatly exceed those in the vibrational excited states, the $\nu^o - \nu_m$ Raman scattering is usually prevalent (also known as the Stokes lines, as opposed to anti-Stokes lines). A vibrational transition is Raman active if the polarizability – or the ability of the electron cloud to be distorted by an electric field – of the molecule changes during the transition.[17]

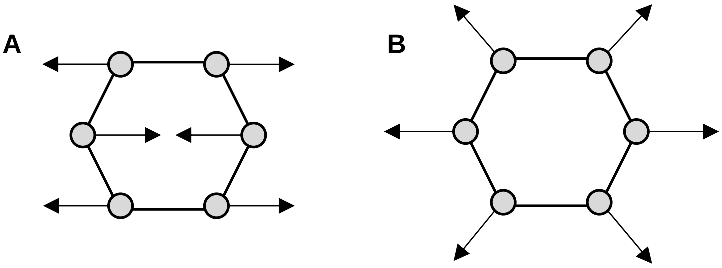

Figure 14 ***A*** *In-plane bond stretching vibration of pairs of sp2 carbon atoms resulting in G band and* ***B*** *breathing mode of six-membered ring leading to D band. Adapted from reference 19.*

Raman spectroscopy is one of the most widely used characterisation techniques of carbon nanomaterials and is well established for the analysis of CNTs.[18] As a quick, relatively easy measurement it can be used as a standard first diagnostic technique to probe the structure of a new material. Graphitic materials have two distinct first order features in their Raman spectra: The G band at ~1580 cm^{-1}, which arises from an E_{2g} in-plane bond stretching of pairs of C sp^2-

hybridized carbon atoms and the D band at ~1360 cm^{-1}, which is attributed to a breathing mode which is forbidden in perfect graphite but is only observed in materials containing six-membered aromatic rings (Figure 14).[19] The intensity ratio I_D/I_G is commonly used to compare the defect density between different materials. Aside from these two major bands, multiple other disorder induced first-order peaks are known, including notably D2 at ~1620 cm^{-1} which merges with the G peak in some materials. The two-phonon overtone of the D band appears at ~2700 cm^{-1} is labelled as G' or 2D in the literature – for the purposes of this thesis, it will be referred to as 2D in line with most reports concerning CNTs. This band does not require disorder and is observed even in perfectly graphitic systems (explaining the alternative nomenclature G').[20]

The D, D2, and 2D bands are dispersive, i.e., their frequency changes with the frequency of the incident laser.[20, 21] The I_D/I_G ratio is also known to depend on the excitation laser frequency.[21] Because all spectra in this thesis are recorded using the same 532 nm laser source, these dependencies can be disregarded herein and all spectra can be compared without consideration of the dispersive properties of the bands.

2.5.1 Raman Spectroscopy: Procedure

Samples were prepared by suspending some milligrams of solid nanomaterial in isopropyl alcohol, then dropping this suspension onto a microscope slide and allowing the solid to dry completely. The instrument used was a JY Horiba Labram Aramis imaging confocal Raman microscope equipped with a 532 nm laser and an 1800 grooves/mm diffraction grating. A silicon wafer was used to calibrate the laser and a minimum of ten spectra at different locations across each sample were taken. The average of these ten spectra was used to characterize the sample.

2.6 UV/Vis Spectroscopy

Light of the ultraviolet or visible (UV/Vis) range of the electromagnetic spectrum (200-800 nm wavelength) carries sufficient energy to cause electronic transitions in many organic molecules. Modern UV/Vis spectrometers can scan through the wavelengths in the UV/Vis range, resulting in an absorbance vs wavelength spectrum. [22] At room temperature, most of the species will initially be in the ground electronic and vibrational state, from which they can be excited to various vibrational states within a higher electronic state, giving rise to the broad peaks seen in UV/Vis spectra. UV/Vis transitions are governed by two selection rules: transitions are allowed if the symmetry of the initial and final state is different but the spin of the electron remains the same. [22]

UV/Vis spectroscopy is a useful and accessible technique for the quantitative analysis of the concentration of a species as the measured absorbance can be related to the path length (l, distance travelled through the solution by the light), the concentration of the molecule (C), and the molar absorptivity (ε, which is characteristic to a molecule at a specific wavelength, and relates to the likelihood of a certain transition occurring) through the Beer-Lambert law (Eq. 6).[22]

$$A = \varepsilon C l \qquad \text{Eq. 6}$$

In this project, UV/Vis spectroscopy was used to measure the conversion of 4-nitrophenol to 4-aminophenol. 4-Nitrophenol has a pKa of 7.15 and is colourless in its protonated form. [23, 24] Deprotonation at high pH leads to increased conjugation between the O^-, benzene, and NO_2, which can be assumed to lower the HOMO/LUMO gap, leading to an associated strong absorbance at 400 nm. To exploit this UV/Vis active transition, and to make sure all 4-nitrophenol in solution would be detected, reaction samples were combined with aqueous NaOH to increase the pH before the spectra were collected.

2.6.1 UV/Vis spectroscopy: Procedure

UV/Visible data were collected on a Cary 60 spectrometer (Agilent) using a quartz cuvette (Helma) with a 1 cm pathlength. Samples were prepared by combining reaction mixture (initially, 5 mM in 4-nitrophenol, 100 μL) with NaOH (3 M, 50 μL) and diluting with MilliQ water (18.2 MΩ cm) to 1 mL. Spectra were compared to a calibration curve which had been prepared by measuring the spectra of varying mixtures of 4-nitrophenol and 4-aminophenol.

2.7 Inductively coupled plasma optical emission spectroscopy (ICP-OES)

The goal of ICP-OES is to detect and quantify the elements present within a sample. The instrumentation is made up of the inductively coupled plasma – which converts the species in the sample into free excited atoms – and the optical emission spectrometer, which detects the electromagnetic radiation that is specific to each element. [25]

The plasma in the ICP-OES instrument is typically Ar based. The torch in which the plasma is formed allows for an outer gas flow, which sustains the plasma, and an internal gas flow used to inject the sample. The top of the torch is surrounded by a copper coil, in which an alternating current (at tens of MHz oscillations, corresponding to a radio frequency generator) is generated, inducing an electromagnetic field. [26] Some Ar atoms in the torch are ionized through the application of a high-voltage spark generated by a Tesla coil, resulting in free electrons that then collide with and ionize more Ar atoms, creating the high temperature (6000 to 10000 K) plasma through a chain reaction. [27] Sample solutions are nebulized and introduced to the ICP torch through the internal Ar flow. The high temperatures and free electrons lead to atomization and ionization/excitation of the sample species. [26] The light emitted by the excited atoms is then detected and analysed by the optical emission spectrometer (OES). The only elements which have a higher ionization potential than Ar and cannot be ionized in Ar-based ICP are fluorine, helium, and neon. [26]

ICP-OES was performed by Dr Anna Forster at the University of Sheffield to probe the concentration of Ni in the reaction mixtures of hydrogenations performed with immobilised Ni-complexes.

2.8 Nuclear magnetic resonance (NMR) spectroscopy

2.8.1 Relevant background of NMR spectroscopy

Nuclear magnetic resonance (NMR) spectroscopy exploits the magnetic moment of the atoms found in the analyte, which is highly sensitive to the environment, both intra- and intermolecular, of the atoms. The nuclear magnetic moment μ can be related to its spin quantum number, I, and its gyromagnetic ratio γ:[28]

$$\mu = \gamma I \qquad \textit{Eq. 7}$$

The spin quantum number depends on the number of unpaired nucleons in the nucleus and has a positive integer or half integer value. A nucleus has $2I+1$ spin-related energy levels that are degenerate unless an external magnetic field B is applied – as, for example, in an NMR spectrometer, which typically employ magnetic fields 10^5 stronger than that of the Earth. [28] The separation of the energy levels depends on the strength of the experienced magnetic field and the gyromagnetic ratio of the nucleus and typically lies in the radiofrequency range. Because of this low energetic difference, the populations of the higher and lower energy levels are nearly equivalent. In any spectroscopic method, the likelihood of exciting a species to the higher level is the same as inducing the reverse transition and the strength of the signal depends on the difference in population of the energy levels. In NMR spectroscopy, ever stronger magnets are used to increase the separation of the energy levels and thus increase the difference in population and the strength of the signal. [28]

Many elements have at least one NMR active isotope, but the most commonly probed nucleus remains the proton (^1H) because of its high μ, its abundance, its presence in many molecules of interest, and its convenient I-1/2 quantum number which causes only two energy levels, simplifying the resulting spectrum. [29] For the purposes of this thesis, one-dimensional ^1H NMR is used to assess conversion of nitrocompounds to the relevant hydroxylamines or amines. This is possible because the actual magnetic field experienced by any one nucleus depends on its electronic environment (electrons around the nucleus induce local magnetic fields that can augment or diminish the applied B) and will differ slightly from the applied B. It follows that any one nucleus will absorb a slightly different frequency of electromagnetic radiation, since the separation of the energy levels depends on the experienced magnetic field B', which leads to the appearance of peaks at different frequencies for non-equivalent positions in a molecule in the NMR spectrum. [29]

The integral of the peaks depends on the number of equivalent protons that the peak represents, as well as the concentration of the molecule. These integrals can be used to assess conversion by calculating the ratio of the integrals of the peaks assigned to the starting material to those assigned to the product(s). If an internal standard of known concentration is added to the sample, the concentrations of the other species can be estimated by comparing the magnitudes of the relevant integrals. [30]

Many of the NMR experiments conducted in this project analysed samples containing an aqueous reaction mixture. The ^1H nuclei in the water molecules would flood the signal and make the spectrum unusable without the application of a water suppression procedure. In simple terms, a focused pulse or pulse sequence targeting the water resonance specifically is applied before the sample is excited and the signal detected – the water ^1H signal is then already saturated and its intensity is greatly diminished in the recorded spectrum.[31]

2.8.2 NMR Spectroscopy: Procedure

Most NMR samples were made up of untreated reaction mixture (90%) mixed with D_2O (10%). The sample was transferred to an NMR tube (‘Wilmad-LabGlass’). Two Bruker AVIIIHD 400 Nanobay instruments equipped with a 9.4T magnet, a 5 mm z-gradient broad-band multinuclear probe, 60-position SampleExpress robotic sample changer and controlled with TOPSPIN 3 software were used interchangeably to run the NMR experiments. The H_2O ^1H signal is suppressed using a standard, pre-programmed Bruker noesygppr1d sequence. Chemical shifts of ^1H NMR spectra are given in ppm and referenced to residual solvent signals, where appropriate (DMSO-d_6: 2.50 ppm, acetonitrile-d_3: 2.06 ppm). Data were processed using MestreNova software. Manual rephasing was performed as required. A Whittaker smoother baseline correction was applied across the spectra. For low-concentration data, a non-local means noise reduction procedure was applied.

2.9 References

(1) Elgrishi, N.; Rountree, K. J.; McCarthy, B. D.; Rountree, E. S.; Eisenhart, T. T.; Dempsey, J. L. A Practical Beginner's Guide to Cyclic Voltammetry. *Journal of Chemical Education* **2018**, *95* (2), 197-206. DOI: 10.1021/acs.jchemed.7b00361.

(2) Jean-Michel Saveant, C. C. Single-Electron Transfer at an Electrode. In *Elements of Molecular and Biomolecular Electrochemistry*, 2019; pp 1-80.

(3) Diffusion layer. In *IUPAC Compendium of Chemical Terminology*, 3.0.1 ed.; Vol. 3; International Union of Pure and Applied Chemistry (IUPAC), 2019.

(4) Szabó, S.; Bakos, I. Reference Electrodes in Metal Corrosion. *International Journal of Corrosion* **2010**, *2010* (1), 756950. DOI: https://doi.org/10.1155/2010/756950.

(5) Hilt, G. Basic Strategies and Types of Applications in Organic Electrochemistry. *ChemElectroChem* **2020**, *7* (2), 395-405. DOI: https://doi.org/10.1002/celc.201901799.

(6) Kempler, P. A.; Nielander, A. C. Reliable reporting of Faradaic efficiencies for electrocatalysis research. *Nature Communications* **2023**, *14* (1), 1158. DOI: 10.1038/s41467-023-36880-8.

(7) Goodhew, P. J. Microscopy with light and electrons. CRC Press, 2000; pp 13-31.

(8) Watt, I. M. The electron microscope family. Cambridge University Press, 1997; pp 59-135.

(9) Krivanek, O. L.; Chisholm, M. F.; Nicolosi, V.; Pennycook, T. J.; Corbin, G. J.; Dellby, N.; Murfitt, M. F.; Own, C. S.; Szilagyi, Z. S.; Oxley, M. P.; et al. Atom-by-atom structural and chemical analysis by annular dark-field electron microscopy. *Nature* **2010**, *464* (7288), 571-574. DOI: 10.1038/nature08879.

(10) Klein, N. D.; Hurley, K. R.; Feng, Z. V.; Haynes, C. L. Dark Field Transmission Electron Microscopy as a Tool for Identifying Inorganic Nanoparticles in Biological Matrices. *Analytical Chemistry* **2015**, *87* (8), 4356-4362. DOI: 10.1021/acs.analchem.5b00124.

(11) McMullan, D. Scanning electron microscopy 1928–1965. *Scanning* **1995**, *17* (3), 175-185. DOI: https://doi.org/10.1002/sca.4950170309.

(12) Watts, J. F.; Wolstenholme, J. Electron Spectrometer Design. In *An Introduction to Surface Analysis by XPS and AES*, 2019; pp 19-67.

(13) Watts, J. F.; Wolstenholme, J. Electron Spectroscopy. In *An Introduction to Surface Analysis by XPS and AES*, 2019; pp 1-18.

(14) Tougaard, S. Practical guide to the use of backgrounds in quantitative XPS. *Journal of Vacuum Science & Technology A* **2021**, *39* (1), 011201-011201. DOI: 10.1116/6.0000661.

(15) Okpalugo, T. I. T.; Papakonstantinou, P.; Murphy, H.; McLaughlin, J.; Brown, N. M. D. High resolution XPS characterization of chemical functionalised MWCNTs and SWCNTs. *Carbon* **2005**, *43* (1), 153-161. DOI: https://doi.org/10.1016/j.carbon.2004.08.033.

(16) Brisk, M. A.; Baker, A. D. Shake-up satellites in X-ray photoelectron spectroscopy. *Journal of Electron Spectroscopy and Related Phenomena* **1975**, *7* (3), 197-213. DOI: https://doi.org/10.1016/0368-2048(75)80061-2.

(17) Ferraro, J. R. *Introductory Raman Spectroscopy*; Elsevier Science & Technology, 2003.

(18) Delhaes, P.; Couzi, M.; Trinquecoste, M.; Dentzer, J.; Hamidou, H.; Vix-Guterl, C. A comparison between Raman spectroscopy and surface characterizations of multiwall carbon nanotubes. *Carbon* **2006**, *44* (14), 3005-3013. DOI: https://doi.org/10.1016/j.carbon.2006.05.021.

(19) Ferrari, A. C.; Robertson, J. Interpretation of Raman spectra of disordered and amorphous carbon. *Physical Review B* **2000**, *61* (20), 14095-14107. DOI: 10.1103/PhysRevB.61.14095.

(20) Pimenta, M. A.; Dresselhaus, G.; Dresselhaus, M. S.; Cançado, L. G.; Jorio, A.; Saito, R. Studying disorder in graphite-based systems by Raman spectroscopy. *Physical Chemistry Chemical Physics* **2007**, *9* (11), 1276-1290, 10.1039/B613962K. DOI: 10.1039/B613962K.

(21) Cançado, L. G.; Jorio, A.; Pimenta, M. A. Measuring the absolute Raman cross section of nanographites as a function of laser energy and crystallite size. *Physical review. B, Condensed matter and materials physics* **2007**, *76* (6). DOI: 10.1103/PhysRevB.76.064304.

(22) Anderson, R. J.; Bendell, D. J.; Groundwater, P. W. *Organic Spectroscopic Analysis*; The Royal Society of Chemistry, 2004. DOI: 10.1039/9781847551566.

(23) Strachan, J.; Barnett, C.; Masters, A. F.; Maschmeyer, T. 4-Nitrophenol Reduction: Probing the Putative Mechanism of the Model Reaction. *ACS Catalysis* **2020**, *10* (10), 5516-5521. DOI: 10.1021/acscatal.0c00725.

(24) Abdollahi, M.; Mohammadirad, A. Nitrophenol, 4. In *Encyclopedia of Toxicology (Third Edition)*, Wexler, P. Ed.; Academic Press, 2014; pp 575-577.

(25) Fassel, V. A.; Kniseley, R. N. Inductively coupled plasma. Optical emission spectroscopy. *Analytical Chemistry* **1974**, *46* (13), 1110A-1120a.

(26) Makonnen, Y.; Beauchemin, D. Chapter 1 - The inductively coupled plasma as a source for optical emission spectrometry and mass spectrometry. In *Sample Introduction Systems in ICPMS and ICPOES*, Beauchemin, D. Ed.; Elsevier, 2020; pp 1-55.

(27) Singh, M. K.; Singh, A. Chapter 18 - Inductively coupled plasma–atomic emission spectrometry. In *Characterization of Polymers and Fibres*, Singh, M. K., Singh, A. Eds.; Woodhead Publishing, 2022; pp 421-434.

(28) Hore, P. J. Introduction. In *Nuclear Magnetic Resonance*, 2 ed.; Oxford University Press, 2015; p 1.

(29) Hore, P. J. Chemical shifts. In *Nuclear Magnetic Resonance*, 2 ed.; Oxford University Press, 2015; p 10.

(30) Simmler, C.; Napolitano, J. G.; McAlpine, J. B.; Chen, S.-N.; Pauli, G. F. Universal quantitative NMR analysis of complex natural samples. *Current Opinion in Biotechnology* **2014**, *25*, 51-59. DOI: https://doi.org/10.1016/j.copbio.2013.08.004.

(31) Giraudeau, P.; Silvestre, V.; Akoka, S. Optimizing water suppression for quantitative NMR-based metabolomics: a tutorial review. *Metabolomics* **2015**, *11* (5), 1041-1055. DOI: 10.1007/s11306-015-0794-7.

3 Doped carbon nanotubes and electrocatalytic reduction of nitro-compounds

The initial motivation for the project described herein stems from work in the Vincent group on the cofactor-free biocatalytic hydrogenation of nitro-groups on hydrogenase-modified carbon particles, described in Sokolova *et al.*[1] This catalyst system employs the hydrogenase enzyme as a dihydrogen oxidation catalyst. The resulting electrons pass through a chain of iron sulfur clusters from the active site to the protein surface and on to the conductive carbon particle, where the nitro group can be reduced electrochemically. As the nitro-to-amine transformation is thought to occur on the conductive carbon surface, replacing the carbon particle by an electrocatalytically active material should offer the possibility to tune this catalyst system. To identify such an active material, a closer look at nitro-reduction potentials on various conductive carbons capable of immobilising hydrogenase enzyme was warranted. CNTs had already been employed as supports for hydrogenases both within the group and beyond; their synthesis is accessible and tuneable, and their doping with heteroatoms has been

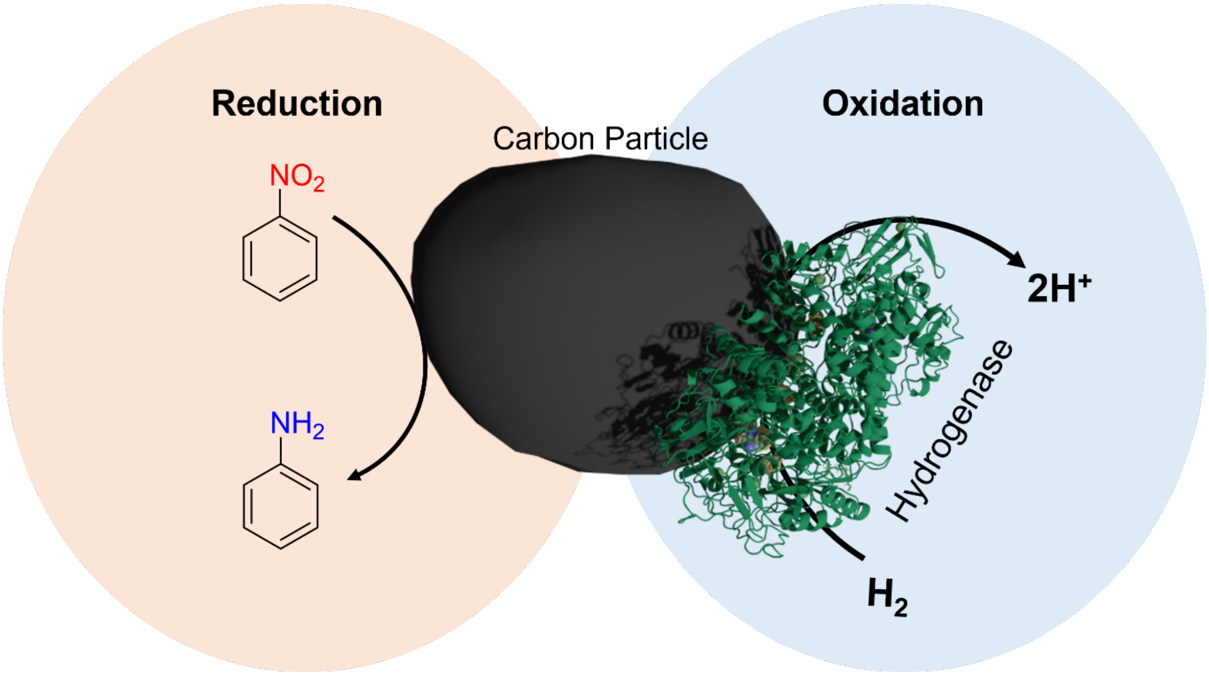

Figure 1 Graphic representation of the biocatalytic hydrogenation of nitro-groups using hydrogenase enzyme on a conductive carbon particle which operates by separated half reactions, developed by the Vincent group.

suggested in literature to lead to electrocatalysis of, for example, the oxygen reduction reaction (ORR).[2] In addition, doping of CNTs introduces polar features and structural defects that improve the water-miscibility of the material, possibly improving their applicability to the hydrogenation system based on hydrogenase on carbon. A collaboration with Dr. Dillon McGurty, then PhD candidate in the Grobert group, made possible an initial cyclic voltammetry experiment to characterize 4-nitrophenol reduction on his nitrogen-doped CNTs, boron-nitrogen-co-doped CNTs (BN-CNTs), and pristine CNTs (Figure 16). The reduction potential of 4-nitrophenol on the NCNTs was observed to be anodically shifted – indicating electrocatalytic activity. This initial result inspired the work described in Chapter 3, which will present the synthesis of a range of doped CNTs and their evaluation as electrocatalysts of the nitro-reduction reaction.

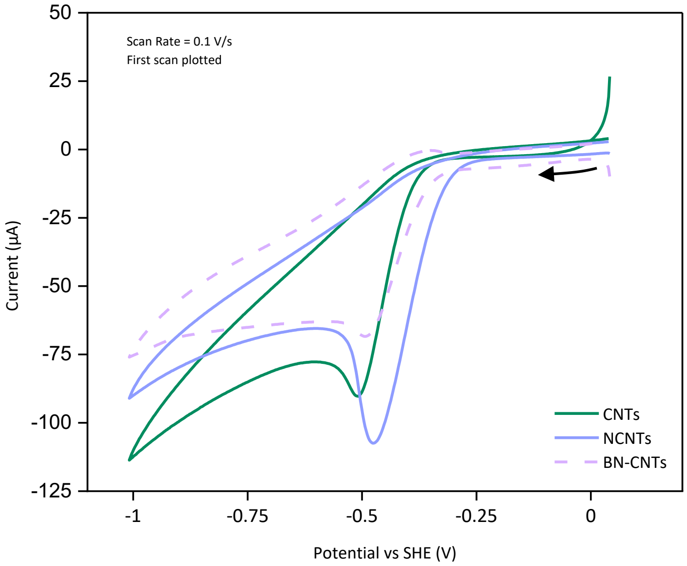

Figure 16 Cyclic voltammograms recorded on PGE WE modified with CNTs, NCNTs, and BN-CNTs, respectively, immersed in 4-nitrophenol (1 mM) containing sodium phosphate electrolyte at 100 mV/s. Materials synthesized by Dr Dillon McGurty.

Table of Contents

3.1 Experimental

3.1.1 Chemicals and buffers

Ferrocene (>99%) was purchased from *Thermo Scientific* and used as received. Benzylamine (*ReagentPlus*, 99%) was purchased from *Sigma-Aldrich* and used as received. 4-Nitrophenol (≥99%) and 1-nitrohexane (98%) were purchased from *Sigma-Aldrich* and used as received.

Aqueous solutions were prepared using MilliQ water (resistivity 18.2 MΩ cm, *Millipore*). Buffer salts and solvents were purchased from *Sigma-Aldrich*. Deuterated solvents were purchased from *Sigma-Aldrich* (D_2O, 99.9% D; DMSO-*d6*, 99.9% D).

Sodium phosphate buffer was prepared by dissolving an appropriate mass of Na_2HPO_4 and NaH_2PO_4 in water after which the pH was adjusted to the desired value by adding HCl(aq) or NaOH(aq) dropwise and monitoring pH using an Ag/AgCl pH electrode (*Fisher*).

3.1.2 Cyclic voltammetry (CV) experiments

A glass electrochemical cell made in-house (glass blower: Terri Adams) with a water jacket adjusted to 25 ^{o}C was equipped with a saturated calomel reference electrode (SCE, Palmsens BV) and a coiled Pt wire as the counter electrode (CE), and charged with sodium phosphate buffer (100 mM, pH 6.0) along with the appropriate nitro-compound (1 mM). A pyrolytic graphite edge (PGE) rotating disk electrode (RDE) as the working electrode (WE) was modified by dropping the relevant nanocarbon slurry (2 μL, 20 mg/mL) onto the electrode and allowing the film to dry completely. Cyclic voltammograms were recorded using a PalmSens 4 potentiostat and the corresponding PSTrace software.

For more detail on chemical vapour deposition (CVD), CNT characterisation, and electrochemical experiments please refer back to Analytical Techniques and Characterisation Methods (Chapter 2).

3.2 Synthesis and characterisation of carbon nanotubes (CNTs)

To further investigate a possible electrocatalytic nitro-reduction activity on NCNTs, a set of doped CNTs of known composition and morphology was needed. CNTs were synthesized by aerosol-assisted chemical vapour deposition, as described in detail in 2.2. Briefly, a carbon precursor solution containing ferrocene as a catalyst is aerosolised and fed into a tube furnace under inert atmosphere and high temperature, where CNT growth occurs. Toluene was used to produce pristine CNTs, while benzylamine was used to produce NCNTs. Nitrogen dopant content was tuned by varying the N/C ratio in the carbon precursor or the synthesis temperature. Reaction time, gas flow rate, and ferrocene catalyst concentration were held constant throughout all experiments; however, feedstock composition or temperature were varied for each synthesis and the reproducibility of CNT production was not studied. The typical yield was lower at approximately 300 mg for doped material, while multiple grams could be collected for pristine CNTs.

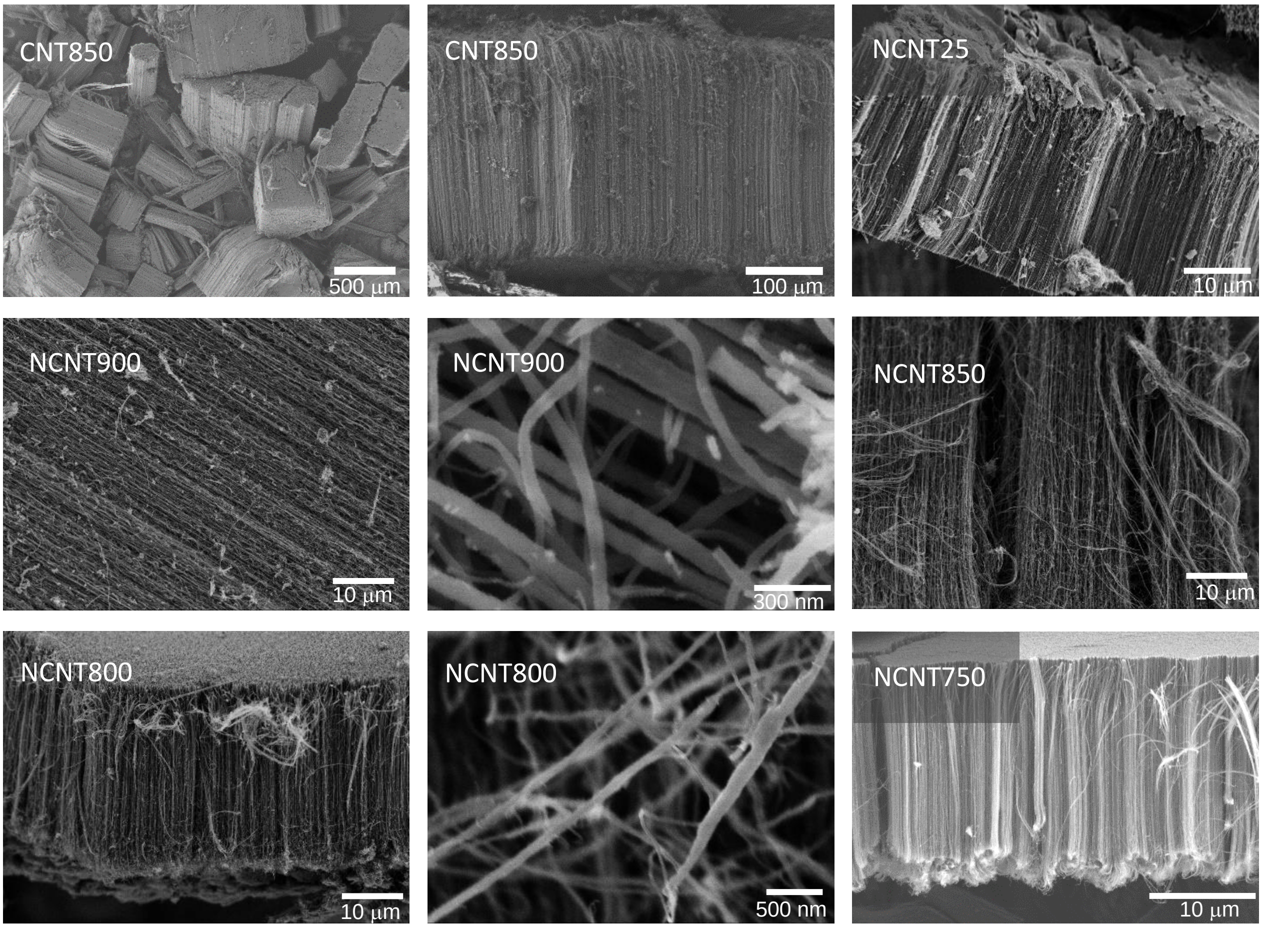

Figure 17 Characteristic SEM micrographs showing flakes of different samples at various magnification. Collected using a JEOL 840F SEM operated at 10 kV acceleration voltage.

Table 2 Sample length as estimated by SEM measurements, with differences in synthesis parameters shown.

Sample	Precursor	Temperature (^{o}C)	Length (µm)	Error (µm)
CNT850	Toluene	850	280	*10*
NCNT25	25% Benzylamine in toluene	800	28	2
NCNT900	Benzylamine	900	120	10
NCNT850	Benzylamine	850	50	*NM*
NCNT800	Benzylamine	800	30	3
NCNT750	Benzylamine	750	17	2

3.2.1 Analysis of size and morphology through electron microscopy

CNTs were collected from the inner walls of the quartz tube used in the CVD furnace. Scanning electron microscopy (SEM) was used to evaluate the general morphology and length of the collected product (Figure 17). Because the material is scraped mechanically from the quartz tube, the carpets are broken up into smaller flakes. While all of the materials were found to have grown in aligned carpets, some bits of tangled, wool-like structures were also observed. The tubes are in the range of 10s to 100s of μm in length, with the sample produced from pure toluene reaching near 300 μm but most doped materials remaining well below 100 μm. Similar trends of slower growth in N-doped materials have already been described in literature, [3] and could be due to the forced incorporation of defects into the hexagonal lattice as well as the formation of five-membered rings that induce an inward curvature of the nanotube walls (which can also lead to a bamboo-type structure, see transmission electron microscopy results described below). Sumpter *et al* have suggested that N atoms preferentially occupy the open edge of growing nanotubes, leading to a slower growth once the edge has been fully saturated.[4] The differences in length of the samples should be considered when interpreting the remaining characterisation data, as the higher ratio of edge to plane-type carbon will influence the observed defect density, for example, and could also change the chemical behaviour of the CNTs. Overall, the SEM data indicates successful synthesis of aligned CNTs with only small amounts of amorphous material observed.

Transmission electron microscopy (TEM) was used to further probe the structure, crystallinity, and purity of the CNTs. As expected, the NCNTs contain closed compartments within the tube, also known as a bamboo-type structure (Figure 18 B and C). This inward curvature is thought to be induced by the formation of five-membered N-heterocycles (defects in the sp2 lattice) that cause the fusion of the CNT walls.[4] On these grounds, the observation of bamboo-structure can be taken as an indication of successful N-incorporation into the CNT walls. Carbon-covered iron nanoparticles and sections of iron-filled CNTs can also be found in all of the prepared samples, with the extend of iron contamination being further probed by X-ray photoelectron spectroscopy (XPS) and thermal gravimetric analysis (TGA) described below.

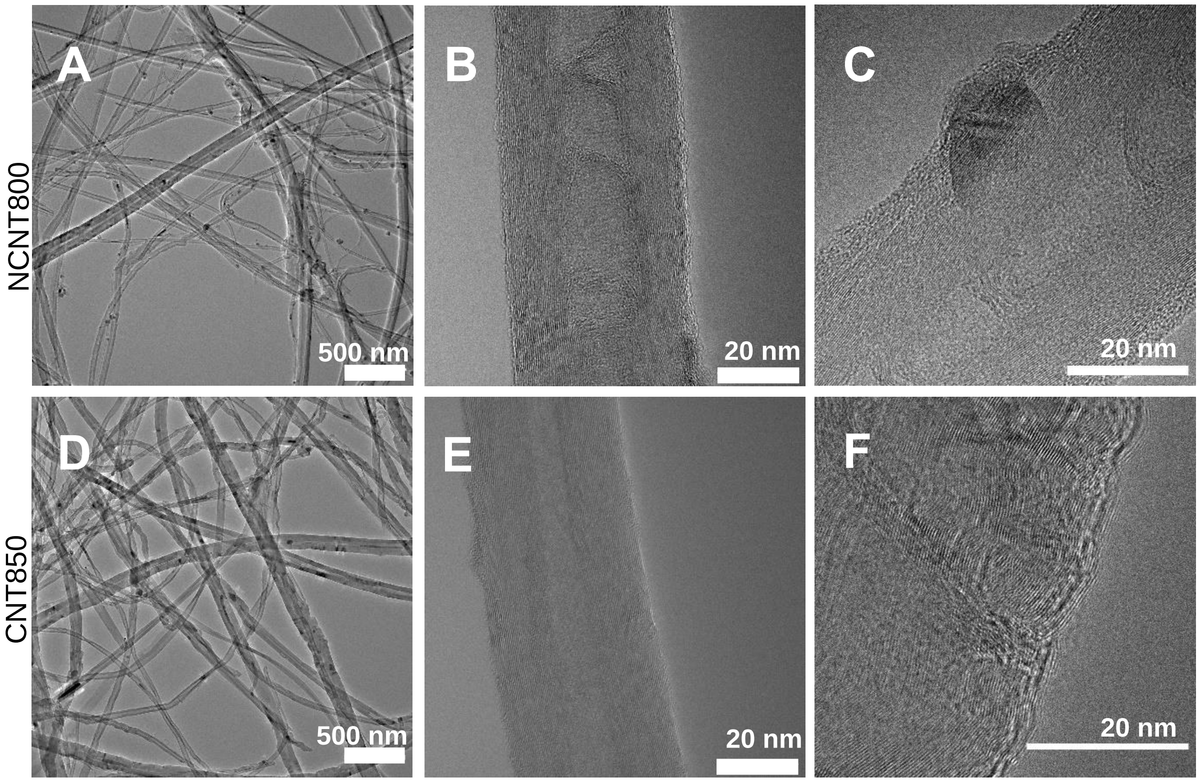

*Figure 18 Transition electron micrographs comparing NCNT800 (**A**-**C**) and CNT850 (**D**-**F**) at increasing magnification. **A** and **D** show presence of Fe nanoparticles. Bamboo-type inner walls typical for NCNTs are visible in **B**. **C** shows carbon-covered Fe nanoparticle. F shows CNT wall with imperfections. Collected using a JEOL ARM-200F STEM microscope in TEM mode.*

TEM was also used to investigate the diameter of the produced materials. Histograms were plotted using diameter measurements from 100 individual tubes per sample from multiple micrographs, with those micrographs shown in Figure 19 being one example per sample. All of the samples are largely made up of CNTs between 30-70 nm in diameter, with large standard deviations of around 30 nm but only few outliers reaching diameters up to 200 nm or below 30 nm.

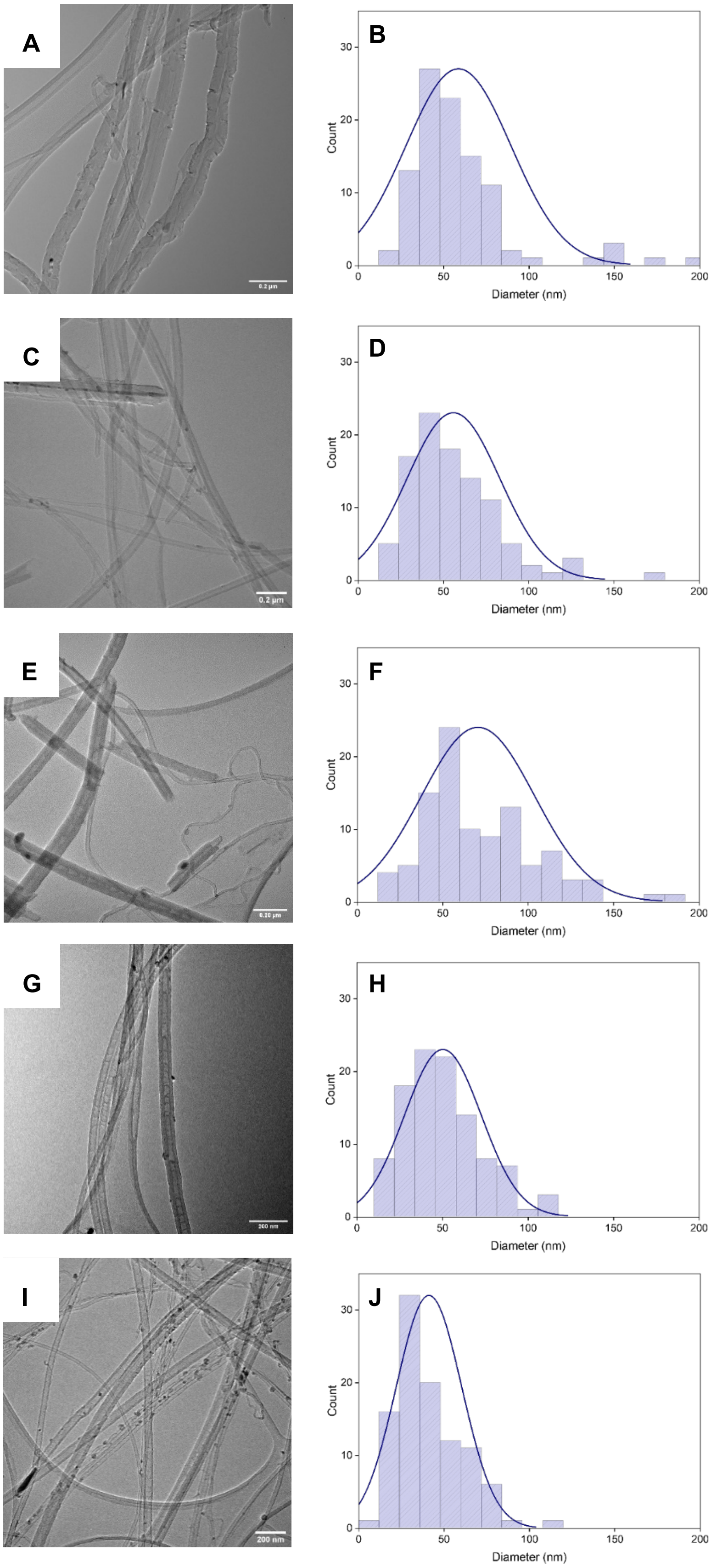

*Figure 19 Example transmission electron micrograph and diameter histogram for sample CNT850 (**A** + **B**). NCNT25 (**C**+**D**), NCNT900 (**E**+**F**), NCNT800 (**G**+**H**), and NCNT750 (**I**+**J**). Collected using a JEOL ARM-200F STEM operated in TEM mode.*

3.2.2 Analysis of dopant incorporation and bonding environment through XPS

XPS, a surface sensitive technique, was used to compare dopant incorporation – while N trapped in the inner walls of the material is likely not detected, the electrochemical activity of the material was thought to be most likely influenced by the surface chemistry of the material.

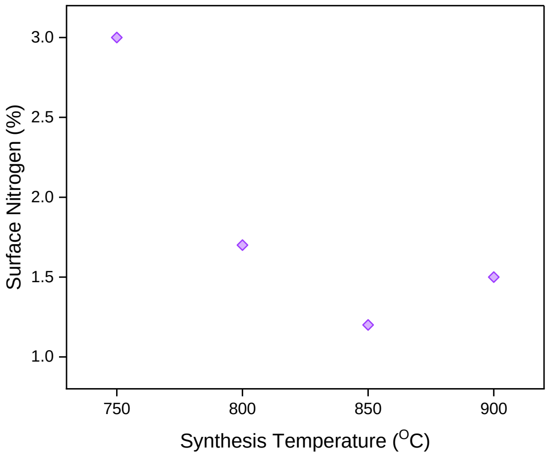

Figure 20 N-incorporation is influenced by synthesis temperature.

The highest doping of 3 at% (Figure 20, Table 3) was detected in the sample synthesized using the highest N/C ratio precursor (0.14:1, pure benzylamine) and the lowest temperature (750 °C). Lower synthesis temperatures have been reported in literature to lead to higher dopant incorporation, which is attributed to the lower crystallinity in materials synthesized at lower temperatures, favouring heteroatom incorporation. [5] In addition, higher temperatures make the

Table 3 Surface concentration of N, O, and Fe in set of CNT samples.

	XPS - Atomic %		
	N	**O**	**Fe**
CNT850	0.0	1.8	0.1
NCNT25	0.5	2.6	0.4
NCNT850	1.2	2.0	ND
NCNT900	1.5	2.1	ND
NCNT800	2.1	2.9	0.4
NCNT750	3.0	4.1	0.7

complete dissolution of any C-N bonds present in the precursor more likely, which would decrease the amount of N bonded in the carbon lattice.[6] Nonetheless, even at 900 ^{O}C more than 1 at% N was detected in the material. To obtain a low-dopant material, the benzylamine precursor was diluted to 25 v/v% using toluene, leading to an approximate N/C ratio in the precursor mixture of 0.04:1, and a resulting material containing only 0.5 at% N as detected by XPS.

Iron contaminant, stemming from the ferrocene catalyst used in the CVD process, is present in all of the synthesized material (as shown by TGA, see below), but the surface value detected by XPS varies. For samples NCNT850 and NCNT900 the surface Fe contamination is below the detection limit of the spectrometer, which lies at around 0.1 at%. Following this observation, NCNT900 was primarily used in the cyclic voltammetry experiments comparing CNTs and NCNTs. Because NCNT850 contains a similar N-doping level to NCNT900, the sample was excluded from the electrochemical experiments and only the samples shown in Table 4 were used.

The bonding environment of the dopant as well as the extent of C-X bonding in the materials was also investigated using the obtained XPS data (see, Figure 21). The N1s peak was deconvoluted to four peaks, representing pyridinic, pyrrolic, and graphitic bonding environments alongside a fourth peak assigned to defective or oxidized nitrogen species, aligned with many reports in literature.[7-10] All materials contain a distribution amongst bonding environments with no clear preferred species. However, it is notable that the materials with lower doping levels contain a higher relative amount of graphitic N as compared to the materials with higher doping levels, in which pyridinic and pyrrolic N overtake the graphitic species. The material synthesized at only 750 ^{o}C is shown to contain a significantly higher amount of oxidized N, which is also reflected in the higher atomic % of O in the overall sample (Table 3).

The C1s peaks of the materials were compared as a source of complementary information. The asymmetric tail of the C1s peak can be deconvoluted to estimate the extent of C-X bonding. In undoped graphitic materials, separate peaks are typically assigned to C-O, C=O and O-C-O, or O=C-O type bonding environments with electrons ejected from more oxidized carbon atoms appearing at higher binding energy. However, the addition of N dopant complicates this assignment. Carbon atoms in nitrogen-containing functional groups lead to signals that are separated by only ~0.5 eV from oxygen-containing groups that are also present in all samples reported here. Overfitting of too many components will lead to peak overlap and a low residual

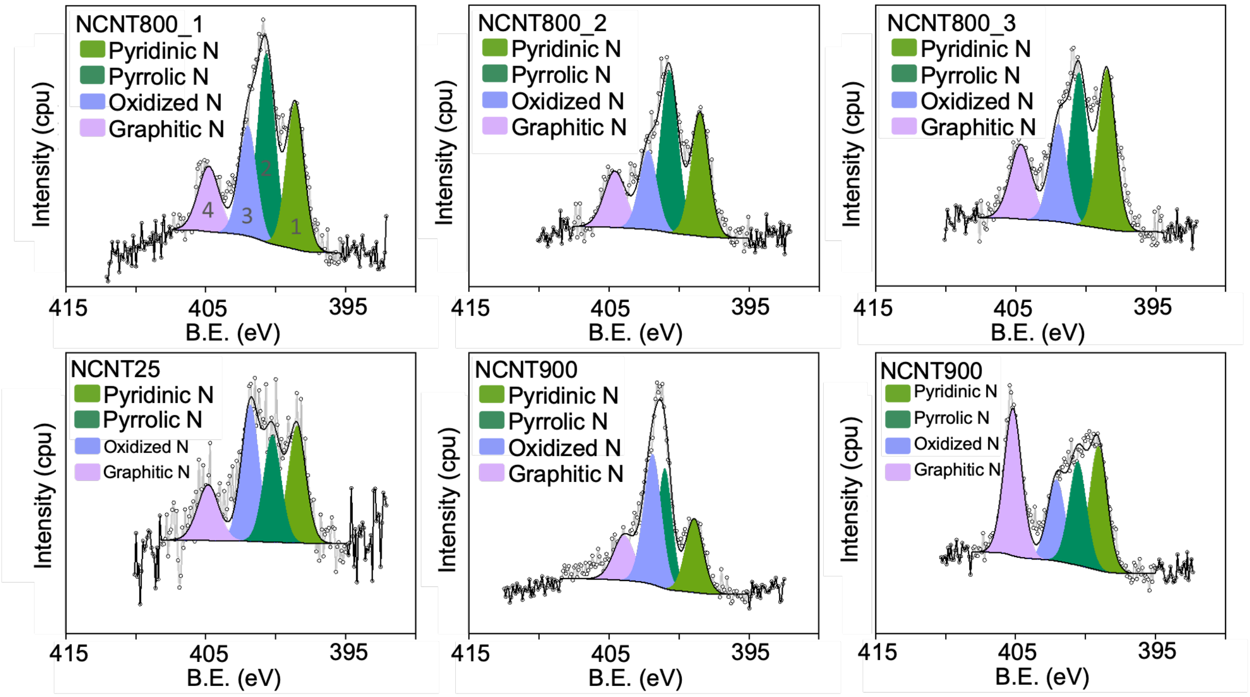

Figure 21 Deconvolution of three batches of NCNT prepared at 800 °C from benzylamine (top), showing minor differences in bonding environment. Deconvolution varies to greater extent for samples prepared at different temperatures (NCNT900 and NCNT750) or from benzylamine/toluene precursor mixture (NCNT25).

Table 4 Average percent assigned to the bonding environments for four representative NCNT samples.

		Graphitic (%)		Pyrrolic (%)		Pyridinic (%)		N-O/N-X (%)	
Sample Name	Overall N (%)	Average	St Dev	Average	St Dev	Average	St Dev	Average	St Dev
N-CNT25	0.5	31.7	0.3	22.1	2.9	26.2	1.2	20.0	4.4
N-CNT900	1.5	35.7	0.6	27.2	2.0	22.9	1.8	14.2	1.3
N-CNT800	2.1	20.4	3.4	31.5	4.1	25.5	2.3	22.6	5.9
N-CNT750	3.0	16.0	1.4	23.7	1.3	26.1	1.5	34.2	2.4

that no longer reflects the actual low quality and high uncertainty of the peak model.[11] To prevent excessive peak overlap, the author chose to simply fit five peak components as C1 through C5, with C1 and C2 representing C-C and C=C, while C3 through C5 represent C-O and C-N functional groups with stepwise increases in oxidation of the carbon atom. Because the components purposefully cover both C-O and C-N bonding, the peak model allows for a slightly broader full width half maximum of 1.5 eV. The overall percentage area corresponding to C3-C5 (or C-X bonding where X = O, N) was compared among produced material and was found to increase with increasing N-dopant incorporation, further indicating successful incorporation of nitrogen into the carbon lattice (Figure 22).

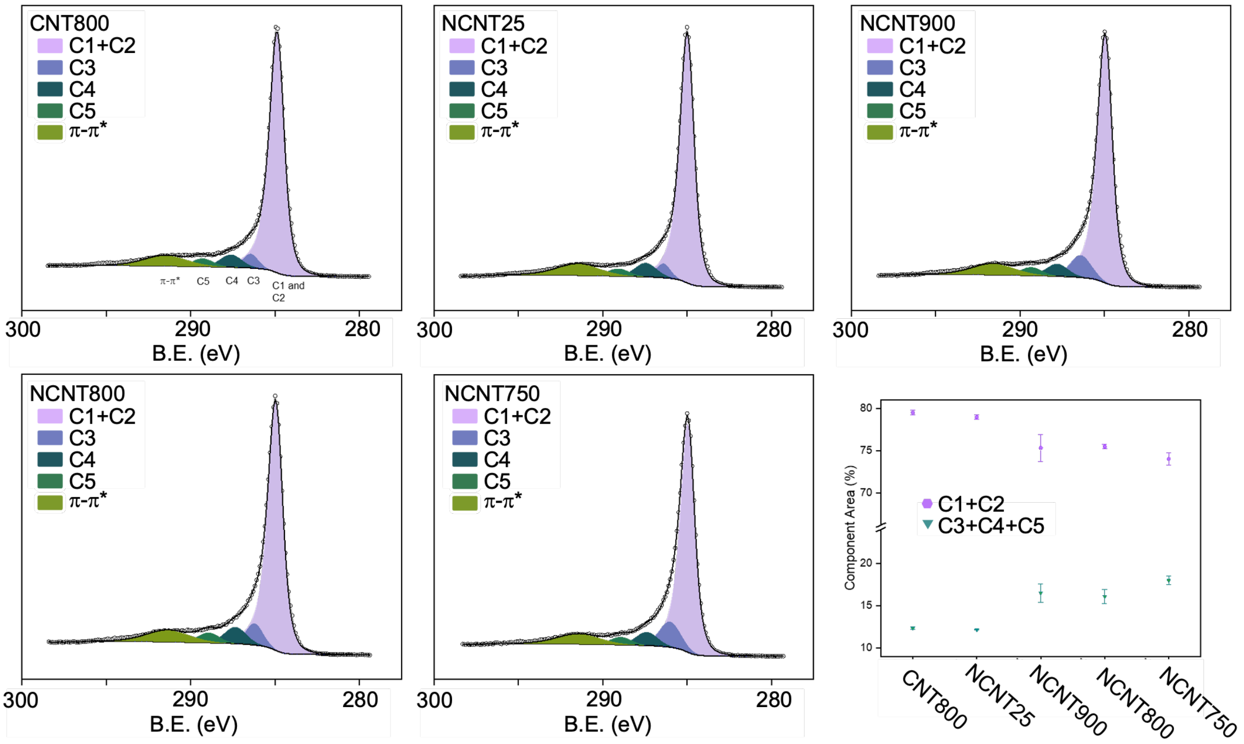

Figure 22 C1s peak devonvolution showing greater C-X bonding (responding to signal at higher BE) for doped material with higher N-content. Error bars stem from fits of three analysed points per sample.

3.2.3 Analysis of crystallinity through Raman Spectroscopy

Raman spectra of graphitic materials offer useful information on defect density and structure of the sp2 lattice. The prominent and recognizable features of these spectra are the D and G peaks, which occur at around 1350 cm^{-1} and 1580 cm^{-1}, respectively. The G peak is observed in all carbon materials containing sp^2 hybridization, and is due to an in-plane stretching mode of pairs of sp^2 carbons. The D peak is attributed to a breathing mode of the six-membered rings, which is forbidden in perfect graphite and only observed in defective materials.[12] The ratio of the intensity of the D and G peaks (I_D/I_G) is commonly used to estimate and compare the defectiveness of various graphitic materials. Because the introduction of dopant increases the defect density of the CNTs, a higher I_D/I_G ratio is expected. Indeed, the samples with higher dopant levels have significantly higher I_D/I_G values, indicating higher defect density and successful disruption of the sp2 carbon lattice (Figure 23). While the shorter length of the samples should also increase the observed defectiveness, the doped samples were observed by SEM to not follow a clear trend in length - i.e., NCNT25, at 28 μm is shorter than both

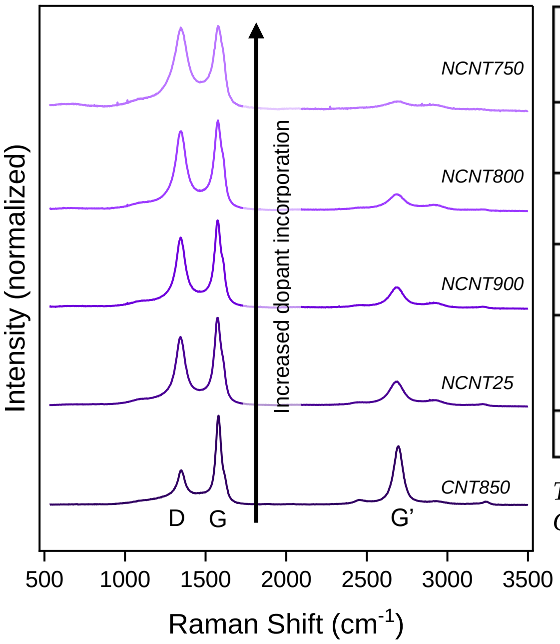

Sample	Precursor	T (°C)	Surface N XPS-determined	I_D/I_G
N-CNT750	Benzylamine	750	3.02%N	1
N-CNT800	Benzylamine	800	2.4%N	0.9
N-CNT900	Benzylamine	900	1.5%N	0.8
N-CNT25	25% Benzylamine in Toluene	800	0.5%N	0.7
CNT850	Toluene	850	*0%N*	0.4

Table 5 I_D/I_G ratio and surface nitrogen concentration of select CNT batches.

Figure 23 Raman spectra of representative NCNT samples showing increasing D-peak with higher dopant incorporation.

NCNT900 (120 μm) and NCNT800 (30 μm), but has a lower I_D/I_G ratio which corresponds well to its lower doping level (Table 5). The intensity of the G’ peak, a symmetry-allowed overtone of the D peak which is always observed even in defect-free samples, decreases significantly in intensity for the doped CNTs. The G’ band is thought to be influenced by the stacking order of graphene layers as well as crystallite size, and the decrease in intensity observed here could be due to the breaking of the stacking order between the walls of the NCNTs because of the heteroatom incorporation, as reported in literature for graphene oxide.[13, 14]

To investigate whether a shift in peak position could be observed with nitrogen-doping, the first-order peaks were subjected to a five-peak fitting model adapted from Chernyak *et al*.[15] While no trend in peak position was extracted, the model underlines the presence of multiple bands that give further information on the graphitic nature of the materials (Figure 24). The D2 peak, for instance, arises from similar sources as the D peak but is only visually obvious in highly ordered materials – in sufficiently disordered structures, it is reported to merge with the G peak.[16] The D2 peak is visible as a shoulder on the G peak in the samples, other than NCNT750, which had already been identified as a high-defect material. The D3 and D4 peaks are attributed to the presence of impurities[16] – because C-O and C-N bonds are present in the samples, it is not surprising that these peaks have significant contributions to the overall line-shape.

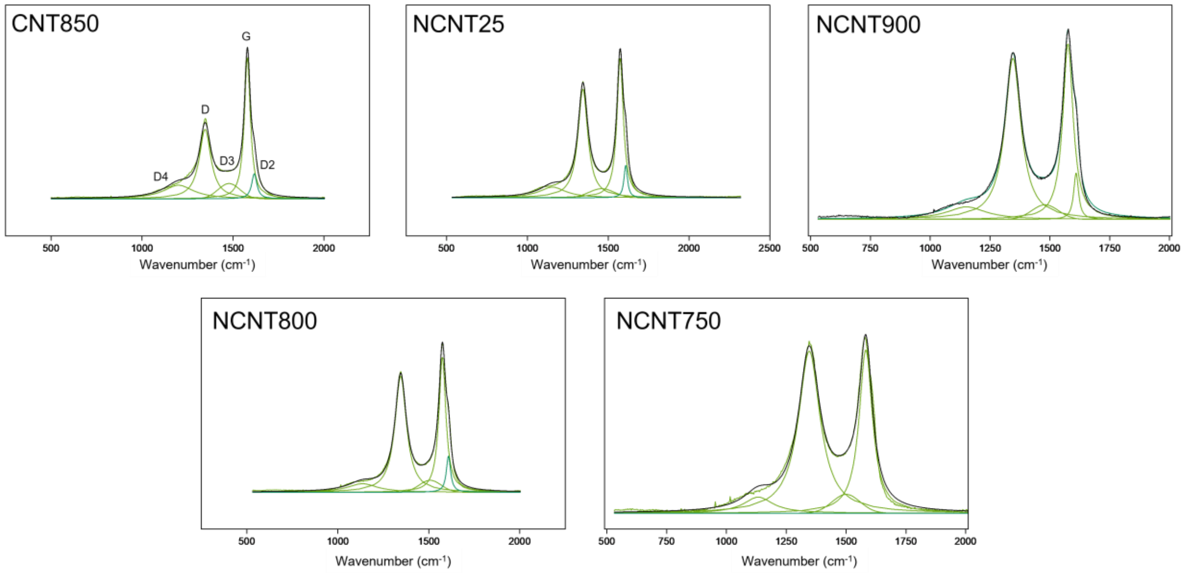

Figure 24 Deconvolution of first order features in Raman CNT spectra.

3.2.4 Analysis of oxidation resistance and residual iron content through thermal gravimetric analysis (TGA)

The oxidation resistance as well as the residual mass after oxidation of the synthesized CNTs was investigated by running TGA experiments, in which the sample is heated from room temperature (RT) to 900 °C under air while the mass of the sample is recorded. Because the lighter elements, here principally carbon, will oxidize and disperse in the form of small molecules, and because there is no evidence of significant amounts of other elements than C, O, N, and Fe (as well as H, presumably), the remaining mass after the temperature increase can be assumed to be constituted of iron oxide. Assuming the iron is oxidized to Fe_2O_3, it follows that about 69.9% of the residual mass is pure Fe. All of the analysed samples were found by TGA to contain significant amounts of Fe (Figure 25). Only very small levels of Fe were detected by XPS, which is a surface sensitive technique; hence, the Fe detected by TGA can be assumed to have been covered by multiple layers of carbon prior to the oxidation step. The sample NCNT900 is the doped sample with the lowest residual Fe mass, with the value even dipping below the toluene-only CNT850 sample. This low Fe mass as compared to the other NCNTs can be explained by the longer length of this sample, which could indicate that more carbon nucleated at each catalytic Fe nanoparticle. Because NCNT900 was found to have the lowest Fe content by TGA as well as XPS, this sample was used as a key comparative material in the subsequent electrochemical experiments presented later in this chapter.

The pristine CNT850 oxidize at significantly hotter temperatures than the doped CNTs – a trend that has been reported in literature[3] and that agrees well with the higher defect density of the NCNTs, which give the material more possible sites for earlier oxidation (Figure 25). The most defective NCNT750 loses mass continually before the main oxidation event, which suggests the presence of significant amounts of amorphous carbon impurities, and which is not observed in the other samples.

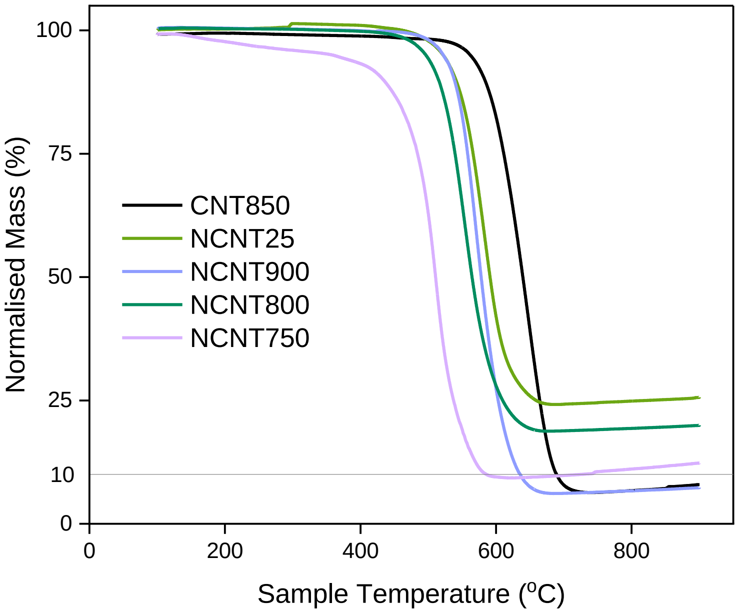

Figure 25 Overlayed TGA traces for the representative CNT batches recorded under flow of air. Recorded using a PerkinElmer TGA8000 instrument.

3.2.5 Summary

To investigate the electrochemical behaviour of NCNTs as electrodes for the reduction of nitro-groups, a set of CNTs had to be produced. Five of the synthesized CNTs were chosen as comparative materials for the electrochemical experiments described below: a pristine CNT850, synthesized from toluene, and four NCNT samples that vary in doping level, iron contamination, and length. Successful nitrogen-doping is supported by XPS data, in which both N1s and C1s peaks suggest C-N bonding, by TEM observations, which show typical bamboo-type structures, by Raman spectroscopy, that shows higher defect density for doped materials, and by TGA, which shows the typical lower oxidation resistance. The NCNTs range from 0.5-3 at% surface nitrogen, as detected by XPS. The sample NCNT900 will be preferably used as a comparative material to the pristine CNT850, because no surface Fe was observed by XPS and TGA showed it contained a similar amount of total Fe to CNT850. These two materials are also simply referred to as CNT and NCNT in the below and in Chapter 4.

3.3 Cyclic voltammetry of 4-nitrophenol

Initially, 4-nitrophenol was chosen as a comparative compound to study the aqueous nitro-reduction on the produced carbon nanomaterials, because it is water-soluble, less toxic than the simpler nitrobenzene, and because it plays an important role in industry as a precursor to paracetamol.[17] In addition, the 4-nitrophenol to 4-aminophenol reaction is accompanied by an obvious colour-change, allowing for UV/Vis monitoring of electrosynthesis experiments.

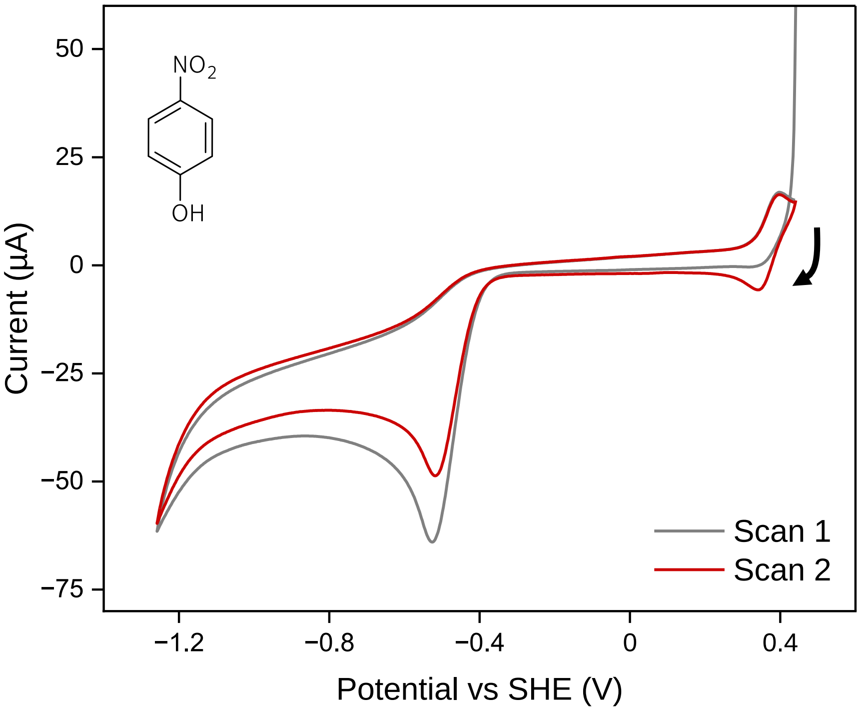

Figure 26 Cyclic voltammogram recorded on clean PGE WE immersed in 4-nitrophenol (1 mM) in sodium phosphate electrolyte (pH 6.0, 100 mV) at 0.01 V/s. Initial high current is due to lack of pre-treatment and is attributed to capacitive charging.

The cyclic voltammogram (CV) of the 4-nitrophenol solution recorded on a pyrolytic graphite edge (PGE) working electrode is dominated by a large, irreversible reduction wave commencing at -0.35 V versus the standard hydrogen electrode (SHE) (Figure 26). After the first reduction in the first scan has occurred, a reversible redox wave appears at 0.4 V vs SHE, indicating the product of the reduction process at -0.35 V is being oxidized (Scheme 5). This process has been attributed to the reversible 2e$^-$ oxidation to the quinoneimine, and the main reductive wave is thought to represent the complete 6 e$^-$ reduction to the amine.[18] This is not always obvious for electrochemical data recorded for other aromatic nitro-compounds, where intermediates such as the hydroxylamine (4e$^-$ reduction) are also observed. Note also the onset of the hydrogen evolution reaction (HER) on the PGE WE at more negative potentials than -1 V vs SHE. In future CVs in this thesis, the window will be narrowed to focus only on the main nitro-reduction peak. For the cyclic voltammetry experiments, carbon materials were suspended in a water/ethanol mixture by sonication, drop-cast onto PGE, which was then used as the working electrode in a standard three-electrode electrochemical cell charged with a sodium phosphate electrolyte containing 1 mM 4-nitrophenol.

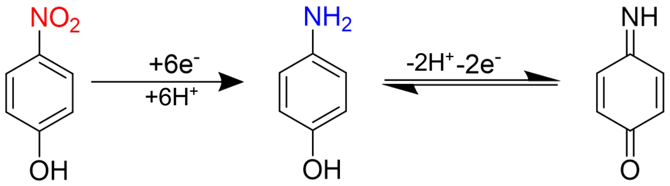

Scheme 5 Reduction of 4-nitrophenol to 4-aminophenol (six electrons) and subsequent reversible oxidation of the amine.

3.4 Parameters for the electrochemical comparison of electrode materials

The initial electrochemical work of this project focused on the evaluation of a suitable parameter for the comparison of carbon materials as nitro-reduction cathodes. An important consideration in the assessment of a novel electrocatalyst is the electrode surface area, as it is directly related to the magnitude of the observed current. Two readily available cyclic voltammetry (CV) methods for estimating the electrochemically active surface area (ECSA) were explored in the early stages of the project. First, the use of ferrocyanide as a reversible redox system allowed the measured peak current to be related to the ECSA using the Randles-Sevcik equation: [19]

$$I_p = 268600 n^{\frac{3}{2}} A D^{\frac{1}{2}} C v^{\frac{1}{2}} \qquad \textit{Eq. 8}$$

Second, the ECSA can be determined from the specific capacitance of the material (C_S) and the double layer capacitance (C_{DL}), which in turn can be extracted from the relationship between the capacitive current (I_C) and the CV scan rate (ν).[20]

$$ECSA = \frac{C_{DL}}{C_S} \qquad \textit{Eq. 9}$$

$$I_C = v \times C_{DL} \qquad \textit{Eq. 10}$$

The first method suffers from low accuracy due to its failure to account for surface features smaller than the diffusion layer. The second method suffers from the wide-spread practice of using a single value for C_S across materials, as its actual value for a specific surface is usually unknown.

Because of these disadvantages and the significant time investment related to ECSA determination, it was decided early in the research project to primarily rely on the onset potential rather than the magnitude of the observed current to measure and compare the applicability of the materials as electrocatalysts to the nitro-reduction reaction. The onset potential, at which the faradaic current begins to increase in magnitude, remains a problematic value for electrocatalyst comparison as it is somewhat undefined. Methods that overly rely on the slope of the reductive wave, for example by defining the onset potential as the point at which the first derivative of the curve reaches a certain value, were deemed ineffective in this particular case because the shape of the surface of the electrode, which changed with each catalytic ink, influences diffusion processes and thus the shape of the voltammogram. To solidify the onset potential for this particular project, a current magnitude below the capacitive current is chosen at which to read the onset potential of the reduction. This potential value will be referred to as an ‘approximation of the onset potential’ and should be considered to be slightly more negative than the accurate onset value.

3.5 Electrocatalytic reduction of nitro-compounds on doped carbon nanotubes

Modification of the PGE with either doped or pristine CNTs increases the ECSA of the electrode and leads to a significantly higher current response as compared to the clean PGE (Figure 27). Modification of the PGE with the different materials led to a similar peak current, suggesting that a similar surface area results from the immobilisation onto the electrode for the materials. The doped materials, however, introduce a new reduction wave at a more positive onset potential – an indication of a new catalytic site that is not present on the pristine CNTs. This anodic shift of more than 100 mV of the 4-nitrophenol reduction was observed reproducibly across the multiple trialled NCNTs (Figure 27). Some of the doped materials show a varyingly intense redox feature around 0 V vs SHE. Because this feature is not visible on NCNT900 (which has the lowest detected iron contamination), and most intense on NCNT750 (which has the highest detected iron contamination), it was assumed to be a redox behaviour of the metal contaminant. The shifted nitrophenol reduction peak occurs for all of the doped materials, regardless of the presence or absence of this redox behaviour around 0 V vs SHE.

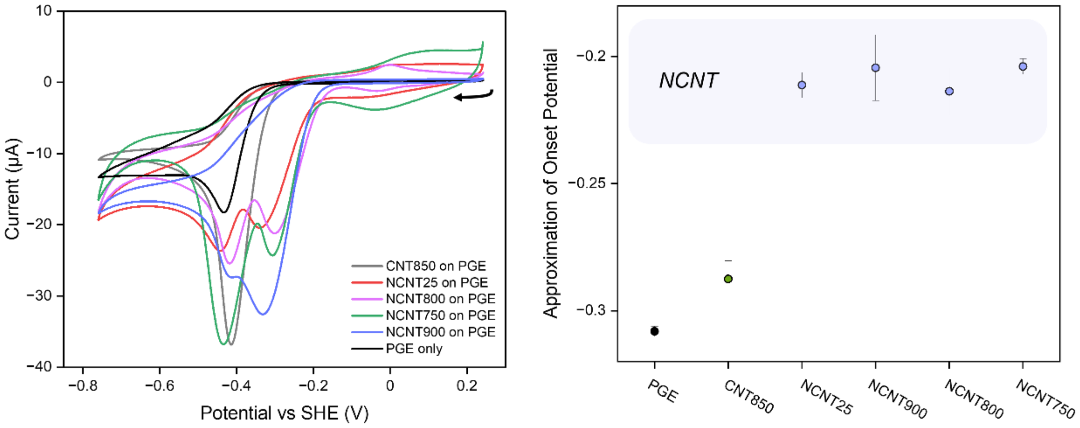

Figure 27 **A** *Cyclic voltammograms of the PGE WE (blank, then modified with CNT (green trace) and NCNT (blue trace) immersed in 4-nitrophenol (1 mM) containing sodium phosphate electrolyte (100 mM, 6.0 pH), scan rate 0.01 V/s.* **B** *Approximate onset potential is reproducibly anodically shifted by around 100 mV for CVs recorded on NCNT-modified WEs. Error bars were established using 3 replicate electrode preparations using the respective nanomaterial.*

The voltammogram recorded on the NCNTs as shown in Figure 27 is not only anodically shifted; instead, it seems a second, milder reduction process is occurring while there is still a peak visible at the same potential as where the reduction occurs on the pristine CNTs. The more negative peak was initially thought to be due to areas of the PGE that remain uncovered and in contact with the solution. In order to probe whether both peaks stem from the catalytic ink or if indeed the more negative reduction simply occurs on the electrode surface, cyclic voltammograms were recorded on an Au disk electrode. The clean Au does show a slight nitro-reduction peak; however, the corresponding current is low and the potential quite negative (Figure 28). The catalyst inks were prepared as before but the immobilisation proved complicated, with the interactions between the clean Au surface and the carbon materials being less favourable. The dried material easily fell off of the electrode, explaining the low currents of the CVs recorded on Au shown in Figure 28. Nonetheless, the collected data prove

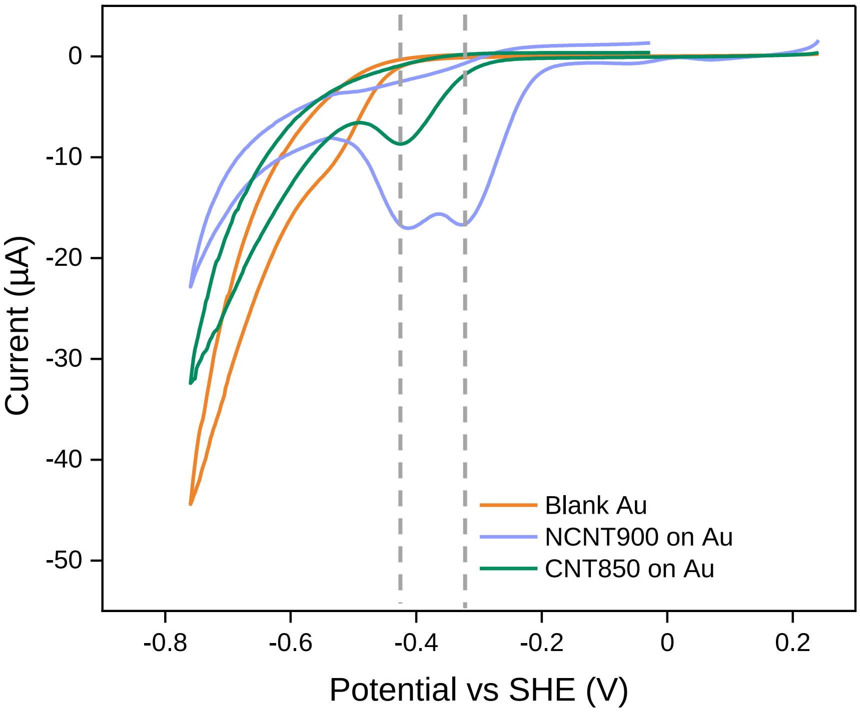

Figure 28 Cyclic voltammograms recorded on Au WE modified with NCNT (blue trace) and CNT (green trace) immersed in 4-nitrophenol (1 mM) containing sodium phosphate electrolyte (100 mM, pH 6.0). Scan rate 0.01 V/s.

interesting: there clearly are two peaks visible when measuring 4-nitrophenol reduction on NCNTs, which indicates that there are two possible active sites or reduction mechanisms occurring. As the second peak lines up well with the position of the single peak observed on the pristine CNTs, it could be a result of the nitro-reduction occurring on areas of the NCNT sample surface that behave similarly to the CNTs, either because of low active site distribution or because of the presence of undoped or amorphous impurities. The NCNTs should be considered to be heterogeneous and to contain some amount of material that behaves more similarly to the CNTs.

3.5.1 Electrocatalytic activity of NCNTs towards nitro-hexane

With the encouraging observation of a reduction wave at milder potentials on the NCNT-modified working electrode for 4-nitrophenol, trials of the electrochemistry of other nitro-compounds were warranted. Because simple aliphatic nitro-compounds tend to require a more

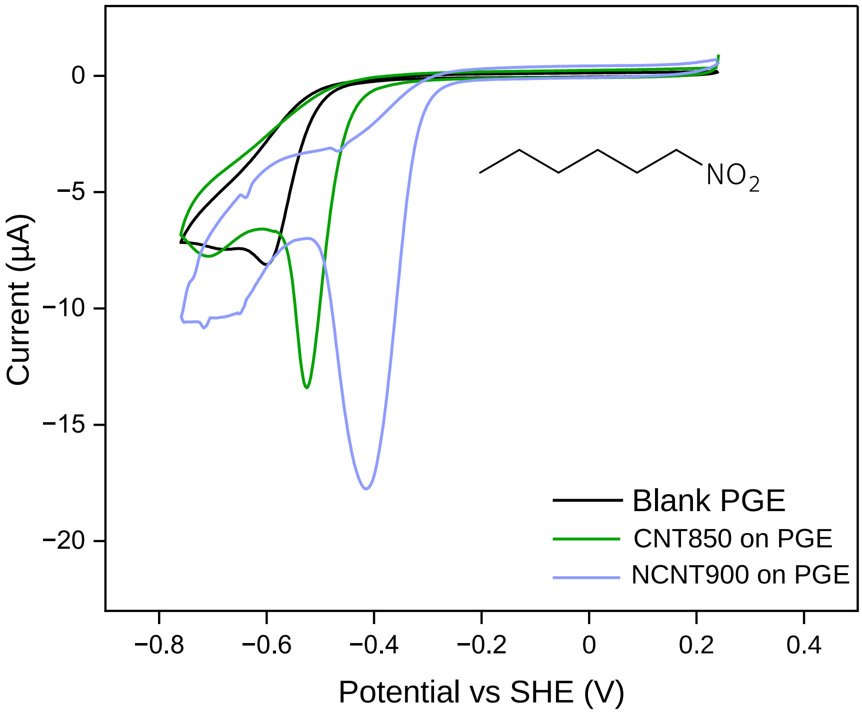

Figure 29 Cyclic voltammograms recorded on PGE WE modified with CNTs (green trace) or NCNTs (blue trace) immersed in nitrohexane (1 mM) containing sodium phosphate electrolyte (pH 6.0, 100 mM) at 0.01 V/s.

negative potential than aromatic compounds,[1] nitro-hexane was chosen as an interesting trial compound. Modification of the working electrode with the NCNT film led, as with the 4-nitrophenol, to a significantly milder onset potential. Notably, the pristine sample CNT850 also seemed to give an advantage (though smaller) when compared to the potential required for the reduction on the blank PGE (Figure 29). The shape of the cyclic voltammogram does not show the same double wave seen on the doped material for the nitrophenol reduction (Figure 27). It is unclear why – possibly this could be caused by the lower solubility of nitrohexane which could lower the availability of the compound near the electrode surface.

3.5.2 Nitro-reduction on commercial carbon black

The Hyd1/C catalyst for the hydrogenation of nitro-compounds has primarily been prepared using commercial carbon black materials[1], warranting a comparison between these carbons and the synthesized CNTs. Many types of carbon have been shown to be applicable to the immobilisation of hydrogenase[21] and the Vincent group primarily relies on the commercial

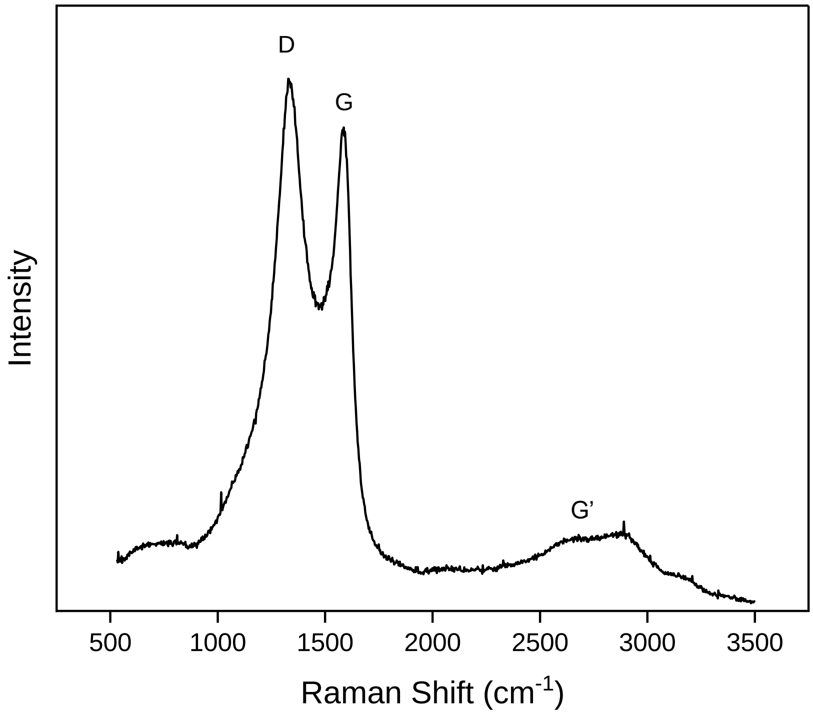

Figure 30 Raman spectrum of commercial carbon black 'BP2000'.

carbon black ‘Black Pearls 2000’ obtained from Cabot Corporation which is typically used as received. This material consists of nanoparticles that are less than 50 nm in diameter[21] and that have significant amorphous character, as confirmed by the significant D peak contribution to the 1st order Raman bands and the near absence of the G’ peak, which suggests the absence of stacking order between graphitic layers (Figure 30). Still, the sharp G peak proves the presence of sp2 hybridized carbon and the D peak is only present in samples containing 6-membered rings, suggesting that BP2000 has some graphitic character.

A main advantage arising from the more amorphous structure of the BP2000 is the greater ease with which it is suspended in aqueous solution as compared to the more graphitic CNTs. The slurries produced through sonication of BP2000 using the same method as was used for the CNTs are more uniform and easier to transfer. While air bubbles were frequently observed on the CNT films on the PGE electrode, the BP2000 films showed greater wettability which may

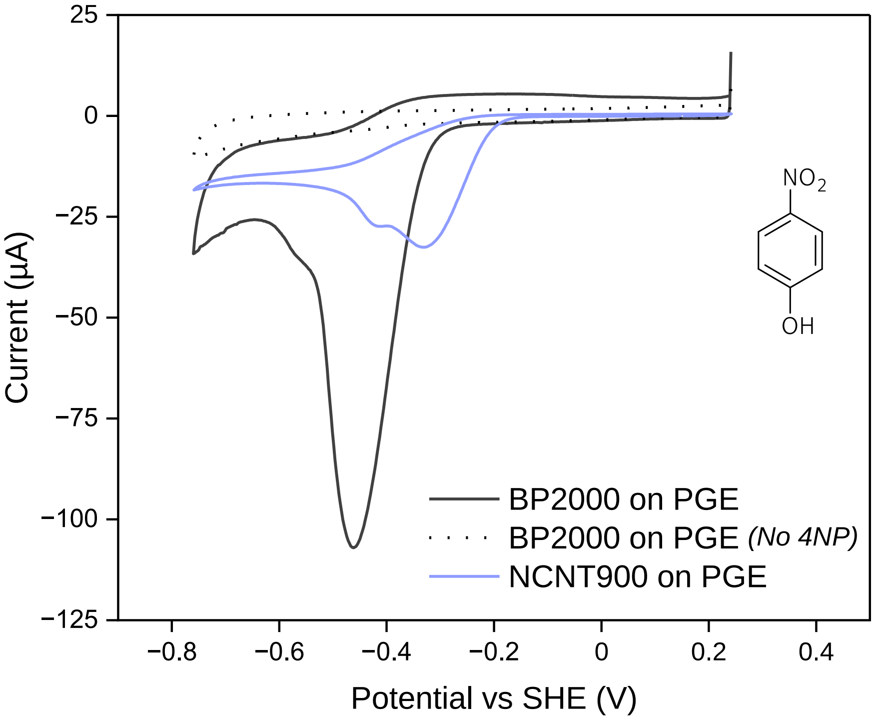

Figure 31 Cyclic voltammograms of PGE WE modified with commercial carbon black ‘BP2000’ (black traces) or NCNT (blue trace) immersed in 4-nitrophenol (1 mM) containing sodium phosphate electrolyte (pH 6.0, 100 mM), scan rate 0.01 V/s.

partially explain the significantly higher capacitive current response, which indicates a higher ECSA (Figure 31). The main reduction occurs at a potential that is similar to that observed on both the pristine CNTs and the clean PGE electrode, indicating that the reduction process likely occurs according to a similar mechanism on these materials.

3.6 Investigations into catalytically active C-N-(Fe) species

3.6.1 Synthesis and electrochemical application of an alternative C-N species

From the electrochemical data presented above, it was assumed that the NCNTs support an active site that is not present on any of the other trialled carbon materials. To investigate whether some C-N species was responsible for the observed electrocatalytic activity, a comparison with a metal contamination-free C-N containing material was targeted. It was hypothesized that the commercial carbon black that is used day-to-day in the Vincent Group, commercially known as 'BP2000', could be modified to contain surface N-functionalisation.

Initially, BP2000 was simply combined with urea (1:4 ratio by weight) and heated to 1000 ^{o}C under argon flow. This procedure led to very low incorporation of N into the sample with only 0.2 at% detected by XPS. Similar methods have been used to modify other amorphous carbon materials; however, the setup used here is not isolated but is subjected to a constant gas flow, which likely removed N-containing species during the furnace heating process at temperatures below those required to force N-incorporation into the carbon material.[22] Subsequently, a method in which the carbon particles were first treated with nitric acid to further increase defect density and create oxidized functional groups on the surface of the material was trialled. The acid-treated carbon was then combined with dicyandiamide in aqueous solution, dried, and pyrolyzed under argon at 700 ^{o}C.[8] The resulting material was found to contain 2.1 at% N by XPS with a mixture of bonding environments. The deconvolution of the N1s peak shows a significant contribution of the pyridinic N at lower binding energy, similar levels of graphitic and pyrrolic N and only a smaller amount of the oxidized or defective N, indicating that nitrogen has successfully been incorporated into a carbon structure on the surface of the carbon nanoparticles (Figure 32).

The resulting material, which will be referred to as N-BP, was then used to modify the PGE WE in a cell charged with 4-nitrophenol (1 mM). When compared to the CV recorded on BP2000, there is no significant difference observed in the line shape and there is no additional reduction event. There is a very slight shift in peak position observed, but the onset of the reduction on the two materials is very similar (Figure 32). N-incorporation onto the BP2000 surface did not lead to similar electrocatalytic behaviour as observed on the NCNTs. It is possible that the electrocatalysis observed on the NCNTs requires the more crystalline surface, or perhaps is influenced by the curvature of the material. It remains possible that the Fe-contamination of the NCNTs leads to the formation of a C-N-Fe site that is active towards the nitro-reduction reaction.

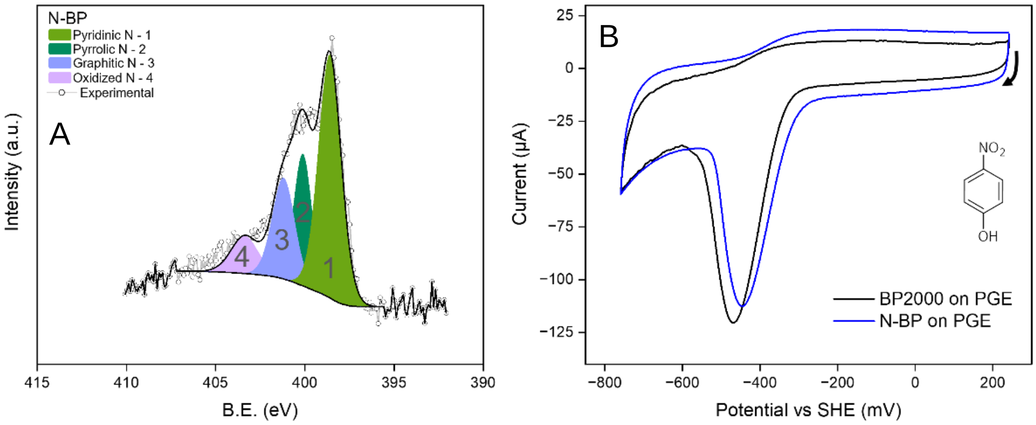

*Figure 32 **A** Deconvolution of N1s peak for N-BP. **B** Cyclic voltammograms on PGE WE modified with ‘BP2000’ (black trace) or N-BP (blue trace).*

3.6.2 *Fe-filled CNTs*

Because of the Fe contamination present in the synthesized CNT samples, it is impossible to exclude a possible Fe-based active site that could be the source of the electrocatalysis observed on the NCNTs. To clarify the importance of the N-dopant, a high-Fe CNT sample was synthesized through the direct pyrolysis of pure ferrocene following a procedure described elsewhere.[23] Briefly, a two-furnace set-up was employed, in which the first furnace contained the solid ferrocene and was set to 250 °C to sublime the ferrocene which was carried by inert gas flow into a second furnace set to 850 °C for pyrolysis. The resulting sample denoted Fe-CNTs contains 32% total Fe, as determined by TGA, but the great majority is covered by layers of carbon and not detected by XPS, which only detects 0.33 at% Fe (Figure 33). Still, this level of surface Fe is similar to that detected in some of the NCNTs and an electrochemical comparison was deemed useful. The CV of the Fe-CNTs on the PGE WE in electrolyte containing 4-nitrophenol also does not feature the mild reduction peak as was observed on the NCNTs (Figure 34). The multiple other redox-processes that are occurring on the Fe-CNTs suggest that there is Fe that is electrochemically active, but that is seemingly not modifying the nitro-reduction behaviour of the material. This result supports the idea that N-doping, rather than increased Fe content in the NCNTs, is responsible for the shift in nitro-reduction onset.

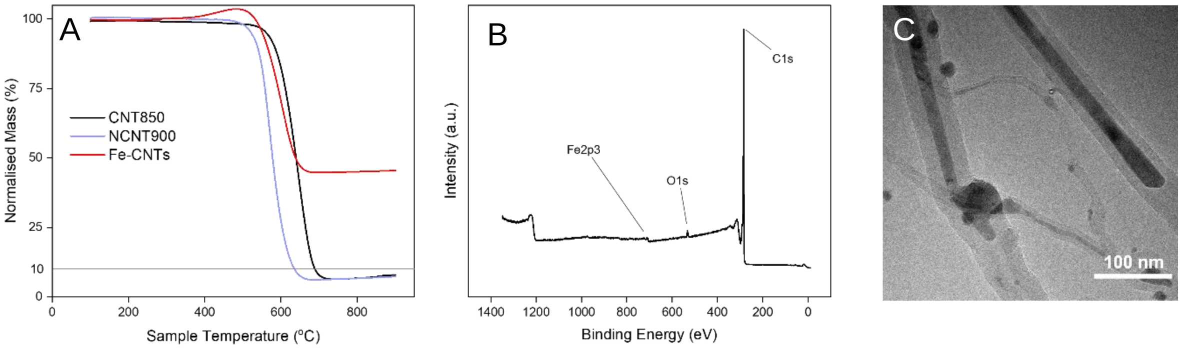

Figure 33 **A** TGA traces comparing Fe-CNTs with NCNT900 and CNT850. **B** XPS survey scan of Fe-CNTs showing Fe, O, and C peaks. **C** Transmission electron micrograph of Fe-CNTs showing filled CNTs.

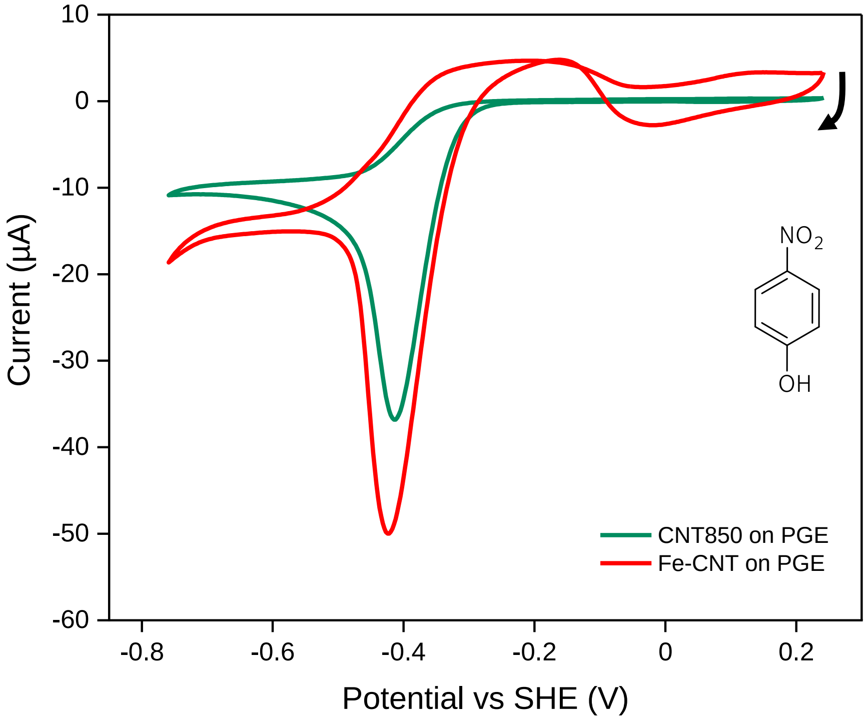

Figure 34 Cyclic voltammograms of PGE WE modified with Fe-CNTs (red trace) or CNTs (green trace) immersed in 4-nitrophenol (1 mM) in sodium phosphate electrolyte (pH 6.0, 100 mV), scan rate 0.01 V/s.

3.6.3 Purification of CNTs through treatment with hydrochloric acid

While it is generally accepted that even rigorous acid-washes do not remove metal-contaminants in their entirety[24, 25], treatment of carbon materials with concentrated HCl can lower the amount of Fe in the sample. Accordingly, the sample NCNT900 was subjected to three consecutive 24 h HCl treatments. The material was analysed for residual Fe content and for its nitro-reduction activity after each treatment. The overall amount of Fe as determined by TGA was lowered significantly to 1 wt% (see grey columns, left hand axis on Figure 35), with no observable depletion of the surface N content determined by XPS (see blue triangles, right hand blue axis on Figure 35). The approximate onset potential for the 4-nitrophenol reduction wave did not change after HCl treatment, indicating that the Fe removed through the acid washes was not part of the electrocatalytically active site (see green circles, right hand green axis on Figure 35).

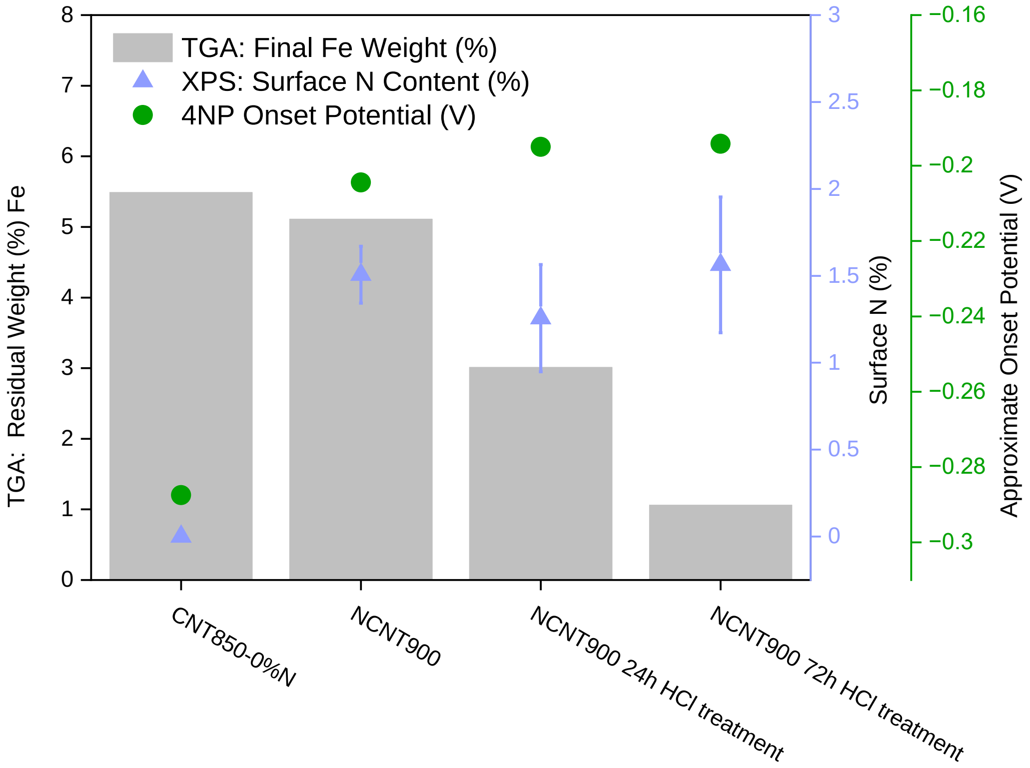

Figure 35 Sequential HCl washing of NCNT900 lowers the total Fe content measured by TGA to 1% while N-content measured by XPS and approximate onset potential for 4-nitrophenol reduction remain the same.

3.6.4 Comparison with commercial nanomaterials

To verify whether the electrocatalytic effect observed above could be reproduced on materials synthesised following different procedures, commercial NCNTs were sourced from ‘ACS Materials LLC’ based in California. These commercial NCNTs will be referred to as ‘NCNT$_{ACS}$’ and were subjected to various analytical techniques in house. Electron microscopy showed that this material is delivered in the form of wool-like bunches of CNTs with a significant amount of nano-scale amorphous material visible on the TEM grid (Figure 36). The overall metal content of this material is lower than that of the unpurified NCNT900 and CNT850 samples, but XPS found surface contamination through both Fe and Ni on the commercial material. The nitrogen doping level was found to be the highest of any sample trialled in this chapter at 5% (Table 6). The slurries produced by sonication of NCNT$_{ACS}$ were immediately homogeneous and indeed, the material behaved more in a hydrophilic manner.

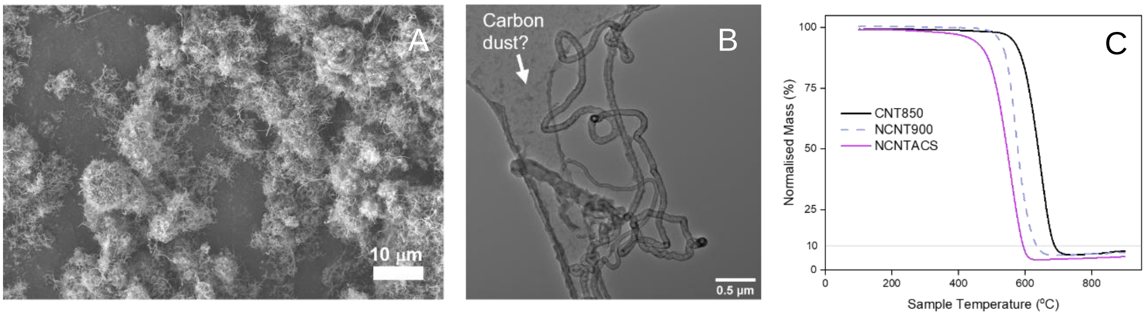

Figure 36 **A** Scanning electron micrograph of commercial NCNTACS. **B** Transition electron micrograph of commercial NCNT$_{ACS}$ showing nano-scale carbon dust on the TEM grid. **C** TGA traces comparing CNT850, NCNT900, and commercial NCNT$_{ACS}$ showing very similar total Fe content.

This can be ascribed to the high heteroatom presence, both N and O, on the surface of this material as well as the high contamination of these CNTs through small amorphous carbon, as seen on the electron micrographs. Interestingly, the casting of a film of NCNT$_{ACS}$ onto the PGE working electrode led to a significant decrease of the observed current. It is possible that not all of the amorphous material present in this sample is conductive, which would lead to a pacification of the electrode. The reduction wave for nitro-hexane shows the same shift towards milder potentials on the commercial NCNTs, which confirms that the effect observed is not specific to the materials produced in-house (Figure 37). While this material is less pure and seems to contain some insolating amorphous fraction, the high hydrophilicity could make

Table 6 Atomic percent of N, Fe, O, and Ni detected by XPS. Commercial NCNTACS contains high N and O levels as well as Ni and Fe contamination.

	XPS - atomic percent (at%)			
Sample	**N**	**Fe**	**O**	**Ni**
CNT850		0.08	1.8	
NCNT900	1.5		2.1	
NCNTACS	5.1	0.02	5.6	0.12

it an interesting candidate for applications in biocatalytic systems, because of the accompanying reliance on aqueous media.

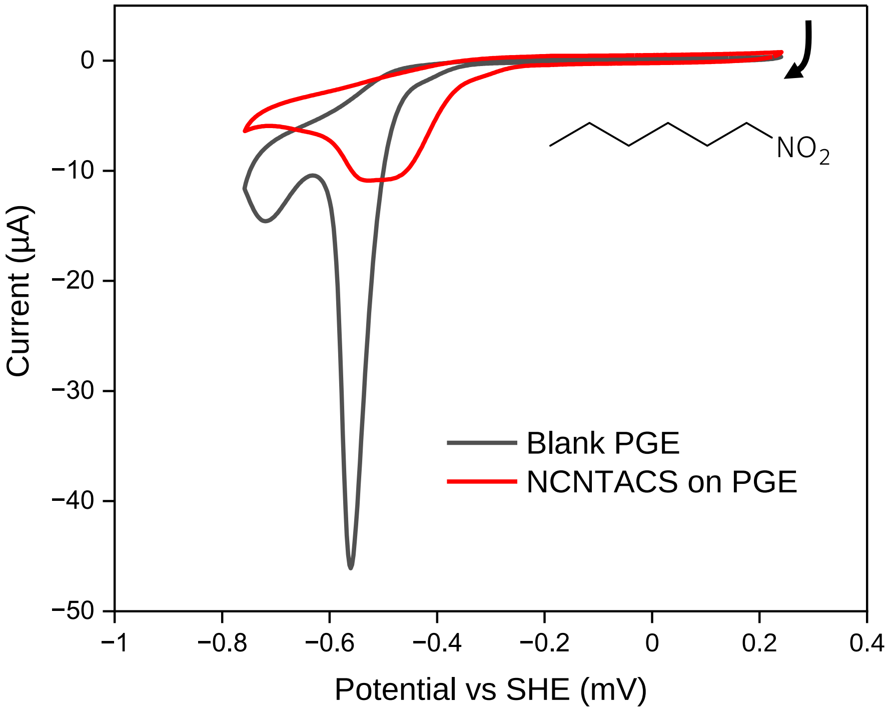

Figure 37 Cyclic voltammograms on PGE WE (grey trace) or modified with commercial NCNT_{ACS} (red trace) immersed in nitrohexane (1 mM) in sodium phosphate electrolyte (pH 6.0, 100 mM) at 0.01 V/s.

3.7 Conclusions and outlook

As published by Sokolova *et al*, [1] hydrogenase enzyme can be combined with a conductive carbon support for the electrochemical reduction of nitro-groups using the electrons provided by the enzyme through dihydrogen oxidation. To investigate whether the carbon could be replaced to tune the reduction event, the electrochemical reduction of 4-nitrophenol and nitrohexane was studied on working electrodes modified with a range of synthesised or commercially sourced carbon nanotubes. The use of NCNTs led to a significant and reproducible cathodic shift of the nitro-reduction wave. The active site that results in this electrocatalytic behaviour remains unclear. Further investigations should focus on characterising the distribution of metal contaminants in the sample, for example by electron energy loss spectroscopy (EELS). For the purposes of this thesis, the observed catalytic effect was exciting because it indicated that the **Hyd/C** system could be combined with this electrocatalyst to tune the activity of the hydrogenation catalyst system. To employ the NCNTs in the synthesis of amines, the following chapter will focus on both electrosynthesis and hydrogen-driven bio-electrosynthesis.

3.8 References

(1) Sokolova, D.; Lurshay, T. C.; Rowbotham, J. S.; Stonadge, G.; Reeve, H. A.; Cleary, S. E.; Sudmeier, T.; Vincent, K. A. Selective hydrogenation of nitro compounds to amines by coupled redox reactions over a heterogeneous biocatalyst. *Nature Communications* **2024**, *15* (1), 7297. DOI: 10.1038/s41467-024-51531-2.

(2) Gong, K.; Du, F.; Xia, Z.; Durstock, M.; Dai, L. Nitrogen-Doped Carbon Nanotube Arrays with High Electrocatalytic Activity for Oxygen Reduction. *Science* **2009**, *323* (5915), 760-764. DOI: 10.1126/science.1168049.

(3) Koós, A. A.; Dowling, M.; Jurkschat, K.; Crossley, A.; Grobert, N. Effect of the experimental parameters on the structure of nitrogen-doped carbon nanotubes produced by aerosol chemical vapour deposition. *Carbon* **2009**, *47* (1), 30-37. DOI: https://doi.org/10.1016/j.carbon.2008.08.014.

(4) Sumpter, B. G.; Meunier, V.; Romo-Herrera, J. M.; Cruz-Silva, E.; Cullen, D. A.; Terrones, H.; Smith, D. J.; Terrones, M. Nitrogen-Mediated Carbon Nanotube Growth: Diameter Reduction, Metallicity, Bundle Dispersability, and Bamboo-like Structure Formation. *ACS Nano* **2007**, *1* (4), 369-375. DOI: 10.1021/nn700143q.

(5) Steinmetz, M.; Lima, D.; Machado, R. R. L.; Sundararaj, U.; Arjmand, M.; da Silva, A. B.; Santos, J. P.; Pessôa, C. A.; Wohnrath, K. Nitrogen-doped carbon nanotubes towards electrochemical sensing: Effect of synthesis temperature. *Diamond and Related Materials* **2020**, *110*, 108093. DOI: https://doi.org/10.1016/j.diamond.2020.108093.

(6) Chizari, K.; Vena, A.; Laurentius, L.; Sundararaj, U. The effect of temperature on the morphology and chemical surface properties of nitrogen-doped carbon nanotubes. *Carbon* **2014**, *68*, 369-379. DOI: https://doi.org/10.1016/j.carbon.2013.11.013.

(7) Ratso, S.; Kruusenberg, I.; Vikkisk, M.; Joost, U.; Shulga, E.; Kink, I.; Kallio, T.; Tammeveski, K. Highly active nitrogen-doped few-layer graphene/carbon nanotube composite electrocatalyst for oxygen reduction reaction in alkaline media. *Carbon* **2014**, *73*, 361-370. DOI: https://doi.org/10.1016/j.carbon.2014.02.076.

(8) Yang, H.; Ko, Y.; Lee, W.; Züttel, A.; Kim, W. Nitrogen-doped carbon black supported Pt–M (M = Pd, Fe, Ni) alloy catalysts for oxygen reduction reaction in proton exchange membrane fuel cell. *Materials Today Energy* **2019**, *13*, 374-381. DOI: https://doi.org/10.1016/j.mtener.2019.06.007.

(9) Wang, S.; Zhao, X.; Cochell, T.; Manthiram, A. Nitrogen-Doped Carbon Nanotube/Graphite Felts as Advanced Electrode Materials for Vanadium Redox Flow Batteries. *J Phys Chem Lett* **2012**, *3* (16), 2164-2167. DOI: 10.1021/jz3008744.

(10) Vesel, A.; Zaplotnik, R.; Primc, G.; Mozetič, M. A Review of Strategies for the Synthesis of N-Doped Graphene-Like Materials. In *Nanomaterials*, 2020; Vol. 10.

(11) Gengenbach, T. R.; Major, G. H.; Linford, M. R.; Easton, C. D. Practical guides for x-ray photoelectron spectroscopy (XPS): Interpreting the carbon 1s spectrum. *Journal of Vacuum Science & Technology A: Vacuum, Surfaces, and Films* **2021**, *39* (1). DOI: 10.1116/6.0000682.

(12) Ferrari, A. C.; Robertson, J. Interpretation of Raman spectra of disordered and amorphous carbon. *Physical Review B* **2000**, *61* (20), 14095-14107. DOI: 10.1103/PhysRevB.61.14095.

(13) Pimenta, M. A.; Dresselhaus, G.; Dresselhaus, M. S.; Cançado, L. G.; Jorio, A.; Saito, R. Studying disorder in graphite-based systems by Raman spectroscopy. *Physical Chemistry Chemical Physics* **2007**, *9* (11), 1276-1290, 10.1039/B613962K. DOI: 10.1039/B613962K.

(14) Krishnamoorthy, K.; Veerapandian, M.; Yun, K.; Kim, S. J. The chemical and structural analysis of graphene oxide with different degrees of oxidation. *Carbon* **2013**, *53*, 38-49. DOI: https://doi.org/10.1016/j.carbon.2012.10.013.

(15) Chernyak, S. A.; Ivanov, A. S.; Stolbov, D. N.; Egorova, T. B.; Maslakov, K. I.; Shen, Z.; Lunin, V. V.; Savilov, S. V. N-doping and oxidation of carbon nanotubes and jellyfish-like graphene nanoflakes through the prism of Raman spectroscopy. *Applied Surface Science* **2019**, *488*, 51-60. DOI: https://doi.org/10.1016/j.apsusc.2019.05.243.

(16) Brubaker, Z. E.; Langford, J. J.; Kapsimalis, R. J.; Niedziela, J. L. Quantitative analysis of Raman spectral parameters for carbon fibers: practical considerations and connection to mechanical properties. *Journal of Materials Science* **2021**, *56* (27), 15087-15121. DOI: 10.1007/s10853-021-06225-1.

(17) John Ralph, S. K., Justin Mobley. Synthesis of paracetamol (acetaminophen) from biomass-derived p-hydroxybenzamide. USA 2018.

(18) Giribabu, K.; Suresh, R.; Manigandan, R.; Munusamy, S.; Kumar, S. P.; Muthamizh, S.; Narayanan, V. Nanomolar determination of 4-nitrophenol based on a poly(methylene blue)-modified glassy carbon electrode. *Analyst* **2013**, *138* (19), 5811-5818, 10.1039/C3AN00941F. DOI: 10.1039/C3AN00941F.

(19) Zhu, P.; Zhao, Y. Cyclic voltammetry measurements of electroactive surface area of porous nickel: Peak current and peak charge methods and diffusion layer effect. *Mater. Chem. Phys.* **2019**, *233*, 60-67. DOI: 10.1016/j.matchemphys.2019.05.034.

(20) Morales, D. M.; Risch, M. Seven steps to reliable cyclic voltammetry measurements for the determination of double layer capacitance. *JPhys Energy* **2021**, *3* (3). DOI: 10.1088/2515-7655/abee33.

(21) Quinson, J.; Hidalgo, R.; Ash, P. A.; Dillon, F.; Grobert, N.; Vincent, K. A. Comparison of carbon materials as electrodes for enzyme electrocatalysis: hydrogenase as a case study. *Faraday Discuss.* **2014**, *172*, 473-496. DOI: 10.1039/c4fd00058g.

(22) Su, Y.; Shi, Y.; Jiang, M.; Chen, S. One-Step Synthesis of Nitrogen-Doped Porous Biochar Based on N-Doping Co-Activation Method and Its Application in Water Pollutants Control. In *International Journal of Molecular Sciences*, 2022; Vol. 23.

(23) Dillon, F. C.; Bajpai, A.; Koós, A.; Downes, S.; Aslam, Z.; Grobert, N. Tuning the magnetic properties of iron-filled carbon nanotubes. *Carbon* **2012**, *50* (10), 3674-3681. DOI: 10.1016/j.carbon.2012.03.040.

(24) Pumera, M. Materials Electrochemists' Never-Ending Quest for Efficient Electrocatalysts: The Devil Is in the Impurities. *ACS Catal.* **2020**, *10* (13), 7087-7092. DOI: 10.1021/acscatal.0c02020.

(25) Banks, C. E.; Crossley, A.; Salter, C.; Wilkins, S. J.; Compton, R. G. Carbon nanotubes contain metal impurities which are responsible for the "electrocatalysis" seen at some nanotube-modified electrodes. *Angew. Chem. Int. Ed. Engl.* **2006**, *45* (16), 2533-2537. DOI: 10.1002/anie.200600033.

4 Tuning the production of amines using NCNTs

With the encouraging electrochemical results established in Chapter 3, the logical next target was to use the electrocatalytic effect observed on the N-doped CNTs through electrosynthesis of amines at milder potential. In Chapter 4, a larger-scale working electrode is fabricated and employed to produce aminophenol and hexylamine on the NCNTs. Once these electro-synthetic experiments had proven that the milder onset potential indeed corresponds to the formation of amine, the NCNTs were combined with the H_2-oxidising Hyd-1 enzyme to tune the cofactor-free biocatalytic nitro-group hydrogenation system **Hyd/C**.

Table of Contents

4.1 Experimental

4.1.1 Chemicals and buffers

4-Nitrophenol (≥99%), 1-nitrohexane (98%), and hexylamine (99%) were purchased from *Sigma-Aldrich* and used as received. Aqueous solutions were prepared using MilliQ water (resistivity 18.2 MΩ cm, *Millipore*). Buffer salts and solvents were purchased from *Sigma-Aldrich*. Deuterated solvents were purchased from *Sigma-Aldrich* (D_2O, 99.9% D; DMSO-*d*6, 99.9% D).

Sodium phosphate buffer was prepared by dissolving an appropriate mass of Na_2HPO_4 and NaH_2PO_4 in water after which the pH was adjusted to the desired value by adding HCl(aq) or NaOH(aq) dropwise and monitoring pH using an Ag/AgCl pH electrode (*Fisher*).

4.1.2 Hydrogenase enzyme samples

Hydrogenase enzyme (*Escherichia coli* (*E. coli*) hydrogenase 1 (Hyd-1)) was prepared and purified in-house by varying Vincent group members under the supervision of Dr. Stephen Carr. Hyd-1 samples (10.5 mg/mL) were stored at -80 ^{o}C and defrosted as needed before each experiment.

4.1.3 Carbon materials

Multiple types of carbon are used in this chapter. CNTs and NCNTs synthesised in-house (Chapter 3) are used without further purification, unless otherwise stated. Commercial NCNTs from *ACS Materials* are used as received. Carbon black ‘Black Pearls 2000’ from *Cabot Corporation* is used as received.

4.1.4 Cyclic voltammetry (CV) experiments performed under flow of H_2

A glass electrochemical cell made in-house (glass blower: Terri Adams) with a water jacket adjusted to 25 ^{o}C was connected to a hydrogen line was equipped with a saturated calomel reference electrode (SCE, *Palmsens BV*) and a coiled Pt wire as the counter electrode (CE). The sodium phosphate electrolyte (pH 6.0, 100 mM) was subjected to H_2 gas flow (100 scc/min – standard cubic centimetres per minute) before the experiment. A pyrolytic graphite edge (PGE) rotating disk electrode (RDE) as the working electrode (WE) was modified with Hyd-1 by dropping the enzyme solution (0.5 μL, 10.5 mg/mL) onto the electrode, allowing the film to incubate for 10 min and then rinsing the electrode with MilliQ water. The WE was mounted onto a rotator (*Metrohm*) and rotated at 3000 RPM during the measurements. Gas flow was directed through the head space of the vial once the WE had been immersed in the electrolyte. The cyclic voltammograms were recorded using an *Autolab PGStat30* potentiostat (*Ecochemie*) and Nova 1.1 software at slow scan rate 1 mV/s.

4.1.5 General procedure for chronoamperometry experiments

A cylindrical glass vial equipped with a stir bar was fitted with a plastic cap in which three holes had been cut to hold the SCE RE, the Pt wire CE within a fritted glass tube, and the connection to the WE. The electrolyte PB (pH 6.0, 100 mM, 5 mL) containing the relevant starting nitro-compound (5 mM) was added to the vial. Chronoamperometry was performed using a *PalmSens* 4 potentiostat and the corresponding *PSTrace* software.

After chronoamperometry experiments in which 4-nitrophenol was the starting material, a UV/Vis spectrum of the reaction mixture was recorded. Then, the product was extracted from the electrolyte into ethyl acetate, dried over magnesium sulphate, the solvent was removed and the resulting solid was dissolved in DMSO-*d6* for subsequent analysis by NMR spectroscopy, in which conversion was estimated based on the relative integral value of the relevant signal. After electrosynthesis of hexylamine, the reaction mixture (400 μL) was combined with sodium trimethylsilylpropanesulfonate (DSS) (50 μL, 10 mM) and D_2O (50 μL) and analysed by NMR spectroscopy.

4.1.6 General procedure for small-scale hydrogenation reactions

Reaction set-up was performed under an inert atmosphere (N_2; $O_2 < 3$ ppm) in a glove box (*Glove Box Technology LTD.*) A 20 mg/mL carbon slurry in sodium phosphate buffer (PB, pH 6.0, 100 mM) was sonicated for 1 hour. For one 2 mL scale reaction with 10 mM concentration of nitrocompound, the carbon black suspension (200 μL, 4 mg C) was transferred to an Eppendorf tube, the Hyd-1 solution (10.5 mg/mL, 9.5 μL, 0.1 mg) was added, the mixture was combined and left on ice for 1 hour. The suspension was centrifuged (3 min, 14100 x *g*), the supernatant was discarded, and the catalyst resuspended in PB (100 μL). The centrifugation step was repeated twice to wash off any free enzyme. The catalyst particles were then resuspended and directly used for the hydrogenation reaction.

Reactions were run either at 2 mL scale with a 10 mM nitrocompound concentration in PB in the reaction vial of an *Asynt Octo Mini Reactor,* which allows eight reactions to be run in parallel under a gas flow (here, 30 mL/min H_2), or at 1 mL scale with a 10 mM nitrocompound concentration in PB a 1.5 mL glass vial with a slitted lid, which was then placed inside a *Büchi Tinyclave* pressure vessel which can be filled to the desired H_2 pressure. The reaction mixtures were analysed by ^{1}H NMR spectroscopy after 24 h.

4.2 Electrosynthesis of amines on CNTs and NCNTs

Chapter 3 outlines the observation of a reduction peak at milder potential in the CVs recorded on an NCNT-modified carbon electrode as opposed to the clean or the CNT-modified electrode. The motivation to explore electrosynthesis on an NCNT-electrode is twofold: first, to identify the product formed at the milder potential through spectroscopic methods, and second, to demonstrate the possibility of using the milder potential to form a useful product.

4.2.1 Development of a large-surface-area working electrode

The current which is passed from a WE to a redox active species in solution is directly proportional to the active surface area of the electrode. [1] Therefore, one method to reach the full conversion of a significant amount of starting material in an electrochemical reactor is to simply increase the surface area of the WE used. Here, the CNT materials had to be immobilised onto some material with sufficiently large or scalable dimensions, with no interaction with the starting material at the potential at which the NCNTs are active, and with some stability so that the experiment could be left to complete over the course of many hours.

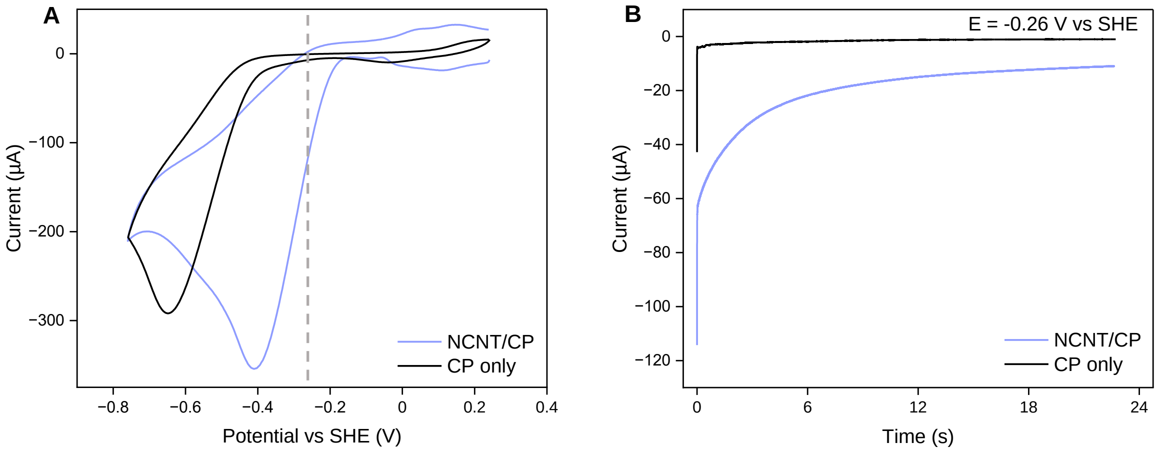

Figure 38 **A** *Cyclic Voltammograms recorded on a carbon paper electrode only or modified with NCNTs, immersed in 4-nitrophenol (5 mM) containing sodium phosphate electrolyte (pH 6.0, 100 mM) at 0.01 V/s. Dashed line indicating potential used during chronoamperometry.* **B** *Chronoamperometry traces recorded on a carbon paper electrode only or modified with NCNTs at -0.26 V vs SHE, immersed in 4-nitrophenol (5 mM) containing sodium phosphate electrolyte (pH 6.0, 100 mM) under stirring at room temperature.*

The first electrode that was trialled was based on a piece of carbon paper (CP) that was placed between two pieces of laminating plastic. A rectangular opening (1x1.5 cm) was cut into the top layer of plastic and a length of an electrical cable, which had been removed from its isolating covering at one end to allow electrical contact to the CP, was placed between the CP and the back layer of laminating plastic. The plastic was sealed to contain the CP and electrical wire using a soldering iron. The NCNT material was suspended in isopropanol through ultrasonication and the resulting slurry was simply drop-cast onto the exposed CP and allowed to dry. To achieve a more homogeneous NCNT slurry that can more reproducibly modify the electrodes, the perfluorinated polymer Nafion was added (0.5% w/v) – this is common practice in the literature concerning CNTs and is not thought to impact the electrocatalytic behaviour of the material.[2] This electrode will be referred to as NCNT/CP. A significant concern with the NCNT/CP method was that the CP was quite unstable when submerged into the electrolyte solution, with pieces of the electrode flaking off immediately or else once the solution was stirred. Nonetheless, the electrode was used in a trial electrochemical experiment consisting of a number of cyclic voltammograms followed by a long chronoamperometry run in a PB solution containing 5 mM 4-nitrophenol. The cyclic voltammetry traces comparing the NCNT/CP electrode to a CP only control clearly demonstrate that the NCNTs have successfully modified the CP surface and are resulting in the expected shift in the cathodic feature (Figure 38). The current observed on the NCNT/CP electrode during the chronoamperometry experiment, during which the WE potential was held at -0.26 V vs SHE targeting the milder reduction peak, is nonetheless quite low, with the total charge passed well below that needed to convert the 4-nitrophenol present in the electrolyte: For a 5 mL solution containing 5 mM 4-nitrophenol, 1.5×10^{-4} mol electrons would be needed (corresponding to the six electron reduction to the amine), corresponding to 14.5 C of charge passed, while in this experiment, only 1.6 C of charge was passed.

To improve the structural rigidity and effectiveness of the WE, a different support in the form of a carbon felt (*Alfa Aesar*), onto which a length of carbon fibre was tied as the electrical contact, was trialled. The carbon felt (CF) was cut into equal pieces (1x2 cm) and was immersed into slurries of CNTs or NCNTs within a glass vial which was then exposed to ultrasonication for 30 min. The modified CF was left to dry under air.

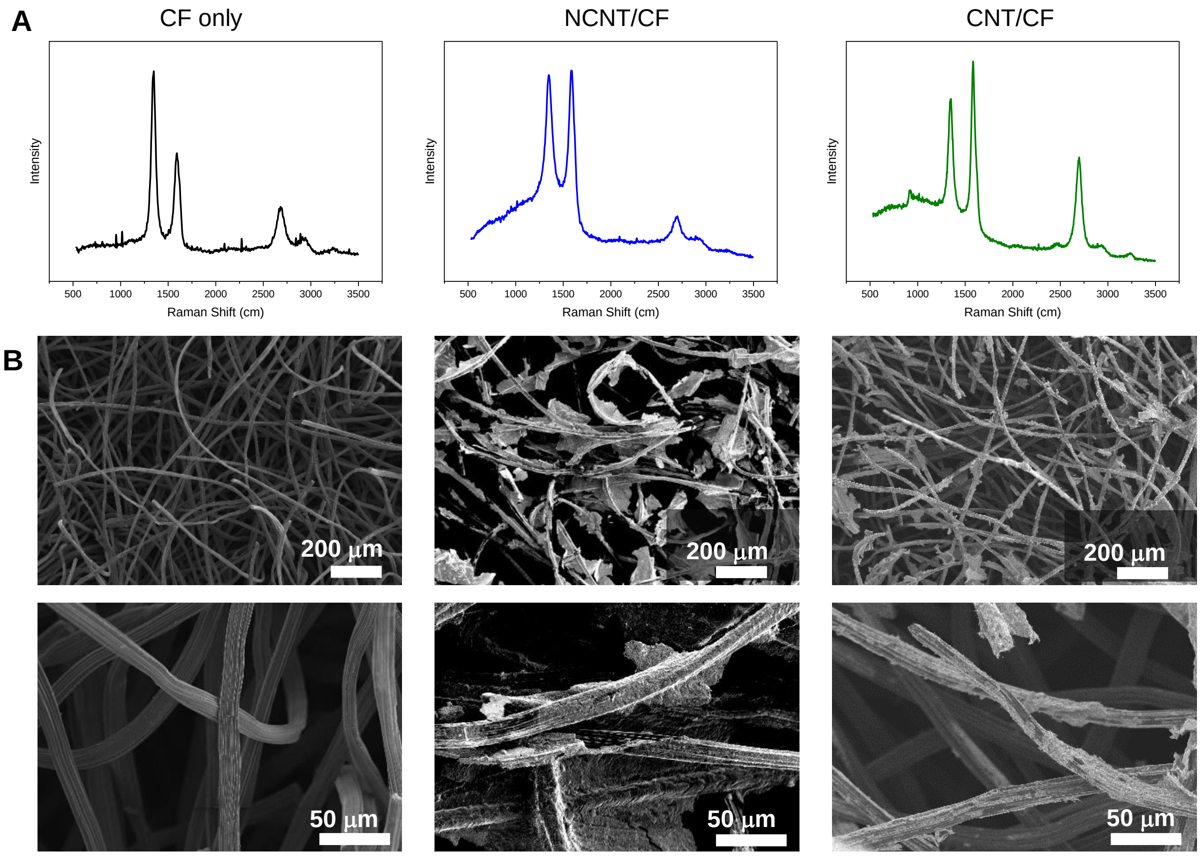

Figure 39 ***A*** *Raman spectra of carbon felt only (left), carbon felt modified with NCNTs (middle), and carbon felt modified with CNTs (right), averaged from 10 points of analysis and normalised.* ***B*** *SEM micrographs obtained on a Merlin-60 SEM of carbon felt only (left), carbon felt modified with NCNTs (middle), and carbon felt modified with CNTs (right).*

The pieces of CF had visibly been modified with CNT material. In addition, SEM and Raman spectroscopy were performed to further characterise these electrodes. The Raman spectra of the electrodes (averaged from 10 points analysed) show a highly defective graphitic material for the carbon felt as purchased, with a distinct G peak indicating sp2 hybridisation and the large D peak representing a high defect density. The I_D/I_G ratio is lower for the NCNT/CF and even lower still for the CNT/CF, which agrees with the differences in Raman spectra of these

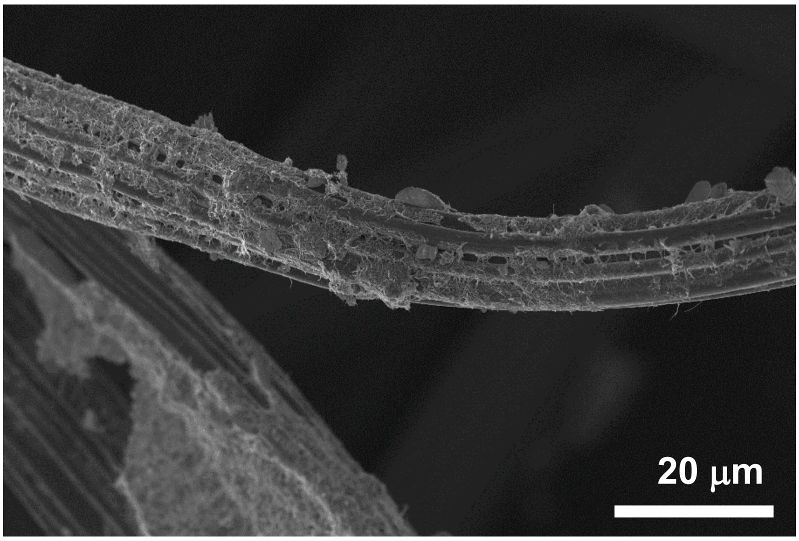

Figure 40 SEM micrograph obtained on a Carl Zeiss Merlin HR FEG SEM of carbon felt modified with NCNTs.

materials, as discussed in the previous chapter. The SEM micrographs show a flakey covering over the fibres that make up the CF, and a higher magnification image of the NCNT/CF material makes visible the hair-like NCNTs covering the much thicker felt fibres (Figure 40). While some of these CNTs may still flake off, the CF itself is more stable than the CP and its macroporous structure could be expected to slightly protect the CNT layer. A trial chronoamperometry experiment led to full conversion of the 4-nitrophenol to the 4-aminophenol, as observed through ^{1}H NMR spectroscopy of the electrolyte. Following this promising initial result, the modified carbon felt was employed as the large-scale working electrode used in a set of electrosynthetic experiments.

4.2.2 *Electrosynthesis of p-aminophenol*

Chronoamperometry experiments were performed at a mild potential (-0.26 V vs SHE) and a more negative potential (-0.36 V vs SHE) on the CF electrodes (CF only, CNT/CF, and NCNT/CF) to probe the two reduction peaks observed in the CVs recorded on NCNT-modified versus CNT-modified electrodes (Figure 41). Analysis of the electrolyte after 22 h by ^{1}H NMR confirmed that the only product formed was 4-aminophenol (Figure 42), while

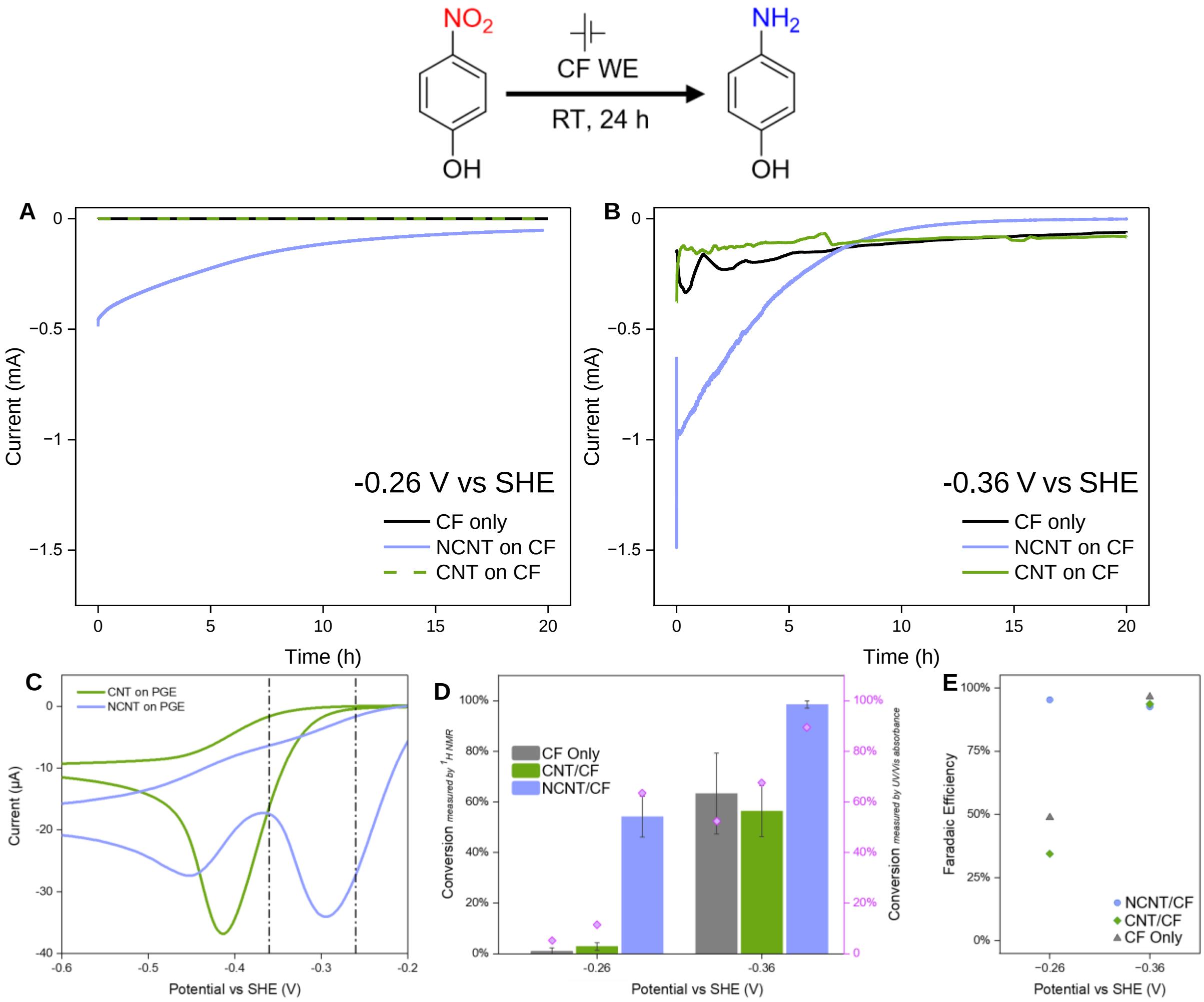

Figure 41 **A** *Chronoamperometry traces recorded using CF, CNT/CF, or NCNT/CF WEs at -0.26 V vs SHE, under stirring, RT, 5 mM 4-nitrophenol in sodium phosphate electrolyte (pH 6.0, 100 mM).* **B** *Chronoamperometry traces recorded using CF, CNT/CF, or NCNT/CF WEs at -0.36 V vs SHE, under stirring, RT, 5 mM 4-nitrophenol in sodium phosphate electrolyte (pH 6.0, 100 mM).* **C** *Cyclic voltammograms recorded on PGE WE modified with CNTs or NCNTs, immersed in 4-nitrophenol (1 mM) containing sodium phosphate electrolyte (pH 6.0, 100 mM) at 0.01 V/s, with dashed lines corresponding to the two potentials used for chronoamperometry experiments.* **D** *Conversion of 4-nitrophenol to 4-aminophenol at the two potentials on CF, CNT/CF, or NCNT/CF. Bars correspond to conversion measured through relative integrals in the ^{1}H NMR spectra, scatter plot to conversion measured through UV/Vis spectroscopy. Error was established by running each experiment in triplicate.* **E** *Faradaic efficiency calculated at the for the two trialled potentials and three electrodes.*

UV/Vis spectroscopy was used as a complementary technique giving confirmation of the conversion calculated from the relative integrals of the relevant signals in the ^{1}H NMR spectra (Figure 43).

The error in conversion amongst multiple repeat reactions was found to be particularly high in samples that had been converted at a potential that does not correspond to a high driving force – see, for example, the difference in error between the milder and harsher potentials on the NCNT/CF WE. This could be explained by the relatively greater influence of parameters such as electrode area or temperature when the driving force is lower. The harsher potential corresponds to a high driving force that gives high conversions regardless of small changes in such parameters.

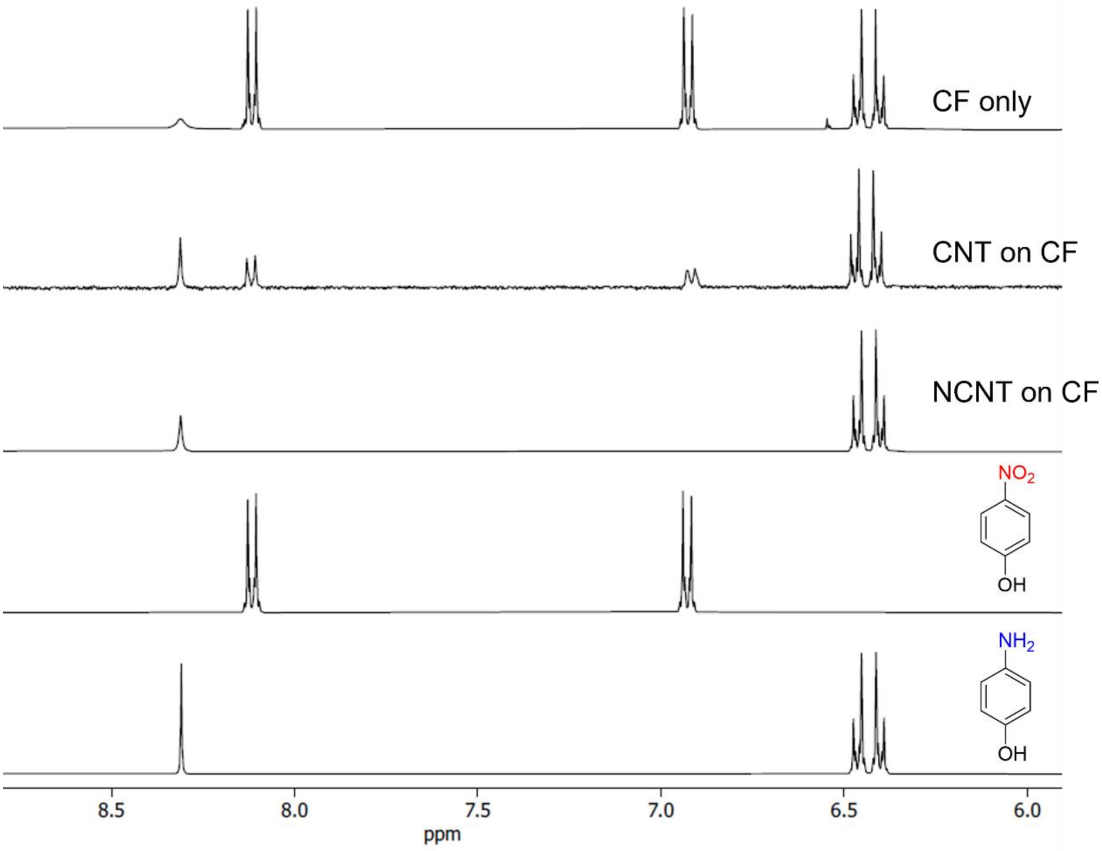

Figure 42 Example ^{1}H NMR (400 MHz, 298 K, DMSO-d6) traces of reaction products after chronoamperometry at -0.36 V vs SHE on CF only, CNT on CF, and NCNT on CF electrodes (from top to bottom), in 5 mM 4-nitrophenol in sodium phosphate electrolyte (pH 6.0, 100 mM) under stirring, RT. NMR spectra of standards 4-nitrophenol and 4-aminophenol shown (bottom two spectra).

The Faradaic efficiency FE was calculated for the six conditions. The high conversion cases show that the FE in this system is excellent at near 100% (Figure 41). The FE at no to low conversion was considered to be not as meaningful, because of the outsize role the capacitive current plays in these cases.

The electrosynthesis of 4-aminophenol on NCNT or CNT modified carbon felt electrodes demonstrates that the electrocatalytic effect observed on the doped material can be employed to produce amines at milder potential and thus at greater energy efficiency. In addition, these results prove that both observed reduction events on the NCNTs lead to the formation of the amine, not to some intermediate or other product, suggesting that the two different peaks correspond to two different mechanisms of the same conversion and not to two different reactions. This in turn supports the hypothesis that the NCNTs contain an additional active site not found on the CNTs, while also still converting the nitro-group at the more negative potential in the same way as the CNTs or other carbon materials.

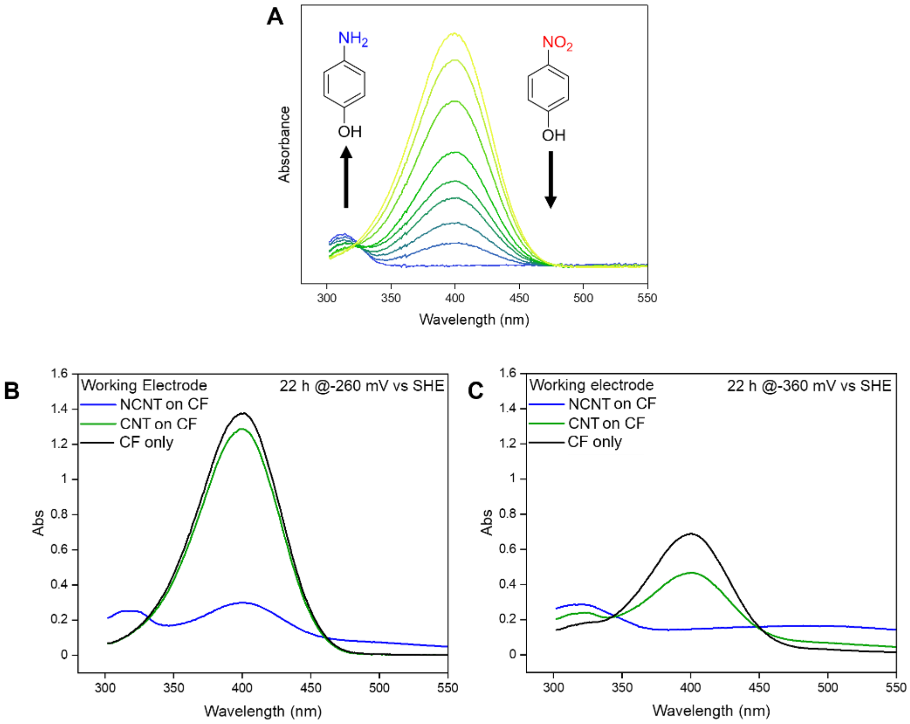

Figure 43 **A** *UV/Vis data collected for calibration curve demonstrating absorbance of mixtures of 4-aminophenol and 4-nitrophenol in aqueous base.* **B** *UV/Vis spectra of electrolyte after 22 h chronoamperometry experiment using CF only, CNT on CF, or NCNT on CF as WE at -0.26 V vs SHE, and* **C** *at -0.36 V vs SHE. Conditions: 5 mM 4-nitrophenol in sodium phosphate electrolyte (pH 6.0, 100 mM) under stirring at RT, held at potential for 22 h.*

4.2.3 Electrosynthesis of hexylamine

As the electrocatalytic effect on the NCNTs had also been observed for the simple aliphatic nitro-hexane, the electrosynthesis experiments were repeated for this starting material. In this

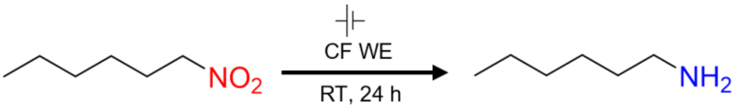

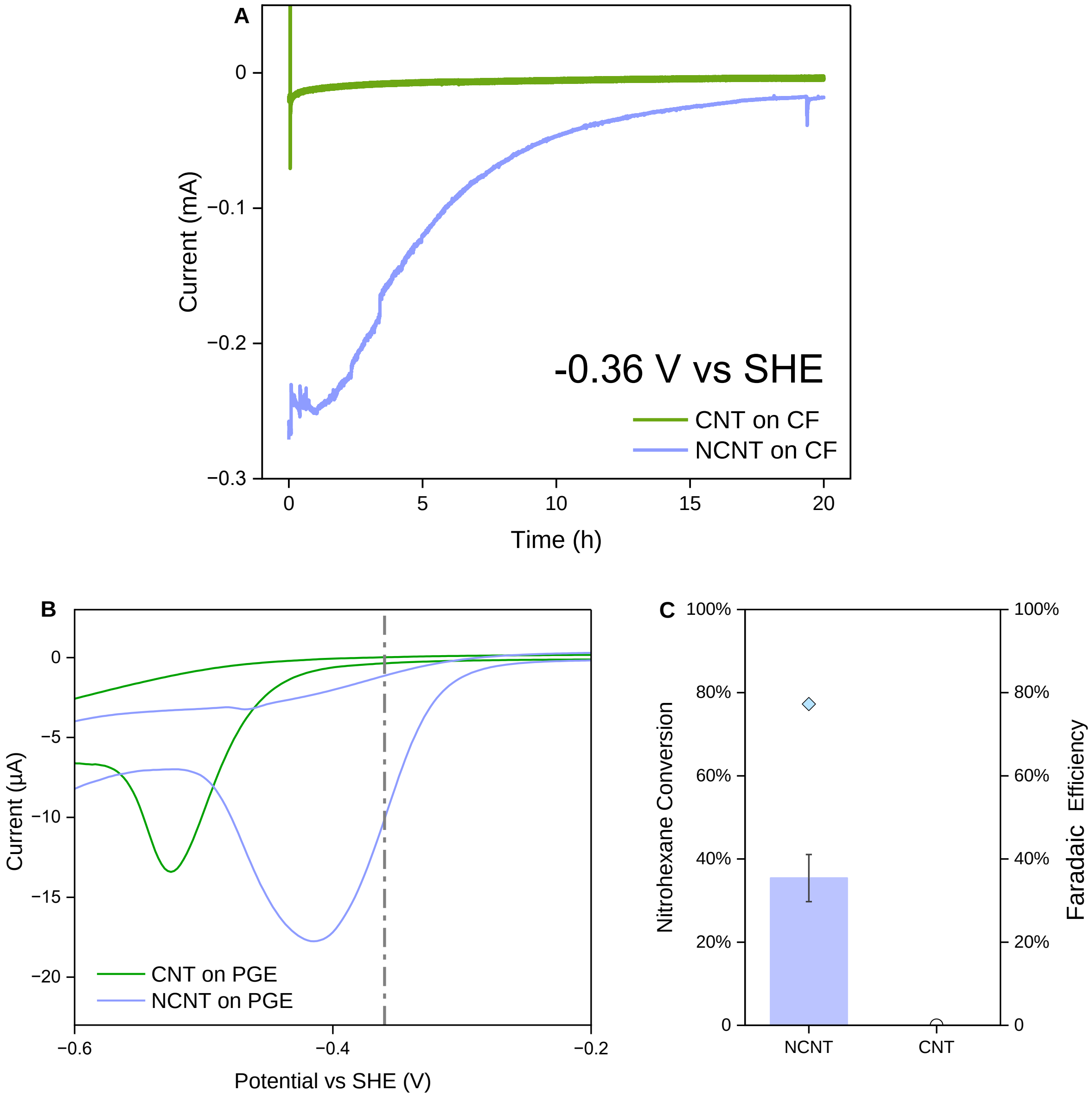

Figure 44 **A** *Example chronoamperometry traces recorded on CNT on CF and NCNT on CF WEs at -0.36 V vs SHE in nitrohexane (5 mM) in sodium phosphate electrolyte (pH 6.0, 100 mM), under stirring, at RT.* **B** *Cyclic voltammograms recorded on PGE WE modified with CNTs or NCNTs, immersed in nitrohexane (1 mM) containing sodium phosphate electrolyte at 10 mV/s, with the dashed line corresponding to the potential used for chronoamperometry experiments.* **C** *Conversion of 4-nitrophenol to 4-aminophenol at the two potentials on CNT/CF or NCNT/CF measured through relative integrals compared to DSS as internal standard in the ^{1}H NMR spectra (columns) and calculated Faradaic efficiency (scatter plot).*

case, only one potential was chosen targeting a value that was expected to lead to conversion on the NCNTs but no conversion on the CNTs. Again, CF electrodes were prepared as described above modified either with NCNTs or CNTs. The potential was held at -0.36 V vs SHE for 22 h (Figure 44 A). The electrolyte was analysed by NMR spectroscopy – here, sodium trimethylsilylpropanesulfonate (DSS) was used as an internal standard to achieve a more quantitative conversion value because no supplementary technique (such as UV/Vis spectroscopy, above) was used. As expected, no product was observed when the CNT/CF electrode was employed, while near 40% conversion was achieved on the NCNT/CF electrode (Figure 44 C). Conversion should be easily improved by using a more negative potential; this was not done here because the experiment was aiming to prove the reaction occurs on the NCNTs where it does not on the CNTs. In addition, note the low solubility of the aliphatic starting material and product. This could artificially deflate the concentration of product seen in the NMR spectrum. Future experiments should add a careful organic extraction step to more rigorously quantify the yield of hexylamine. Nonetheless, the experiment is successful in demonstrating the electrocatalytic reduction of nitrohexane on the NCNTs produced in-house. This result inspired a combination of the NCNTs with Hyd-1 enzyme to investigate whether this electrocatalysis could be employed to widen the substrate scope of the batch hydrogenation catalyst system **Hyd1/C**.

4.3 Tuning the Hyd1/C nitro-group hydrogenation system using NCNTs

The Vincent group has established a nitro-hydrogenation system, **Hyd/C**, based on hydrogenase enzyme immobilised on commercial carbon black particles, in which the hydrogenase provides electrons through H_2 oxidation to the conductive carbon. The nitro-group is thought to be electrochemically reduced on the carbon particles. The enzyme most commonly employed by the group, **Hyd-1**, is chosen for its stability and high H_2 oxidation activity but has a slight overpotential of around 80-100 mV beyond the thermodynamic H_2 oxidation potential. At pH 6 and 1 bar H_2 pressure, the enzyme catalyses H_2 oxidation at an onset potential of about -0.296 V vs SHE. [3] Previous experiments in the Vincent group had already shown that **Hyd1/C**, where C is the commercial carbon black 'BP2000' (*Cabot Corporation*), does not reduce nitrohexane to hexylamine at pH 6 and 1 bar H_2. The onset potential shift observed on the NCNTs could tune the catalyst system to expand the substrate scope to include simple aliphatics such as nitrohexane.

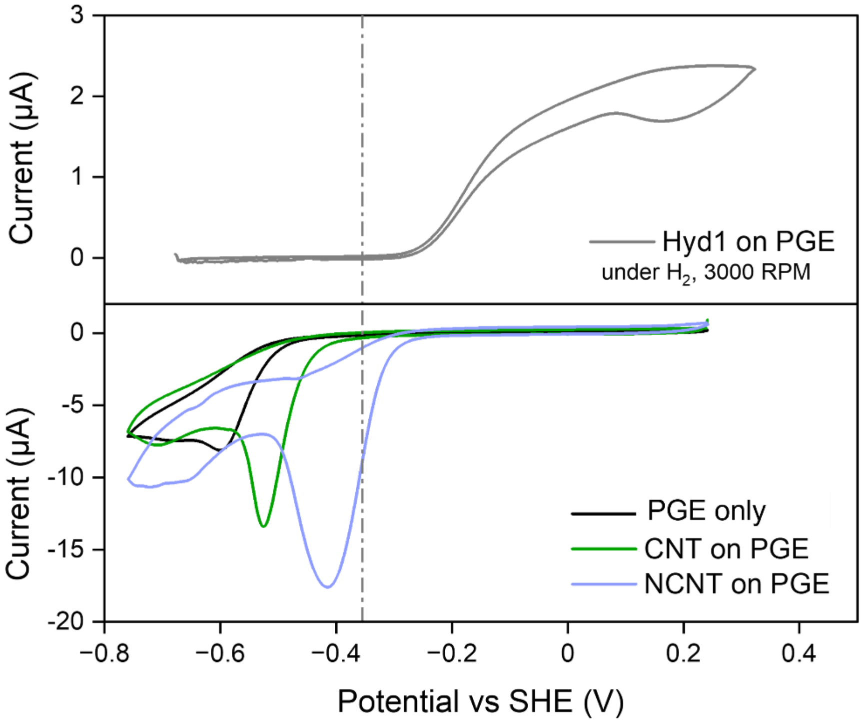

Figure 45 Comparison of the CV showing H_2 oxidation catalysed by Hyd-1 immobilised onto a PGE WE (rotating at 3000 RPM in sodium phosphate buffer (pH 6.0, 100 mM) saturated with H_2), scan rate 0.001 V/s – top panel – and cyclic voltammograms showing nitrohexane reduction on a PGE WE (black) or NCNT-modified PGE WE (blue) immersed in nitrohexane (1 mM) in sodium phosphate buffer (pH 6.0, 100 mM), scan rate 0.01 V/s – bottom panel. Dashed line indicates thermodynamic $E(H_2, 2H^+)$ of -0.355 V vs SHE.

When stacking the CVs showing H_2 oxidation as catalysed by Hyd-1 over the CVs showing the reduction of nitrohexane on the NCNTs, it is not immediately obvious that the overlap in redox features would suffice to push the nitro-reduction (Figure 45). However, it is important to note that the actual onset of the reduction lies right at the first appearance of the foot of the catalytic wave – if the very beginnings of the two redox features are compared, a slight overlap can be identified, indicating that Hyd-1 should deliver electrons of sufficient energy to reduce the nitro-group. Note also that the overpotential reflects not the thermodynamically necessary energy for any given process, but rather a kinetic sluggishness, meaning that some H_2 oxidation is possible even before the catalytic wave is unambiguously visible.

The enzyme was immobilised on the NCNTs following the same method as was used for the commercial carbon black materials in Sokolova *et al*: The appropriate amounts of each were simply well combined and then allowed to interact on ice for one hour before the NCNTs were washed with buffer to remove any non-adsorbed enzyme. As compared with the conditions published by the group in Sokolova *et al*,[3] where 1.32 mg of enzyme were used per mmol of starting nitro-compound, the enzyme loading was increased significantly to 5 mg/mmol to achieve good conversion within 24 h. The resulting modified **Hyd1/NCNT** catalyst system was added to a vial containing nitrohexane in PB buffer (pH 6.0) with dimethylsulfoxide (10% v/v) added as cosolvent and the vial was placed into a *Büchi* Tiniclave pressure vessel, which was filled to 1 bar H_2. Control reactions using **Hyd1/C** with the same elevated enzyme loading were placed within the same pressure vessel to ensure that all outside parameters would be identical.

Because the pressure vessel displays pressure above the ambient pressure in the laboratory, if the vessel is set to 1 bar this corresponds to roughly 2 bar H_2 pressure. The thermodynamic potential of the $2H^+/H_2$ couple depends on the pressure, as represented in Figure 46, with higher pressure leading to a slightly more negative equilibrium potential. Thus, the reactions performed in the pressure vessel reactor should have a driving force that is slightly higher than any performed in a reaction vial in the *Asynt Octo Mini Reactor*, which is also used throughout this thesis and which is simply connected to a H_2 line set to 30 mL/min gas flow.

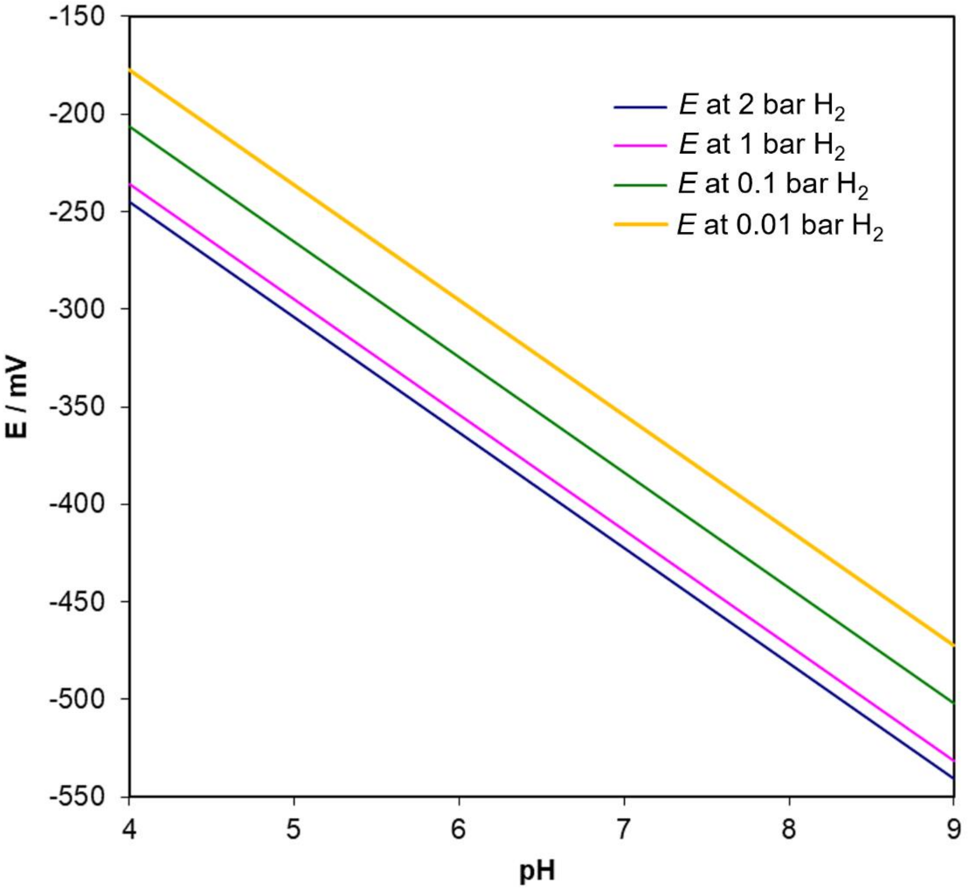

Figure 46 Variation in E(H^+/H_2) with pH and pH_2, based on the Nernst equation.

The reactions were analysed after 24 h by ^{1}H NMR, which showed full conversion using the **Hyd1/NCNT** catalyst system with only minimal hexylamine also visible in the **Hyd1/C** catalysed reaction (Figure 47). These results demonstrate that the electrocatalysis observed in the electrochemical analysis of the NCNTs can be successfully combined with **Hyd-1** catalysed H_2 oxidation to reach more stabilised nitro-groups.

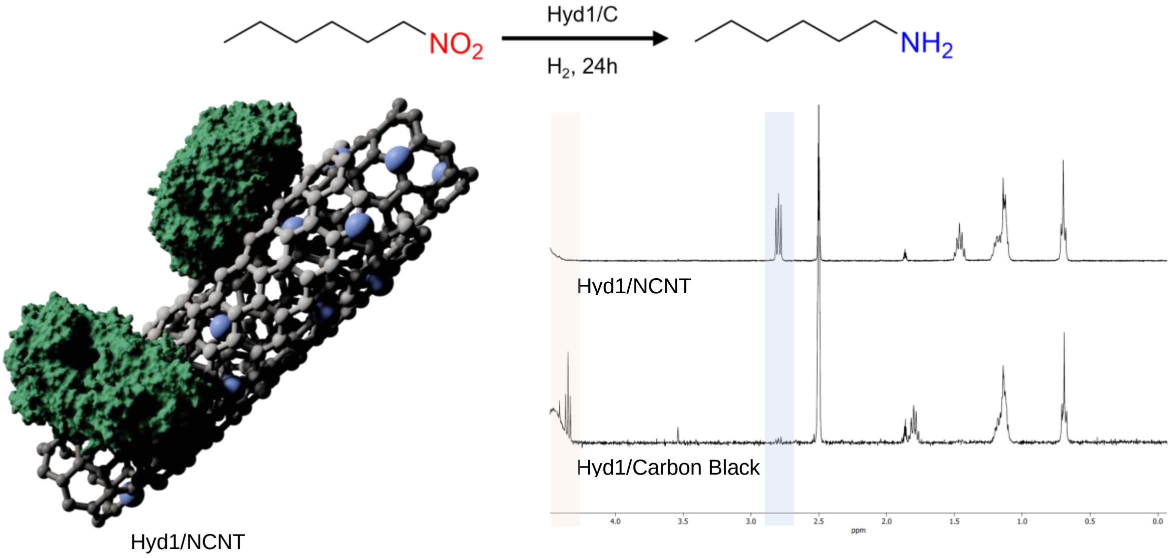

Figure 47 Graphic representation of Hyd1/NCNT catalyst and ^{1}H NMR (400 MHz, 298 K, 10% D2O in PB, 100 mM, pH 6.0) spectra of reaction mixtures of hydrogenation performed using Hyd1/NCNT or Hyd1/C catalyst systems, with characteristic amine or nitro peaks marked in blue or red, respectively. Conditions: 10 mM nitrohexane, sodium phosphate buffer (pH 6.0, 100 mM), Buchi vessel filled to 1 bar H_2, RT, 24 h.

4.3.1 Defective commercial NCNTs as a less hydrophobic enzyme support

As introduced in Chapter 3, commercially available NCNTs (*ACS Materials*) were purchased during this project to establish whether the electrocatalytic behaviour of the NCNTs produced in-house was somehow unique to the production method used here or if it could be reproduced on other NCNTs. Indeed, a similarly shifted onset potential for the electrochemical reduction of nitrohexane was observed on this commercial material. The purchased NCNTs were found to be highly defective and to contain a significant amount of amorphous nano-scale carbon particles (for detailed characterisation, see 3.6.4). They are readily suspended in water even without sonication, which could be an advantage as compared to the purer NCNTs synthesised by the author for use as an enzyme support material for batch reactions in buffer.

Accordingly, Hyd-1 was immobilised on the commercial NCNT$_{ACS}$ through simple physical adsorption as described above. Because the material immediately disperses in the aqueous buffer, the ultrasonication preparation step can be skipped, making the catalyst system simpler and more economical. The **Hyd1/NCNT$_{ACS}$** catalyst system was found to convert nitrocyclohexane (Figure 48) and nitrohexane to the corresponding amines within 24 h in the *Asynt Octo Mini Reactor* exposed to 30 mL/min H_2 gas flow, as qualitatively determined through ^{1}H NMR spectroscopy of the reaction mixtures. Future work could investigate whether the greater hydrophilicity of the $NCNTs_{ACS}$ improves enzyme adsorption or rate of reaction of the nitro-hydrogenation. The NCNTs synthesised in-house could be combined with more amorphous carbon nanomaterials to mirror the amorphous carbon dust found in the commercial material, possibly improving enzyme adsorption, slurry homogeneity, and lowering cost of the **Hyd1/NCNT** catalyst system.

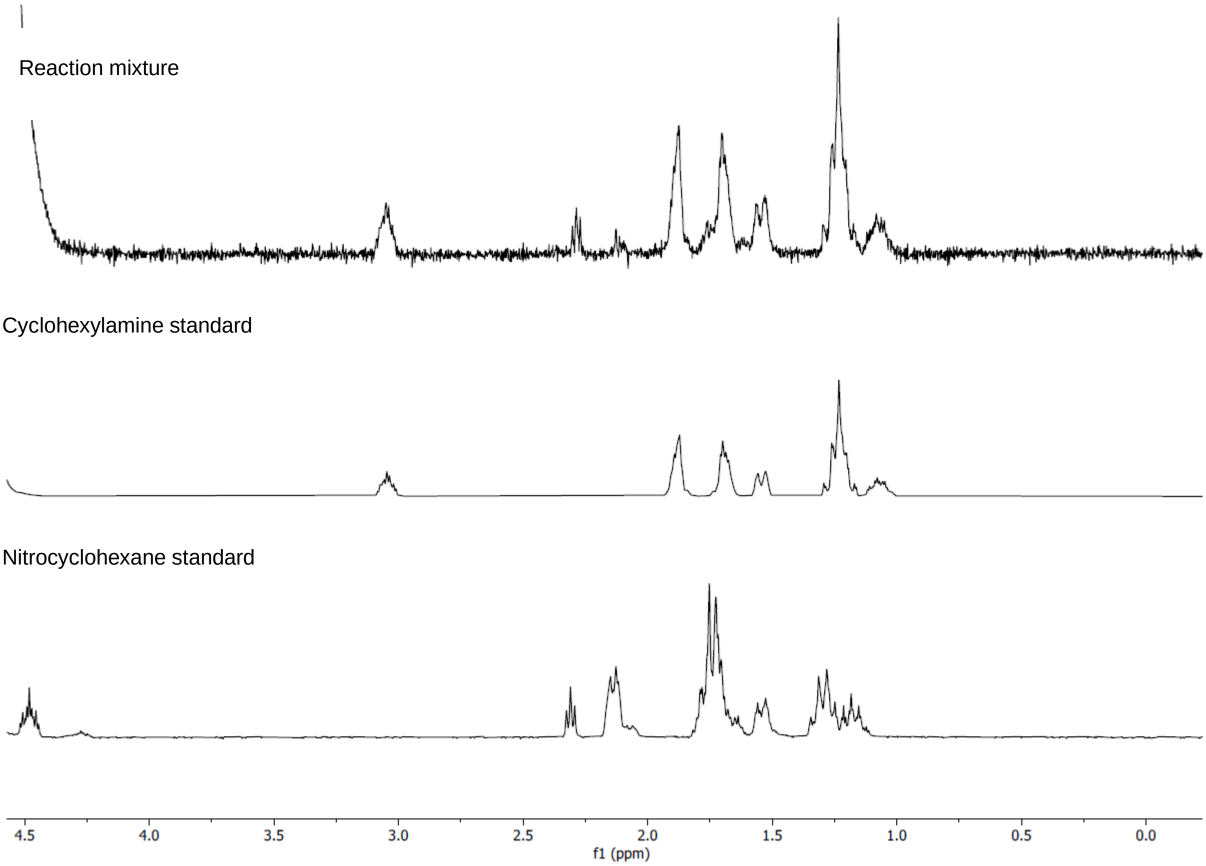

Figure 48 ^{1}H NMR (400 MHz, 298 K, 10% D2O in PB, 100 mM, pH 6.0) spectra of reaction mixture of hydrogenation of nitrocyclohexane using Hyd1/$NCNT_{ACS}$ catalyst system, 24 h, RT, 30 mL/min H_2 flow, 10 mM nitrocyclohexane. ^{1}H NMR spectra of starting material and product standards. See appendix equivalent data for the hydrogenation of nitrohexane.

4.4 Conclusions and Outlook

In Chapter 4, the electrocatalytic activity of both the NCNTs produced in house and the commercial NCNT_{ACS} was exploited to tune the Hyd1/C catalyst system to access the more difficult to reduce aliphatic nitrocompounds. Before this, the NCNTs produced by CVD were successfully immobilised onto a carbon felt electrode to electrosynthesize 4-aminophenol and hexylamine from the respective nitrated precursor at lower energetic cost than when using the CNTs or the felt only. This progress opens many doors towards future research. For example, the cost and environmental impact of the NCNT electrocatalyst could be lowered by combining it with a more readily available conductive carbon. The NCNT/CF electrode was sufficient for the experiments conducted herein. However, a more stable and thus reusable alternative electrode would make the electrosynthetic method more attractive for the production of amines. Finally, a substrate scope could investigate whether the electrochemical nitroreduction on the NCNTs is selective enough to produce complex APIs or similar industrially relevant molecules.

4.5 References

(1) Jean-Michel Saveant, C. C. Single-Electron Transfer at an Electrode. In *Elements of Molecular and Biomolecular Electrochemistry*, 2019; pp 1-80.

(2) Wang, J.; Musameh, M.; Lin, Y. Solubilization of Carbon Nanotubes by Nafion toward the Preparation of Amperometric Biosensors. *Journal of the American Chemical Society* **2003**, *125* (9), 2408-2409. DOI: 10.1021/ja028951v.

(3) Sokolova, D.; Lurshay, T. C.; Rowbotham, J. S.; Stonadge, G.; Reeve, H. A.; Cleary, S. E.; Sudmeier, T.; Vincent, K. A. Selective hydrogenation of nitro compounds to amines by coupled redox reactions over a heterogeneous biocatalyst. *Nature Communications* **2024**, *15* (1), 7297. DOI: 10.1038/s41467-024-51531-2.

5 Hydrogenation of nitrocompounds using a DuBois-type $[Ni(P^R{}_2N^R{}_2)_2]^{2+}$ complex

As introduced throughout the previous chapters in this thesis, the Vincent group has established a catalytic system based on hydrogenase enzyme immobilised on a conductive carbon support that can hydrogenate a wide variety of nitro-compounds selectively at room temperature, atmospheric hydrogen pressure, without cofactors or co-catalysts, and with a high associated recyclability of the catalyst.[1] This catalyst system combines the atom economy of heterogeneous hydrogenation with the mild conditions and excellent selectivity of biocatalysis, while the biocatalyst is only responsible for the H_2 oxidation. Nonetheless, there could be benefits to developing a non-biocatalytic system inspired by these previous results. Hydrogenase enzyme production is currently only possible at small scale, while some synthetic inorganic catalysts can be produced using well-established methods of chemical synthesis available to most industrial and academic laboratories. In addition, the mild conditions of the **Hyd/C** system that are needed to prevent enzyme denaturation may not always be appropriate depending on the reactivity or solubility of the starting nitro-compound. A non-biocatalytic system could open the possibility to use organic solvents, higher starting material concentrations, as well as higher pressures and temperatures. From these considerations it was decided to attempt to replace the hydrogenase enzyme with a 'DuBois-type' $[Ni(P^R{}_2N^R{}_2)_2]^{2+}$ complex, which has been developed to mimic the active site found in hydrogenases by DuBois, Shaw, Dutta, and others and which is well-known in H_2 fuel cell research. [2-4]

Table of Contents

5.1 Experimental

5.1.1 Reagents

Nitrobenzene (99%) was purchased from *Alfa Aesar*. 4-Nitrotoluene (99%), 4-nitrophenol (≥99%), 1-fluoro-4-nitrobenzene (99%), 1-chloro-4-nitrobenzene (99%), 1-nitrohexane (98%), and hexylamine (99%) were purchased from *Sigma-Aldrich*. 2-Nitrotoluene (99%), 3-nitrotoluene (95%), 2-nitrophenol (95%), 3-nitrophenol (99%), 1-bromo-4-nitrobenzene (95%), 4-nitrobenzyl alcohol (99%), 4-nitrobenzaldehyde (98%), 4-nitrobenzonitrile (97%), and 1-ethynyl-4-nitrobenzene (95%) were purchased from *Fluorochem*. 4-Nitrostyrene (98%) was purchased from *Themo Scientific*. Carbon black (C) VULCAN XC72 was purchased from *Cabot* and used as received.

All chemicals were used as received without further purification and all aqueous solutions were prepared using MilliQ water (resistivity 18.2 MΩ cm, Millipore).

Buffer salts and solvents were purchased from *Sigma-Aldrich*. Deuterated solvents were purchased from *Sigma-Aldrich* (D_2O, 99.9% D).

Sodium phosphate buffer was prepared by dissolving an appropriate mass of Na_2HPO_4 and NaH_2PO_4 in water after which the pH was adjusted to the desired value by adding HCl(aq) or NaOH(aq) dropwise and monitoring pH using an Ag/AgCl pH electrode (*Fisher*).

5.1.2 *Ni-complex samples*

Samples of the nickel complexes, $[Ni(P^{Cy}{}_2N^{Arg}{}_2)_2]^{2+}$ (NiArg) and $[Ni(P^{Cy}{}_2N^{Pyr}{}_2)_2]^{2+}$ (NiPyr) as well as the ligand $P^{Cy}{}_2N^{Arg}{}_2$ were synthesized and kindly provided by Dr Bertrand Reuillard at the Laboratoire de Chimie et Biologie des Metaux in Grenoble (LCBM), according to published procedures.[5, 6] The NiArg complex was frozen at millimolar conc. in aqueous solution, stored at -80 ^{o}C and defrosted as required. The NiPyr complex was stored in the same manner but in acetonitrile. The ligand was stored at room temperature under inert N_2 atmosphere.

5.1.3 *Procedure for cyclic voltammetry (CV) experiments performed under flow of H_2*

A glass electrochemical cell made in-house (glass blower: Terri Adams) with a water jacket adjusted to 25 ^{o}C was connected to a hydrogen line and was equipped with a saturated calomel reference electrode (SCE, *Palmsens BV*) and a coiled Pt wire as the counter electrode (CE). The sodium phosphate electrolyte (pH 6.0, 100 mM) was subjected to H_2 gas flow (100 scc/min) before the experiment. A pyrolytic graphite edge (PGE) rotating disk electrode (RDE) as the working electrode (WE) was modified with the relevant Ni complex by dropping a millimolar solution of the complex onto the electrode, allowing the film to incubate for 10 min and then rinsing the electrode with MilliQ water. The WE was mounted onto a rotator (*Metrohm*) and rotated at 3000 RPM during the measurements. Gas flow was directed through the head space of the vial once the WE had been immersed in the electrolyte. The cyclic voltammograms were recorded using an *Autolab PGStat30* potentiostat (*Ecochemie*) and Nova 1.1 software.

5.1.4 General procedure for small-scale hydrogenation reactions

Reaction set-up was performed under inert atmosphere (N_2, $O_2 < 3$ ppm) in a glove box (*Glove Box Technology LTD.*) For the heterogeneous Ni/C catalyst, a 20 mg/mL carbon black slurry in sodium phosphate buffer (PB, pH 6.0 unless stated otherwise, 100 mM) was sonicated for 1 hour. For one 2 mL scale reaction with 10 mM concentration of nitrocompound, the carbon black suspension (298 μL, 5.9 mg C) was transferred to an Eppendorf tube, the NiArg solution (20 μL, 0.15 mg, 0.0001 mmol; amounts varied throughout the chapter to achieve different loadings) was added, the mixture was combined and left on ice for 1 hour. The suspension was centrifuged (3 min, 14100 x *g*), the supernatant was discarded, and the catalyst resuspended in PB (100 μL). The centrifugation and resuspension steps were repeated twice to wash off any free complex. The catalyst particles were then resuspended and directly used for the hydrogenation reaction. Reactions were run at 2 mL scale with a 10 mM nitrocompound concentration in PB. Some compounds were dissolved in acetonitrile leading to a final acetonitrile concentration of 10% v/v in the reaction mixture. A stock solution of the starting material was transferred to the reaction vial of an *Asynt Octo Mini Reactor*, which allows eight reactions to be run in parallel under the same atmosphere. The catalyst suspension was added to the reaction mixture and the volume was adjusted to 2 mL. The reactor was sealed, removed from the glove box and connected to a H_2 line set to 30 mL/min. Time points were taken after first placing the reactor back into the glove box at 24, 48, and 72 hours and analysed by ^1H NMR spectroscopy.

For the hydrogenation reactions using complex only, the complex (0.1-0.5% catalyst loading) in solution was added directly to the stock solution of nitrocompound, the reaction volume was adjusted to 2 mL, and the hydrogenation was performed as above.

5.2 Hydrogenation of nitroarenes using a $[Ni(P^{Cy}{}_2P_2{}^{Arg})_2]^{2+}$ complex

5.2.1 *Electrochemistry of Ni complex and nitrobenzene*

The driving force of the nitro-to-amine transformation using electrons supplied through H_2 oxidation depends on the potential at which these electrons are supplied, as well as the potential at which the nitro-group is reduced. For the purposes of this project, a $[Ni(P^R{}_2N^R{}_2)_2]^{2+}$ complex decorated with arginine ligands on the pendent N bases was chosen (Figure 49). This complex is well-known for its high H_2 oxidation activity in aqueous media, and has been reported to adsorb to carbon surfaces through possible interactions between the guanidinium groups of arginine and the oxygen functional groups found on carbon materials. [2, 4, 7] To investigate the possibility of driving the nitro-reduction reaction using H_2 oxidation catalysed by this DuBois-type Ni complex (referred to in this chapter as '**NiArg**'), the electrochemistry of the complex under H_2 at atmospheric pressure and near-neutral pH was studied. A pyrolytic graphite edge (PGE) working electrode (WE) was modified by drop-casting a millimolar aqueous solution of the NiArg, allowing it to physically adsorb and then rinsing off any excess. The WE was immersed into a sodium phosphate electrolyte (pH 6.0, 100 mM) which had been saturated with H_2 and which was temperature-controlled at 25 °C. The thermodynamic H_2 oxidation potential at these conditions can be calculated using the Nernst equation to equal -0.355 V versus the standard hydrogen electrode (SHE). The oxidation feature observed when using the NiArg-modified WE begins near this value with minimal overpotential while the reduction of

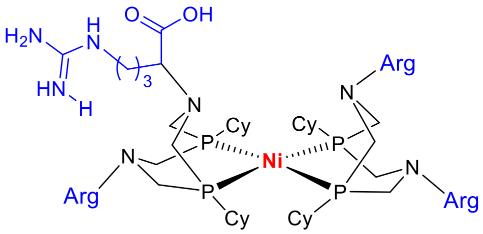

Figure 49 Structure of the $[Ni(P^{Cy}{}_2P_2{}^{Arg})_2]^{2+}$ complex, referred to in this chapter as NiArg, where Arg = arginine (structure shown in blue).

nitrobenzene on a PGE WE at pH 6.0 and 25 °C commences at a significantly more positive potential of approximately -0.2 V (Figure 50). It follows that the driving force provided by H_2 oxidation catalysed by **NiArg** should suffice to push the nitrobenzene reduction at a carbon particle modified with **NiArg** subjected to atmospheric pressures of H_2. It is unclear why the return sweep of the voltammogram shows a significantly lower current for the H_2 oxidation catalysed by the NiArg complex. The scan rate used was quite low at 1 mV/s, which could allow the catalyst to fall off the electrode surface during the experiment. In experiments described below the catalyst is used for multiple days, which indicates that it should not deteriorate to an extent that would explain the loss in current seen in Figure 50.

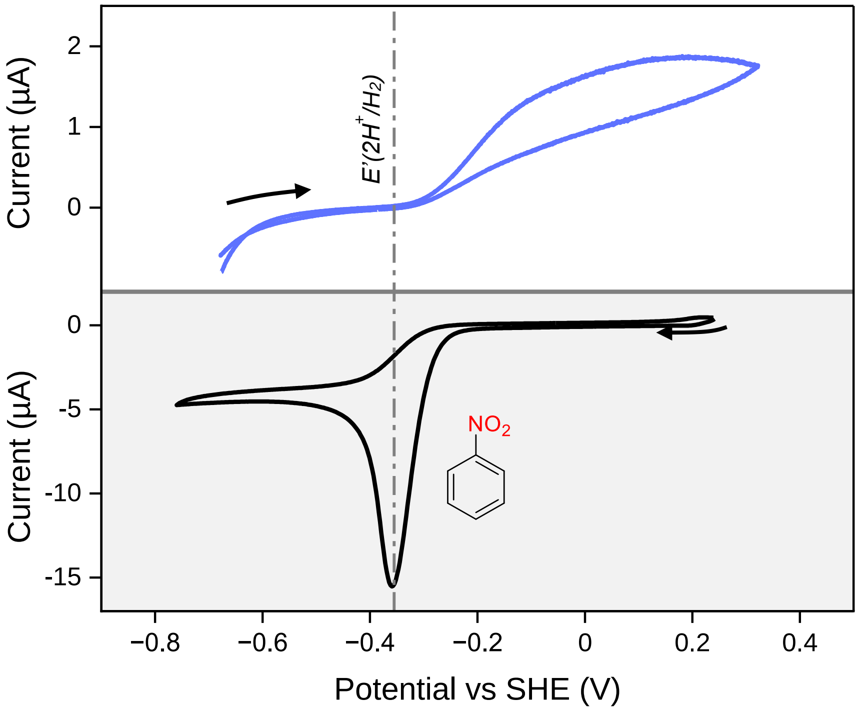

Figure 50 Comparison of the CV showing H_2 oxidation at the NiArg complex immobilised onto a PGE WE (rotating at 3000 RPM in sodium phosphate buffer (pH 6.0, 100 mM) saturated with H_2, 0.001 V/s) – top panel – and a CV showing nitrobenzene reduction on a clean PGE WE immersed in nitrobenzene (1 mM) in sodium phosphate buffer (100 mM, pH 6.0) at 0.01 V/s – bottom panel.

5.2.2 Hydrogenation of nitrobenzene using NiArg/C as the catalyst

Initial hydrogenation experiments were performed with conditions identical to those used for the enzymatic catalytic system in Sokolova et al, [1] while the catalyst loading and the carbon-to-complex ratio, whose optimal values were assumed to differ from those relevant to the much larger hydrogenase, were investigated. Catalyst preparation is described in detail in 4.1.6. Briefly, a slurry of a commercial carbon black (here, Vulcan XC72 from 'Cabot Corporation') in sodium phosphate buffer (pH 6.0) was prepared by sonication, the carbon was then combined with an aqueous solution of **NiArg** which was allowed to adsorb for one hour, after which the particles were washed, recollected, and used as the catalyst system in the hydrogenation of nitrobenzene. Interestingly, the control reactions performed without the addition of any carbon black led to the clean production of the phenyl-hydroxylamine (**1B**) after 24h (Table 7, Entry 1 and 2), with no starting material (**1A**) or amine (**1C**) observed. This observed hydrogenation activity for the complex in solution adds an interesting layer of understanding

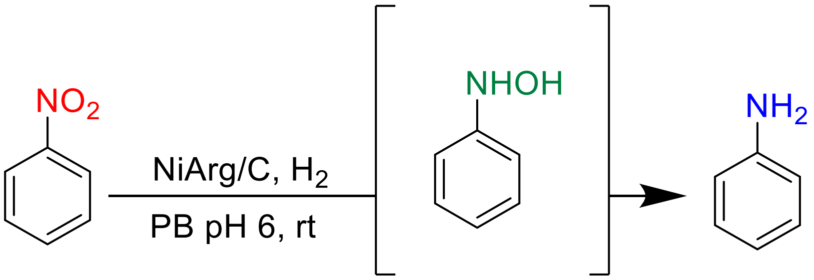

1A **1B** **1C**

Table 7 Product of nitrobenzene hydrogenation depending on the carbon-to-catalyst ratio used, defined by weight. Conversions are estimated by the relative integrals in the relevant ^{1}H NMR (400 MHz, 298 K, 10% D2O in PB, 100 mM, pH 6.0) spectra.

Entry	Catalyst loading (mol/mol)	Carbon:Complex (w:w)	Product		
			A	B	C
1	0.1%	No carbon	0	1	0
2	0.3%	No carbon	0	1	0
3	0.3%	5:1	0	>0.95	<0.05
4	0.3%	10:1	0	~0.9	~0.1
5	0.3%	40:1	0	0	1

Conditions: 10 mM starting material, varying NiArg and carbon loading, room temperature, H_2 gas flow 30 mL/min, PB (pH 6.0, 100 mM), 24 h reaction time.

to the behaviour of the Ni complex, which has typically been studied only for its ability to oxidize or produce H_2. The addition of increasing amounts of carbon led to the production of **1C**, with only **1C** observed after 24 h with a carbon-to-complex ratio of 40:1 (Table 7, Entry 5). As mainly **1B** was produced with a carbon to complex ratio of 5:1 (Table 7, Entry 3), it should also be possible to find a ratio that allows the clean production of **1B** using a heterogeneous catalyst as opposed to the complex in solution, which could simplify the removal of the complex from the organic product. The fact that the addition of carbon seems to favour the completion of the six-electron nitro-reduction could be due to several factors. The nitro-compound could more readily interact with the hydrophobic carbon surface, making full reduction more likely. In addition, the carbon particle could act as an electron reservoir, allowing an immediate transfer of several electrons, where the complex should only be able to transfer two electrons at any one time from the oxidation of H_2. The heterogeneous version of the hydrogenation catalyst will be referred to as **NiArg/C** below.

To investigate the course of the reaction, aliquots were taken and analysed by ^{1}H NMR spectroscopy where conversion was estimated through the relative integrals of the relevant signals. For the **NiArg/C** catalyst system, the nitrobenzene **1A** was consumed rapidly to produce the phenylhydroxylamine **1B**, with the subsequent reduction to the aniline **1C** occurring slowly over the course of 24 h (Figure 51). This observation suggests that the carbon particle is not acting as an electron reservoir to push the six-electron reduction immediately, because the final and slowest step seems to be the two-electron reduction of **1B** to **1C**. For the homogeneous **NiArg** in solution, no production of **1C** is observed and the rate of reaction to **1B** is slightly slower.

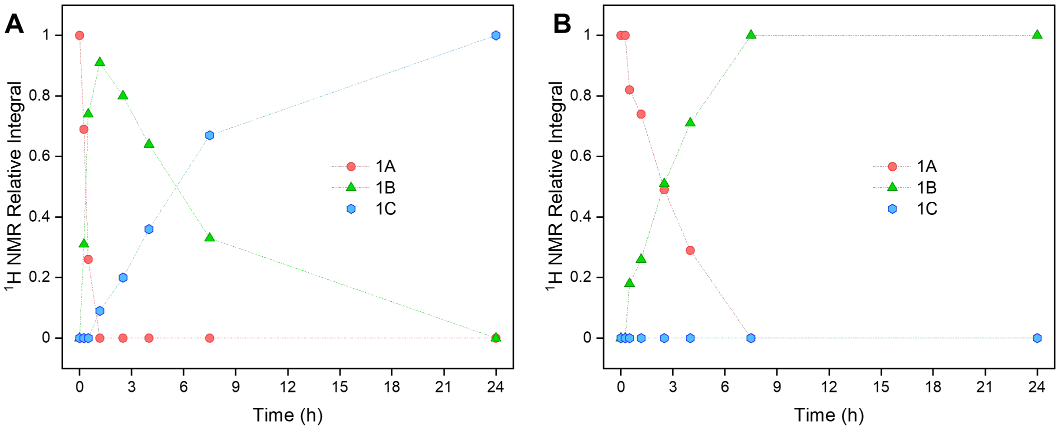

Figure 51: Time points showing the relative conversion of nitrobenzene 1A to hydroxylamine 1B or aniline 1C, respectively. ***A*** *– using NiArg/C and* ***B*** *- using NiArg only as the catalyst. Conditions: 10 mM starting material, NiArg loading of 0.5 mol% and 40:1 carbon to complex ratio for* **A**, *room temperature, H_2 gas flow of approximately 30 mL/min, PB (pH 6.0, 100 mM), 24 h reaction time. Conversion at the time points was estimated from the relative intensity of the integrals under the appropriate signals in the ^{1}H NMR (400 MHz, 298 K, 10% D2O in PB, 100 mM, pH 6.0) spectra of the reaction mixture.*

The yield observed at 1 hour, estimated by using 4-nitrophenol as an internal standard in the ^{1}H NMR sample, was used to calculate turnover frequency (TOF) values towards **1B** for both the heterogeneous (Table 8, Entry 1) and homogeneous system (Table 8, Entry 2). The heterogeneous catalyst system **NiArg/C** leads to a TOF value about double that of the homogeneous catalyst, underlining the importance of the carbon particles. The TOF value calculated for the reaction towards the amine using **NiArg/C** is relatively low (0.0034 s^{-1}), as determined using the estimated yield from the ^{1}H NMR spectrum using 4-nitrophenol as an internal standard after six hours. Future experiments could investigate whether the reaction rate could be increased by varying temperature, pressure, catalyst loading, or other parameters. However, for the purposes of this project, the results described above were encouraging and led to the pursuit of a substrate scope of substituted nitroarenes to probe the selectivity of this catalyst system.

Table 8 Turnover frequency calculated for the nitrobenzene hydrogenation using NiArg/C or NiArg only

Entry	**Catalyst**	**TOF (s^{-1}) to 1B**	**TOF (s^{-1}) to 1C**
1	NiArg/C	0.013	0.0034
2	NiArg	0.0075	

Conditions: 10 mM starting material, NiArg loading of 0.5 mol% and 40:1 carbon to complex ratio for NiArg/C, room temperature, H_2 gas flow 30 mL/min, PB (pH 6.0, 100 mM). TOF was calculated using estimated conversions from the relative intensity of the integrals under the appropriate signals in the ^{1}H NMR (400 MHz, 298 K, 10% D2O in PB, 100 mM, pH 6.0) spectra of the reaction mixture at 1 h for the conversion to 1B (hydroxylamine) and 6 h for conversion to 1C (amine).

5.2.3 Substrate scope: substituted nitroarenes

*Table 9 Conversions to the relevant hydroxylamine (**B**) and amine (**C**) for various starting materials as estimated from relative integral values for the corresponding signals in the ^{1}H NMR spectra (400 MHz, 298 K, 10% D2O in PB, 100 mM, pH 6.0) of the reaction mixtures after 24 h, ⸸ after 48 h,* ‡ after 72 h. *Conditions: 10 mM starting material, 0.5% NiArg loading, room temperature, H_2 gas flow 30 mL/min, PB pH 6.0 with 10% v/v acetonitrile. *performed at pH 8.0.*

	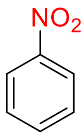		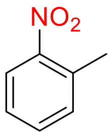		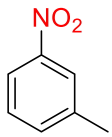		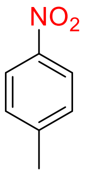	
	1A		**2A**		**3A**		**4A**	
Catalyst	**B**	**C**	**B**	**C**	**B**	**C**	**B**	**C**
NiArg only	100%	0%	100%⸸	0%	100%⸸	0%	100%⸸	0%
NiArg/C	0%	100%	0%	100%	0%	100%	0%	100%
	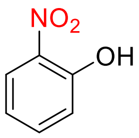		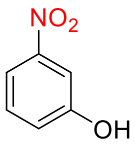		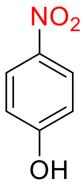		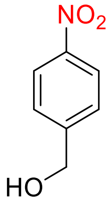	
	5A		**6A**		**7A**		**8A**	
Catalyst	**B**	**C**	**B**	**C**	**B**	**C**	**B**	**C**
NiArg only	0%	100%	100%	0%	0%	60%‡	100%	0%
NiArg/C	0%	100%	0%	100%	0%	100%	0%	100%
	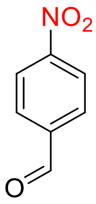		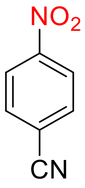		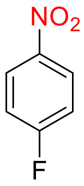		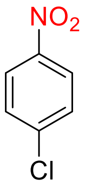	
	9A		**10A**		**11A**		**12A**	
Catalyst	**B**	**C**	**B**	**C**	**B**	**C**	**B**	**C**
NiArg only	100%	0%	100%	0%	100%	0%	100%	0%
NiArg/C	0%	100%‡	0%	100%⸸	0%	100%	0%	100%
	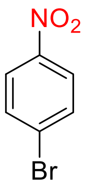		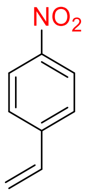		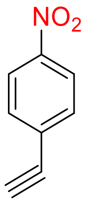			
	13A		**14A**		**15A***			
Catalyst	**B**	**C**	**B**	**C**	**B**	**C**		
NiArg only	100%	0%	100%	0%	100%	0%		
NiArg/C	0%	100%	66%	34%	63%	37%		

For the substrate scope presented here, the catalyst loading was held steady at 0.5% (mol complex to mol nitroarene) and the carbon-to-complex ratio for the heterogeneous system was held at 40:1 by weight. The conversion was estimated by the relative integrals under the relevant ^{1}H NMR peaks. Acetonitrile (10% v/v) was added to improve solubility of the organic starting materials. The substrate scope was chosen to trial the selectivity of the hydrogenation by including compounds with other unsaturated bonds (**9**, **10**, **14**, **15**) and halogenated compounds (**11**, **12**, **13**) which are known to undergo dehalogenation over hydrogenation catalysts described in literature.[8] All of the trialled compounds (other than *o*- and *p*-nitrophenol) were converted cleanly to the corresponding amine **C** using **NiArg/C** and to the hydroxylamine **B** using **NiArg** only. For some substrates, the reaction time was extended to reach full conversion, as indicated in Table 9. For the three trialled nitro-toluenes (**2-4**), the reaction time towards the hydroxylamine using the homogeneous NiArg catalyst had to be extended to 48 h, while the amine was reached within 24 h, which supports the assumption that the more hydrophobic starting materials will be more readily reduced using the heterogeneous **NiArg/C** on the hydrophobic carbon surface. Phenols **5-7** were also readily hydrogenated; however, no hydroxylamine was produced for the *o*- and *p*-isomers, for which even without the addition of the carbon black powder only amine was observed. No dehalogenation was observed for substrates **11-13** and the selectivity of the system towards the hydrogenation of the nitro-group was demonstrated by the conversion of nitroarenes substituted with aldehyde (**9**), nitrile (**10**), alkene (**14**), or alkyne (**15**) groups, while the reaction of **15** was performed at pH 8 to prevent alkyne hydration. These results align well with those presented in Sokolova *et al.* [1], were the Hyd/C system was used, indicating that replacing Hyd1 with NiArg has not altered the excellent selectivity of the hydrogenation system. Both the **NiArg** and **NiArg/C** catalysts could have broad applicability in the production of amines and hydroxylamines and could possibly be employed for late-stage functionalisation of complex starting materials containing other unsaturated groups or halogens.

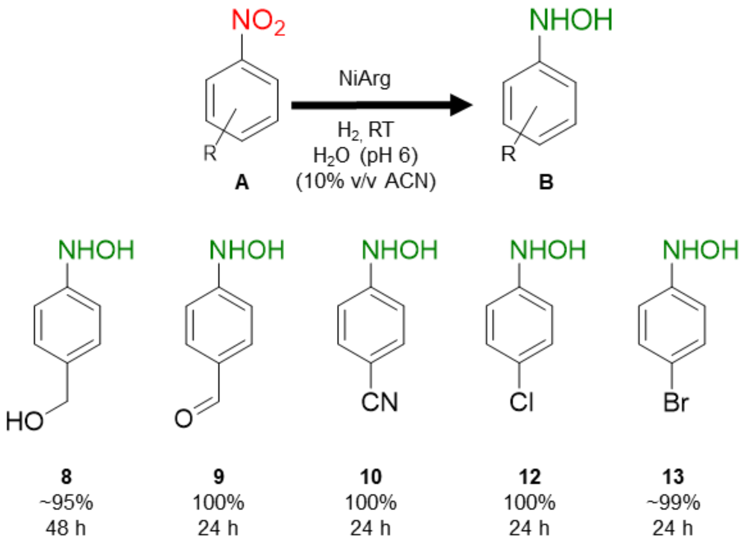

Figure 52 Conversions to hydroxylamine for a selection of substituted nitroarenes from hydrogenations performed in water using NiArg only, estimated from relative integrals from 1H NMR (400 MHz, 298 K, 10% D2O in PB, 100 mM, pH 6.0) spectra. Conditions: 10 mM starting material, 0.5% NiArg loading, room temperature, H_2 gas flow 30 mL/min, H_2O pH 6.0 with 10% v/v acetonitrile.

The buffer salts used in the experiments above significantly diminish the atom economy associated with the process and greatly complicate the purification of the products, necessitating multiple washing steps. Even while the nitro-hydrogenation requires protons, the pH in the solution should remain unchanged as the H_2 oxidation is constantly providing the equivalent number of protons, so the buffering function should not be necessary. For this reason, the reactions were trialled in MilliQ water that had been adjusted to pH 6 using HCl containing acetonitrile (10% v/v). The homogeneous reaction led to excellent conversions to pure hydroxylamine for a range of nitroarenes (see Figure 52). The heterogeneous catalyst system also converted all starting material but produced a mixture of hydroxylamine and amine for all of the trialled nitroarenes, even after 72 hours. The presence of the buffer seems to be influencing the efficiency of the reaction, perhaps by changing proton mobility. [9] In addition, some of the substrates, intermediates, or products seemed to be less soluble in the pure MilliQ water, possibly because of a lower likelihood of protonation. Future experiments should probe whether the reaction can occur more efficiently in water adjusted to more acidic pH, and, importantly, in either protic organic solvents such as alcohols or in nonprotic solvents containing some percentage of water. This would also open the process to less soluble substrates or higher starting material concentrations.

5.3 Hydrogenation of aliphatic nitro-compounds using a $[Ni(P^{Cy}{}_2P_2{}^{Arg})_2]^{2+}$ complex

The reduction of simple aliphatic nitro-compounds requires a more negative applied potential than that observed for most simple nitro-arenes. As previously trialled, the Hyd-1 and carbon black catalytic system does not provide sufficient driving force to access hexylamine, for example. Because the NiArg complex oxidises H_2 very close to the thermodynamic potential while Hyd-1 has a slight overpotential of around 80-100 mV, the **NiArg/C** system has a slightly better overlap with the nitrohexane reduction potential. Indeed, **NiArg/C** was shown to hydrogenate nitropentane, nitrohexane (Figure 53), and nitrocyclohexane at room temperature and atmospheric H_2 pressures. Quantitative investigation of the conversion was made difficult

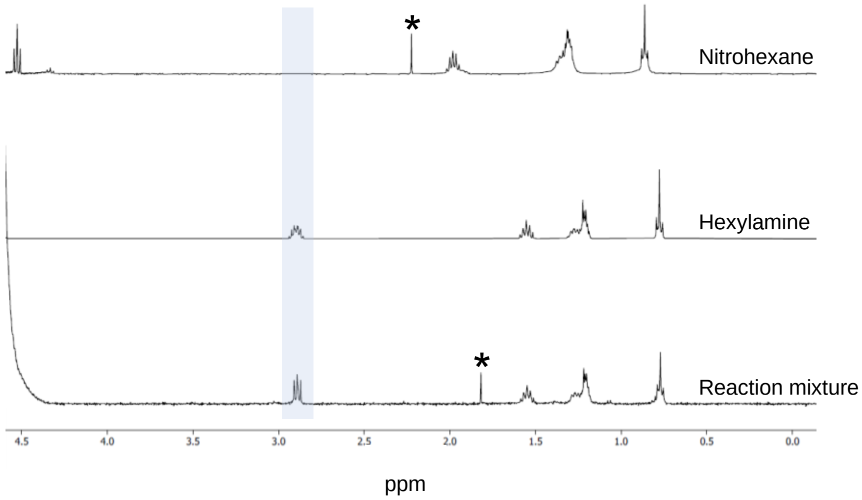

*Figure 53 ^1H NMR (400 MHz, 298 K, 10% D2O in PB, 100 mM, pH 6.0) spectra of standards nitrohexane and hexylamine and the reaction mixture of the hydrogenation of nitrohexane using NiArg/C after 24 h. Conditions: 10 mM starting material, 0.5% NiArg loading, 40:1 carbon to complex ratio by weight, room temperature, H_2 gas flow 30 mL/min, PB pH 6.0. *unidentified impurity (acetone?)*

by the possible evaporation of the aliphatics in the reactor which is subjected to a constant gas stream and by the low solubility of these compounds in the applied conditions.

5.3.1 Combination with NCNTs produced in-house to improve driving force

While the NiArg complex combined with commercial carbon black was able to hydrogenate nitrocyclohexane, it was hypothesized that the NCNTs synthesised in-house described in Chapters 3 and 4 could improve the rate of reaction. This doped material was shown to electro-catalyse the nitro-reduction and was successfully combined with Hyd-1 to access aliphatic amines. The CV of the nitro-reduction on carbon black shows a reduction wave that is more negative than the H_2 oxidation potential (Figure 54); however, the onset of the reduction must be slightly more positive as some conversion is observed when using carbon black as the catalyst support, underlining the difficulties in determining actual onset potentials discussed in

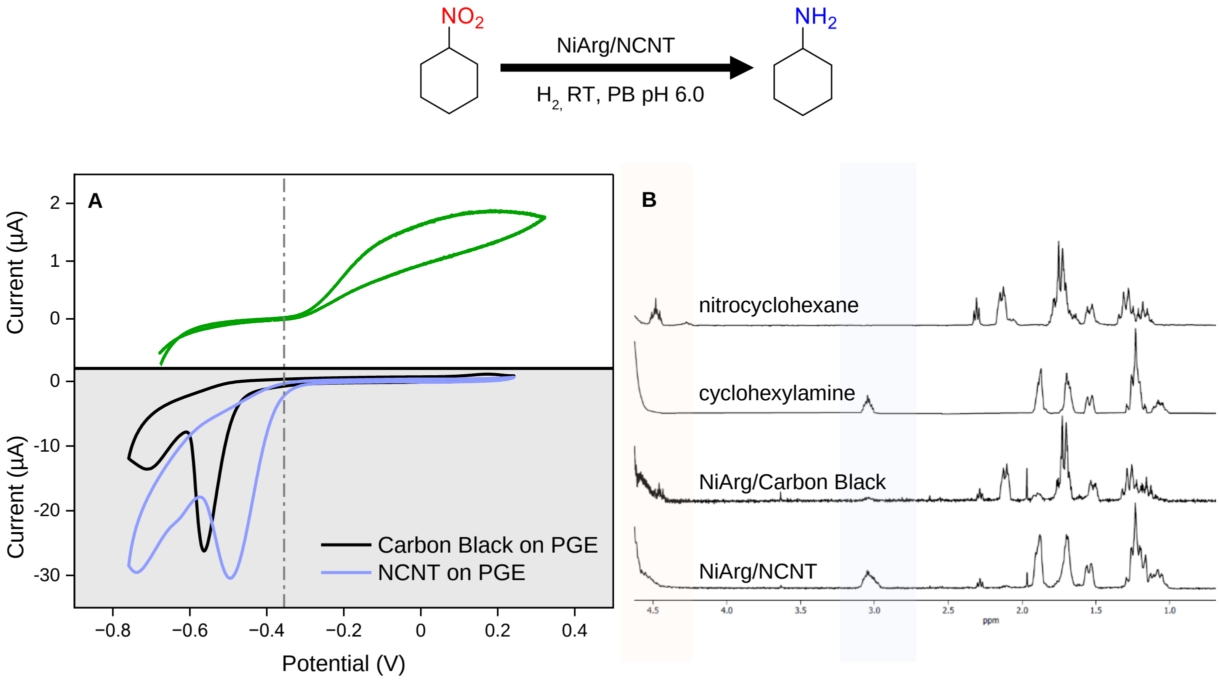

Figure 54 ***A*** *CVs showing the H_2 oxidation feature using NiArg-modified WE (rotating at 3000 RPM in sodium phosphate buffer (pH 6.0, 100 mM) saturated with H_2, scan rate 0.001 V/s), repeat data from Figure 51 – top panel – and the nitro-reduction features of nitrocyclohexane (1 mM in in sodium phosphate buffer (pH 6.0, 100 mM), scan rate 0.01 V/s) on commercial carbon black or the synthesised NCNTs on a PGE WE (bottom panel). ^{1}H NMR (400 MHz, 298 K, 10% D2O in PB, 100 mM, pH 6.0)* ***B*** *Spectra of starting material and product standards as well as the reaction mixtures resulting from NiArg/NCNT and NiArg/C catalysts. Conditions: 10 mM starting material, 0.5% NiArg loading, 40:1 carbon to complex ratio by weight, room temperature, 1 bar H_2, PB pH 6.0, Reaction time 4h.*

Chapter 3. The CVs of the nitrocyclohexane reduction supported this approach as the cathodic feature is shifted significantly on the NCNTs. Accordingly, the complex was physically adsorbed onto the NCNT material. The resulting modified NCNTs were used as the catalyst system in the hydrogenation of nitrocyclohexane alongside a control reaction containing NiArg on commercial carbon black. To prevent evaporation of the starting material, the reaction was performed inside a sealed *Büchi* Tiniclave pressure vessel which was charged to one bar H_2. Indeed, the ^1H NMR spectra of the reactions after four hours show near complete conversion for the **NiArg/NCNT** catalyst system with only minor conversion visible for the original **NiArg/C**.

5.4 Varying complex preparation and ligand scaffold

5.4.1 *Comparison to the hydrogenation activity of a $[Ni(P^{Cy}{}_2P^{Pyr}{}_2)_2]^{2+}$ complex*

Many types of Ni complexes based on the DuBois-type bisdiphosphine ligand scaffold have been reported by varying the substituents on the P and N positions. [10] While the N-arginine complex introduced above showed good activity and ease of handling, it was hypothesized that an equivalent N-pyrene complex may improve the complex to carbon interaction through π-π stacking. [11] In addition, the $[Ni(P^{Cy}{}_2P^{Pyr}{}_2)_2]^{2+}$ is not water soluble, which could further favour the non-covalent adsorption to the carbon particles within aqueous media. However, the change from arginine to pyrene in the outer coordination sphere could lower the freedom of movement of protons and solvent molecules near the metal site. [10] The two complex-on-carbon catalyst systems were prepared as before by simply combining a millimolar solution of the complex with a slurry of commercial carbon black. To investigate the stability of the two Ni/C systems,

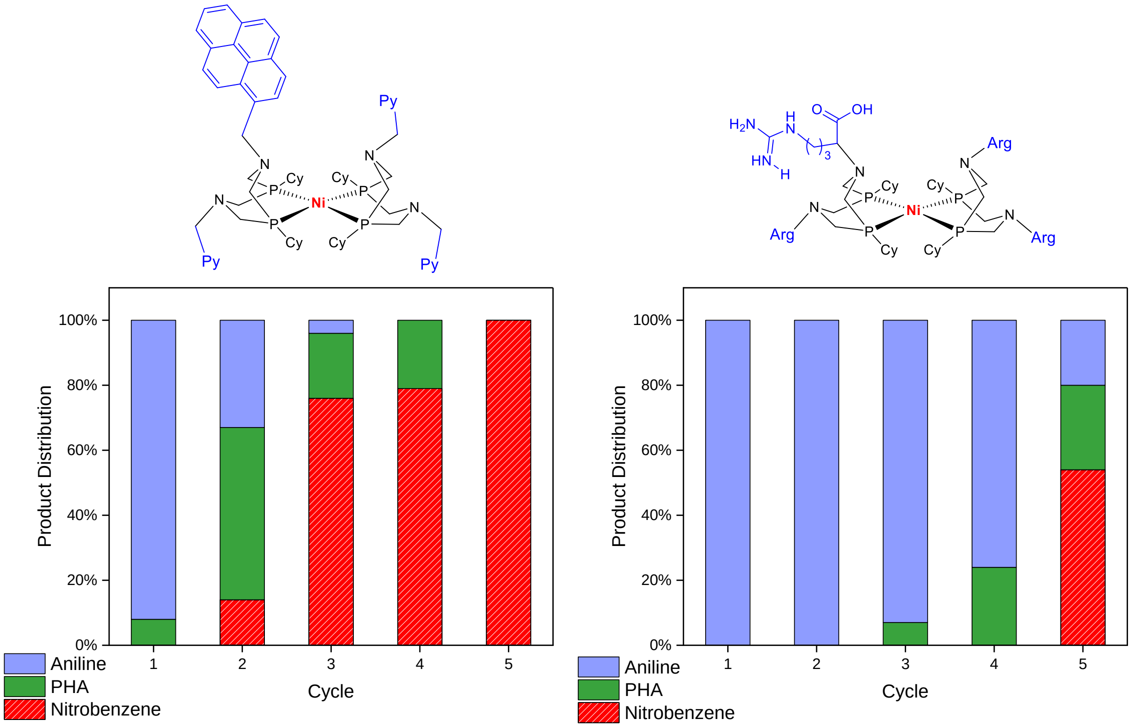

Figure 55 Product distribution for five cycles of 24 h nitrobenzene hydrogenation reactions. Catalyst particles were collected by centrifugation after each cycle and reused immediately. Conditions: 10 mM starting material, 0.5% Ni complex loading, 40:1 carbon to complex ratio by weight, room temperature, H_2 gas flow 30 mL/min, PB pH 6.0, 24 h reaction time per cycle. Product distribution estimated from relative integrals from 1H NMR (400 MHz, 298 K, 10% D2O in PB, 100 mM, pH 6.0) spectra.

the catalyst particles were collected by centrifugation and reused after each of five consecutive nitrobenzene hydrogenation reactions. Even in the first cycle, the **NiPyr/C** catalyst did not lead to full conversion to the amine, while the **NiArg/C** catalyst could be reused to produce pure aniline within 24 h for two cycles, and remained highly active for four cycles (Figure 55). This result indicates that while the **NiPyr/C** is able to hydrogenate nitrobenzene, the improved proton mobility in the outer coordination sphere as well as the more favourable interactions of the **NiArg/C** with water and buffer may improve the activity of this catalyst system. It is encouraging to observe the **NiArg/C** catalyst system remain active over multiple cycles, which indicates multi-day stability of the complex and good adsorption to the carbon surface. To study the differences between the two complexes in further detail, the efficiency of the complex adsorption should be verified, for example by measuring the complex concentration in the discarded supernatant after the adsorption step.

5.4.2 Investigation of metal leaching into the reaction mixture

The US Pharmacopeia publishes maximum permissible values for metal contamination of chemical products used in pharmaceutical production. While the actual acceptable value may depend on the further use and treatment of the species, this value can be used as a guideline to assess whether the removal of the Ni/C catalyst by centrifugation used in this project is sufficiently effective. For Ni, the USP limit is set at 20 μg/g (=20 ppm) in oral drug products.[12] To investigate Ni leaching in the Ni/C systems used herein, samples of the relevant reaction mixtures were sent to Dr. Anna Foster at the University of Sheffield for analysis by inductively coupled plasma-optical emission spectroscopy (ICP-OES), a technique with a 0.02 ppm detection limit for Ni. Four reaction mixtures that had been exposed to different catalyst systems were analysed: First, the catalyst system **NiArg/C** (in triplicate); then a sample in which NiArg complex and carbon had been added separately to the reaction mixture (NiArg + C) to verify the importance of the adsorption step; third, the homogeneous NiArg (in triplicate), and finally a sample in which the **NiPyr/C** system had been used. The highest Ni contamination detected in a reaction mixture in which **NiArg/C** had been the catalyst was 0.04 ppm (Figure 56). Assuming full conversion in the 2 mL scale reactions of 10 mM nitrobenzene to aniline as well as subsequent perfect isolation of aniline, each reaction would produce 1.86 mg product. Accordingly, if all leached Ni remained in the product during any purification steps, a Ni contamination of 0.04 ppm would correspond to a contamination of 43 μg/g of aniline. While this value is above the USP limit for drug products, it is encouraging to see that it remains within the same order of magnitude and relies on several assumptions – indeed, any isolation step removing aniline from the aqueous reaction mixture is likely to also decrease contamination from ionic Ni species. Still, the observation that there is significant Ni

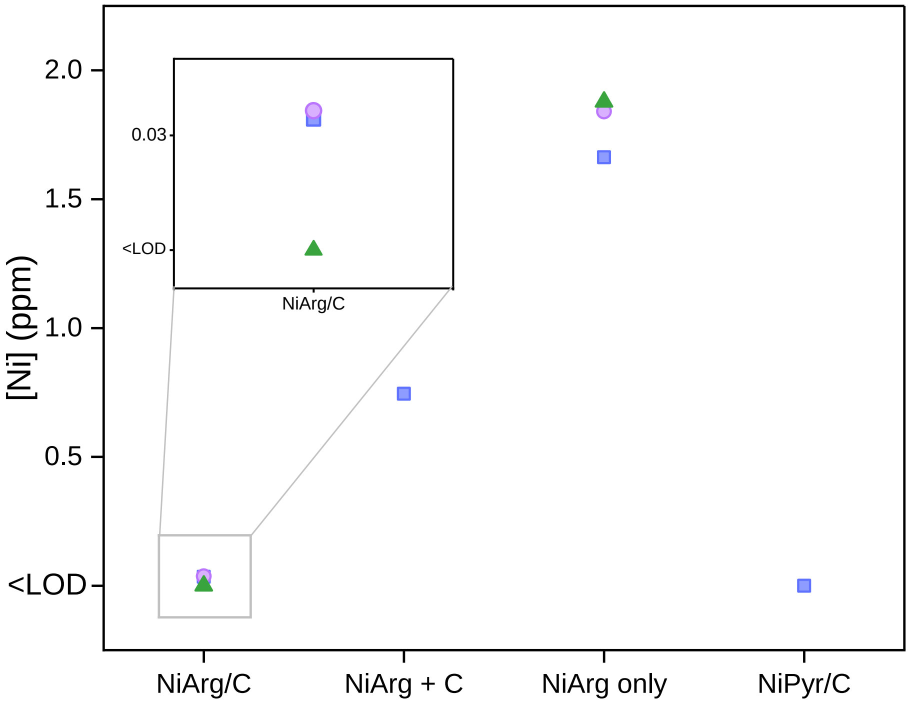

Figure 56 Ni concentration detected in reaction mixtures after hydrogenation using either NiArg/C, NiArg and C added separately to the reaction mixture, NiArg only, or NiPyr/C. Conditions: 10 mM starting material, 0.5% Ni complex loading, 40:1 carbon to complex ratio by weight where appropriate, room temperature, H_2 gas flow 30 mL/min, PB pH 6.0, 24 h reaction time. Solids were removed by centrifugation and subsequent filtration before samples were provided to the University of Sheffield for ICP/OES analysis.

contamination indicates that future trials using covalent bonds between the complex and the carbon surface, for example through pyrene-based anchors as reported in literature,[4] may be appropriate.

For sample NiArg + C, in which the appropriate amount of carbon black and NiArg were added separately directly to the reaction mixture, a Ni concentration in the reaction mixture of 0.75 ppm was detected (after the solid carbon was removed by centrifugation and filtration), which is well below that seen for the carbon-free experiments (see Figure 56) but significantly higher than that seen for the NiArg/C samples in which the complex was allowed to adsorb to the carbon for one hour and catalyst particles were washed by centrifugation. The NiArg + C catalyst system led to the production of the hydroxylamine after 24 h, with only minor amounts of nitrobenzene and aniline observed in the corresponding ^{1}H NMR spectrum, while the NiArg/C catalyst led to clean production of aniline. These results underline the importance of the adsorption step both for sufficient chemical contact between the complex and the carbon for the system to efficiently hydrogenate nitrobenzene and for the prevention of excessive Ni contamination.

5.4.3 In-situ preparation of the catalyst on carbon without isolation of the complex

Greater ease of catalyst preparation can make a system more attractive to possible industrial application. The original synthesis of the DuBois-type $[Ni(P^R{}_2P_2{}^R)_2]^{2+}$ complexes, reported by DuBois and coworkers,[5] relies on a moisture sensitive hexakisacetonitrilenickel(II) precursor,

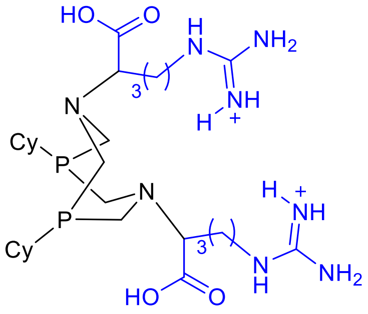

Figure 57 Structure of $P^{Cy}{}_2P_2{}^{Arg}$ ligand.

which is synthesized from metallic Ni through oxidation by nitrosonium cations in acetonitrile – a procedure that is not trivial in its execution. Jane *et al* found that the synthesis can be simplified by starting with a hydrated Ni complex in acetonitrile and treating this mixture with two equivalents of the relevant diphosphine ligand.[13] Drawing inspiration from this approach and to reduce the steps needed for the catalyst synthesis, the carbon black material was treated with the isolated ligand ($P^{Cy}_2P_2^{Arg}$, Figure 57), then resuspended in acetonitrile along with $[Ni(H_2O)_6](BF_4)_2$ and stirred overnight. The resulting modified carbon particles were washed and resuspended in water, and then used as the catalyst system in the hydrogenation of nitrobenzene (**1A**), leading to full conversion to the amine **1C** within 24h (Figure 58). This procedure negates the need to isolate and purify the final NiArg complex and starts from a relatively affordable and accessible $[Ni(H_2O)_6](BF_4)_2$ precursor.

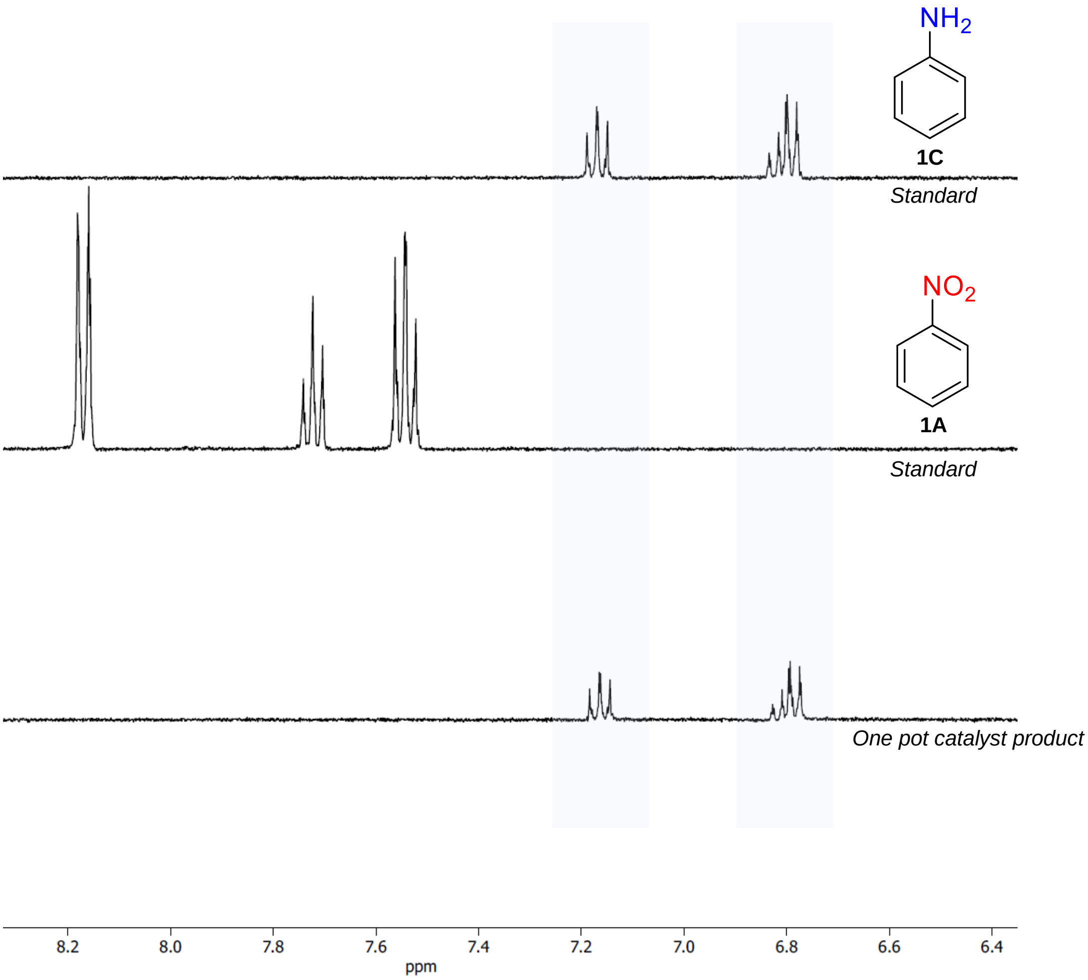

Figure 58 ^{1}H NMR (400 MHz, 298 K, 10% D2O in PB, 100 mM, pH 6.0) spectra of aniline standard (top), nitrobenzene standard (middle), and the reaction mixture of the hydrogenation of nitrobenzene performed using the catalyst prepared 'in situ' using Ni salt and the carbon black modified with the appropriate ligand. Conditions: 10 mM starting material, 0.5% Ni complex loading, room temperature, H_2 gas flow 30 mL/min, PB pH 6.0, 24 h reaction time.

5.5 Conclusions and outlook

A novel application for a Ni bisdiphosphine complex that is usually studied for its excellent catalysis of H_2 production and oxidation was established by employing it as a catalyst for the hydrogenation of nitrocompounds at atmospheric pressures of H_2 and room temperature. A complex of this family decorated with arginine ligands, **NiArg**, produced pure hydroxylamines from many substituted nitroarenes when used as a homogeneous complex, while it produced pure amines when employed as a heterogeneous system on a commercial carbon black support. The selectivity of these systems was demonstrated by trialling the hydrogenation of nitroarenes containing a variety of unsaturated bonds or halogens. Only minor Ni leaching was observed for the heterogeneous **NiArg/C** system; nonetheless, future work could explore the use of a pyrene linker, for example, to further prevent Ni contamination of the product. The **NiArg/C** system can produce aliphatic amines from aliphatic nitro-compounds. This reaction is faster when the complex is immobilised onto NCNTs produced in house, whose electrocatalytic activity was discussed in previous chapters. In comparison to the biocatalytic system **Hyd/C**, the possible scaling of the system presented in this chapter should be more readily achievable because the techniques needed to synthesize the complexes are well-established in chemical industry, while hydrogenase enzymes are currently produced at small scale only. Future work should focus on trialling reaction conditions that would further set apart **NiArg/C** from the biocatalytic **Hyd/C** by employing organic solvents or higher temperatures, or pressures.

5.6 References

(1) Sokolova, D.; Lurshay, T. C.; Rowbotham, J. S.; Stonadge, G.; Reeve, H. A.; Cleary, S. E.; Sudmeier, T.; Vincent, K. A. Selective hydrogenation of nitro compounds to amines by coupled redox reactions over a heterogeneous biocatalyst. *Nature Communications* **2024**, *15* (1), 7297. DOI: 10.1038/s41467-024-51531-2.

(2) Dutta, A.; DuBois, D. L.; Roberts, J. A.; Shaw, W. J. Amino acid modified Ni catalyst exhibits reversible H2 oxidation/production over a broad pH range at elevated temperatures. *Proc Natl Acad Sci U S A* **2014**, *111* (46), 16286-16291. DOI: 10.1073/pnas.1416381111.

(3) Helm, M. L.; Stewart, M. P.; Bullock, R. M.; DuBois, M. R.; DuBois, D. L. A Synthetic Nickel Electrocatalyst with a Turnover Frequency Above 100,000 s−1 for H2 Production. *Science* **2011**, *333* (6044), 863-866. DOI: 10.1126/science.1205864.

(4) Reuillard, B.; Blanco, M.; Calvillo, L.; Coutard, N.; Ghedjatti, A.; Chenevier, P.; Agnoli, S.; Otyepka, M.; Granozzi, G.; Artero, V. Noncovalent Integration of a Bioinspired Ni Catalyst to Graphene Acid for Reversible Electrocatalytic Hydrogen Oxidation. *ACS Appl Mater Interfaces* **2020**, *12* (5), 5805-5811. DOI: 10.1021/acsami.9b18922.

(5) Wilson, A. D.; Newell, R. H.; McNevin, M. J.; Muckerman, J. T.; Rakowski DuBois, M.; DuBois, D. L. Hydrogen Oxidation and Production Using Nickel-Based Molecular Catalysts with Positioned Proton Relays. *Journal of the American Chemical Society* **2006**, *128* (1), 358-366. DOI: 10.1021/ja056442y.

(6) Dutta, A.; Roberts, J. A. S.; Shaw, W. J. Arginine-Containing Ligands Enhance H_2 Oxidation Catalyst Performance. *Angewandte Chemie International Edition* **2014**, *53* (25), 6487-6491. DOI: https://doi.org/10.1002/anie.201402304.

(7) Reuillard, B.; Costentin, C.; Artero, V. Deciphering Reversible Homogeneous Catalysis of the Electrochemical H2 Evolution and Oxidation: Role of Proton Relays and Local Concentration Effects. *Angewandte Chemie International Edition* **2023**, *62* (36), e202302779. DOI: https://doi.org/10.1002/anie.202302779.

(8) Orlandi, M.; Brenna, D.; Harms, R.; Jost, S.; Benaglia, M. Recent Developments in the Reduction of Aromatic and Aliphatic Nitro Compounds to Amines. *Org. Process Res. Dev.* **2016**, *22* (4), 430-445. DOI: 10.1021/acs.oprd.6b00205.

(9) Agmon, N.; Goldberg, S. Y.; Huppert, D. Salt effect on transient proton transfer to solvent and microscopic proton mobility. *Journal of Molecular Liquids* **1995**, *64* (1), 161-195. DOI: https://doi.org/10.1016/0167-7322(95)92828-Y.

(10) Shaw, W. J.; Helm, M. L.; DuBois, D. L. A modular, energy-based approach to the development of nickel containing molecular electrocatalysts for hydrogen production and oxidation. *Biochimica et Biophysica Acta (BBA) - Bioenergetics* **2013**, *1827* (8), 1123-1139. DOI: https://doi.org/10.1016/j.bbabio.2013.01.003.

(11) Tran, P. D.; Le Goff, A.; Heidkamp, J.; Jousselme, B.; Guillet, N.; Palacin, S.; Dau, H.; Fontecave, M.; Artero, V. Noncovalent Modification of Carbon Nanotubes with Pyrene-Functionalized Nickel Complexes: Carbon Monoxide Tolerant Catalysts for Hydrogen Evolution and Uptake. *Angewandte Chemie International Edition* **2011**, *50* (6), 1371-1374. DOI: https://doi.org/10.1002/anie.201005427.

(12) Elemental Impurities—limits. In *United States Pharmacop. Natl. Formul.*, United States Pharmacopeia Convention, 2012.

(13) Jane, R. T.; Tran, P. D.; Andreiadis, E. S.; Pécaut, J.; Artero, V. A simple method for the preparation of bio-inspired nickel bisdiphosphine hydrogen-evolving catalysts. *Comptes Rendus Chimie* **2015**, *18* (7), 752-757. DOI: https://doi.org/10.1016/j.crci.2015.03.005.

6 Conclusions and Outlook

The aim of this thesis was to further explore a biocatalytic, cofactor-free catalyst system established by the Vincent group for the hydrogenation of nitrocompounds which combines hydrogenase enzyme and a conductive carbon particle. The nitro-group can be reduced electrochemically on the carbon surface towards the corresponding amines using electrons provided by the dihydrogen oxidation catalysed by the hydrogenase.[1] In the first part of this thesis, the conductive carbon was replaced by NCNTs to tune the nitro-reduction potential; while in the second part of the thesis the hydrogenase enzyme was replaced by an inorganic complex to establish a non-bio version of the catalyst system.

A library of CNTs of various N-doping levels was synthesized using chemical vapour deposition. The materials were shown by XPS to contain between 0 and 3 atomic percent surface N and were further subjected to a wide range of characterisation techniques discussed in Chapter 3. These (N)CNTs were used as the electrode surface in an electrochemical study of the reduction of 4-nitrophenol and nitrohexane. Employing the doped materials instead of the pristine CNTs led to a significant shift of around 100 mV of the cathodic feature towards milder potentials – an effect that was reproducible across batches of NCNTs.

The electrocatalysis observed by cyclic voltammetry in Chapter 3 was then used in Chapter 4 to electro-synthesize 4-aminophenol from 4-nitrophenol over a carbon felt electrode modified with the CNTs produced in-house. The modification of the carbon felt using NCNTs allowed the electrosynthesis to be efficiently performed at milder potential. The same procedure was used to produce hexylamine from nitrohexane. The carbon felt modified with NCNTs led to the formation of hexylamine at a potential at which the carbon felt modified with CNTs did not.

Interestingly, this potential shift of the onset potential on the doped material allowed the nitrohexane reduction to occur at a potential more positive than that needed to oxidize dihydrogen using hydrogenase-1 (Hyd-1), an oxygen-tolerant enzyme produced by *E. coli* commonly used for biocatalytic approaches in the Vincent group. Accordingly, Hyd-1 combined with the NCNTs was shown to act as a hydrogenation catalyst system under atmospheric H_2 pressures and at room temperature for the hydrogenation of nitrohexane. This reaction had not occurred when using Hyd-1 immobilised on commercial carbon black, upon which the nitrohexane reduction occurs at a significantly more negative potential. Thus, the NCNTs produced in house were successfully used to tune the hydrogenation system established by the Vincent group in Sokolova *et al.* [1]

Nonetheless, several open questions remain. The active site of the electrocatalysis has not been elucidated. More detailed characterisation, for example by Electron Energy Loss Spectroscopy, could shed light on the dispersion of iron contaminant on the NCNT surface. [2] Future experiments could attempt to pacify any available iron sites, for example using carbon monoxide, before recording cyclic voltammograms of the nitro-reduction. [3] In addition, the NCNT production as performed in this project comes with a high energy cost, low percentual yield, and relies on fossil precursors.[4] It could be beneficial to explore conductive carbon supports from renewable and less energy-intensive sources.

In the final part of this thesis, a Ni-based complex typically studied in literature for its excellent H_2 oxidation and production activity, $[Ni(P^{Cy}{}_2N^{Arg}{}_2)_2]^{2+}$ (NiArg), was used to replace the enzyme in the catalyst system described above. The resulting NiArg/C catalyst was shown to hydrogenate nitroarenes at room temperature, atmospheric pressure, and in aqueous solution, in line with the environmentally friendly conditions used in Sokolova *et al.* for the biocatalytic hydrogenation system. [1] Many sensitive compounds (such as the nitrostyrene and a set of halogenated nitrobenzenes) were successfully converted to the corresponding amine, indicating that the sensitivity of the catalyst system was not lost upon replacement of the hydrogenase enzyme. In the course of control experiments employing the complex in solution, it was found that the complex leads to the formation of the partially reduced hydroxylamine for the great majority of the substrate scope.

The NiArg/C catalyst system was found to be recyclable and led to only minimal Ni contamination of the reaction mixture after removal of the heterogeneous catalyst particles by centrifugation and filtration. In addition, the in-situ formation of the catalyst from a nickel hexahydrate salt and carbon black particles modified with the appropriate $P^{Cy}{}_2N^{Arg}{}_2$ ligand led to active catalyst that showed full conversion of nitrobenzene to the aniline within 24 h, greatly simplifying catalyst preparation for possible industrial use.

The chapter on the NiArg(/C) nitro-hydrogenation catalyst system presented herein opens up many exciting avenues for future work. First and foremost, the compatibility of the catalyst system with organic solvents should be investigated. This could lead to the more efficient conversion of hydrophobic substrates and could allow the use of higher substrate concentrations. Because of the time constraints inherent to a doctoral project, only two ligand scaffolds were trialled here – the $P^{Cy}{}_2N^{Arg}{}_2$ and a pyrene decorated $P^{Cy}{}_2N^{Pyr}{}_2$ alternative. It could be interesting, for example, to investigate a covalent linker towards the carbon surface to stabilise the system. For the homogeneous use of the complex in solution, which led to the formation of the partially reduced hydroxylamine, it could be worthwhile to heterogenize the complex by anchoring it onto a non-conductive matrix that would not participate in the reduction. This would simplify the purification of any synthesized product.

6.1 References

(1) Sokolova, D.; Lurshay, T. C.; Rowbotham, J. S.; Stonadge, G.; Reeve, H. A.; Cleary, S. E.; Sudmeier, T.; Vincent, K. A. Selective hydrogenation of nitro compounds to amines by coupled redox reactions over a heterogeneous biocatalyst. *Nature Communications* **2024**, *15* (1), 7297. DOI: 10.1038/s41467-024-51531-2.

(2) Leapman, R. D. Detecting single atoms of calcium and iron in biological structures by electron energy-loss spectrum-imaging. *Journal of Microscopy* **2003**, *210* (1), 5-15. DOI: https://doi.org/10.1046/j.1365-2818.2003.01173.x.

(3) von Deak, D.; Singh, D.; King, J. C.; Ozkan, U. S. Use of carbon monoxide and cyanide to probe the active sites on nitrogen-doped carbon catalysts for oxygen reduction. *Applied Catalysis B: Environmental* **2012**, *113-114*, 126-133. DOI: https://doi.org/10.1016/j.apcatb.2011.11.029.

(4) Upadhyayula, V. K. K.; Meyer, D. E.; Curran, M. A.; Gonzalez, M. A. Life cycle assessment as a tool to enhance the environmental performance of carbon nanotube products: a review. *Journal of Cleaner Production* **2012**, *26*, 37-47. DOI: https://doi.org/10.1016/j.jclepro.2011.12.018.

7 Supporting Data

7.1 Conversion of 4-nitrophenol after chronoamperometry

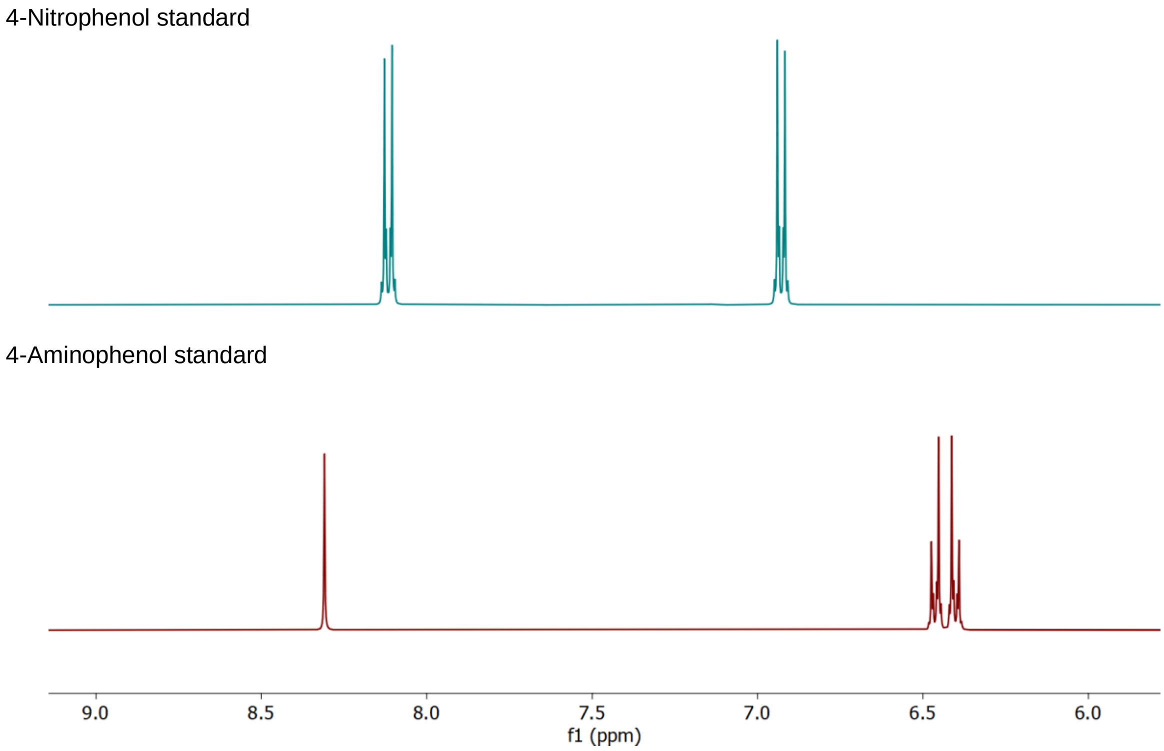

Figure 59: ^{1}*H NMR spectra of starting material and product standard in DMSO-d6.*

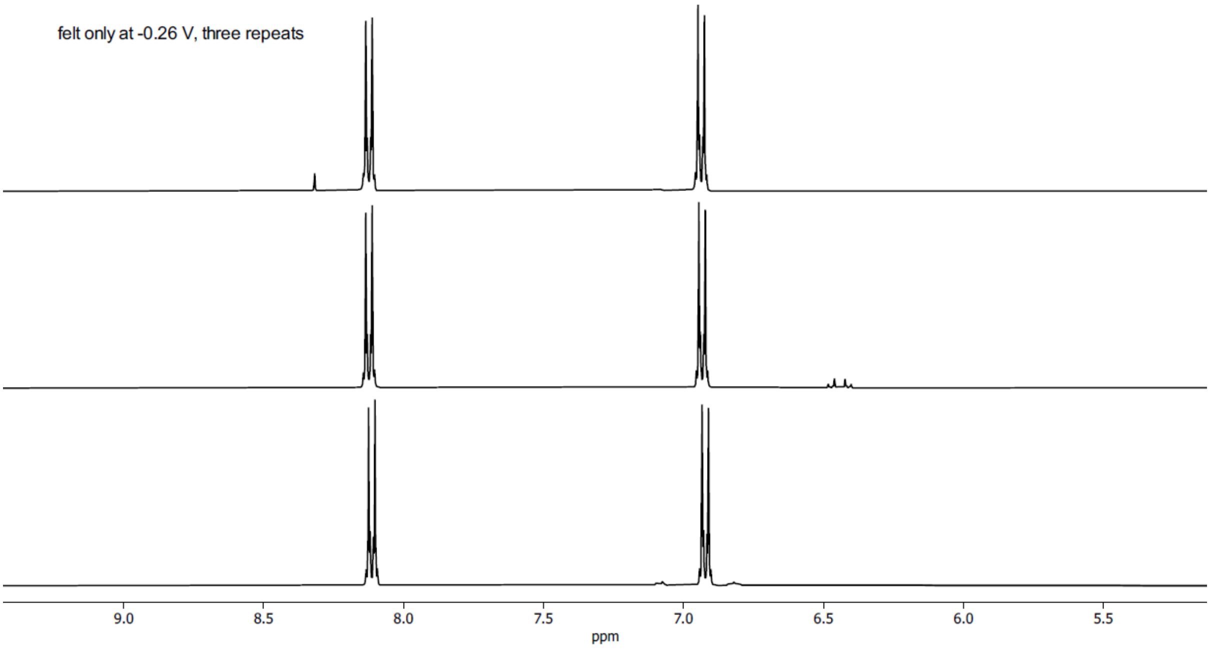

Figure 60 ^{1}H NMR spectra of organic phase extracted and resolubilised in DMSO-d6 after chronoamperometry, performed on CF only electrode at -0.26 V vs SHE, 5 mM 4-nitrophenol in PB (pH 6.0, 100 mM), 24 h, RT, three repeats shown.

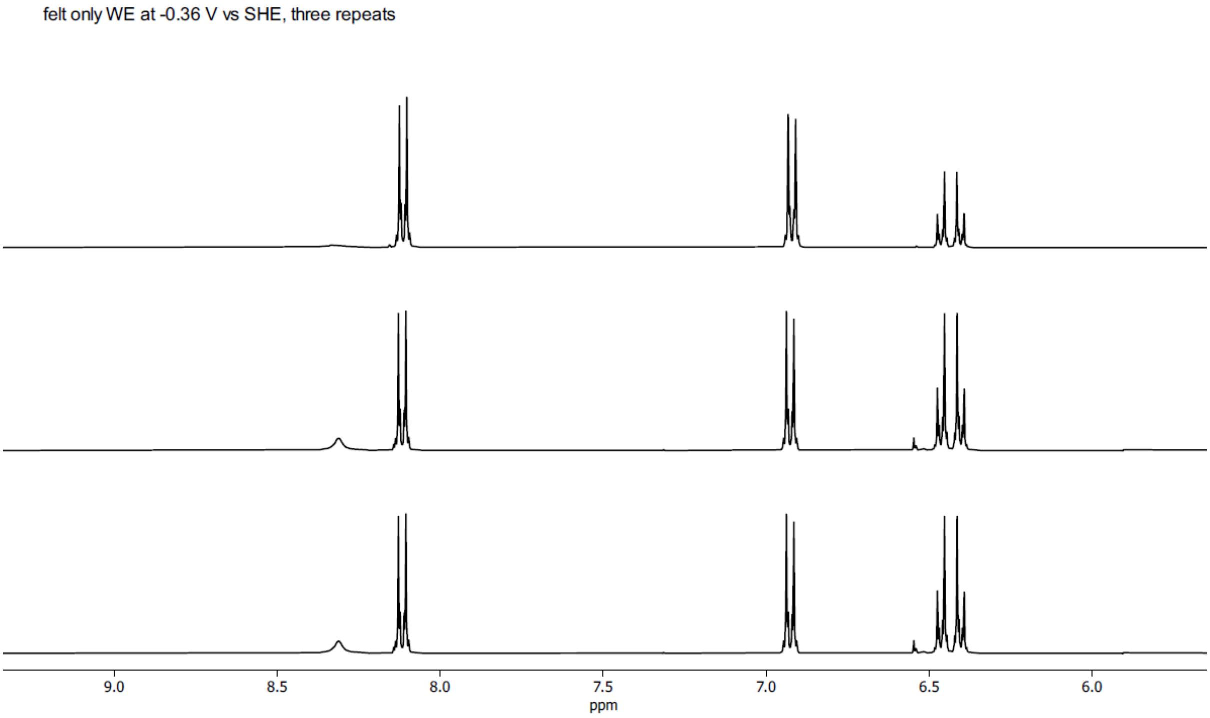

Figure 61 ^{1}H NMR spectra of organic phase extracted and resolubilised in DMSO-d6 after chronoamperometry, performed on CF only electrode at -0.36 V vs SHE, 5 mM 4-nitrophenol in PB (pH 6.0, 100 mM), 24 h, RT, three repeats shown.

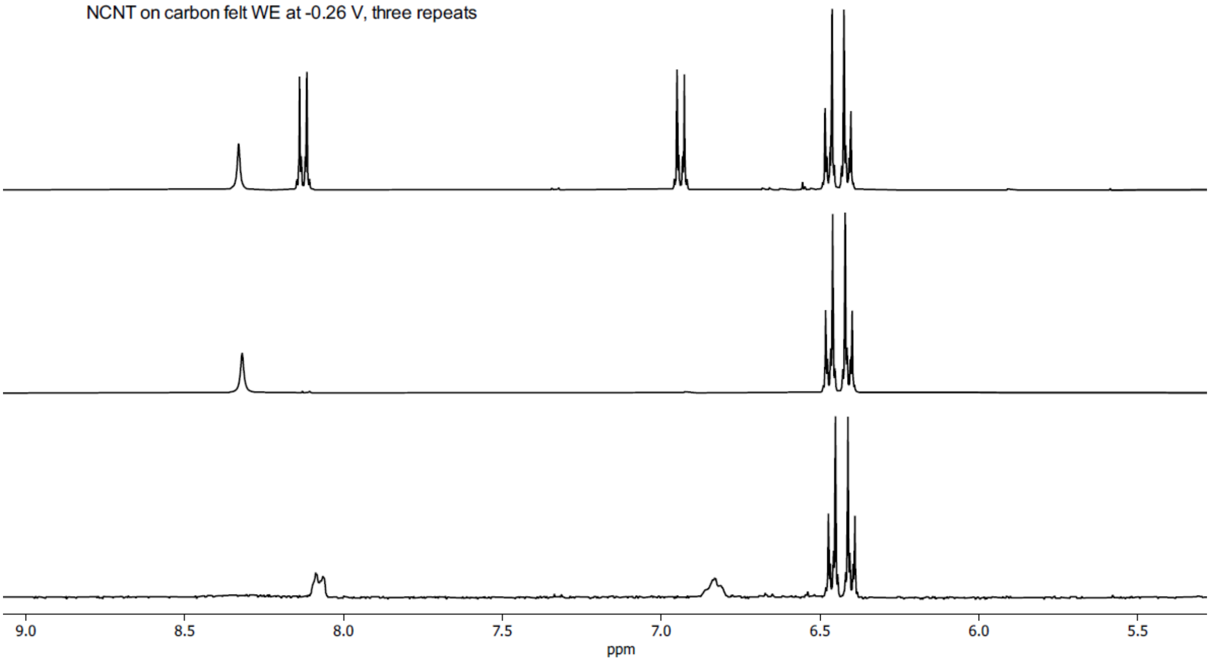

Figure 62 ^{1}H NMR spectra of organic phase extracted and resolubilised in DMSO-d6 after chronoamperometry, performed on NCNT/CF electrode at -0.26 V vs SHE, 5 mM 4-nitrophenol in PB (pH 6.0, 100 mM), 24 h, RT, three repeats shown.

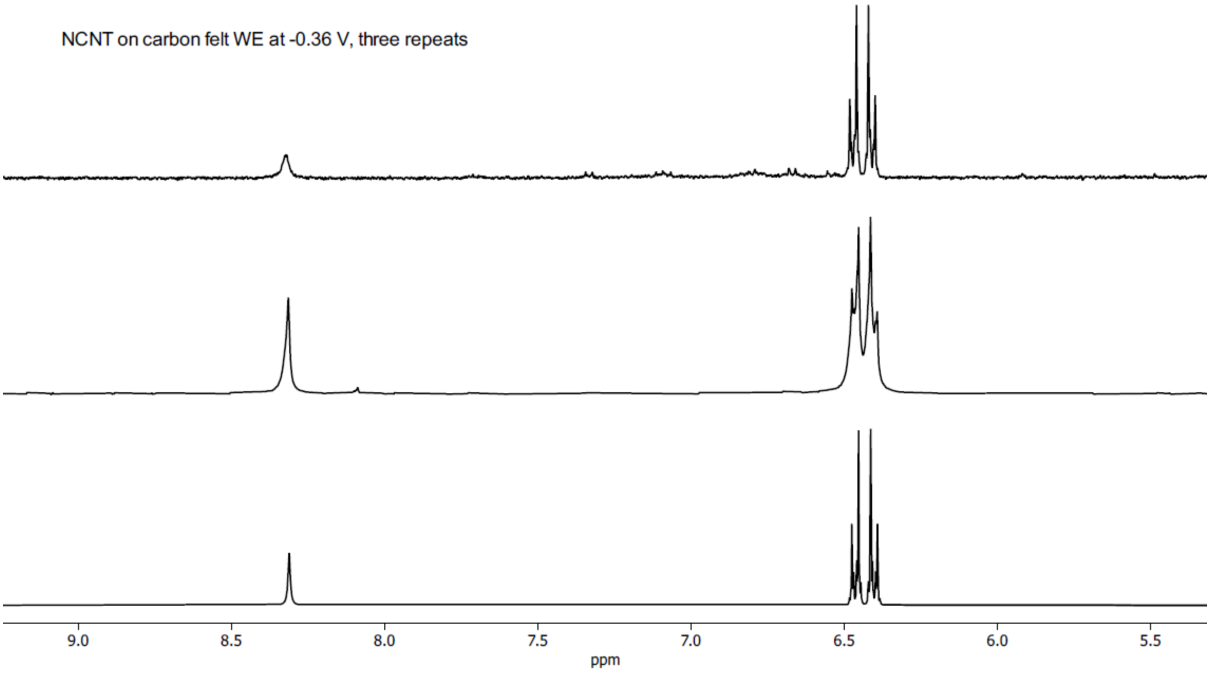

Figure 63 ^{1}H NMR spectra of organic phase extracted and resolubilised in DMSO-d6 after chronoamperometry, performed on NCNT/CF electrode at -0.36 V vs SHE, 5 mM 4-nitrophenol in PB (pH 6.0, 100 mM), 24 h, RT, three repeats shown.

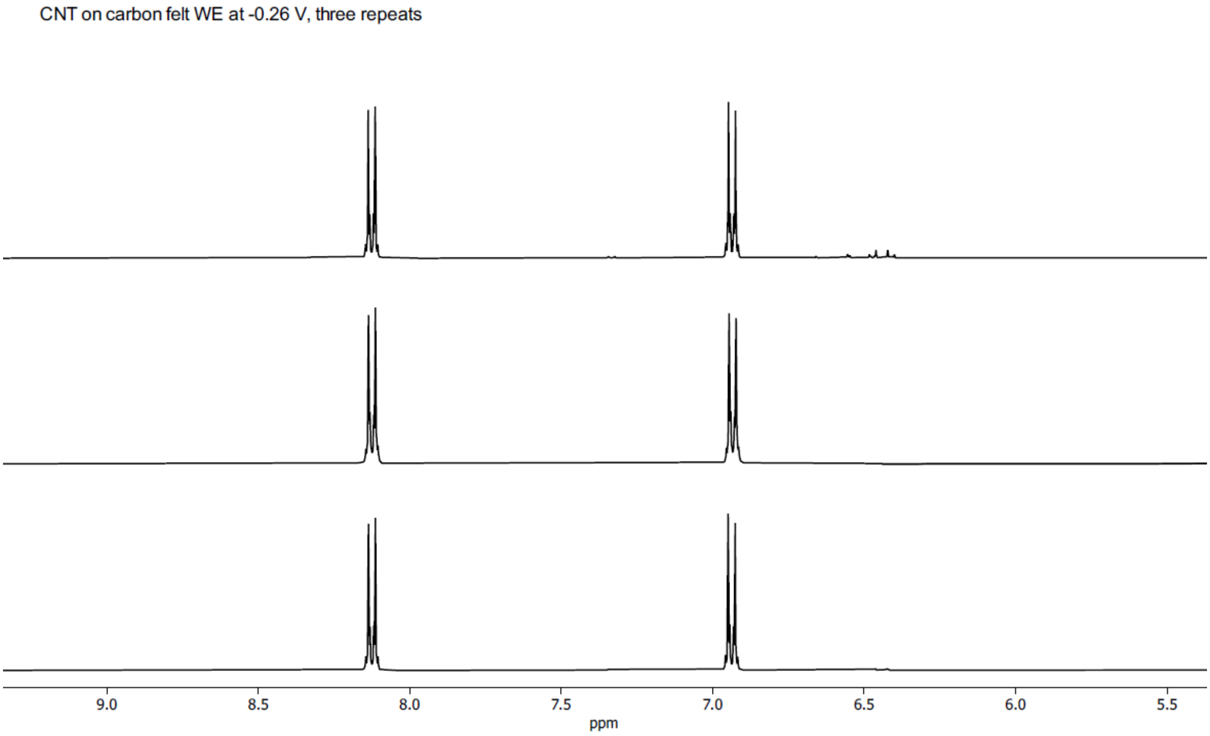

Figure 64 ^{1}H NMR spectra of organic phase extracted and resolubilised in DMSO-d6 after chronoamperometry, performed on CNT/CF electrode at -0.26 V vs SHE, 5 mM 4-nitrophenol in PB (pH 6.0, 100 mM), 24 h, RT, three repeats shown.

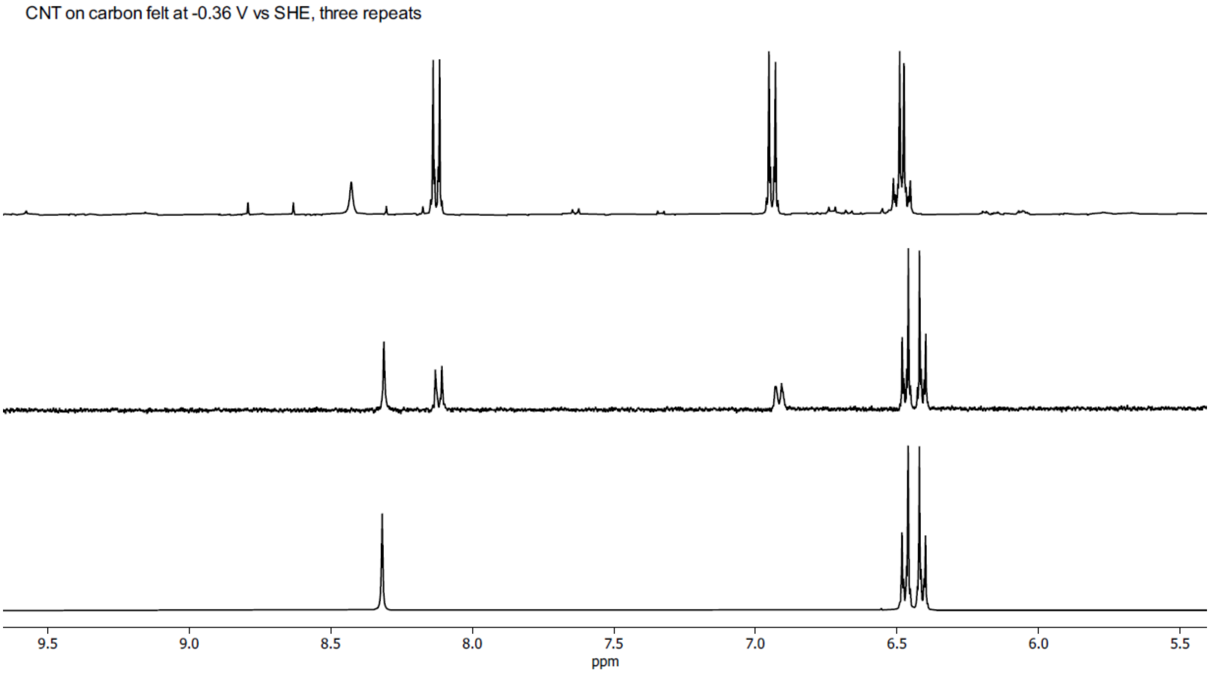

Figure 65 ^{1}H NMR spectra of organic phase extracted and resolubilised in DMSO-d6 after chronoamperometry, performed on CNT/CF electrode at -0.36 V vs SHE, 5 mM 4-nitrophenol in PB (pH 6.0, 100 mM), 24 h, RT, three repeats shown. Top spectrum contains unidentified impurities.

7.2 Conversion of n-nitrohexane after chronoamperometry

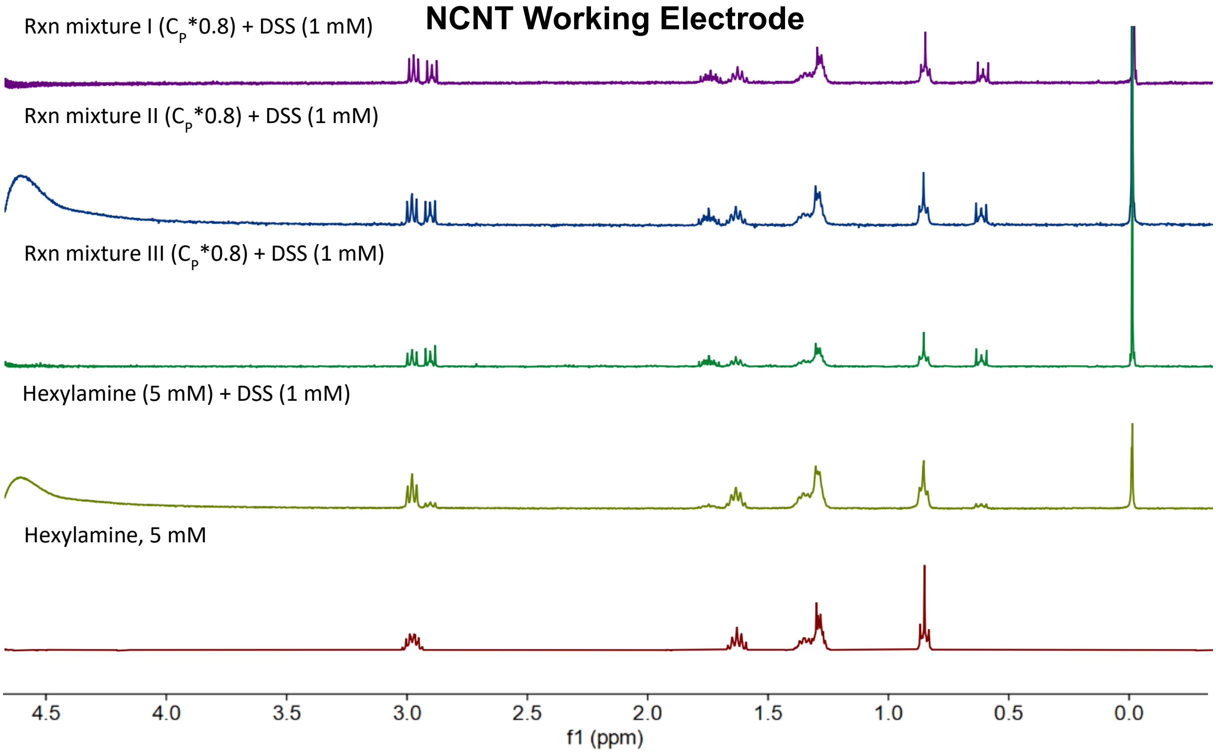

Figure 66 ^{1}H NMR spectra of reaction mixture after chronoamperometry, performed on NCNT/CF electrode at -0.36 V vs SHE, 5 mM n-nitrohexane in PB (pH 6.0, 100 mM), 24 h, RT, three repeats shown, samples contain 1 mM DSS internal standard. C_P – concentration of product.

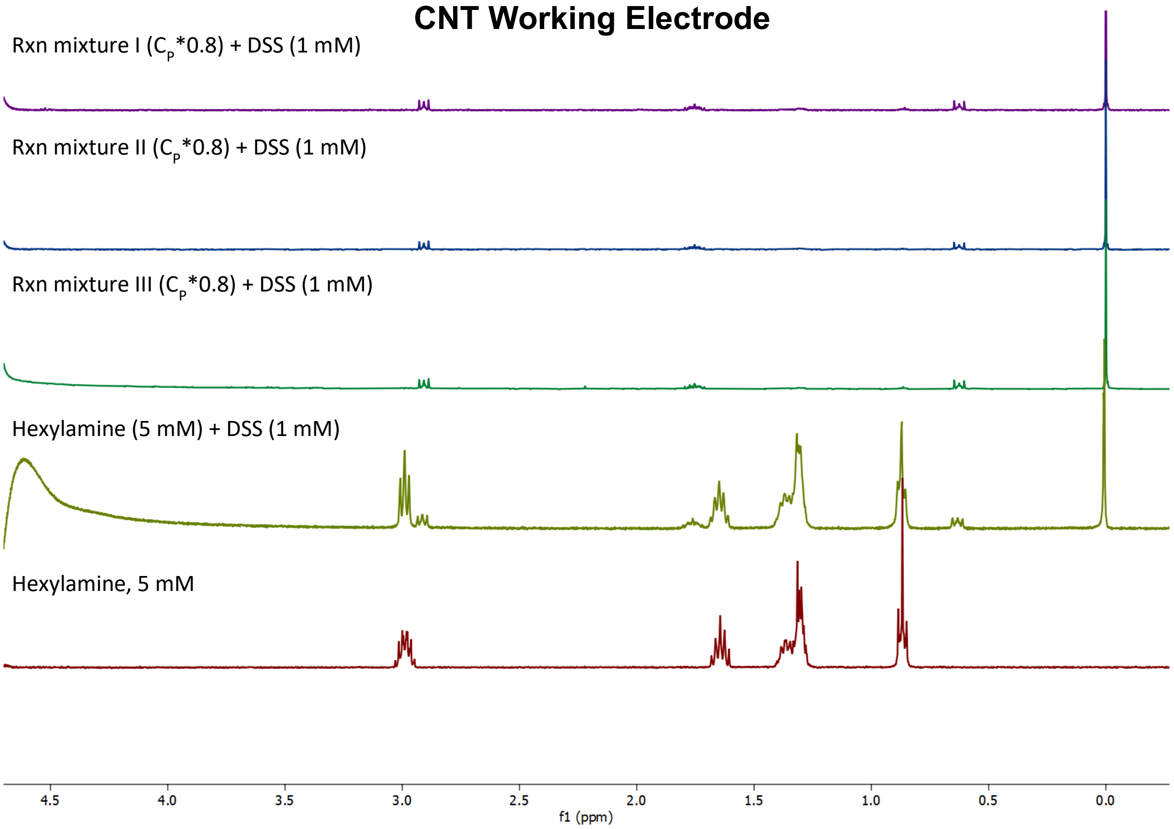

Figure 67 ^{1}*H NMR spectra of reaction mixture after chronoamperometry, performed on CNT/CF electrode at -0.36 V vs SHE, 5 mM n-nitrohexane in PB (pH 6.0, 100 mM), 24 h, RT, three repeats shown, samples contain 1 mM DSS internal standard.* C_P *– concentration of product.*

7.3 Conversion of aliphatic nitro-compounds using Hyd1/NCNT$_{ACS}$

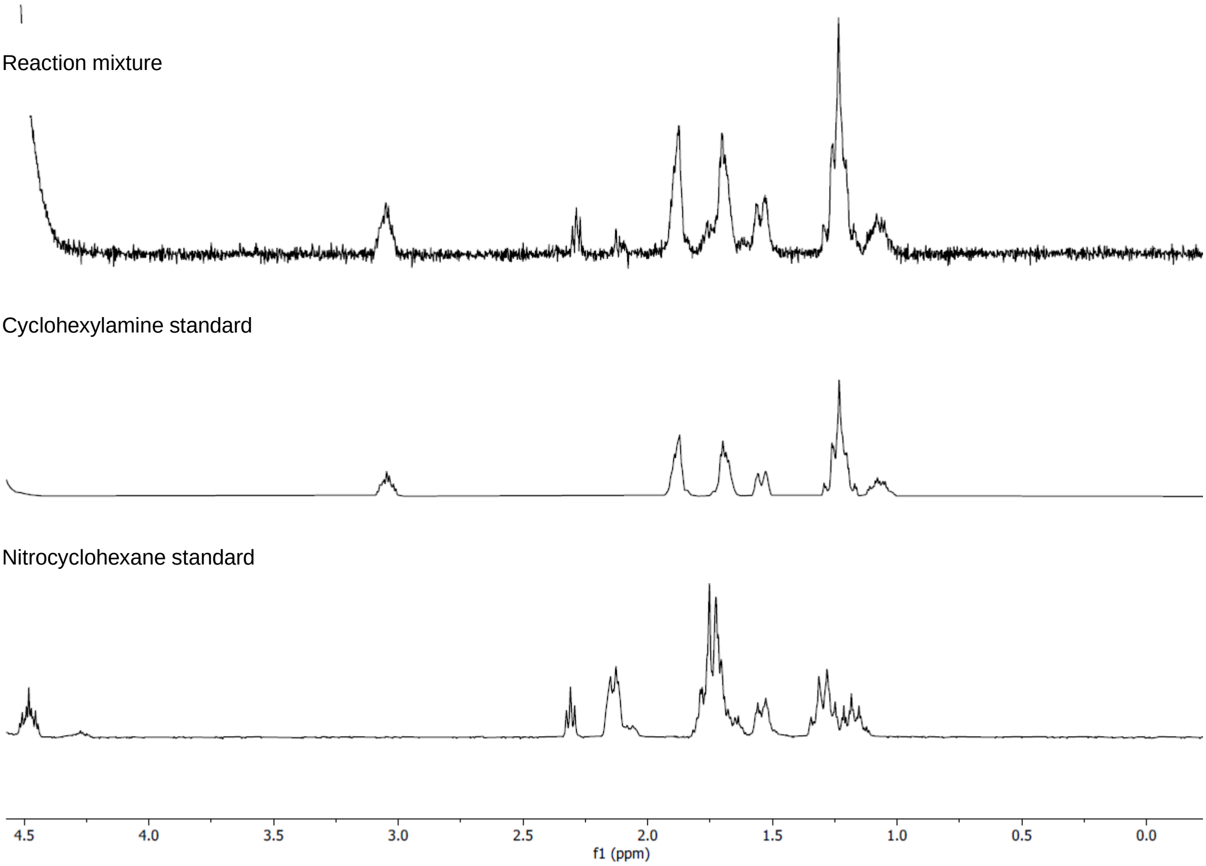

Figure 68 ^{1}*H NMR spectra of reaction mixture of hydrogenation of nitrocyclohexane using Hyd1/NCNT*$_{ACS}$ *catalyst system, 24 h, RT, 30 mL/min* H_2 *flow, 10 mM nitrocyclohexane.* ^{1}*H NMR spectra of starting material and product standards.*

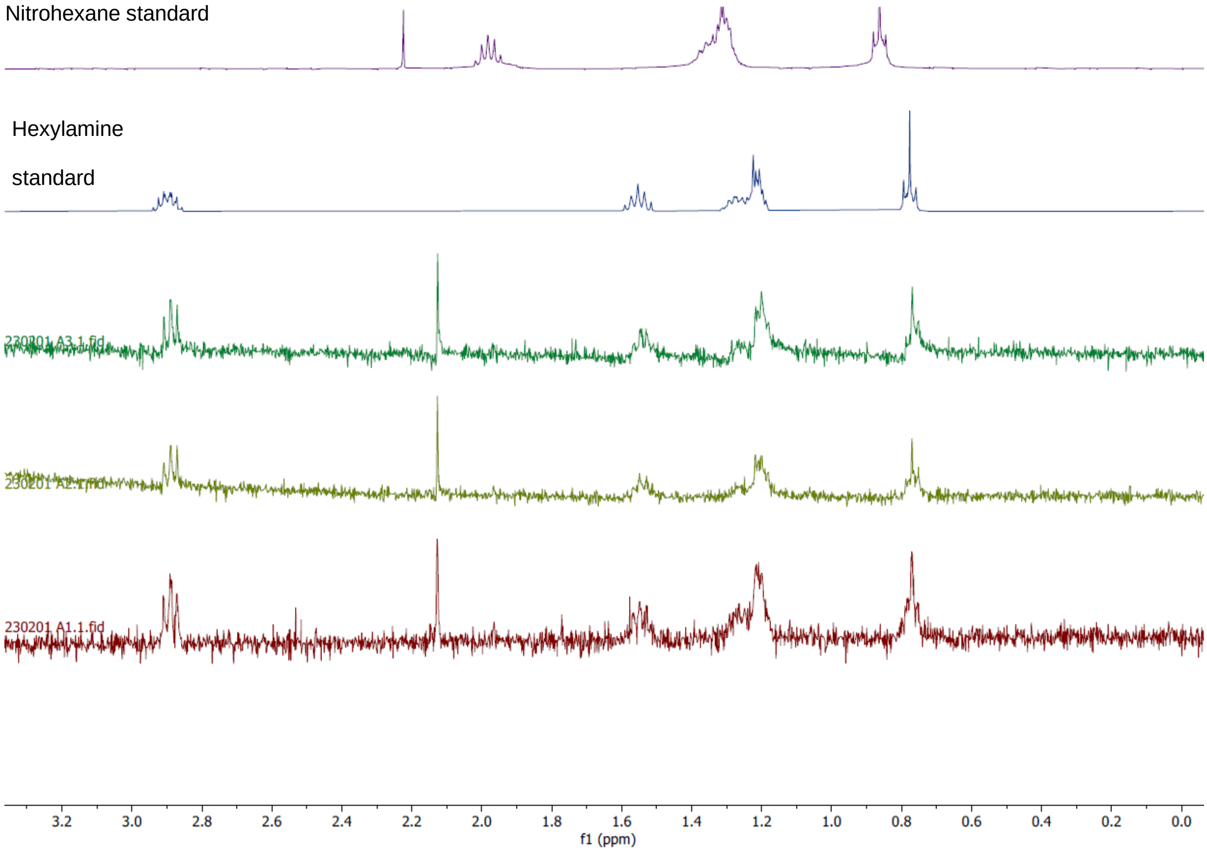

Figure 69 ^{1}H NMR spectra of reaction mixtures of hydrogenation of nitrohexane using Hyd1/NCNT$_{ACS}$ catalyst system, 24 h, RT, 30 mL/min H_2 flow, 10 mM nitrohexane. ^{1}H NMR spectra of starting material and product standards (top)

7.4 Conversion of nitro-compounds using NiArg/C

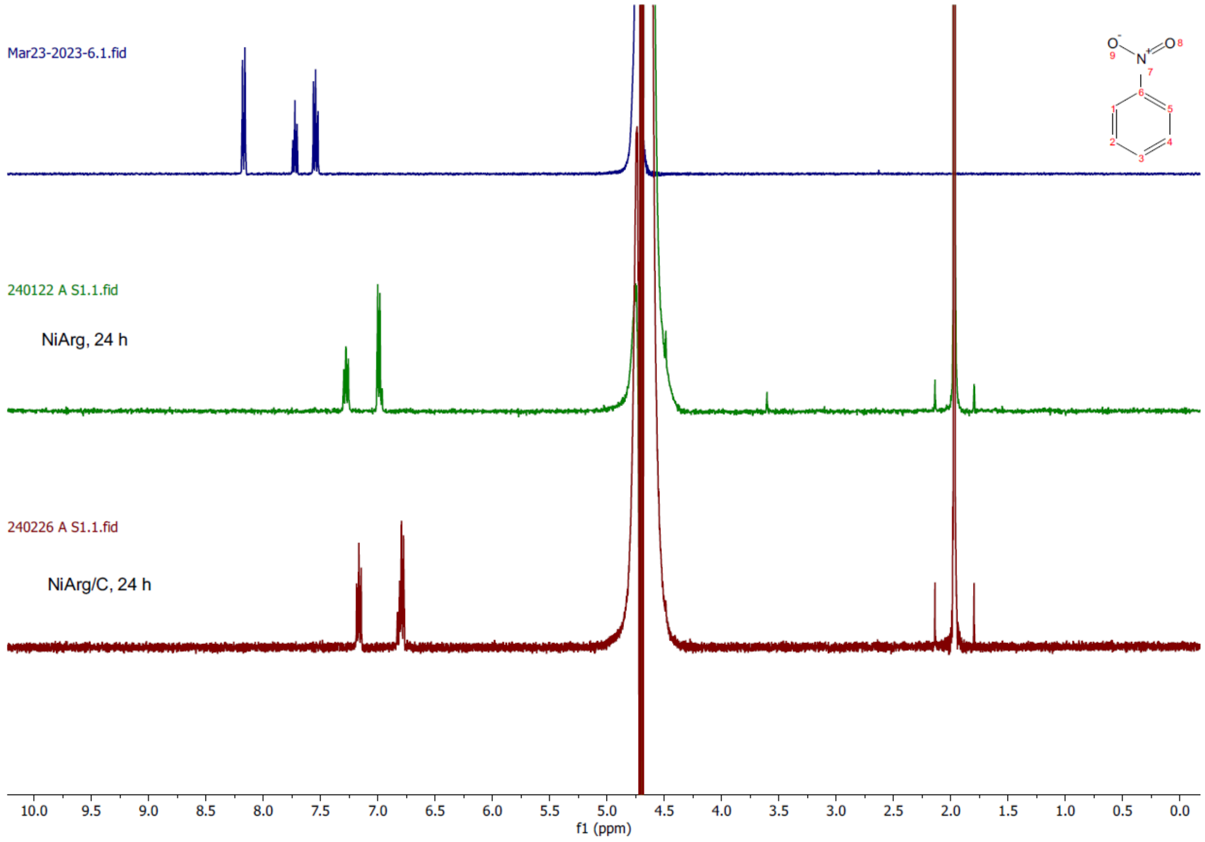

Figure 70 1H-NMR spectra (400 MHz, 298 K, 10% D2O in PB, 100 mM, pH 6.0, 10 % v/v acetonitrile) of substrate 1 and reaction mixture after hydrogenation using NiArg only (middle), and product after hydrogenation using NiArg/C catalyst system.

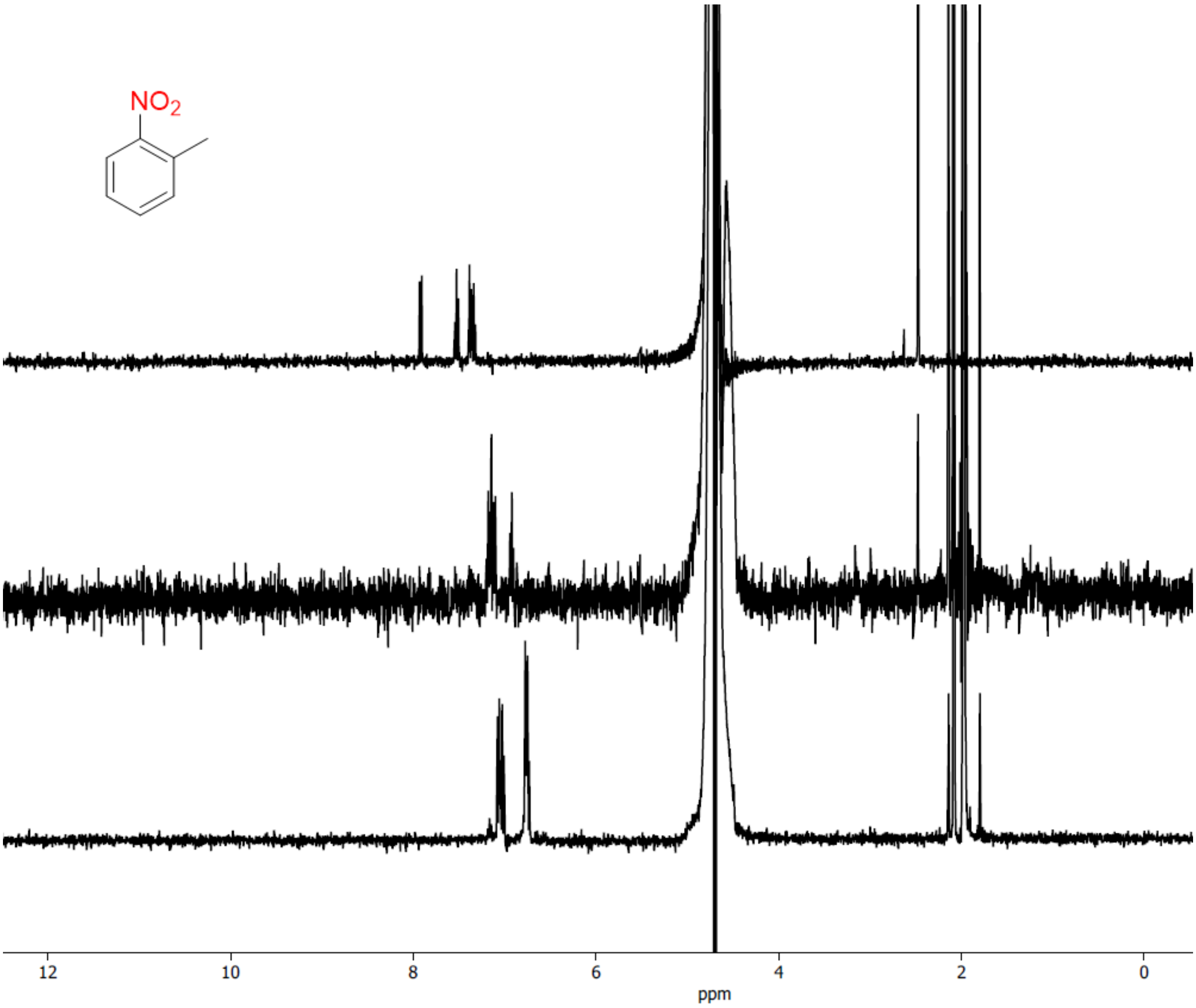

Figure 71 1H-NMR spectra (400 MHz, 298 K, 10% D2O in PB, 100 mM, pH 6.0, 10 % v/v acetonitrile) of substrate 2 and reaction mixture after hydrogenation using NiArg only (middle), and product after hydrogenation using NiArg/C catalyst system.

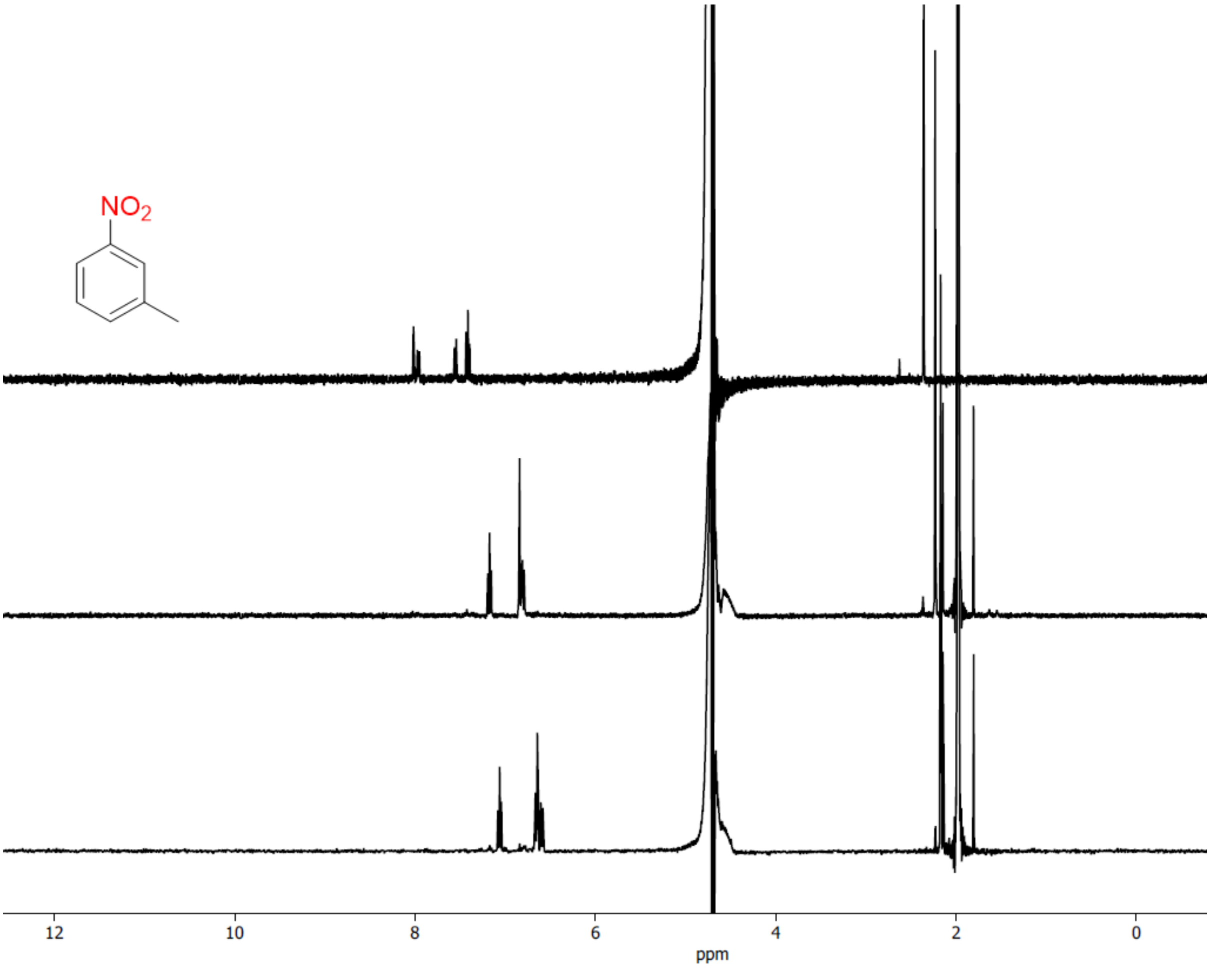

Figure 72 1H-NMR spectra (400 MHz, 298 K, 10% D2O in PB, 100 mM, pH 6.0, 10 % v/v acetonitrile) of substrate 3 and reaction mixture after hydrogenation using NiArg only (middle), and product after hydrogenation using NiArg/C catalyst system.

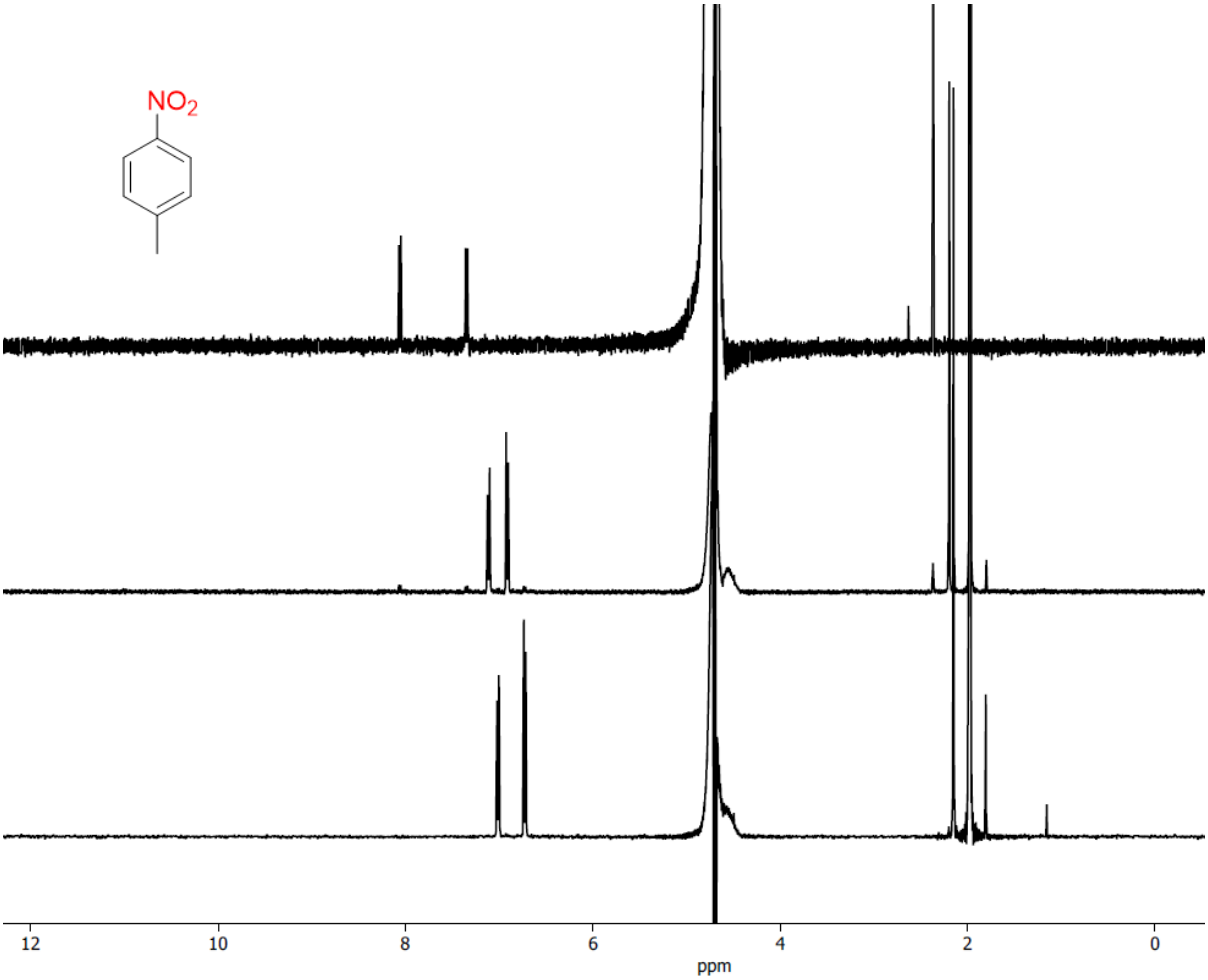

Figure 73 1H-NMR spectra (400 MHz, 298 K, 10% D2O in PB, 100 mM, pH 6.0, 10 % v/v acetonitrile) of substrate 4 and reaction mixture after hydrogenation using NiArg only (middle), and product after hydrogenation using NiArg/C catalyst system.

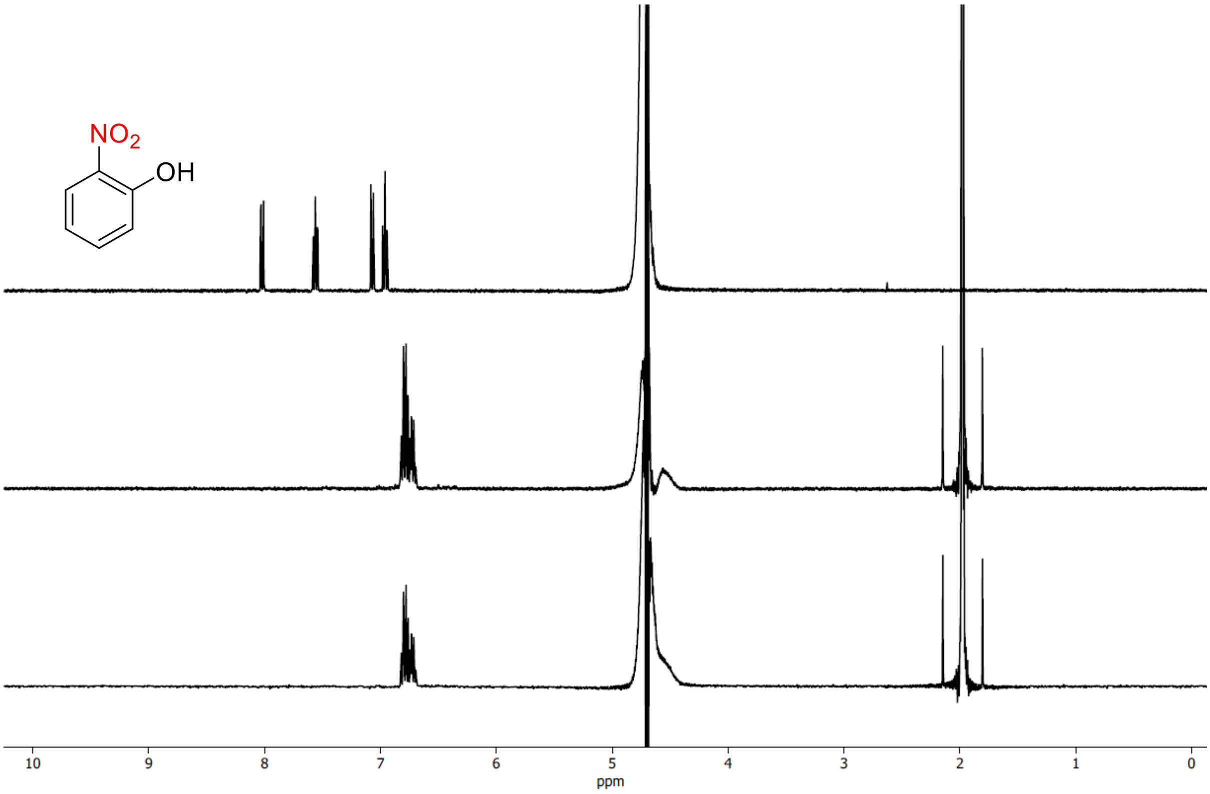

Figure 74 1H-NMR spectra (400 MHz, 298 K, 10% D2O in PB, 100 mM, pH 6.0, 10 % v/v acetonitrile) of substrate 5 and reaction mixture after hydrogenation using NiArg only (middle), and product after hydrogenation using NiArg/C catalyst system.

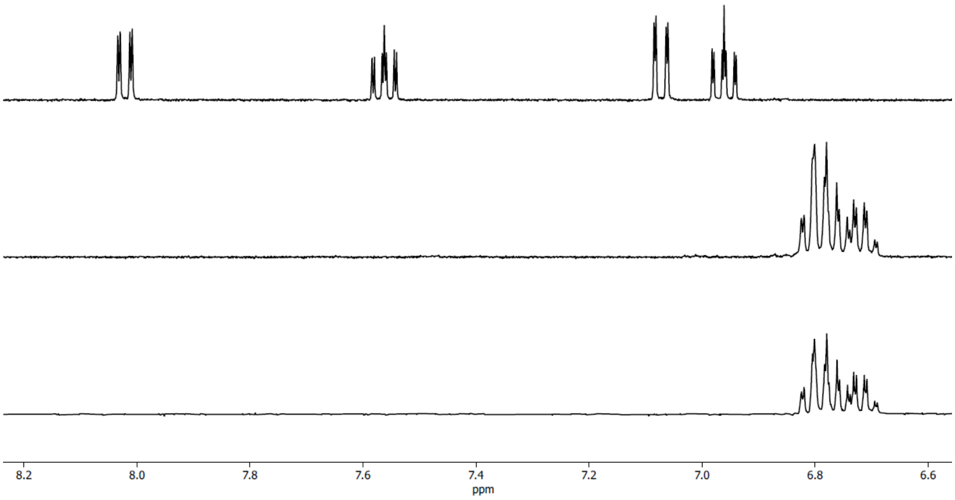

Figure 75 1H-NMR spectra (400 MHz, 298 K, 10% D2O in PB, 100 mM, pH 6.0, 10 % v/v acetonitrile) of substrate 5 and reaction mixture after hydrogenation using NiArg only (middle), and product after hydrogenation using NiArg/C catalyst system, in detail.

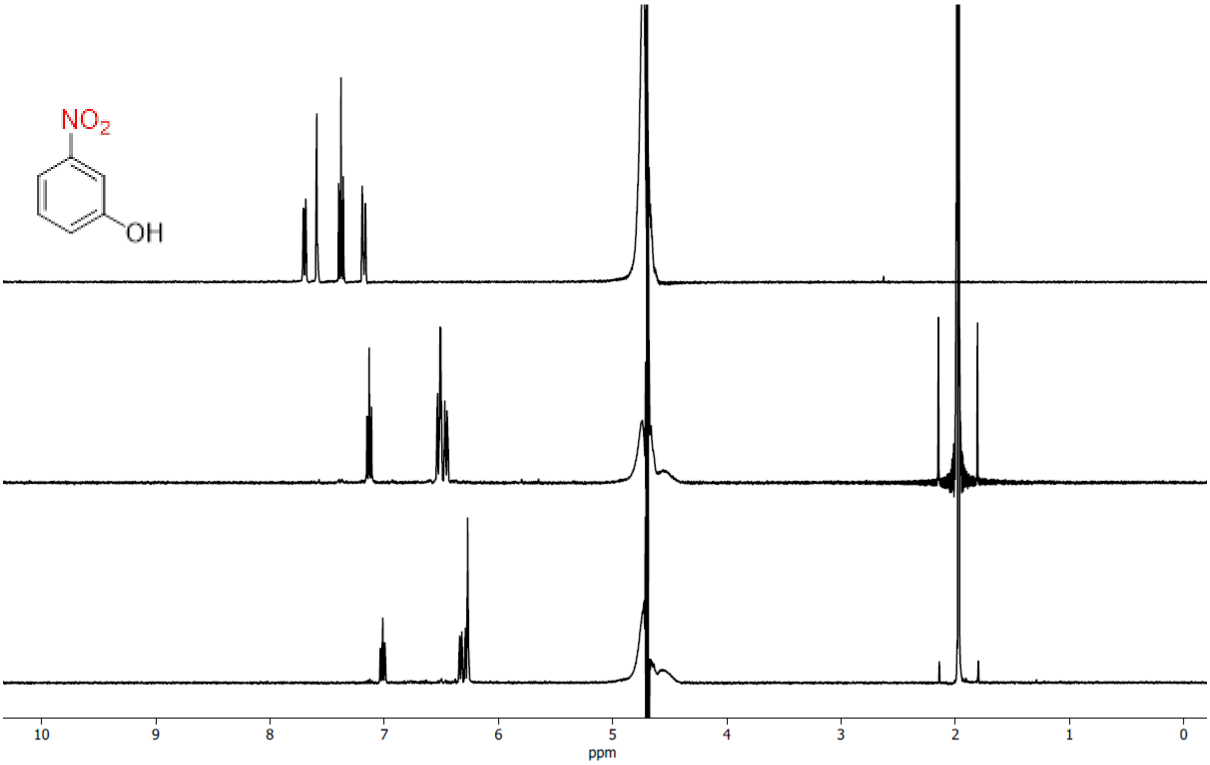

Figure 76 1H-NMR spectra (400 MHz, 298 K, 10% D2O in PB, 100 mM, pH 6.0, 10 % v/v acetonitrile) of substrate 6 and reaction mixture after hydrogenation using NiArg only (middle), and product after hydrogenation using NiArg/C catalyst system.

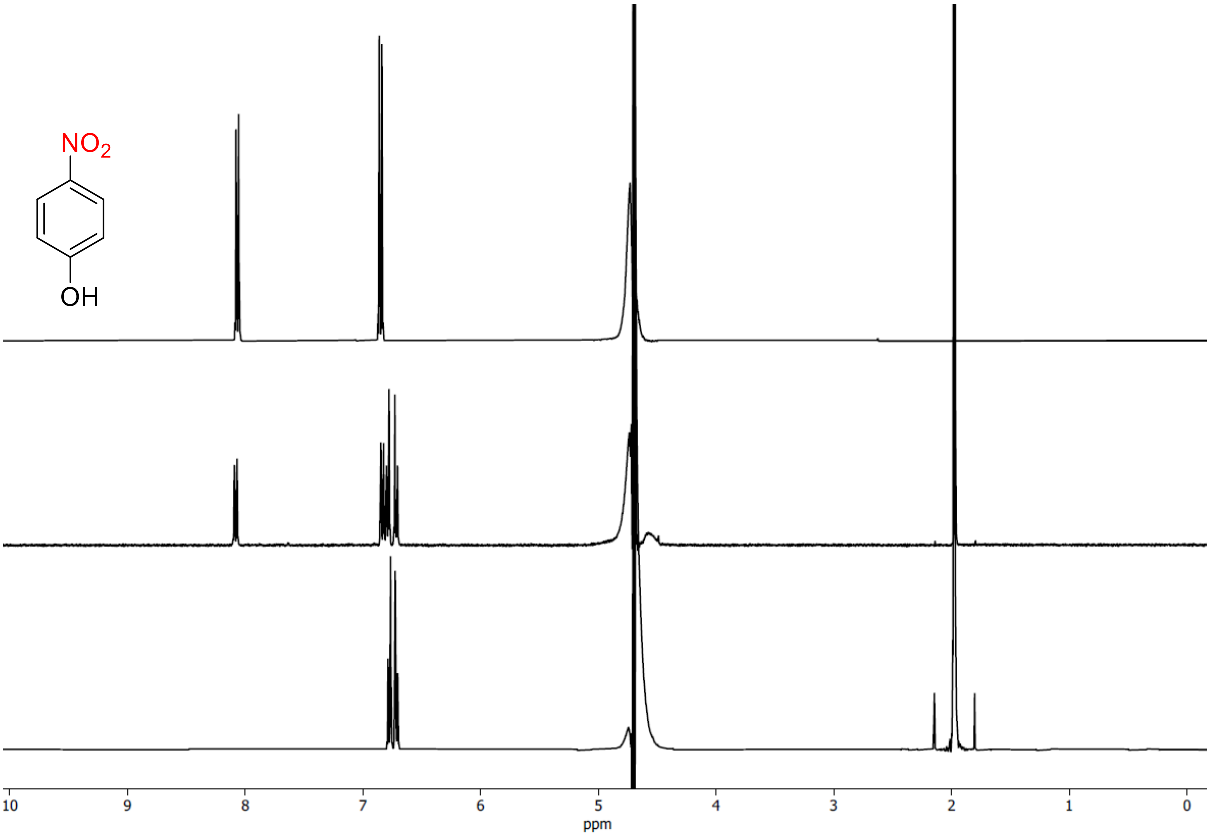

Figure 77 1H-NMR spectra (400 MHz, 298 K, 10% D2O in PB, 100 mM, pH 6.0, 10 % v/v acetonitrile) of substrate 7 and reaction mixture after hydrogenation using NiArg only (middle), and product after hydrogenation using NiArg/C catalyst system.

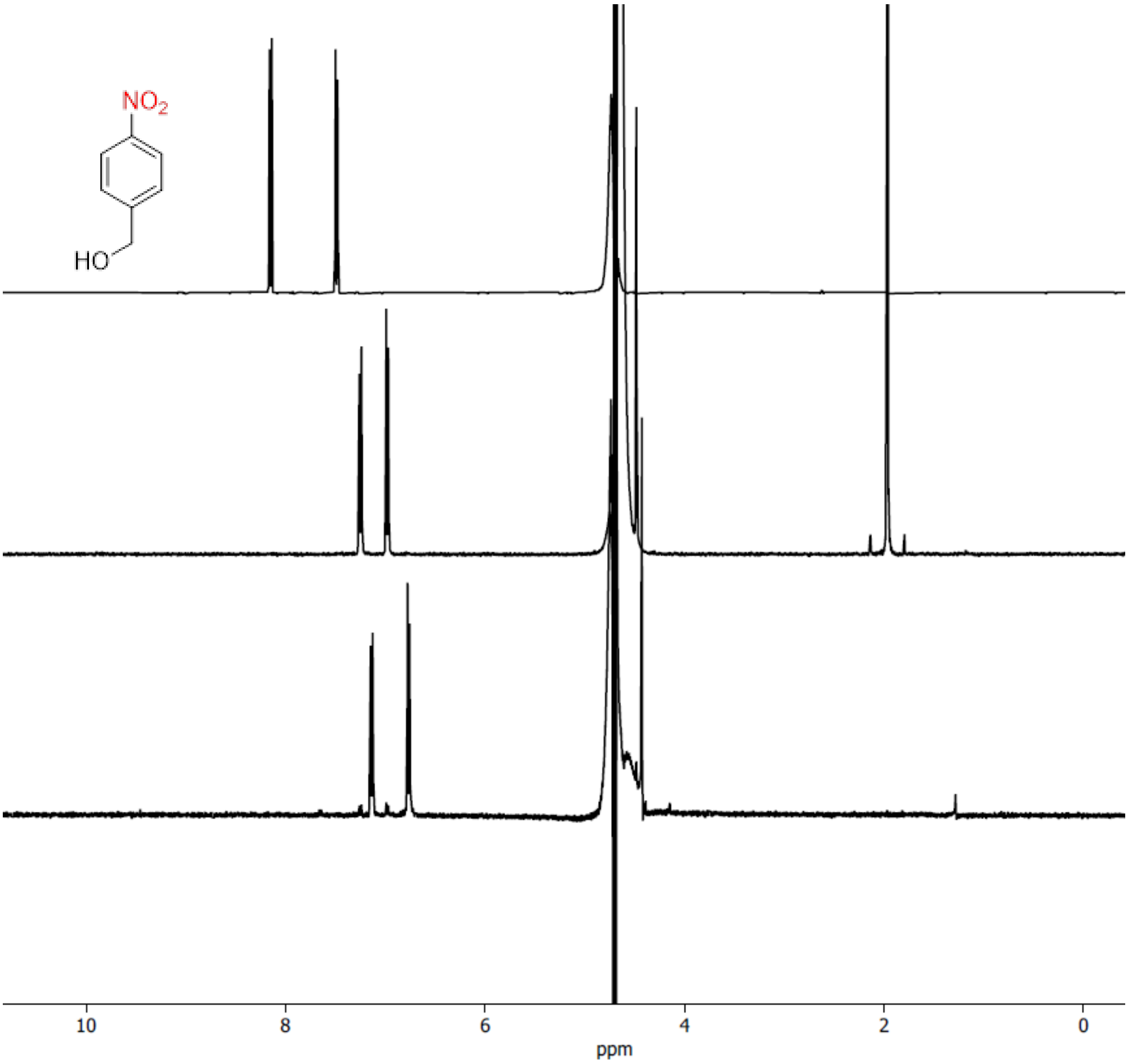

Figure 78 1H-NMR spectra (400 MHz, 298 K, 10% D2O in PB, 100 mM, pH 6.0, 10 % v/v acetonitrile) of substrate 8 and reaction mixture after hydrogenation using NiArg only (middle), and product after hydrogenation using NiArg/C catalyst system.

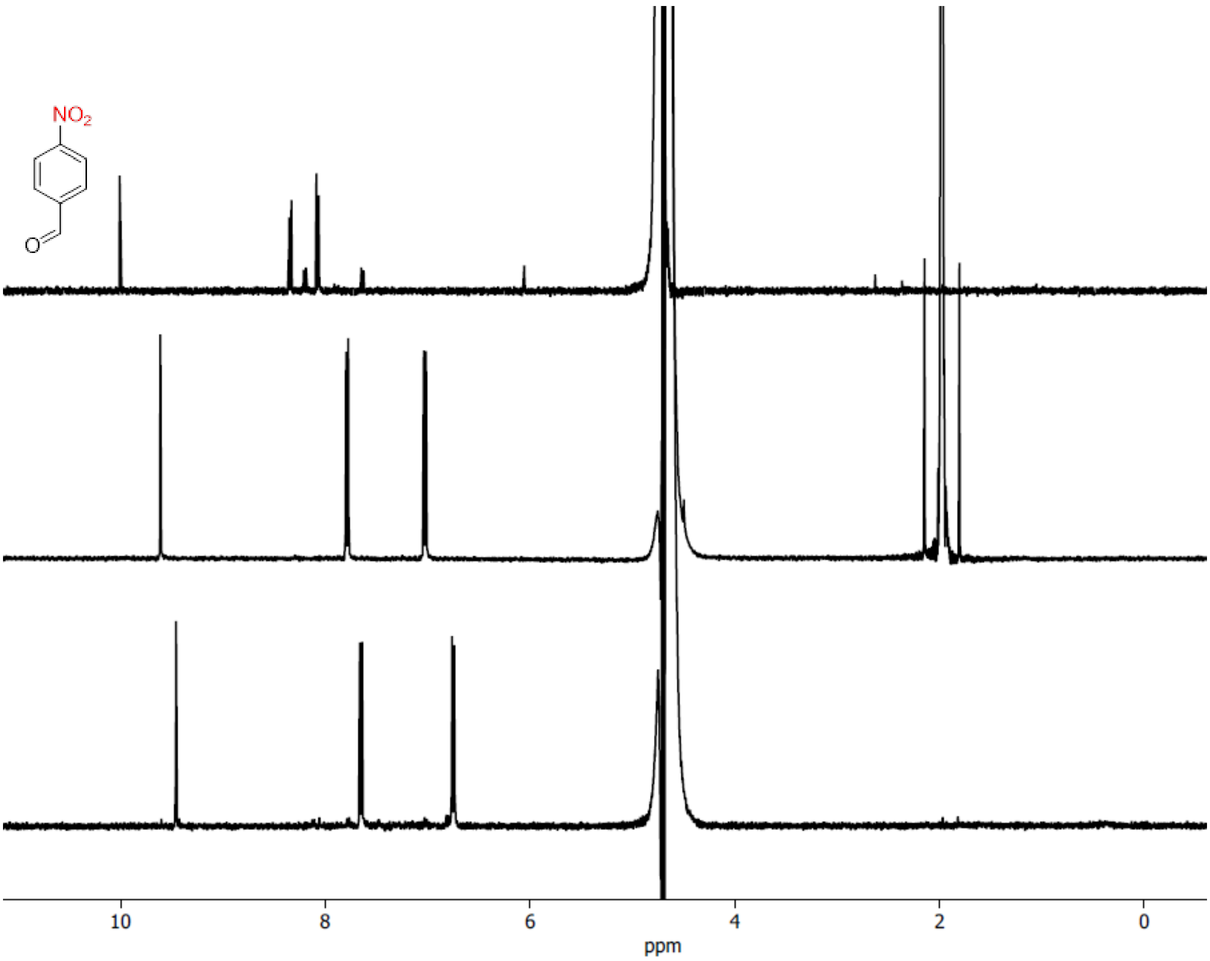

Figure 79 1H-NMR spectra (400 MHz, 298 K, 10% D2O in PB, 100 mM, pH 6.0, 10 % v/v acetonitrile) of substrate 9 and reaction mixture after hydrogenation using NiArg only (middle), and product after hydrogenation using NiArg/C catalyst system.

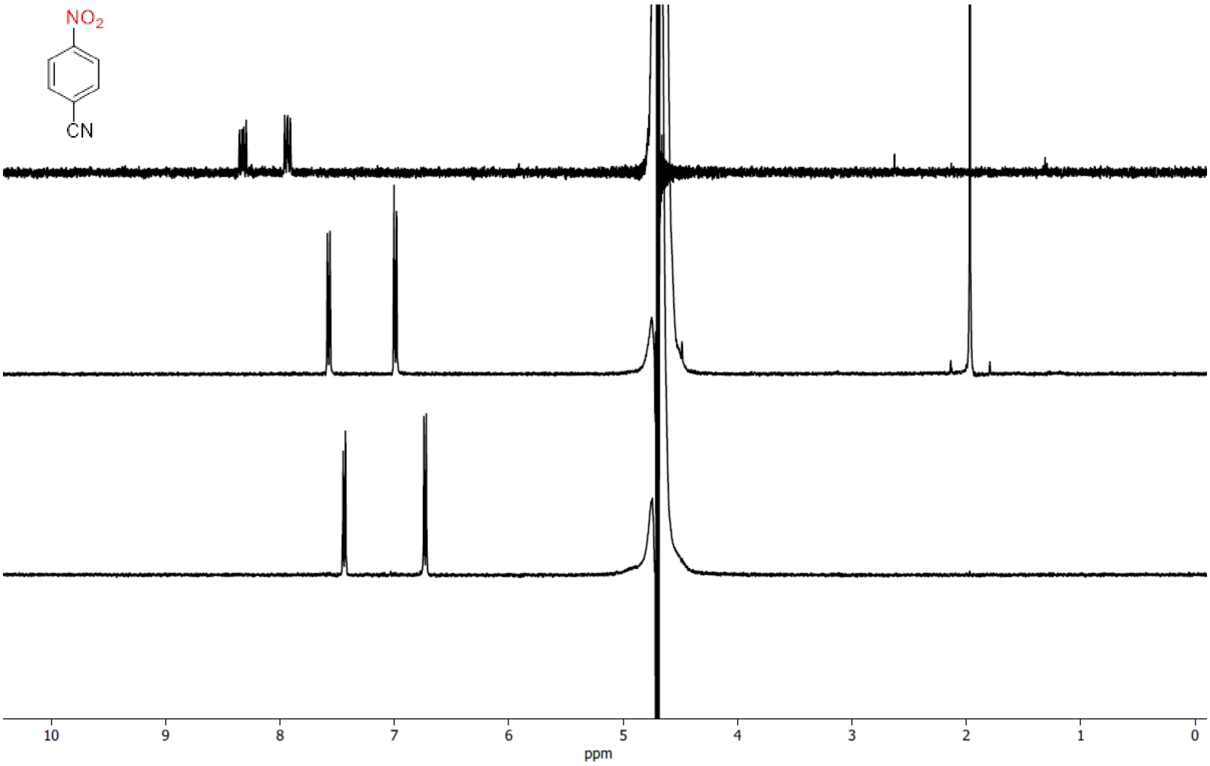

Figure 80 1H-NMR spectra (400 MHz, 298 K, 10% D2O in PB, 100 mM, pH 6.0, 10 % v/v acetonitrile) of substrate 10 and reaction mixture after hydrogenation using NiArg only (middle), and product after hydrogenation using NiArg/C catalyst system.

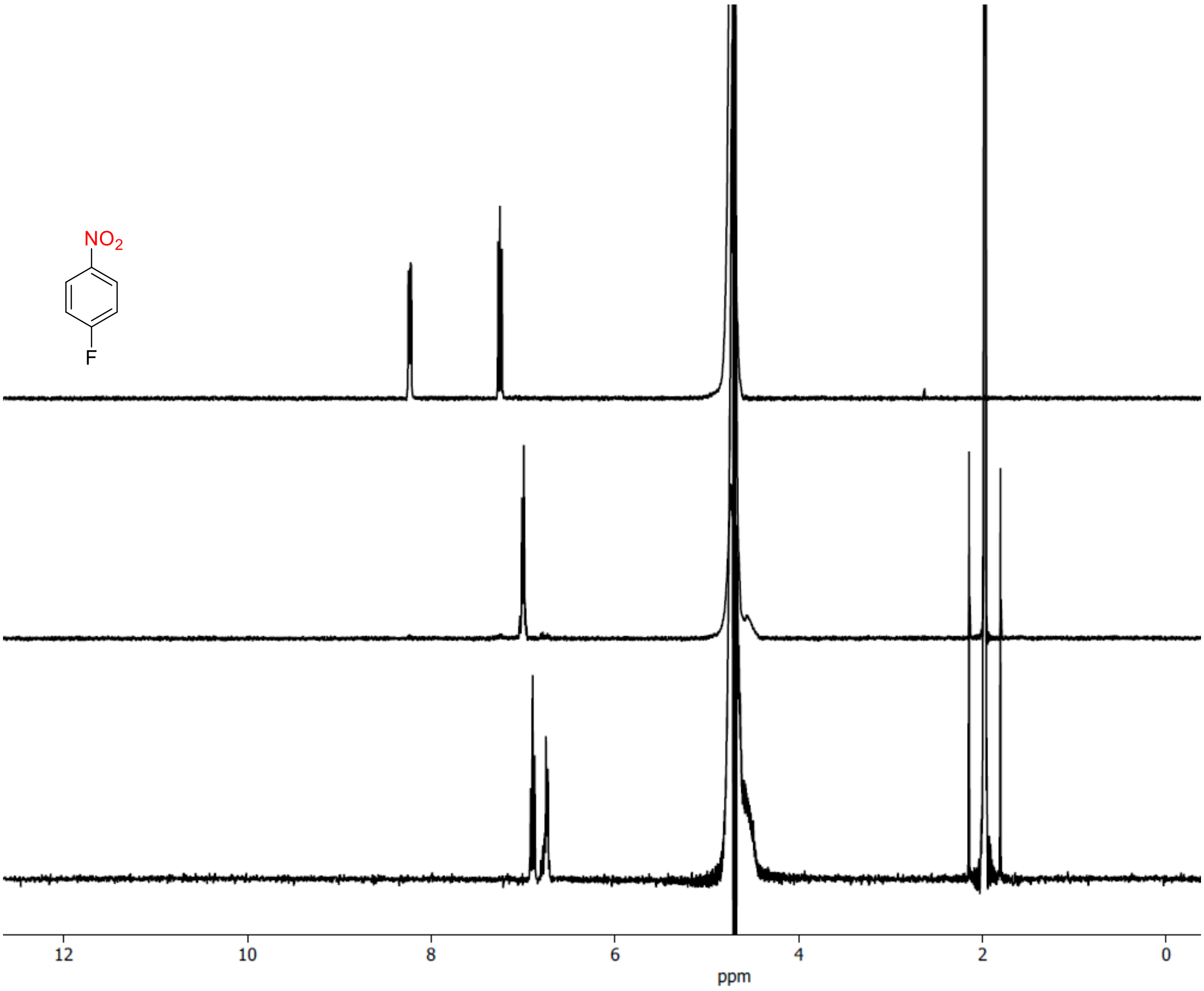

Figure 81 1H-NMR spectra (400 MHz, 298 K, 10% D2O in PB, 100 mM, pH 6.0, 10 % v/v acetonitrile) of substrate 11 and reaction mixture after hydrogenation using NiArg only (middle), and product after hydrogenation using NiArg/C catalyst system.

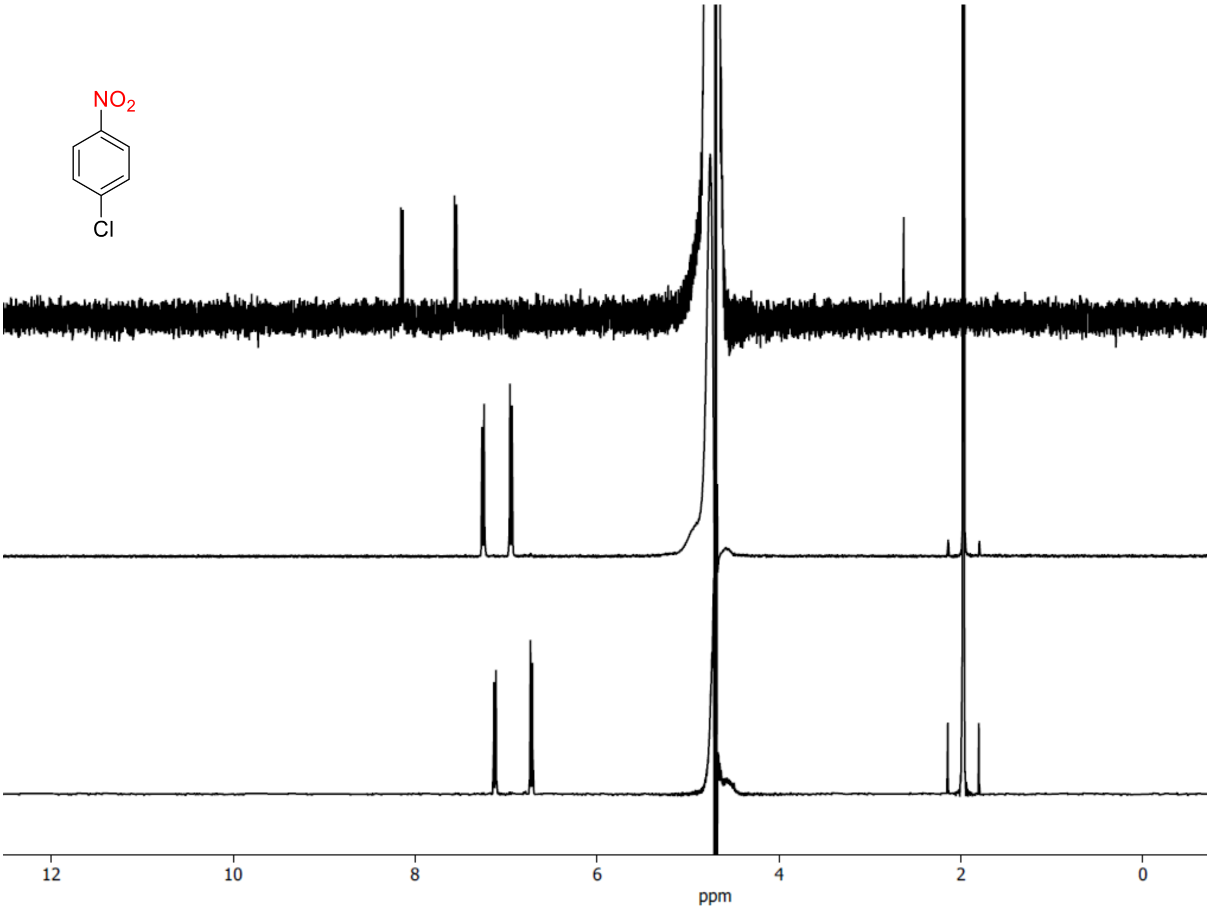

Figure 82 1H-NMR spectra (400 MHz, 298 K, 10% D2O in PB, 100 mM, pH 6.0, 10 % v/v acetonitrile) of substrate 12 and reaction mixture after hydrogenation using NiArg only (middle), and product after hydrogenation using NiArg/C catalyst system.

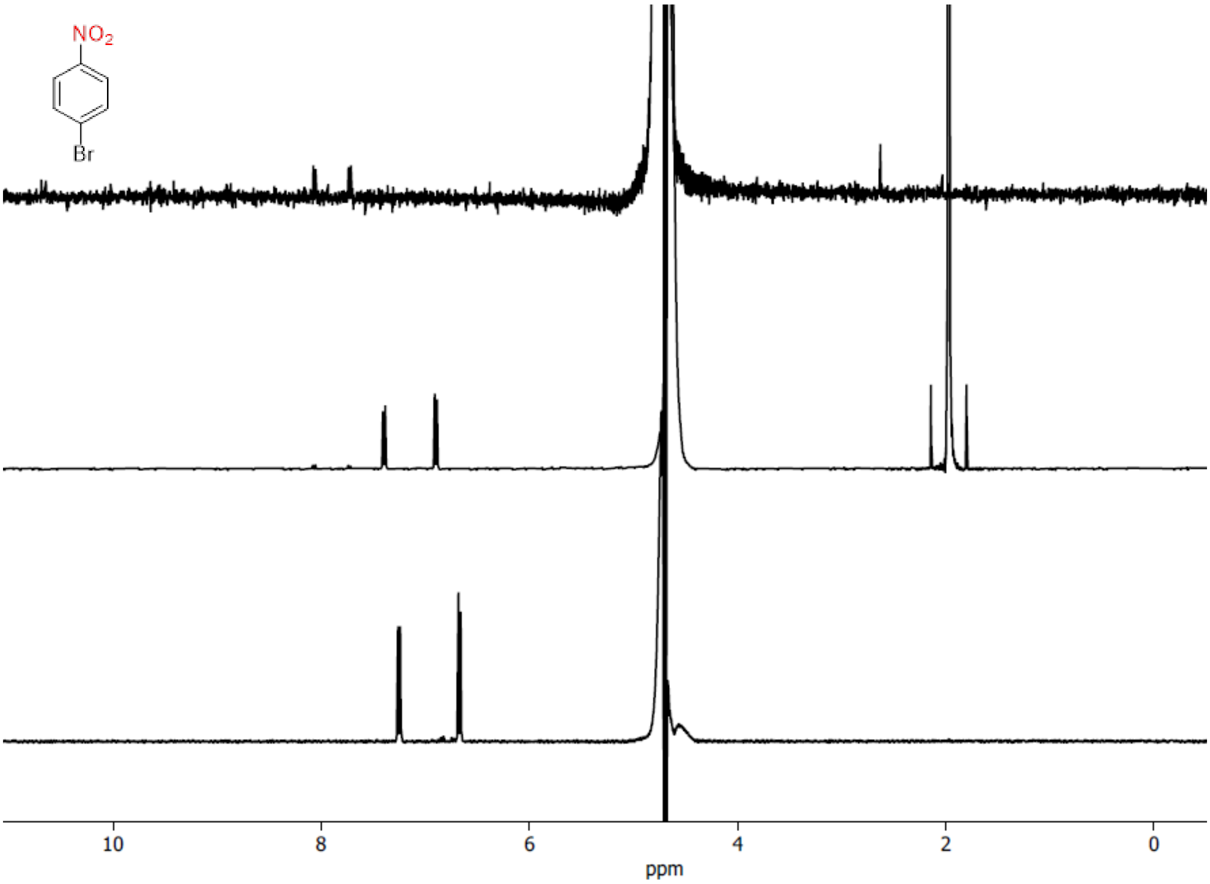

Figure 83 1H-NMR spectra (400 MHz, 298 K, 10% D2O in PB, 100 mM, pH 6.0, 10 % v/v acetonitrile) of substrate 13 and reaction mixture after hydrogenation using NiArg only (middle), and product after hydrogenation using NiArg/C catalyst system.

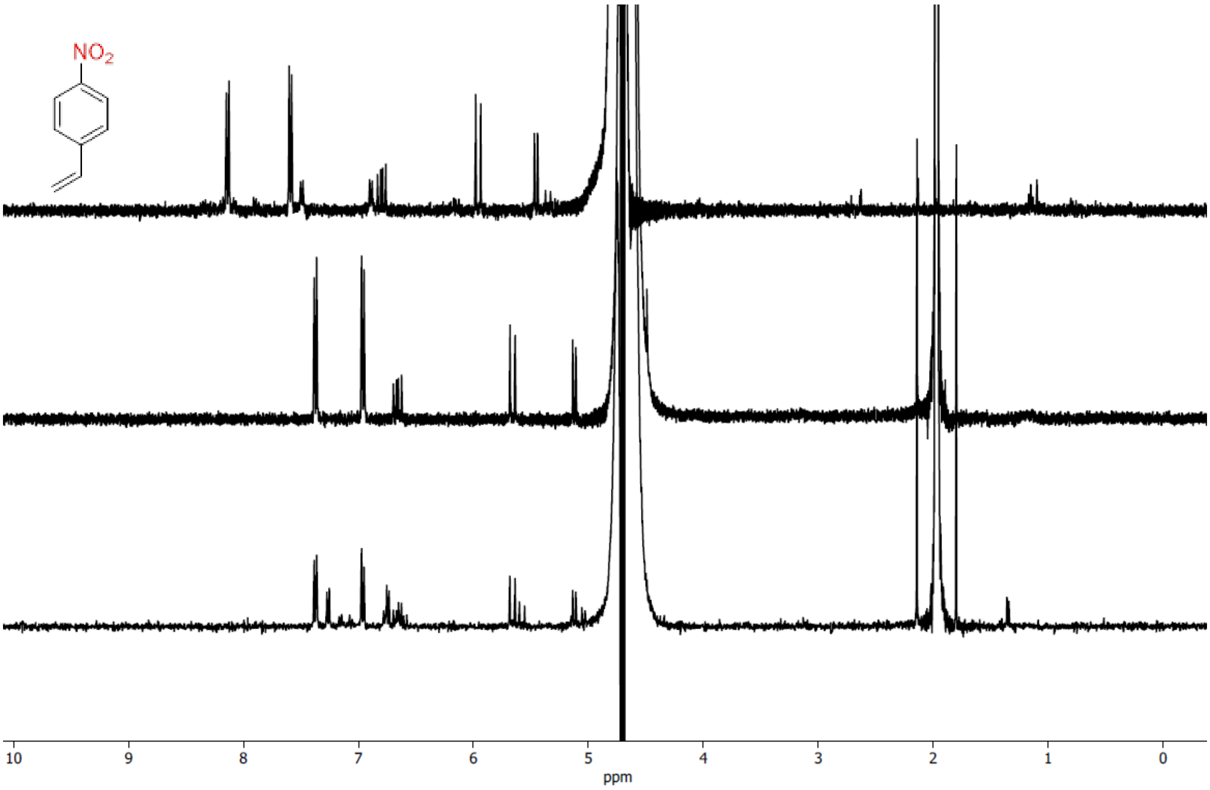

Figure 84 1H-NMR spectra (400 MHz, 298 K, 10% D2O in PB, 100 mM, pH 6.0, 10 % v/v acetonitrile) of substrate 14 and reaction mixture after hydrogenation using NiArg only (middle), and product after hydrogenation using NiArg/C catalyst system.

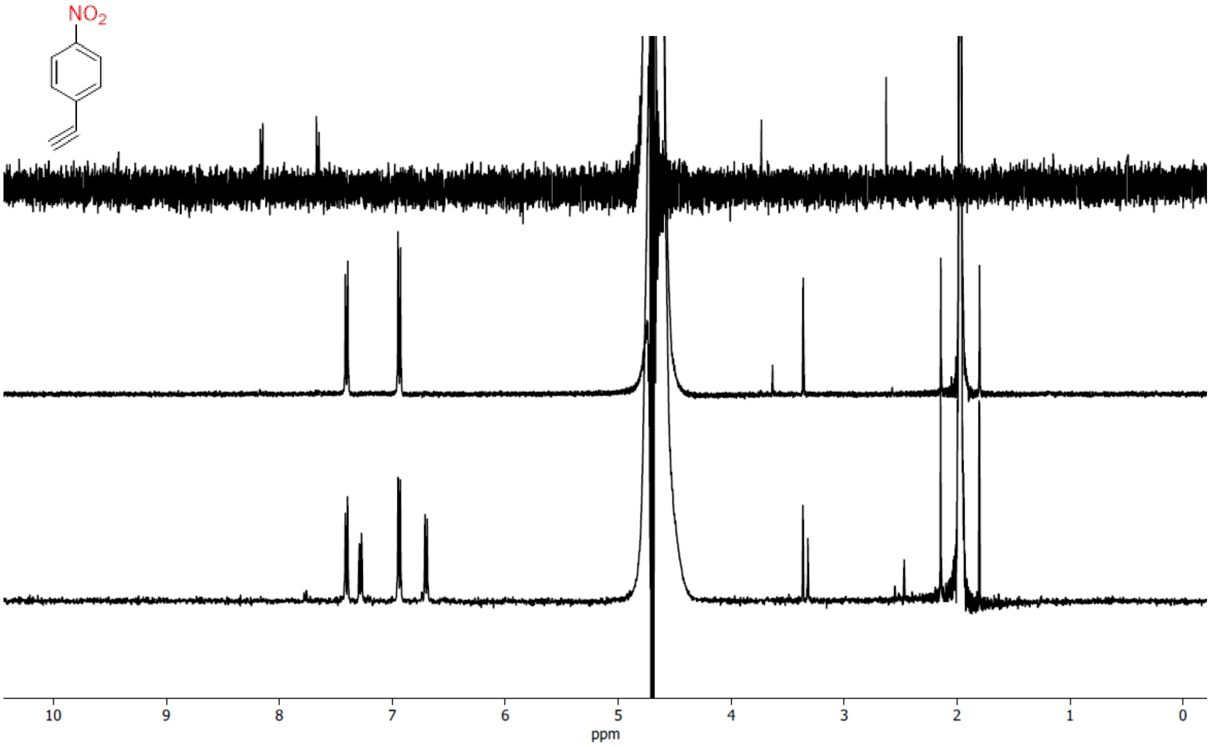

Figure 85 1H-NMR spectra (400 MHz, 298 K, 10% D2O in PB, 100 mM, pH 6.0, 10 % v/v acetonitrile) of substrate 15 and reaction mixture after hydrogenation using NiArg only (middle), and product after hydrogenation using NiArg/C catalyst system.

7.5 Conversion of nitro-compounds in water using NiArg only

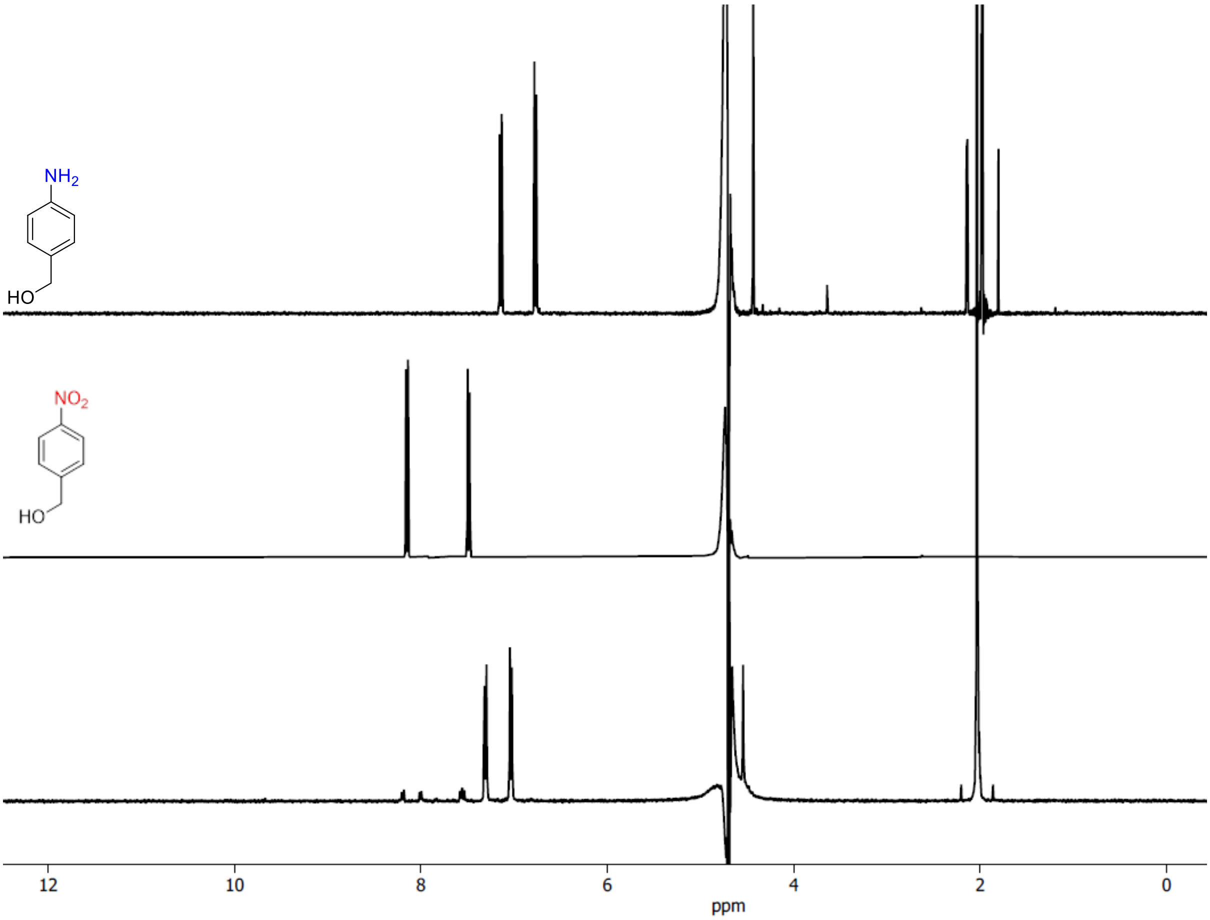

Figure 86 1H-NMR spectra (400 MHz, 298 K, 10% D2O in H_2O, 10 % v/v acetonitrile) of substrate 8 (middle) and reaction mixture after hydrogenation using NiArg only (bottom), amine spectrum shown (top).

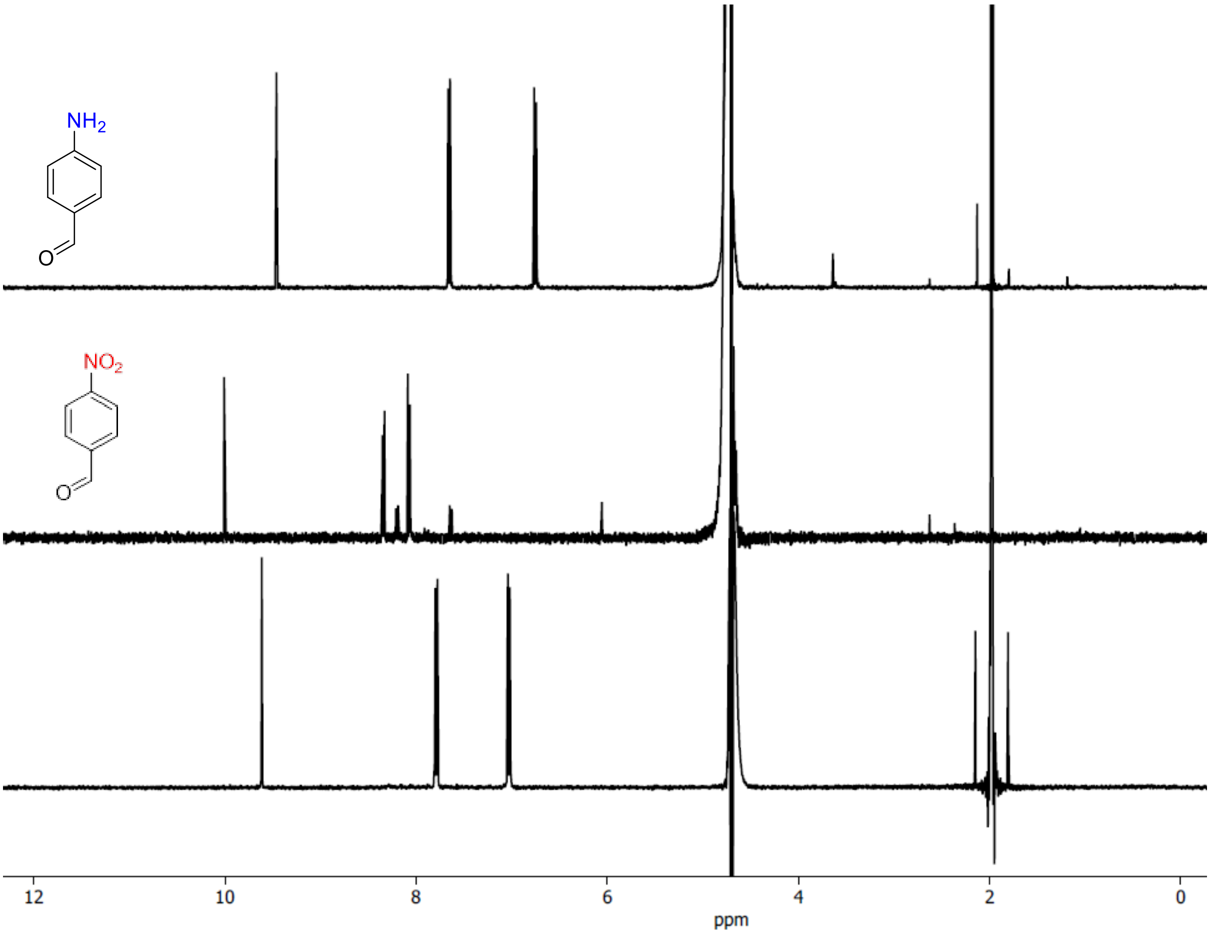

Figure 87 1H-NMR spectra (400 MHz, 298 K, 10% D2O in H_2O, 10 % v/v acetonitrile) of substrate 9 (middle) and reaction mixture after hydrogenation using NiArg only (bottom), amine spectrum shown (top).

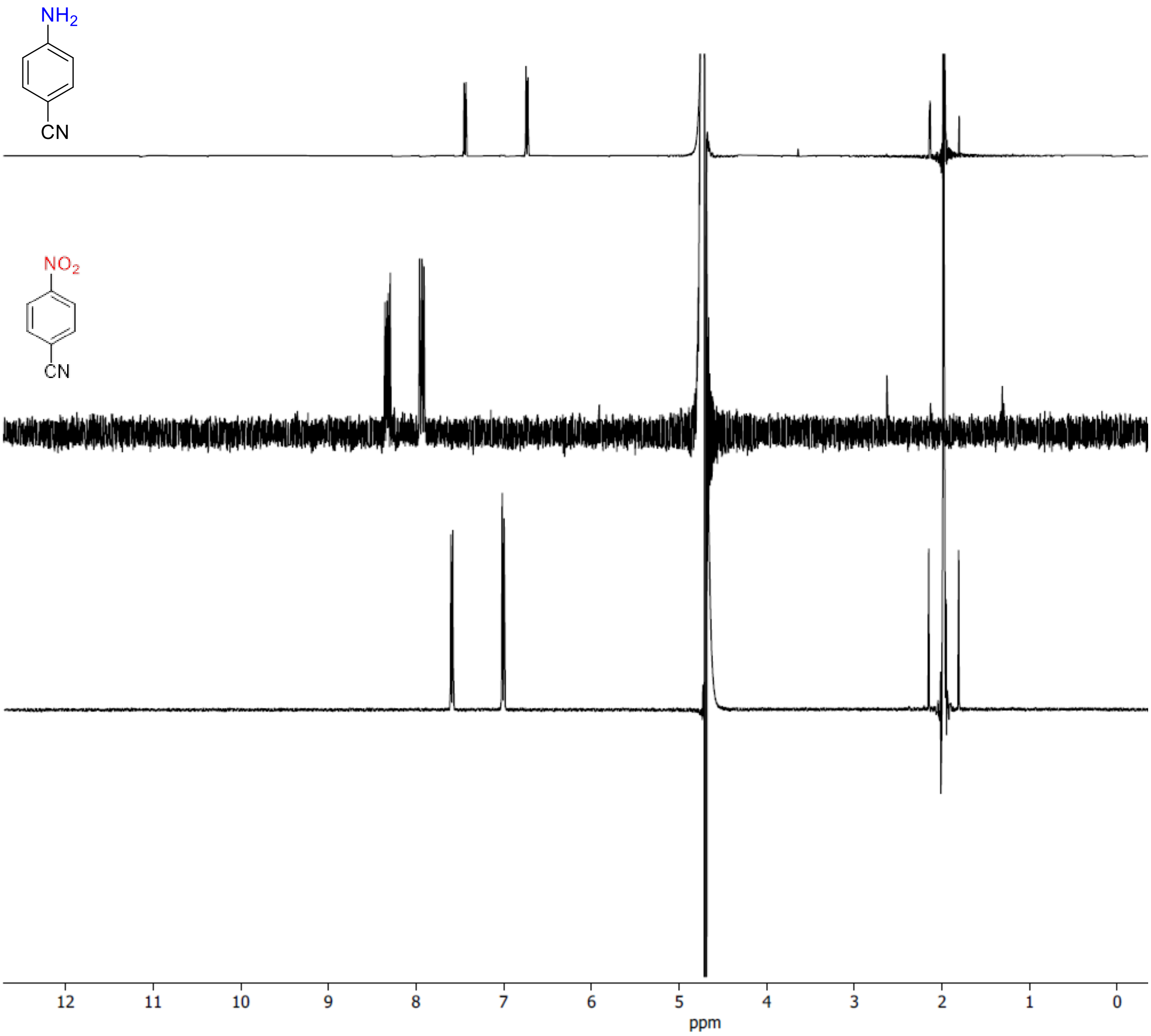

Figure 88 1H-NMR spectra (400 MHz, 298 K, 10% D2O in H_2O, 10 % v/v acetonitrile) of substrate 10 (middle) and reaction mixture after hydrogenation using NiArg only (bottom), amine spectrum shown (top).

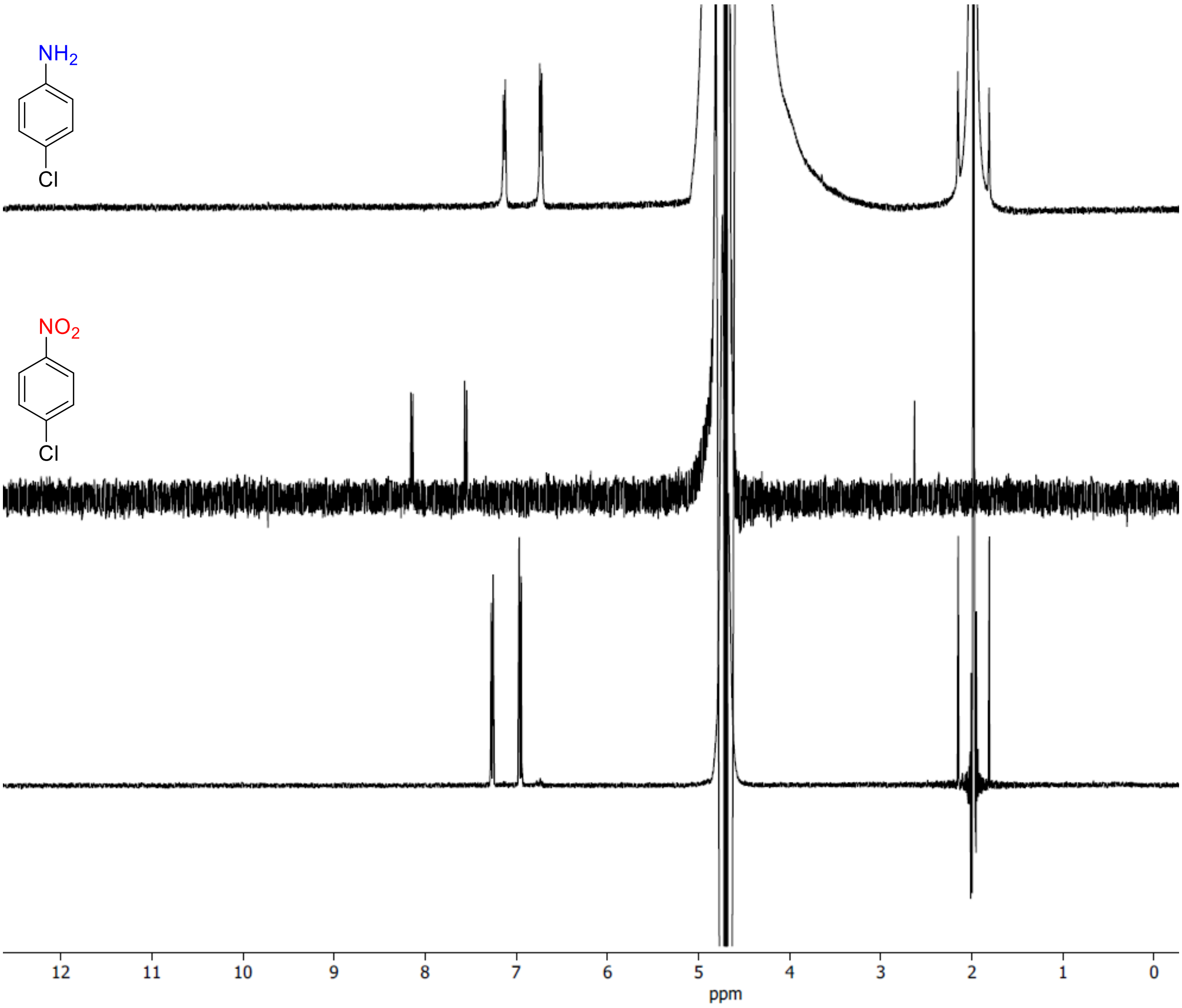

Figure 89 1H-NMR spectra (400 MHz, 298 K, 10% D2O in H_2O, 10 % v/v acetonitrile) of substrate 12 (middle) and reaction mixture after hydrogenation using NiArg only (bottom), amine spectrum shown (top).

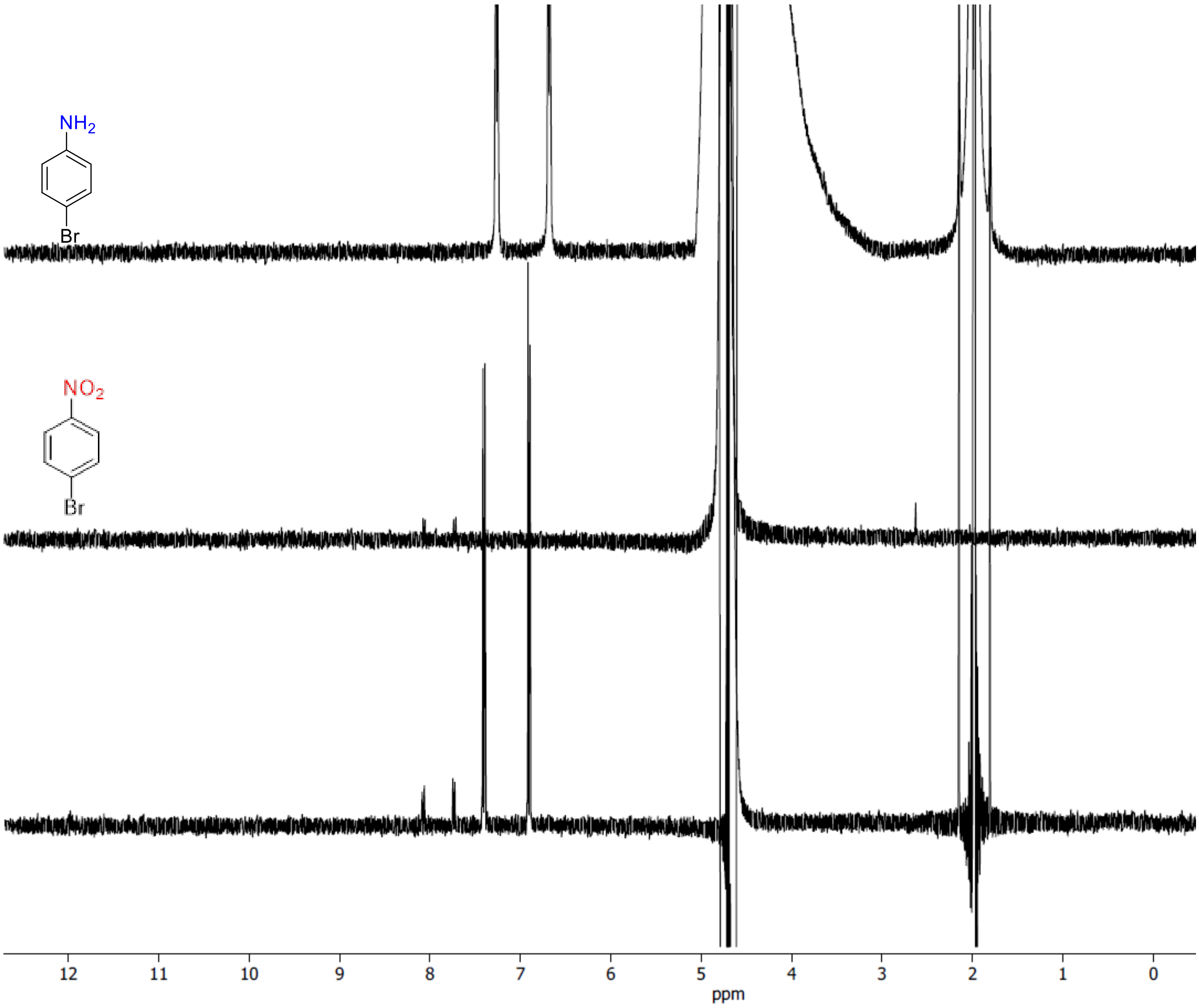

Figure 90 1H-NMR spectra (400 MHz, 298 K, 10% D2O in H_2O, 10 % v/v acetonitrile) of substrate 13 (middle) and reaction mixture after hydrogenation using NiArg only (bottom), amine spectrum shown (top).

7.6 Recycling of Ni/C catalyst systems

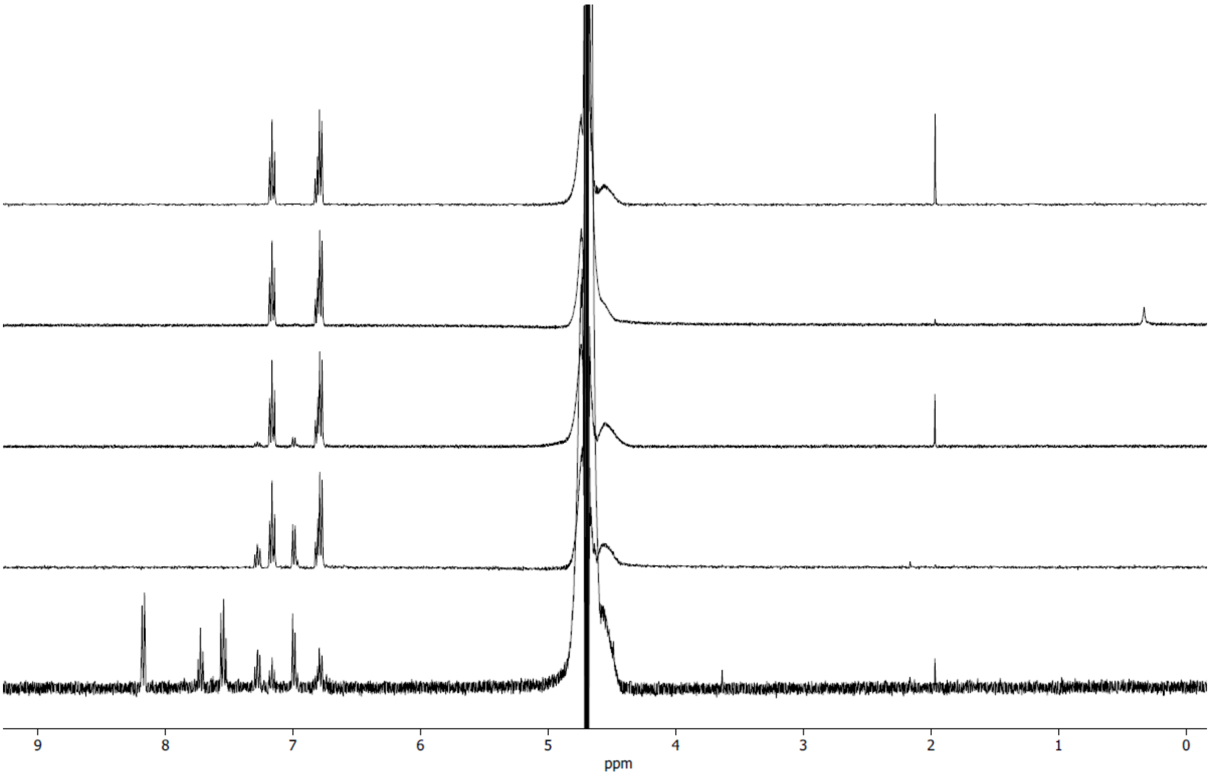

Figure 91 1H-NMR spectra (400 MHz, 298 K, 10% D2O in PB, 100 mM, pH 6.0) of reaction mixture after hydrogenation of substrate 1 using NiArg/C catalyst system, recollected after each experiment by centrifugation and used for the next cycle of hydrogenation, cycle 1 through 5 shown from top to bottom.

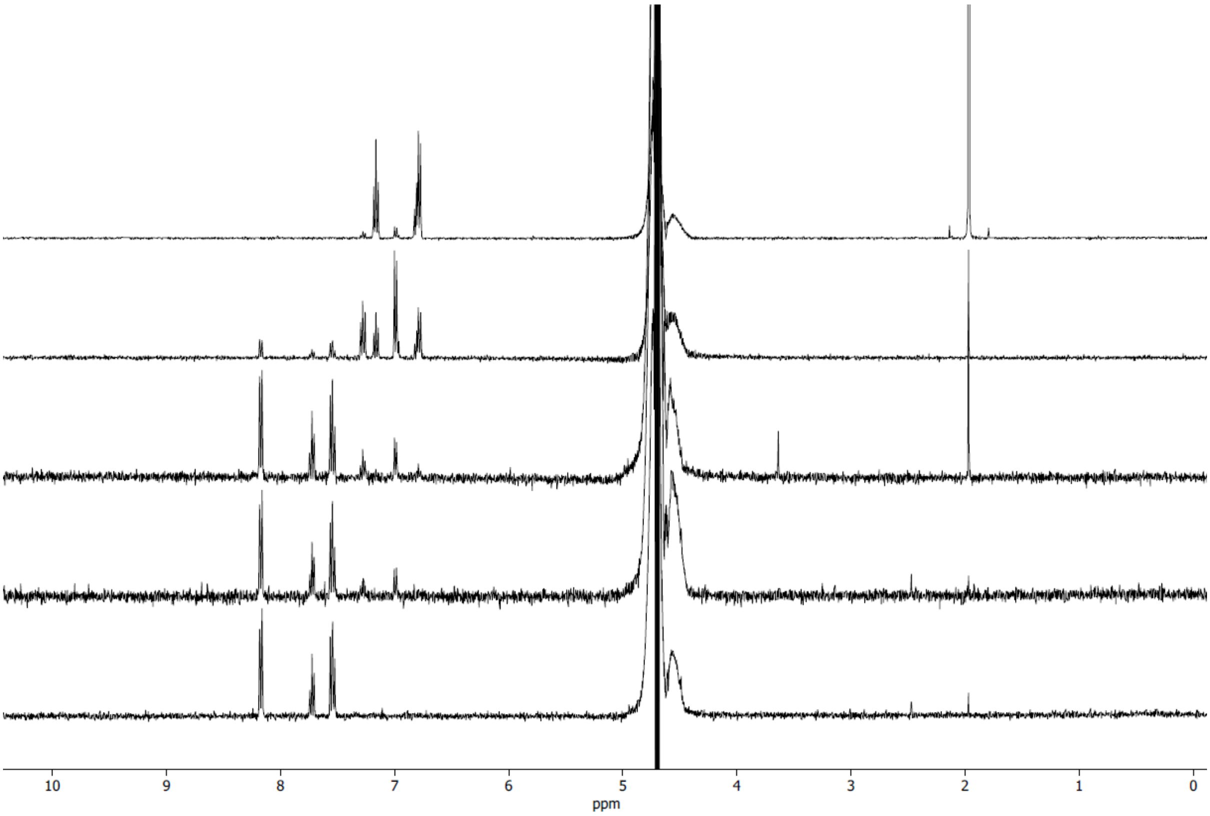

Figure 92 1H-NMR spectra (400 MHz, 298 K, 10% D2O in PB, 100 mM, pH 6.0) of reaction mixture after hydrogenation of substrate 1 using NiPyr/C catalyst system, recollected after each experiment by centrifugation and used for the next cycle of hydrogenation, cycle 1 through 5 shown from top to bottom.